Università degli Studi di Padova
Dipartimento di Fisica e Astronomia "Galileo Galilei"

Measurement of the D^0 meson production in Pb–Pb and p–Pb collisions with the ALICE experiment at the LHC

Direttore della Scuola: Ch.mo Prof. Andrea Vitturi
Supervisore: Dott. Andrea Dainese

Dottorando: Andrea Festanti

Scuola di dottorato di ricerca in Fisica
XXVII CICLO

Abstract

This thesis presents the measurement of the charmed D^0 meson production relative to the reaction plane in Pb–Pb collisions at the centre-of-mass energy per nucleon–nucleon collision of $\sqrt{s_{\mathrm{NN}}} = 2.76$ TeV, and the measurement of the D^0 production in p–Pb collisions at $\sqrt{s_{\mathrm{NN}}} = 5.02$ TeV with the ALICE detector at the CERN Large Hadron Collider.

The D^0 azimuthal anisotropy with respect to the reaction plane is sensitive to the interaction of the charm quarks with the high-density strongly-interacting medium formed in ultra-relativistic heavy-ion collisions and, thus, to the properties of this state of matter. In particular, this observable allows to establish whether low-momentum charm quarks participate in the collective expansion of the system and whether they can reach thermal equilibrium with the medium constituents. The azimuthal anisotropy is quantified in terms of the second coefficient v_2 in a Fourier expansion of the D^0 azimuthal distribution and in terms of the nuclear modification factor R_{AA}, measured in the direction of the reaction plane and orthogonal to it. The measurement of the D^0 production in p–Pb collisions is crucial to disentangle the effects induced by cold nuclear matter from the final state effects induced by the hot medium formed in Pb–Pb collisions.

The D^0 production is measured in both systems by reconstructing the two-prong hadronic decay $\mathrm{D}^0 \rightarrow \mathrm{K}^-\pi^+$ in the central rapidity region, exploiting the separation of the decay vertex from the primary vertex. The raw signal is obtained with an invariant mass analysis, and corrected for selection and reconstruction efficiency.

A positive elliptic flow v_2 is observed in Pb–Pb collisions in the centrality class 30–50%, with a mean value of $0.204^{+0.099}_{-0.036}$ in the interval $2 < p_{\mathrm{T}} < 6$ GeV/c, which decreases towards more central collisions. Consequently, the nuclear modification factor shows a stronger suppression in the direction orthogonal to the reaction plane. The v_2 and the R_{AA} measured in two azimuthal regions with respect to the reaction plane are compared to theoretical calculations of charm quark transport and energy loss in high-density strongly-interacting matter. The models that include substantial elastic interactions with an expanding medium provide a good description of the observed anisotropy.

The D^0 nuclear modification factor R_{pPb} in p–Pb collisions is compatible with unity within uncertainties. The measured R_{pPb} is compared to theoretical models including initial state effects, as well as to the nuclear modification factor measured in central Pb–Pb collisions. The D^0 R_{pPb} results are consistent with the modification of the nucleon parton distribution functions induced by the nuclear environment, and provide experimental evidence that the modification of the D meson momentum spectrum observed in Pb–Pb with respect to pp collisions is due to strong final state effects induced by the hot medium.

Riassunto

La tesi presenta la misura della produzione di mesoni D^0 rispetto al piano di reazione in collisioni Pb–Pb all'energia nel centro di massa di $\sqrt{s_{\mathrm{NN}}} = 2.76$ TeV per coppia di nucleoni e la misura della produzione di D^0 in collisioni p–Pb all'energia di $\sqrt{s_{\mathrm{NN}}} = 5.02$ TeV con l'esperimento ALICE situato al Large Hadron Collider del CERN.

L'anisotropia azimutale dei mesoni D^0 rispetto al piano di reazione è sensibile alle interazioni del quark charm con il mezzo ad alta densità e fortemente interagente prodotto in collisioni tra ioni pesanti ad energia ultra-relativistica e, di conseguenza, alle proprietà di questo stato della materia. In particolare, permette di stabilire se i quark charm partecipano all'espansione collettiva del sistema e se raggiungono l'equilibrio termico con i costituenti del mezzo. L'anisotropia azimutale è quantificata tramite il secondo coefficiente v_2 dello sviluppo in serie di Fourier della distribuzione azimutale dei mesoni D^0 e tramite la misura del fattore di modifica nucleare R_{AA} nel piano di reazione e nella direzione ortogonale ad esso. La misura della produzione di D^0 in collisioni p–Pb permette di studiare gli effetti indotti dalla materia nucleare fredda, in modo da poterli distinguere da quelli indotti dal mezzo denso fortemente interagente prodotto in collisioni Pb–Pb.

La produzione di mesoni D^0 è stata misurata attraverso la ricostruzione dei decadimenti adronici a due corpi $\mathrm{D}^0 \to \mathrm{K}^-\pi^+$ nella regione centrale di rapidità, sfruttando la separazione dei vertici secondari di decadimento rispetto al vertice primario d'interazione. Il segnale è stato ottenuto attraverso un'analisi della distribuzione di massa invariante e corretto per l'efficienza di ricostruzione e selezione dei decadimenti.

Il coefficiente di flusso ellittico v_2 dei mesoni D^0 misurato in collisioni Pb–Pb nella classe di centralià 30–50% è positivo, il valore medio nell'intervallo $2 < p_{\mathrm{T}} < 6$ GeV/c è pari a $0.204^{+0.099}_{-0.036}$. Di conseguenza, il fattore di modifica nucleare è minore nella direzione ortogonale al piano di reazione. Il v_2 osservato decresce all'aumentare della centralità delle collisioni. Il v_2 e l'R_{AA} misurato in due regioni azimutali ortogonali rispetto al piano di reazione sono stati confrontati con calcoli teorici per il trasporto e la perdita di energia dei quark charm nella materia densa fortemente interagente. L'anisotropia osservata è descritta dai modelli che includono le interazioni elastiche tra i quark all'interno di un mezzo in espansione.

Il fattore di modifica nucleare dei mesoni D^0 R_{pPb} è compatibile con l'unità entro le incertezze. R_{pPb} è stato confrontato con predizioni teoriche che descrivono gli effetti di stato iniziale e con il fattore di modifica nucleare misurato in collisioni Pb–Pb centrali. I risultati sono consistenti con effetti dovuti alla modifica delle funzioni di distribuzione partoniche all'interno dei nucleoni legati e dimostrano che la modifica della distribuzione del momento trasverso dei mesoni D osservata in collisioni Pb–Pb rispetto a quella in collisioni pp è dovuta alla perdita di energia dei quark charm nel mezzo denso fortemente interagente.

Contents

Introduction

This thesis presents the measurement of the azimuthal anisotropy of the D^0 meson production in Pb–Pb collisions at $\sqrt{s_{NN}} = 2.76$ TeV and the measurement of the production of prompt D^0 mesons in p–Pb collisions at $\sqrt{s_{NN}} = 5.02$ TeV, using the $D^0 \to K^-\pi^+$ channel, with the ALICE detector.

The strong interaction between quarks is described by the theory of Quantum-Chromo Dynamics (QCD). QCD is characterized by the fact that the gauge vector bosons that mediate the interaction, the gluons, carry a colour charge and, thus, they can interact with each other. The gluon self-coupling is related to two peculiar properties of the theory: asymptotic freedom and confinement. Asymptotic freedom allows to consider partons as free within hadrons, in processes with high momentum transfer, where the coupling of the interaction is very small. On the other hand, the coupling of the strong interaction increases when the exchanged momentum decreases and it reaches a potential wall for distances of the order of the hadron size. Quarks and gluons are thus confined within hadrons.

Asymptotic freedom suggests that nuclear matter can change state when the strong interaction among quarks and gluons is weakened by increasing density or temperature of the matter. In particular, at extremely high temperature or density, a deconfined Quark-Gluon Plasma (QGP) phase is expected. In the QGP phase the density of quarks and gluons is so high that partons interact directly and are not confined into hadrons. The hot Big Bang model of cosmology assumes that the early Universe was in a state of plasma of deconfined quarks and gluons until about 10 μs after the Big Bang, and that it has reached the hadronic phase during the expansion and cooling down of the system. The structure of the QCD phase diagram has been studied on the basis of thermodynamical considerations and QCD calculations. Experimentally, the deconfined phase can be investigated with ultra-relativistic heavy-ion collisions, since the energy density and temperature reached in these collisions allow to form the QGP.

High energy beams of heavy ions have been available since 1990s at the Alternating Gradient Synchrotron (AGS) and at the Super Proton Synchrotron (SPS) at CERN. There, several fixed-target experiments gave results, on various physical observables, indicating that a new state of matter is formed in the early stage of the collisions. Heavy

ion physics entered the collider era with the Relativistic Heavy Ion Collider (RHIC, since 2000) and the Large Hadron Collider (LHC, since 2010). The results from the experiments at these two colliders have provided further evidence for the QGP, and the deconfined phase is being investigated at different collision energies, up to $\sqrt{s_{\rm NN}} =$ 2.76 TeV at LHC.

The first chapter of this thesis, after an introduction on the basics of QCD, describes the order parameters of the phase transition. Lattice QCD calculations, that allow to estimate the order parameters and the critical temperature of the phase transition, are also introduced. The second part of the chapter is devoted to a review of the main results obtained by the experiments at the CERN LHC in Pb–Pb collisions at the energy of $\sqrt{s_{\rm NN}} = 2.76$ TeV.

The second chapter of the thesis is focused on heavy-quark production in proton–proton, p–Pb and Pb–Pb collisions. Charm and beauty quarks are important probes of the QGP since they are produced in hard scattering processes in the early stage of the ion–ion collision before the medium is formed. They, thus, experience the full evolution of the system, interacting with the constituents of the medium. Heavy quarks can be used to investigate both initial state and final state effects induced by "cold" (ordinary) nuclear matter and the QGP, respectively. In particular, charm and beauty are expected to lose energy in the medium via both collisional and radiative mechanisms depending on the properties of the QGP. In Au–Au and Pb–Pb collisions a strong modification of the $\rm D^0$ meson $p_{\rm T}$ distribution was measured with respect to pp at RHIC and LHC. In order to disentangle the effects induced by the deconfined medium from the cold nuclear matter effects, it is crucial to measure the modification of $\rm D^0$ production in p–Pb collisions with respect to pp collisions. This measurement is one of the goals of this thesis.

Correlation patterns were observed in nucleus–nucleus collisions at RHIC and LHC for several hadron species, demonstrating that the multiple interactions in the medium generate a collective flow of the outgoing particles. This behaviour is investigated through the measurement of the azimuthal anisotropy of the final state hadrons. Low-$p_{\rm T}$ heavy quarks or heavy quarks quenched by in-medium energy loss can also participate in the collective expansion of the system. The measurement of the $\rm D^0$ meson azimuthal anisotropy in Pb–Pb collisions at $\sqrt{s_{\rm NN}} = 2.76$ TeV is crucial to determine whether charm quarks participate in the collective expansion. This is one of the main objectives of this thesis.

The experimental observables that were studied to address the objectives of this thesis are defined in chapter 4. The azimuthal anisotropy of the $\rm D^0$ production in Pb–Pb collisions is measured through:

– the elliptic flow v_2,

– the azimuthal dependence of the nuclear modification factor with respect to pp collisions $R_{\rm AA}$.

The observables that were measured to study the $\rm D^0$ production in minimum-bias p–Pb collisions are:

– the $p_{\rm T}$- and y- differential cross sections,

– the nuclear modification factor with respect to pp collisions $R_{\rm pPb}$,

– the nuclear modification with respect to pp collisions in event-activity classes $Q_{\rm pPb}$,

– the yields as a function of charged-particle multiplicity.

A Large Ion Collider Experiment (ALICE) is the heavy-ion dedicated experiment at the LHC. An overview of the ALICE setup and performance, focusing on the detectors that are used for the charm analysis, is given in chapter 3. The analysis of charmed hadrons is based on the reconstruction of secondary decay vertices, displaced of a few hundred microns from the primary vertex. The detector that is fundamental for the reconstruction of primary and secondary vertices is the Silicon Pixel Detector, which is part of the Inner Tracking System.

The fifth chapter presents the $\rm D^0$ meson analysis in Pb–Pb and p–Pb collisions. These mesons are reconstructed via their weak hadronic decay channel $\rm D^0 \rightarrow K^-\pi^+$, exploiting the secondary vertex reconstruction and the decay particle identification. The study of the systematic uncertainties is presented in chapter 6.

The two last chapters present the results on the azimuthal anisotropy of $\rm D^0$ production in Pb–Pb collisions, and on the study of $\rm D^0$ production in p–Pb collisions, respectively. The $\rm D^0$ v_2 and $R_{\rm AA}$ azimuthal dependence results are presented and compared to theoretical models in chapter 8. Chapter 9 focuses on the results obtained in p–Pb collisions: the minimum-bias $\rm D^0$ production cross section and $R_{\rm pPb}$, compared with models including initial state effects, and the event-activity dependence of $\rm D^0$ production.

1

Physics of Ultra-Relativistic Heavy-Ion Collisions

The strong interaction between the elementary constituents of matter (quarks and gluons) is described by the theory of Quantum Chromodynamics (QCD). The basic ingredients of this quantum field theory will be explained in Section 1.1 and its peculiar properties driven by the running of the strong coupling constant will be addressed in Section 1.2. These properties lead to the prediction that strongly-interacting matter can exist in different phases depending on the temperature and the density of the system. Nuclear matter at extremely high temperatures and energy densities is obtained with ultra-relativistic heavy-ion collisions, which allow to create a state of matter where quarks and gluons are interacting without being confined into hadrons. According to the hot Big Bang model, this state of matter should have appeared after the electro-weak phase transition, a few microseconds after the Big Bang. The Lattice QCD approach, which is introduced in Section 1.3, allows to obtain quantitative predictions on the basic properties of the QCD phase diagram and on the phase transition, which are described in Section 1.4. The second part of the chapter (Section 1.5) is devoted to a review of the first results obtained by the experiments at the CERN Large Hadron Collider (LHC) in Pb–Pb collisions at the energy of $\sqrt{s_{\mathrm{NN}}} = 2.76$ TeV per nucleon–nucleon (NN) collision, also compared with the measurements performed at lower energies at the Relativistic Heavy-Ion Collider (RHIC) at the Brookhaven National Laboratory (BNL).

1.1 Quantum Chromodynamics

Quantum Chromodynamics is the gauge field theory that describes quarks, gluons and their strong interaction. As in Quantum Electrodynamics (QED) the electrons, for example, carry the electric charge, quarks carry the charge of the strong interaction: the

colour. Whereas there is only one kind of electric charge, colour charge comes in three varieties, usually labelled as red, green and blue. Antiquarks have corresponding anti-colour. The gluons in QCD are the massless gauge vector bosons of the theory, like the photons of QED, but while the photons are electrically neutral, gluons are not colour neutral. They can be thought of as carrying both colour and anticolour charge. There are eight possible different combinations of (anti)colour for gluons. Another difference between QCD and QED lies in its coupling strength α_s, the analogue to the fine-structure constant α in QED. It depends on the momentum transfer $\mathcal{Q}^2$ as explained in Section 1.2.1 and its value ranges from $\alpha_s \sim 1$ at a scale of 0.5 GeV, to $\alpha_s = 0.08$ at a scale of 5 TeV. In the QCD Lagrangian quarks are represented by a spinor carrying also a colour index a, which runs from $a = 1$ to $N_c = 3$:

$$\psi_a = \begin{pmatrix} \psi_1 \\ \psi_2 \\ \psi_3 \end{pmatrix} . \tag{1.1}$$

The quark part of the Lagrangian (for a single flavour[1]) can be written as

$$\mathcal{L}_q = \bar{\psi}_a (i\gamma^\mu \partial_\mu \delta_{ab} - g_s \gamma^\mu t^C_{ab} \mathcal{A}^C_\mu - m_q)\psi_b \,, \tag{1.2}$$

where the γ^μ are the usual Dirac matrices, $\mathcal{A}^C_\mu$ are the gluon fields, with Lorentz index μ and a colour index C that goes from 1 to $N_c^2 - 1 = 8$, and m_q is the quark mass. Quarks are in the fundamental representation of the SU(3) (colour) group, while gluons transform under the adjoint representation of the SU(3) (colour) group. Each of the eight gluon fields acts on the quark colour through one of the generator matrices of the SU(3) group, the t^C_{ab} factor in Equation (1.2). The matrices can be written as $t^A \equiv \frac{1}{2}\lambda^A$, in terms of the hermitean and traceless Gell-Mann matrices of SU(3), λ^A. When a gluon interacts with a quark it rotates the quark's colour in SU(3) space, taking away one colour and replacing it with another. The likelihood with which this happens is governed by the strong coupling constant $g_s = \sqrt{4\pi\alpha_s}$. The second part of the QCD lagrangian is purely gluonic:

$$\mathcal{L}_G = -\frac{1}{4} F^A_{\mu\nu} F^{A\mu\nu} \,. \tag{1.3}$$

The gluon field tensor $F^A_{\mu\nu}$ is given by

$$F^A_{\mu\nu} = \partial_\mu \mathcal{A}^A_\nu - \partial_\nu \mathcal{A}^A_\mu - g_s f_{ABC} \mathcal{A}^B_\mu \mathcal{A}^C_\nu \qquad [t^A, t^B] = i f_{ABC} t^C \,, \tag{1.4}$$

[1] In the Standard Model of particles flavour is the property that distinguishes different particles in the two groups of building blocks of matter, the quarks and the leptons. There are six flavours of subatomic particle within each of these two groups: six leptons (the electron, the muon, the tau and the three associated neutrinos) and six quarks (up, down, charm, strange, top and bottom). In QCD flavour is a global symmetry, this means that flavour changing processes are mediated only by electroweak interaction.

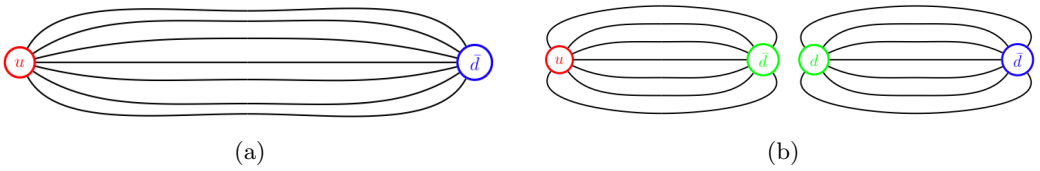

(a) (b)

FIGURE 1.1: (a) Bound quark-antiquark pair. Gluons exchange is responsible of the binding and it is represented by the flux tube containing the field lines. (b) Pulling apart the quarks, the energy of the gluon field increases until the flux tube breaks up in a new quark-antiquark pair.

where f_{ABC} are the structure constants of SU(3). The main difference with QED here is the presence of a term $g_{\rm s} f_{ABC} \mathcal{A}^B_\mu \mathcal{A}^C_\nu$ with two gluon fields that is responsible for the fact that gluons interact directly with gluons.

Predictive methods for QCD include lattice gauge theory and perturbative expansions in the coupling.

The fundamental parameters of QCD are the coupling $g_{\rm s}$ (or $\alpha_{\rm s} = g_{\rm s}^2/4\pi$) and the quark masses m_q.

1.2 Asymptotic Freedom and Confinement

Neither quarks nor gluons are observed as free particles. Hadrons are colour-singlet (i.e. colour-neutral) combinations of quarks and antiquarks. Conversely, partons (quarks and gluons) behave like free particles in high-energy (i.e. short distance) reactions. Asymptotic freedom refers to the weakness of the short-distance interaction, while the confinement of quarks follows from its strength at long distances. The concept of quark confining can be illustrated considering the static quark-antiquark potential:

$$V(r) = -\frac{4}{3}\frac{\alpha_{\rm s}}{r} + \kappa r \,. \tag{1.5}$$

The potential contains a Coulomb-like term and a term that rises linearly with the quark-antiquark distance (r). The two quarks can be thought as bound by a colour string and κ is the string tension. The linear part, which becomes relevant at large distances, is responsible of the fact that pulling the quarks apart the energy in the gluon field connecting the quarks becomes larger than the mass of a quark-antiquark pair. Thus, it becomes energetically favorable for the gluons to produce a new quark-antiquark pair. Starting from a meson for example, trying to pull apart its constituents will result in two new mesons instead of two isolated quarks as illustrated in Figure 1.1. Because of this, at low energies one can not observe individual quarks, they immediately confine (or hadronize) into hadronic bound states.

In QED, if we consider the interaction between two heavy electric charges, the polarization of the vacuum induced by fermion-antifermion loops acts to screen each of the original charges, as seen by the other. Each of the incoming charges may be thought as surrounded by a cloud of light charged pairs. If the incoming charges are far apart, each sees a very large cloud which serves to decrease the effective charge of the other. As the charges come closer, they get inside the clouds and the screening become less effective. In QCD, as in QED, the effect of virtual corrections is to surround the (nonabelian) charged particles by clouds of charge. The important difference, however, is that in the nonabelian case the emission of a gluon does not leave the nonabelian charge of the particle unchanged. Although the total charge is conserved, it "leaks away" into the cloud of virtual particles. Thus, when the two heavy particles stay far apart, they are actually more likely to see each other's true charge. As they come closer they penetrate further and further into each other's charge clouds and are less and less likely to measure the true charge. From this heuristic argument we may expect antiscreening for the nonabelian theory and naively explain asymptotic freedom.

1.2.1 Running Coupling Constant

The effect of vacuum polarization reflects in the running of the QCD coupling as a function of the energy scale. QCD does not predict the actual size of α_s at a particular energy scale, but its energy dependence can be precisely determined. If the coupling $\alpha_s(\mu^2)$ can be fixed (i.e. measured) at a given scale μ^2, QCD predicts the size of α_s at any other energy scale $\mathcal{Q}^2$ through the renormalization group equation

$$\mathcal{Q}^2 \frac{\partial \alpha_s(\mathcal{Q}^2)}{\partial \mathcal{Q}^2} = \beta(\alpha_s(\mathcal{Q}^2)) \,. \tag{1.6}$$

The perturbative expansion of the β function is calculated up to four-loop corrections [1]. A solution of Equation (1.6) in the one-loop approximation is

$$\alpha_s(\mathcal{Q}^2) = \frac{\alpha_s(\mu^2)}{1 + \alpha_s(\mu^2)\beta_0 \ln(\mathcal{Q}^2/\mu^2)} \qquad \text{with} \qquad \beta_0 = \frac{11N_c - 2n_f}{12\pi} \,, \tag{1.7}$$

where N_c is the number of colours and n_f the number of active flavours at the energy scale $\mathcal{Q}^2$. Equation (1.7) gives the relation between $\alpha_s(\mathcal{Q}^2)$ and $\alpha_s(\mu^2)$ and also demonstrates the property of asymptotic freedom, which was discovered in 1973 by D. J. Gross, F. Wilczek and H. D. Politzer [2–6]. If $\mathcal{Q}^2$ becomes large and β_0 is positive, i.e. if $n_f < 17$, $\alpha_s(\mathcal{Q}^2)$ will decrease to zero. Likewise, Equation (1.7) indicates that $\alpha_s(\mathcal{Q}^2)$ grows to large values and actually diverges to infinity at small $\mathcal{Q}^2$: with $\alpha_s(\mu^2 = M_{Z^0}^2) = 0.12$ and for typical values of n_f=2–5, $\alpha_s(\mathcal{Q}^2)$ exceeds unity for $\mathcal{Q}^2 \leq \mathcal{O}(0.1\ \text{GeV}^2\text{–}1\ \text{GeV}^2)$. This is the region where perturbative expansions in α_s are no longer meaningful and confinement sets in.

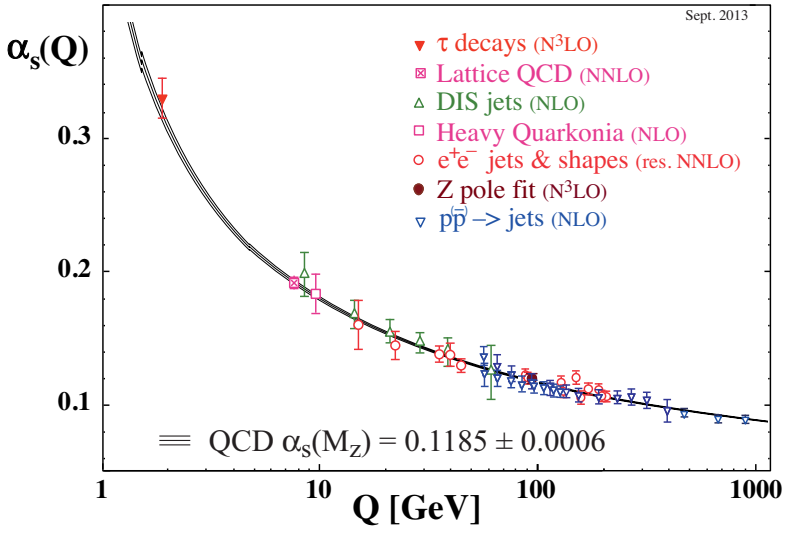

FIGURE 1.2: Summary of measurements of α_s as a function of the energy scale $\mathcal{Q}$. The respective degree of QCD perturbation theory used in the extraction of α_s is indicated in brackets (NLO: next-to-leading order; NNLO: next-to-next-to leading order; res. NNLO: NNLO matched with resummed next-to-leading logs; N^{3}LO: next-to-NNLO) [7].

The running of α_s is confirmed by experiments. The strength of the strong interaction can be measured for different processes, at various scales, and Figure 1.2 [7] shows a compilation of such measurements, together with the running of an average over many measurements, $\alpha_s(M_Z) = 0.1185 \pm 0.0006$, illustrating the good consistency of the measurements with the expected running.

In very high energy reactions, where the momentum transfer is large, the effective strong coupling becomes small and asymptotic freedom is responsible for the fact that quarks behave like free particles at short distances. In this regime, the quark-antiquark potential is screened by the free color charges and quarks and gluons are no more constrained into colourless hadrons. The QCD potential can be parametrized as

$$V(r) = \left(-\frac{4}{3}\frac{\alpha_s}{r} + \kappa r \right) e^{-\frac{r}{r_D}} , \tag{1.8}$$

vanishing rapidly for $r > r_D$. r_D, the Debye radius, sets the maximum distance at which two quarks can be considered as bound, and it is reduced below the typical hadron size (~ 1 fm) by the presence of free colour charges.

1.3 Lattice QCD

A perturbative approach for QCD is possible only at high $\mathcal{Q}^2$. The growth of the coupling constant in the infrared regime requires the use of non-perturbative methods

to determine the low energy properties of QCD. Lattice gauge theory, developed by K. Wilson in 1974 [8], provides such a method: it gives a non-perturbative definition of vector-like gauge field theories like QCD. In lattice regularized QCD, commonly called lattice QCD or LQCD, Euclidean space-time is discretized, usually on a hypercubic lattice with spacing a, with quark fields placed on sites and gauge fields on the links between sites. The continuum theory is recovered by taking the limit of vanishing lattice spacing ($a \to 0$). The QCD action can be defined on the lattice and the observables of interest are calculated as expectation values averaging over all the possible configurations of the fields generated on the lattice.

Lattice results have statistical and systematic errors that must be quantified for any calculation in order for the result to be a useful input to phenomenology. The statistical error is due to the use of Monte-Carlo sampling to evaluate the field configurations. Typical systematic errors arise from the continuum and finite volume limits. Physical results are obtained in the limit of lattice spacing a going to zero and the scaling of the discretization errors with a has to be taken into account.

The LQCD approach allows to study the QCD phase structure at finite temperature and density. The starting point for these studies is the definition of the QCD thermodynamics on the lattice. The behaviour of the order parameters that characterize QCD matter as a function of the temperature and density can be calculated on the lattice and, thus, quantitative predictions about confinement of quarks become possible.

1.4 The QCD Phase Diagram and the Quark-Gluon Plasma

Even before QCD had been established as the fundamental theory of the strong interaction, it had been argued that the basic properties of strongly-interacting hadrons must lead to some form of critical behaviour at high temperature and/or density. Since a hadron has a finite size of about 1 fm^3 (for pions), there is a limit to the density (and, thus, to the temperature) of a hadronic system beyond which hadrons start to "superimpose". Moreover, the number of observed resonances which grows exponentially as the energy (temperature) of the system increases, indicates the existence of a limit temperature for hadronic matter [9]. The subsequent formulation of QCD led to the suggestion that this should be the limit between confined matter and a new phase of strongly-interacting matter, the Quark-Gluon Plasma (QGP) [10].

Asymptotic freedom is one of the most crucial properties in the nonabelian gauge theory of quarks and gluons. The fact that the coupling constant runs towards smaller values with increasing energy scale anticipates that QCD matter at high energy densities

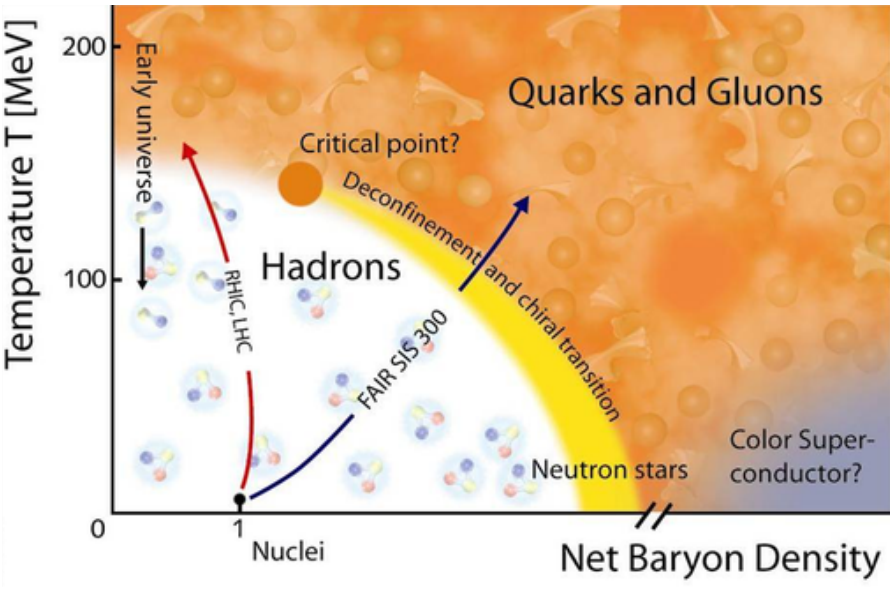

FIGURE 1.3: Phase diagram of QCD matter as a function of temperature and net baryon density ρ_B.

undergoes a phase transition from a state with confined hadrons into a new state of matter with on-shell (real) quarks and gluons.

The current understanding of the QCD phase diagram is based on thermodynamical considerations and LQCD calculations. The phase transition of strongly-interacting matter is driven by the temperature and the baryonic chemical potential μ_B, defined as the energy needed to increase by one unity the total number of baryons and antibaryons ($\mu_B = \partial E/\partial N_B$). Figure 1.3 shows an illustration of the phase structure of strongly-interacting matter as a function of its temperature and net baryon density $\rho_B \propto \mu_B$.

The phase structure of QCD can be summarized as in the following. At low temperatures and for $\mu_B \sim 1$ GeV, strongly-interacting matter is in its standard conditions (atomic nuclei). Increasing the energy density of the system, thus increasing the temperature, or increasing the baryo-chemical potential, an hadronic gas phase is reached. If the energy density is further increased, a deconfined QGP phase sets in. The density of quarks and gluons in this phase becomes so high that partons are still interacting but not confined within hadrons anymore. The transition to the QGP phase is predicted by recent LQCD calculations to occur at a critical temperature, T_c of the order of 170 MeV, corresponding to an energy density $\varepsilon_c \simeq 1$ GeV/fm^3 [11]. If μ_B is very large ($\mu_B \gg 1$ GeV), the ground state of QCD matter at low T should form Cooper pairs leading to colour superconductivity [12].

Different paths on the phase diagram can be followed by the phase transition, depending on the temperature and the baryo-chemical potential. In the early Universe (about 10 μs after the Big Bang), for example, the transition from a QGP phase to

a confined one took place for $\mu_{\mathrm{B}} \sim 0$ as a consequence of the expansion and cooling of the Universe. On the other hand, neutron stars are formed as a consequence of the gravitational collapse that causes an increase in the baryonic density at a temperature very close to zero.

Phase transitions are usually classified according to the behaviour of the free energy of the system at the transition temperature. The transition is of the first order if it occurs with a discontinuous pattern in the first derivative of the free energy. In a first order transition, entropy varies with discontinuity and latent heat is present. If the phase transition occurs with discontinuous derivatives after the first, it is of the second order. Phase transitions can also occur without fast modification of the parameters of the system, but with continuos behaviuor of the free energy and its derivatives. This type of transition is called crossover.

The nature of the QCD phase transition, e.g. its order and details of the critical behaviour, are controlled by global symmetries of the QCD Lagrangian. Such symmetries only exist in the limits of either infinite or vanishing quark masses. For any non-zero, finite value of the quark masses the global symmetries are explicitly broken. In the limit of infinitely-heavy quarks, the large distance behaviour of the heavy-quark free energy, $F_{\bar{q}q}$ provides a unique distinction between confinement below T_c and deconfinement for $T > T_c$. The expectation value of the Polyakov loop,

$$L(\mathbf{x}) = \mathcal{P} \exp\left[-ig \int_0^\beta \mathrm{d}x_4 \mathcal{A}_4(\mathbf{x}, x_4)\right] , \qquad \beta = 1/T \,, \tag{1.9}$$

which depends on the behaviour of the heavy-quark free energy at large distances, is an order parameter of the deconfinement transition:

$$\langle L \rangle \quad \begin{cases} = 0 & \Leftrightarrow \quad \text{confined phase,} \quad & T < T_c \\ > 0 & \Leftrightarrow \quad \text{deconfined phase,} \quad & T > T_c \end{cases} .$$

The phase transition in the infinite quark mass limit is suggested to be of the first order. In the limit of vanishing quark masses the QCD Lagrangian is invariant under chiral symmetry transformations; for n_f massless quark flavours the symmetry is $\mathrm{U_A}(1) \times \mathrm{SU_L}(n_f) \times \mathrm{SU_R}(n_f)$. Only the $\mathrm{SU}(n_f)$ part of this symmetry is spontaneously broken in the vacuum, which gives rise to $(n_f^2 - 1)$ massless Goldstone particles, the pions. The basic observable which reflects the chiral properties of QCD is the chiral condensate,

$$\langle \bar{\psi}\psi \rangle = \langle \bar{\psi}_{\mathrm{R}}\psi_{\mathrm{L}} + \bar{\psi}_{\mathrm{L}}\psi_{\mathrm{R}} \rangle \,, \tag{1.10}$$

where colour and flavour indices of the quark fields are to be summed. In the limit of vanishing quark masses the chiral condensate stays non-zero as long as chiral symmetry is spontaneously broken. The chiral condensate thus is an order parameter in the chiral

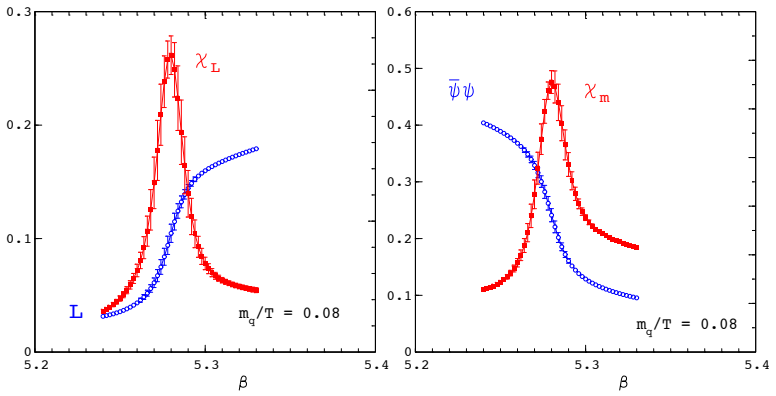

FIGURE 1.4: Deconfinement and chiral symmetry restoration in 2-flavour QCD: $\langle L \rangle$, the order parameter for deconfinement in the limit of $m_q \to \infty$, and its susceptibility (left), and $\bar{\psi}\psi$, the order parameter for chiral symmetry breaking in the chiral limit ($m_q \to 0$) and its susceptibility (right) as a function of the coupling $\beta = 6/g^2$ [11].

limit,

$$\langle \bar{\psi}\psi \rangle \quad \begin{cases} > 0 & \Leftrightarrow \quad \text{symmetry broken phase,} \quad T < T_c \\ = 0 & \Leftrightarrow \quad \text{symmetric phase,} \quad T > T_c \end{cases} .$$

A sudden change in the long distance behaviour of the heavy-quark potential or the chiral condensate as a function of the temperature can be observed through the corresponding susceptibilities: the Polyakov loop susceptibility (χ_{L}) and the chiral susceptibility (χ_m). The behaviour of these observables is shown in Figure 1.4 for the case of two-flavour QCD with light quarks [11]. The points of most rapid change in $\langle L \rangle$ and $\langle \bar{\psi}\psi \rangle$, corresponding to the maxima of the susceptibilities, coincide. This provides an indication of the fact that chiral symmetry restoration and deconfinement occur at the same temperature.

For light quarks the global chiral symmetry is expected to control the critical behaviour of the QCD phase transition. In particular, the order of the transition is expected to depend on the number of light or massless flavours. In the real world, none of the quarks is exactly massless, therefore, it is useful to draw a phase diagram by treating quark masses as external parameters. The basic features of the phase diagram have been established in numerical calculations. The resulting diagram of 3-flavour QCD at vanishing baryo-chemical potential is shown in Figure 1.5. Isospin degeneracy is assumed ($m_u = m_d \equiv m_{ud}$). The first order chiral transition and the first order deconfinement transition at finite temperature are indicated by the left-bottom region and the top-right region, respectively. For a broad range of quark mass values, the transition to the high temperature regime is not a phase transition but a continuos crossover. The thermal transition for physical quark masses is likely to be a crossover [13].

Deconfinement in QCD means that a large number of new degrees of freedom gets

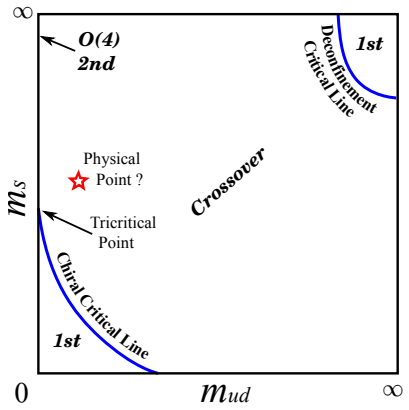

FIGURE 1.5: Schematic figure of the Columbia phase diagram in 3-flavour QCD at $\mu_B = 0$ on the plane with the light and heavy-quark masses [13].

liberated at the (phase) transition temperature: quarks and gluons which at low temperature are confined in colourless hadrons and thus do not contribute to the thermodynamics, suddenly become liberated and start contributing to the bulk thermodynamic observables like the energy density or pressure. Due to asymptotic freedom the QCD energy density and pressure will approach the ideal gas values at infinite temperature. The equation of state of an equilibrated ideal gas of massless particles with n_{dof} degrees of freedom is

$$p = \frac{\pi^2}{90} n_{\mathrm{dof}} T^4 \tag{1.11}$$

and

$$\varepsilon = 3p\,. \tag{1.12}$$

The dramatic increase of p/T^4 and ε/T^4 near T_c (Figure 1.6) can be interpreted as due to the change of n_{dof} from 3 in the pion gas phase to $(16 + \frac{21}{2} n_f)$ in the deconfined phase with n_f quark flavours, where the additional colour and quark flavour degrees of freedom are available[2].

1.5 Heavy-Ion Collisions and the QGP

Ultra-relativistic heavy-ion collisions enable the study of the properties of strongly-interacting matter at energy densities far above those of normal nuclear matter. In this regime, the expected transition from a hadronic gas to the QGP occurs. Through heavy-ion collisions at ultra-relativistic energies it is then possible to search for the QGP and to study its properties. Research conducted over the past decades at the

[2] In a pion gas the degrees of freedom are the 3 values of the isospin for π^+, π^0 and π^-. In a QGP with n_f quark flavours the degrees of freedom are $n_g + \frac{7}{8}(n_q + n_{\bar{q}}) = (8\times2) + \frac{7}{8}(2\times3\times2\times n_f) = (16 + \frac{21}{2} n_f)$. The factor 7/8 takes into account the difference between Bose-Einstein (gluons) and Fermi-Dirac (quarks) statistics.

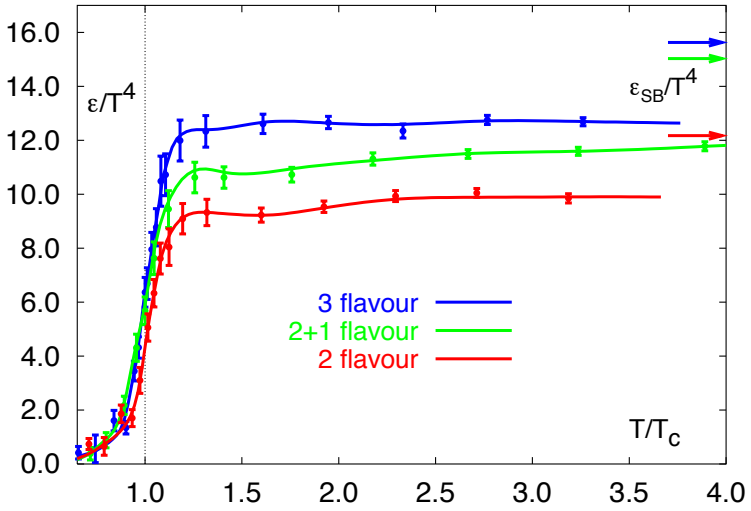

FIGURE 1.6: The energy density in lattice QCD with different number of degrees of freedom (2 and 3 light quarks and 2 light plus 1 heavier quarks) as a function of temperature [14].

Alternating Gradient Synchrotron (AGS, $\sqrt{s_{\rm NN}} = 4.6$ GeV per nucleon pair), Super Proton Synchrotron (SPS, $\sqrt{s_{\rm NN}} = 17.2$ GeV per nucleon pair) Relativistic Heavy-Ion Collider (RHIC, up to $\sqrt{s_{\rm NN}} = 200$ GeV per nucleon pair) and Large Hadron Collider (LHC, $\sqrt{s_{\rm NN}} = 2.76$ TeV per nucleon pair[3]) has led to the discovery of the QGP. The collision is thought to result in the formation of a dense, non-thermal QCD plasma with highly occupied gauge fields modes, sometimes called "glasma". The system thermalizes rapidly and the QCD matter forms a nearly (locally) thermal quark-gluon plasma, whose evolution can be described in terms of relativistic viscous hydrodynamics because of its very small shear viscosity. The QGP expands and cools down until it converts to a gas of hadron resonances when its temperature falls below the critical temperature T_c. At about that temperature the chemical composition of the produced hadrons gets frozen, $T_{ch} \neq T_c$ (in general), but the spectral distribution of the hadrons is still modified by final-state interactions until kinetic freeze-out ($T_{kin} < T_{ch} \leq T_c$). A schematic representation of the space-time evolution of a relativistic heavy-ion collision is reported in Figure 1.7.

Different observables in the final state are sensitive to the various stages of the evolution of the system created in heavy-ion collisions. The bulk of the particles emitted in a heavy-ion collision are soft (low-momentum) hadrons, which decouple from the collision region in the late hadronic freeze-out stage of the evolution. The parameters that characterize the freeze-out distributions constrain the dynamical evolution and thus yield indirect information about the early stages of the collision. They provide

[3]During LHC Run 2 the energy will reach $\sqrt{s_{\rm NN}} = 5.1$ TeV per nucleon pair, and during Run 3 its design value of $\sqrt{s_{\rm NN}} = 5.5$ TeV per nucleon pair.

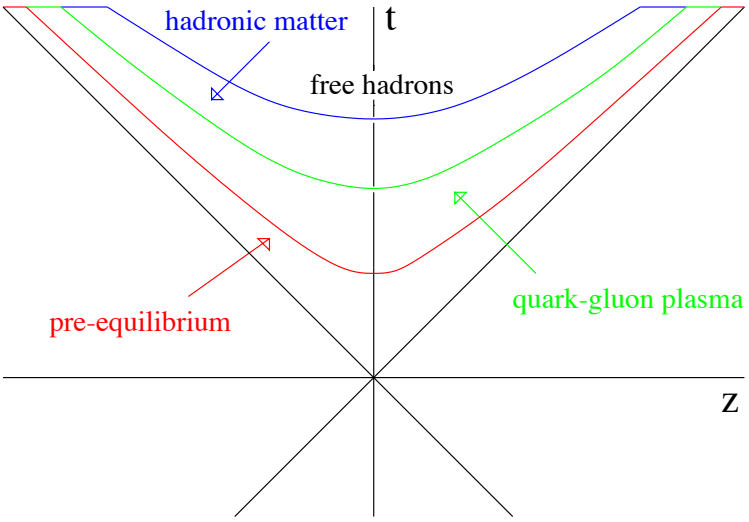

FIGURE 1.7: Schematic representation of the expected space-time evolution of a ultra-relativistic heavy-ion collision.

information on the chemical and kinetic freeze-out temperature and chemical potential, radial expansion velocity, hydrodynamical properties of the medium, size parameters as extracted from two-particle correlations, momentum spectra, event-by-event fluctuations and correlations of hadron momenta and yields. The study of jets originating from hard partons and of heavy-flavour hadrons provides insights into the interaction mechanisms inside the QGP. Photons do not interact strongly, thus they probe the state of the matter at the time of their production: thermal photons radiated off the quarks which undergo collisions with other quarks and gluons in a thermal bath can be used to measure the temperature of the medium.

Heavy-ion collisions are an important part of the physics programme of the LHC, which started operation at the end of 2009. In particular, the heavy-ion programme at LHC has the aim of precisely characterizing the QGP parameters at the highest collision energy. A selection of the results from the first years of ion physics at the LHC at the centre-of-mass energy of $\sqrt{s_{\mathrm{NN}}} = 2.76$ TeV per nucleon pair, also compared with previous experiments, is presented in the following paragraphs. The description of the collision geometry will be given and then some observables which allow to characterize the properties of the Pb–Pb events will be presented, as well as an example of a hard probe such as the quarkonium production. The aspects directly related to this thesis work are treated in Chapter 2.

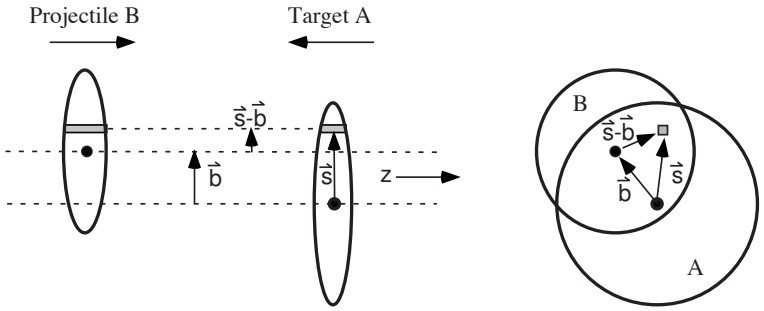

FIGURE 1.8: Schematic representation of the optical Glauber model geometry with transverse and longitudinal views.

1.5.1 Geometry of the Collision

Nuclei are extended objects compared to the scales of interest in high energy physics. For this reason, the geometry of the collision plays an important role in the study of nuclear matter effects and QGP formation. In the centre-of-mass frame, the two colliding nuclei can be seen as two thin disks of transverse size $2R_A \simeq 2A^{1/3}$ fm (A is the atomic mass number), since they are Lorentz contracted along the beam direction by a factor $\gamma = E_{\text{beam}}/M$ (E_{beam} is the energy of the accelerated nuclei and M their mass). The quantities used to characterize the collision geometry are:

- The impact parameter, which is the distance between the centres of the two colliding nuclei. The impact parameter characterizes the centrality of the collision: a central collision is one with small impact parameter in which the two nuclei collide almost head-on, a peripheral collision is one with large impact parameter.
- The number of participant nucleons, N_{part}, within the colliding nuclei, which is the total number of protons and neutrons that undergo at least one inelastic collision.
- The number of binary collisions, N_{coll}, is the total number of nucleon–nucleon collisions.

These quantities can be derived from a probabilistic Glauber model [15]. Two heavy ions colliding with impact parameter $\mathbf{b}$ can be represented as in Figure 1.8. The two flux tubes located at a displacement $\mathbf{s}$ with respect to the centre of the target nucleus and at a distance $\mathbf{s}-\mathbf{b}$ from the centre of the projectile, overlap during the collision. If $\rho_A(\mathbf{s}-z_A)$ is the probability per unit volume, normalized to unity, for finding a given nucleon at $(\mathbf{s}-z_A)$, the probability per unit transverse area of the nucleon being located in the target flux tube is $T_A(\mathbf{s}) = \int \rho_A(\mathbf{s}-z_A)\mathrm{d}z_A$. The product $T_A(\mathbf{s})T_A(\mathbf{s}-\mathbf{b})\mathrm{d}^2s$ then gives the joint probability per unit area of nucleons being located in the respective overlapping target and projectile flux tubes of differential area d^2s. Integrating this

product over all values of **s** defines the nuclear overlap function $T_{AB}(b)$:

$$T_{AB}(b) = \int T_A(\mathbf{s}) T_B(\mathbf{s}-\mathbf{b}) \mathrm{d}^2 s \,, \tag{1.13}$$

where b is the magnitude of the impact parameter vector **b**. $T_{AB}(b)$ has the unit of inverse area and can be interpreted as the effective overlap area for which a specific nucleon in A can interact with a given nucleon in B. The probability of an interaction occurring is then $T_{AB}(b)\sigma_{\mathrm{inel}}^{\mathrm{NN}}$, where $\sigma_{\mathrm{inel}}^{\mathrm{NN}}$ is the nucleon–nucleon inelastic cross section. The probability of having n such interactions between nucleus A (with A nucleons) and nucleus B (with B nucleons) is given by a binomial distribution

$$P(n,b) = \left(\begin{array}{c} AB \\ n \end{array} \right) \left[T_{AB}(b)\sigma_{\mathrm{inel}}^{\mathrm{NN}} \right]^n \left[1 - T_{AB}(b)\sigma_{\mathrm{inel}}^{\mathrm{NN}} \right]^{AB-n} , \tag{1.14}$$

where the first term is the number of combinations for finding n collisions out of $A \cdot B$ possible nucleon–nucleon interactions, the second term is the probability for having exactly n collisions, and the last term is the probability of exactly $A \cdot B - n$ misses. Based on this probability distribution, the relevant quantities that characterize the collision geometry can be determined. The number of nucleon–nucleon collisions[4] is

$$N_{\mathrm{coll}}(b) = \sum_{n=1}^{AB} nP(n,b) = ABT_{AB}(b)\sigma_{\mathrm{inel}}^{\mathrm{NN}} \,. \tag{1.15}$$

The number of participants at impact parameter b is given by

$$\begin{aligned} N_{\mathrm{part}}(b) &= A \int T_A(\mathbf{s}) \Big\{ 1 - \left[1 - T_B(\mathbf{s}-\mathbf{b})\sigma_{\mathrm{inel}}^{\mathrm{NN}} \right]^B \Big\} \mathrm{d}^2 s + \\ &+ B \int T_B(\mathbf{s}-\mathbf{b}) \Big\{ 1 - \left[1 - T_A(\mathbf{s})\sigma_{\mathrm{inel}}^{\mathrm{NN}} \right]^A \Big\} \mathrm{d}^2 s \,, \end{aligned} \tag{1.16}$$

where the integral over the bracketed terms give the respective inelastic cross sections for nucleus–nucleus collisions. This formulation of the Glauber model (optical limit) is based on continuous nucleon density distributions: each nucleon in the projectile sees the oncoming target as a smooth density.

Neither impact parameter nor N_{part} or N_{coll} are directly measured experimentally. Mean values of such quantities can be extracted for classes of measured events via a mapping procedure. Typically, a measured distribution is mapped to the corresponding distribution obtained from phenomenological analytic or Monte Carlo Glauber calculations. This is done by defining centrality classes in both the measured and calculated distributions and then connecting the mean values from the same centrality class in the two distributions (Figure 1.9).

[4] Alternatively the number of nucleon–nucleon collisions is expressed as $N_{\mathrm{coll}}(b) = T_{\mathrm{AB}}(b)\sigma_{\mathrm{inel}}^{\mathrm{NN}}$ if $\rho_A(\mathbf{s} - z_A)$ is normalized to A. This convention is used, for example, in [16].

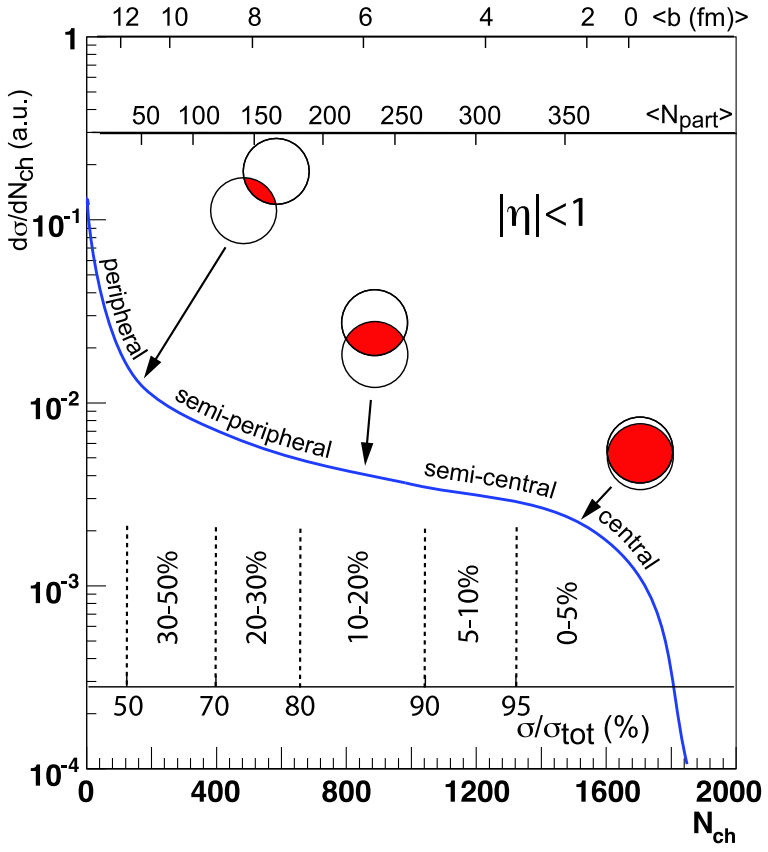

FIGURE 1.9: Illustration of the correlation between the final state observable N_{ch} and Glauber calculated quantities (b, N_{part}).

Two experimental observables related to the collision geometry are the charged-particle multiplicity N_{ch} and the energy carried by particles close to the beam direction and deposited in the forward zero-degree calorimeters, called the zero-degree energy E_{ZDC}. E_{ZDC} is directly related to the number of spectator nucleons, which constitute the part of the nuclear volume not involved in the interaction.

Particle multiplicity is monotonically related to the impact parameter b. One possibility to define centrality classes is to measure the charged-particle multiplicity distribution ($\mathrm{d}\sigma/\mathrm{d}N_{\mathrm{ch}}$). Knowing the total integral of the distribution, one can define centrality classes by binning the distribution based upon the fraction of the total integral. The centrality classes are obtained defining shape cuts on the distribution, which correspond to well defined percentile intervals of the hadronic cross section σ_{tot} (0–5%, 5–10%, etc.). The same procedure is then applied to a calculated distribution and for each centrality class, the mean value of Glauber quantities, e.g. $\langle N_{\mathrm{part}} \rangle$ and $\langle N_{\mathrm{coll}} \rangle$, is extracted.

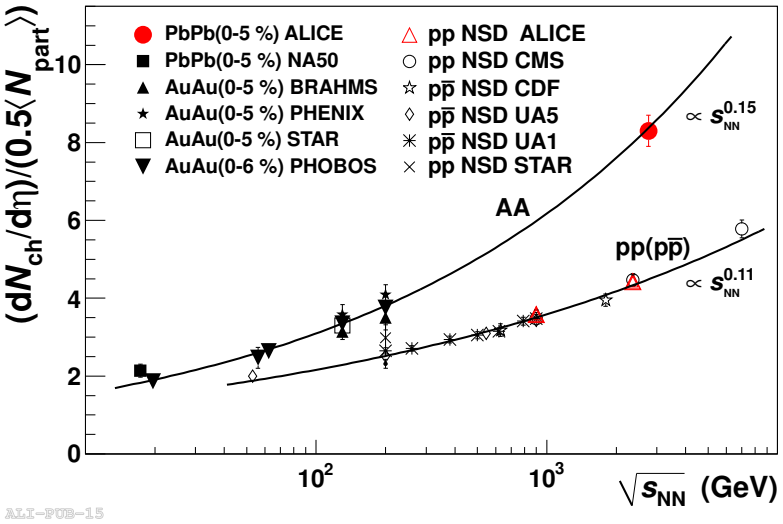

FIGURE 1.10: Charged-particle pseudorapidity density per participant pair for central A–A and non-single diffractive pp (p$\bar{\text{p}}$) collisions as a function of $\sqrt{s_{\text{NN}}}$. The solid lines $\propto s_{\text{NN}}^{0.15}$ and $\propto s_{\text{NN}}^{0.11}$ are superimposed on the heavy-ion and pp (p$\bar{\text{p}}$) data, respectively [17].

1.5.2 Global Event Properties

Global event properties describe the state and dynamical evolution of the bulk matter created in a heavy-ion collision by measuring characteristics of the soft particles (with momentum below few GeV/c), which represent the large majority of produced particles. They include multiplicity distributions, which can be related to the initial energy density reached in the collision, yields and momentum spectra of identified particles, which are determined by the conditions at and shortly after hadronization, and correlation between particles, which measure both size and lifetime of the dense matter state.

1.5.2.1 Particle Multiplicity

The first step in characterizing the system produced in heavy-ion collisions is the measurement of the number of charged particles produced per unit of pseudorapidity[5] ($\mathrm{d}N_{\text{ch}}/\mathrm{d}\eta$). This can be related to the initial energy density using the formula proposed by Bjorken [18]:

$$\varepsilon = \frac{\mathrm{d}E_{\text{T}}/\mathrm{d}\eta}{\tau_0 \pi R_A^2} = \frac{3}{2}\langle E_{\text{T}}/N\rangle \frac{\mathrm{d}N_{\text{ch}}/\mathrm{d}\eta}{\tau_0 \pi R_A^2}\,, \tag{1.17}$$

[5]The pseudorapidity is defined as $\eta = -\ln[\tan(\theta/2)]$, where θ is the polar angle with respect to the beam direction. For a particle with velocity $v \to c$, $\eta \approx y$, being y the longitudinal rapidity. The longitudinal rapidity of a particle with four-momentum $(E, \vec{p})$ is defined as $y = \frac{1}{2}\ln\left(\frac{E+p_z}{E-p_z}\right)$, being z the direction of the beam.

where τ_0 denotes the thermalization time, R_A is the nuclear radius and $E_T/N \sim 1$ GeV is the transverse energy per emitted particle, and the factor 3/2 derives from the assumption that particle multiplicity is dominated by pions (π^+, π^-, π^0) and $dN_{ch}/d\eta$ measures only the charged pions $\pi^{\pm}$.

In order to compare the bulk particle production in different collision systems and at different energies, the charged-particle density is scaled by the number of participating nucleons in the collision (N_{part}). The charged particle pseudorapidity density normalized per participant pair, $dN_{ch}/d\eta/(0.5\langle N_{part}\rangle)$ measured by ALICE in central Pb–Pb collisions at $\sqrt{s_{NN}} = 2.76$ TeV is shown in Figure 1.10, compared to the lower-energy measurements for Au–Au and Pb–Pb, and non-single diffractive (NSD) pp and p$\bar{\text{p}}$ collisions over a wide range of collision energies. The energy dependence is steeper for heavy-ion collisions than for pp and p$\bar{\text{p}}$ collisions. Particle production follows a power law $\propto s_{NN}^{0.15}$ in heavy-ion collisions and $\propto s_{NN}^{0.11}$ in pp and p$\bar{\text{p}}$ collisions.

The charged-particle pseudorapidity density measured in central collisions at LHC is $dN_{ch}/d\eta \approx 1600$ [17]. This value implies that the initial energy density (at $\tau_0 = 1$ fm/c) is about 15 GeV/fm^3 [19] ($\gg \varepsilon_c$, the critical energy density), approximately a factor of three higher than in Au–Au collisions at the top energy of RHIC.

1.5.2.2 Identical Boson Correlations

The freeze-out volume (the size of the matter at the time when strong interactions cease) and the total lifetime of the created system (the time between collision and freeze-out) can be studied using identical boson interferometry (also called Hanbury-Brown-Twiss or HBT) [20]. This technique exploits the Bose-Einstein enhancement of identical bosons emitted close-by in the phase space, which leads to a modification of the two-particle correlation function measured in energy and momentum variables. The space and time distribution of the emitting source, i.e. the space-time hyper surface of last rescattering, can be inferred via a Fourier transformation. Results from HBT correlation measurements are shown in Figure 1.11 for central collisions from very low energies up to LHC as a function of the charged-particle density [21]. Compared to top RHIC energy, the locally comoving freeze-out volume (Figure 1.11(a)) increases by a factor two (to about 5000 fm^3) and the system lifetime (Figure 1.11(b)) increases by about 30% (to 10 fm/c). These results contribute to indicate that the fireball formed in nuclear collisions at the LHC lives longer and expands to a larger size at freeze-out as compared to lower energies.

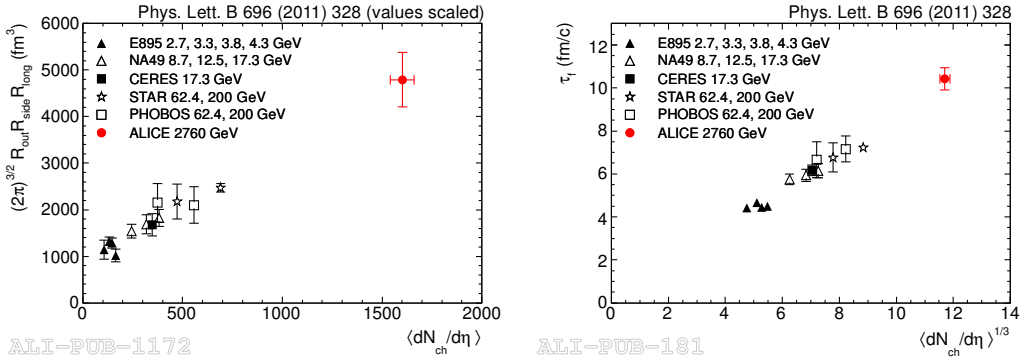

(a) (b)

FIGURE 1.11: (a) Product of the three pion HBT radii measured by ALICE in red compared to those obtained for central gold and lead collisions at lower energies at the AGS, SPS and RHIC. (b) The system lifetime (decoupling time) τ_f measured by ALICE (red filled dot) compared to results from lower energies [21].

1.5.3 Photon Spectrum

One of the signals expected for the QGP is the radiation of "thermal photons", with a spectrum reflecting the temperature of the system. These photons come from secondary interactions among medium constituents and leave the reaction zone created in a nucleus–nucleus collision without interacting, since their mean-free path is much larger than nuclear scales. Therefore, they provide a direct probe to examine the early hot phase of the collision. Thermal photons are produced during the entire evolution of the QGP and also after the transition to a hot gas of hadrons. The experimental challenge in detecting them comes from the huge background of photons from hadron decays (predominantly neutral pions and η mesons). At the LHC, ALICE measured the spectrum of direct photons in central Pb–Pb collision at $\sqrt{s_{\rm NN}} = 2.76$ TeV, defined as the photons not coming from hadron decays but from initial hard primary QCD interactions among partons. An excess of photons of about 15% was observed for $1 < p_{\rm T} < 5$ GeV/c, with respect to the expectation for hard scattering (Figure 1.12). In this region, the spectrum has an exponential shape and the inverse slope parameter, $T = 304 \pm 51$ (stat. + syst.) MeV, is larger than the value observed in Au–Au collisions at RHIC at $\sqrt{s_{\rm NN}} = 0.2$ TeV, $T = 221 \pm 19$ (stat.) ± 19 (syst.) MeV [22]. This parameter can be interpreted as an effective temperature averaged over the time evolution of the hot system.

1.5.4 Hard Processes

Hard processes, involving high momentum or high mass scales, have much larger cross sections at LHC with respect to RHIC, due to the increased energy of heavy-ion collisions. Energetic quarks or gluons can be observed as jets or single particles with $p_{\rm T}$

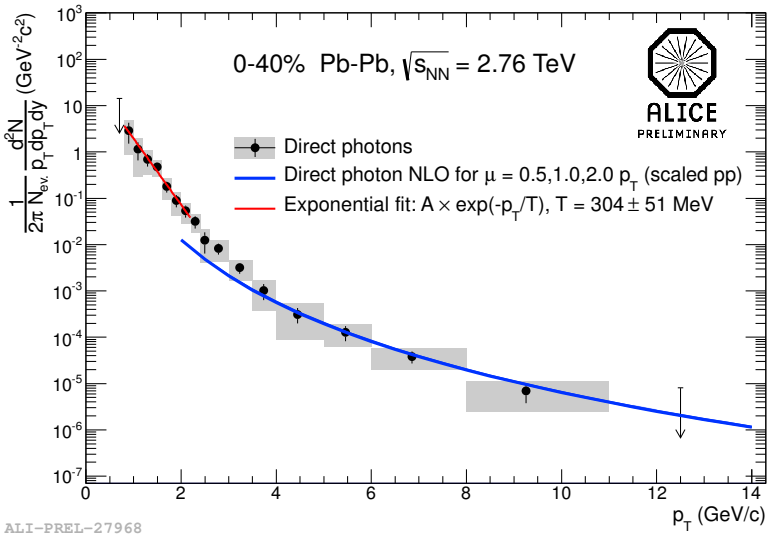

FIGURE 1.12: ALICE preliminary direct photons p_{T} spectrum measured in Pb–Pb collisions at $\sqrt{s_{\mathrm{NN}}} = 2.76$ TeV for 40% most central collisions compared at low p_{T} with an exponential fit and with a direct-photon NLO calculation for pp collisions at $\sqrt{s} = 2.76$ TeV scaled by the number of nucleon–nucleon binary collisions.

reaching 100 GeV/c and beyond. Similarly, high p_{T} photons, charmonium and bottomonium states and even the weak vector bosons W and Z are copiously produced. The details of the production and propagation of these high p_{T} probes can be used to explore the mechanisms of parton energy loss and deconfinement in the medium. The description of the parton energy loss process in a hot medium will be given in Chapter 2.

1.5.4.1 Quarkonium Suppression

The colour screening model [23], predicts that charmonium and bottomonium states ($c\bar{c}$ and $b\bar{b}$ bound states, respectively) dissociate in the medium, resulting in a suppression of the observed yields. The dissociation is due to the screening of the binding potential of heavy quark-antiquark pairs by the deconfined colour charges in the QGP. In a deconfined medium the heavy-quark potential gets screened, as introduced in Section 1.2.1, and at sufficiently high temperature the screening radius (Debye radius, r_D) will be smaller than the typical size of a quarkonium state. The screening radius magnitude depends on the temperature of the medium, and, in particular it is expected to become smaller as the temperature increases. Therefore, the resulting dissociation of the quarkonium states, and thus the suppression of the yields, depends on the temperature of the medium, and it is expected to occur sequentially, reflecting the increasing values of their binding energies (i.e. the states with higher binding energy have smaller radius and, thus, they dissociate at higher temperatures).

In the charmonium sector, a significant suppression of the J/ψ has been observed at SPS ($\sqrt{s_{\mathrm{NN}}} = 17.3$ GeV), RHIC ($\sqrt{s_{\mathrm{NN}}} = 39,\ 62.4,\ 200$ GeV) and LHC ($\sqrt{s_{\mathrm{NN}}} =$

2.76 TeV) energies. The results obtained at LHC by ALICE [24] and CMS [25] at forward rapidity are reported in Figure 1.13(a). At forward rapidity the J/ψ $R_{\rm AA}$, defined as the ratio of the $p_{\rm T}$ distribution measured in Pb–Pb collisions to that measured in pp collisions scaled by the average number of nucleon–nucleon collisions, exhibits a strong $p_{\rm T}$ dependence and decreases by a factor of 2 from low $p_{\rm T}$ to high $p_{\rm T}$. This behaviour strongly differs from that measured by PHENIX at RHIC top energy, which exhibits a strong suppression also at low $p_{\rm T}$. A qualitative description of the results can be obtained assuming that, in addition to the dissociation by colour screening, a regeneration process takes place in the case of high-energy collisions. At $\sqrt{s_{\rm NN}} = 2.76$ TeV, the charm quark yield in the collisions increases with respect to SPS and RHIC energies, because of the large increase of the $c\bar{c}$ cross-section towards LHC energy. This may result in the enhancement of the probability to create J/ψ mesons from recombination of initially uncorrelated charm quarks. The recombination mechanism is expected to lead to an increase of the $R_{\rm AA}$ at the LHC with respect to the one observed at RHIC. Furthermore, in order to recombine, two charm quarks need to be close enough in phase space, so that low transverse momentum J/ψ production is expected to be favoured.

With the high collision energies and luminosities recently available at RHIC and LHC, it has been also possible to study bottomonium production in heavy-ion collisions. Compared with the J/ψ case, the probability for the Υ states to be regenerated in the medium is much smaller due to the lower production cross section of $b\bar{b}$ pairs. However, the feed-down contributions from higher-mass resonances into the observed quarkonium yields, as well as several competing nuclear and medium effects have to be taken into account. The CMS Collaboration measured the midrapidity production of bottomonium states in Pb–Pb collisions at $\sqrt{s_{\rm NN}} = 2.76$ TeV. The Υ(1S) yield is suppressed by approximately a factor of two with respect to the expectation from pp collisions and scaling of the hard process yield with the number of binary nucleon–nucleon collisions. Moreover, the suppression of Υ(2S) is stronger than that of Υ(1S), as shown in Figure 1.13(b), and the Υ(3S) is almost completely suppressed [26]. The measurement of the inclusive Υ(1S) production at forward rapidity and down to zero transverse momentum was carried out by ALICE [27]. The observed suppression of inclusive Υ(1S) results stronger in central than in semi-peripheral collisions and shows a pronounced rapidity dependence over the large domain covered by ALICE ($2.5 < y < 4$) and CMS ($|y| < 2.4$). The data support the hypothesis of increased suppression of less strongly bound states, but a precise measurement of the feed-down contribution to the Υ(1S) state and an accurate estimate of the cold nuclear matter effects is required to make a stringent comparison with models.

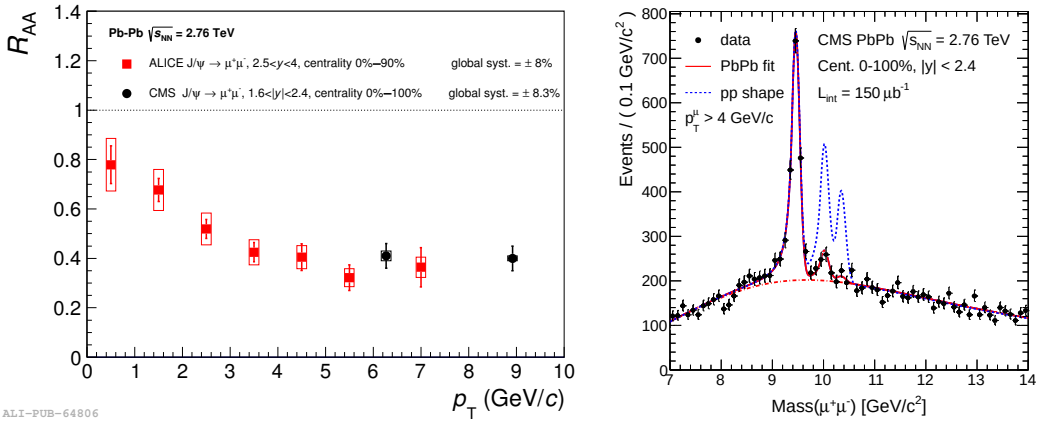

(a) (b)

FIGURE 1.13: (a) Transverse momentum dependence of the centrality integrated nuclear modification factor of the J/ψ p_{T} distribution in Pb–Pb at $\sqrt{s_{\mathrm{NN}}}$ = 2.76 TeV with respect to pp collisions. ALICE result refer to the rapidity range $2.5 < y < 4$ [24], CMS one to $1.6 < y < 2.4$ [25]. (b) Dimuon invariant mass distribution from Pb–Pb data at $\sqrt{s_{\mathrm{NN}}} = 2.76$ TeV. The red line shows the fit to Pb–Pb data. The blue dashed line shows the shape obtained from the fit to pp data. For a better comparison, the background shape, background yield, mass peak width, mass peak tail shape and the Υ(1S) yields in the blue line are fixed to the Pb–Pb fit, while the Υ(2S)/Υ(1S) and Υ(3S)/Υ(1S) ratios are fixed to the pp fit values [26].

2

Heavy-Flavour Probes in Heavy-Ion Collisions

Heavy quarks (charm and beauty) provide sensitive probes of the heavy-ion collision dynamics at both short and long timescales. On one hand, heavy-flavour production is an intrinsically perturbative phenomenon which involves large momentum transfer due to the large mass of the quarks ($m_c \simeq 1.5$ GeV/c^2 and $m_b \simeq 5$ GeV/c^2) and, thus, takes place on a short timescale, smaller than the formation time of the QGP. On the other hand, the long lifetime of charm and beauty quarks allows them to live through the thermalization phase of the plasma and to possibly interact with the constituents of the medium.

The measurement of charm and beauty production in proton–proton and proton–nucleus collisions provides the necessary baseline for the study of medium effects in nucleus–nucleus collisions, and it is of great interest *per se*, as a test of both perturbative and non-perturbative sectors of QCD. Moreover, proton–nucleus collisions allow to investigate the cold nuclear matter effects, which are present also in nucleus–nucleus collisions and need to be disentangled from final state effects in order to understand the heavy-flavour interaction mechanisms with the medium.

In this chapter, after a brief introduction on the heavy-flavour production in proton–proton collisions in Section 2.1, the interaction mechanisms of heavy quarks and the relation to the medium properties will be discussed in Section 2.2 and Section 2.3. Finally, in Section 2.4, the cold nuclear matter effects, which can be investigated in proton–nucleus collisions, are described.

2.1 Heavy-Flavour Production in pp Collisions

Charm and beauty quarks are produced in parton scattering processes involving large momentum transfers (large virtuality). In these conditions, asymptotic freedom allows to perform perturbative calculations in terms of $\alpha_{\mathrm{s}}(\mathcal{Q}^2)$, where $\mathcal{Q}^2$ is the scale of the process, of the order of the energy of the produced particles. Heavy-flavour hadron production in proton–proton collisions is described, following the collinear factorization approach, as a convolution of three terms: the parton distribution functions, the hard partonic scattering cross section and the fragmentation function. The inclusive differential cross section for the production of a heavy-flavour hadron H_Q can be expressed as:

$$\begin{aligned} \mathrm{d}\sigma^{\mathrm{pp}\to\mathrm{H}_Q X}(\sqrt{s}, m_Q, \mu_{\mathrm{F}}^2, \mu_{\mathrm{R}}^2) &= \sum_{i,j=q,\bar{q},g} f_i(x_1, \mu_{\mathrm{F}}^2) \otimes f_j(x_2, \mu_{\mathrm{F}}^2) \otimes \\ &\otimes \mathrm{d}\hat{\sigma}^{ij\to Q(\bar{Q})\{k\}}(\alpha_{\mathrm{s}}(\mu_{\mathrm{R}}^2), \mu_{\mathrm{F}}^2, m_Q, x_1 x_2 s) \otimes \\ &\otimes D_Q^{\mathrm{H}_Q}(z, \mu_{\mathrm{F}}^2)\,. \end{aligned} \tag{2.1}$$

The partonic cross section $\mathrm{d}\hat{\sigma}^{ij\to Q(\bar{Q})\{k\}}$ is calculated as a perturbative series in the strong coupling α_{s}, which depends on the energy scale of the process, indicated here as renormalization scale, μ_{R}; currently, calculations are performed up to next-to-leading order (NLO), $\mathcal{O}(\alpha_{\mathrm{s}}^3)$ (MNR [28], GM-VFNS [29–31], MC@NLO [32, 33]), or at fixed order with next-to-leading-log resummation (FONLL [34–36]). The Parton Distribution Function (PDF), $f_i(x_1, \mu_{\mathrm{F}}^2)$ encodes the partonic structure of the colliding protons and can be interpreted as the probability to find a parton i inside the proton with fraction of momentum $x_1 = p_i/p_{\mathrm{p}}$ (Bjorken x). The fragmentation function $D_Q^{\mathrm{H}_Q}(z, \mu_{\mathrm{F}}^2)$ parametrizes the probability for the heavy quark Q to fragment into a hadron H_Q with a momentum fraction $z = p_{\mathrm{H}_Q}/p_Q$. The PDFs and the fragmentation functions depend on the energy scale of the process, in particular they evolve as a function of the momentum transfer $\mathcal{Q}^2$. In the cross section calculations they are evaluated at a given scale called factorization scale μ_{F}. The renormalization and factorization scales are usually taken of the same order of the momentum transfer of the hard process $\mu_{\mathrm{R}} \sim \mu_{\mathrm{F}} \sim \sqrt{m_Q^2 + p_{\mathrm{T},Q}^2}$.

The measurement of charm and beauty production at different centre-of-mass energies provides an interesting test of perturbative QCD (pQCD). Moreover, at LHC energies, the measurement of charm production in the low transverse momentum region probes the parton distribution functions of the proton at small values of parton fractional momentum x ($\sim 10^{-4}$) and squared momentum transfer $\mathcal{Q}^2$. Since at LHC energies heavy quarks are mainly produced through gluon-gluon fusion processes ($gg \to Q\bar{Q}$), charm production in pp collisions, in particular, could probe the gluon enhancement, expected in the low-x regime, arising from non-linear evolution of the parton densities [37].

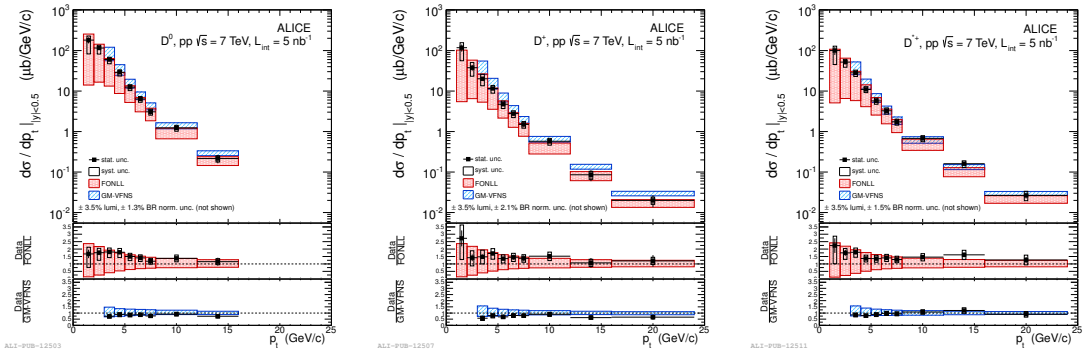

(a) (b) (c)

FIGURE 2.1: p_{T}-differential inclusive cross section in pp collisions at $\sqrt{s} = 7$ TeV of prompt D^0 (a), D^+ (b), and D^{*+} (c) compared with pQCD calculations [38].

Charm production was measured at LHC using prompt charmed mesons D^0, D^+, D^{*+}, and D_s^+ in pp collisions at $\sqrt{s} = 2.76$ and 7 TeV [38–42]. The D meson p_{T}-differential cross sections at both energies are described by pQCD calculations, even though the central predictions of FONLL [34–36] (GM-VFNS [29–31]) underestimates (overestimates) charm production, as can be observed e.g. at $\sqrt{s} = 7$ TeV in Figure 2.1. Both calculations use CTEQ6.6 parton distribution functions, which do not include non-linear effects in the evolution towards small x [43]. Reaching $p_{\mathrm{T}} = 1$ GeV/c, this measurement probes the gluon distribution in the x range of a few 10^{-4} and squared momentum transfer $\mathcal{Q}^2 \sim (4\ \mathrm{GeV})^2$, but with the current uncertainties of the experimental measurement and of the theoretical predictions, it is not possible to draw conclusions about small-x gluon saturation effects.

The total charm production cross section was estimated by extrapolating to $p_{\mathrm{T}} = 0$ GeV/c and dividing the total D meson production cross section by the relative production yield for a charm quark hadronizing to a particular species of D meson. The dependence of the total nucleon–nucleon charm production cross section on the collision energy (shown in Figure 2.2) is described by pQCD calculations.

2.2 Heavy-Flavour Production in Pb–Pb and p–Pb Collisions

For hard processes, such as heavy-flavour production, in the absence of nuclear and medium effects, a nucleus–nucleus (AA) (or proton–nucleus, pA) collision would behave as a superposition of independent nucleon–nucleon (NN) collisions. The charm and beauty differential yields would then scale from pp to AA (or pA) proportionally to the

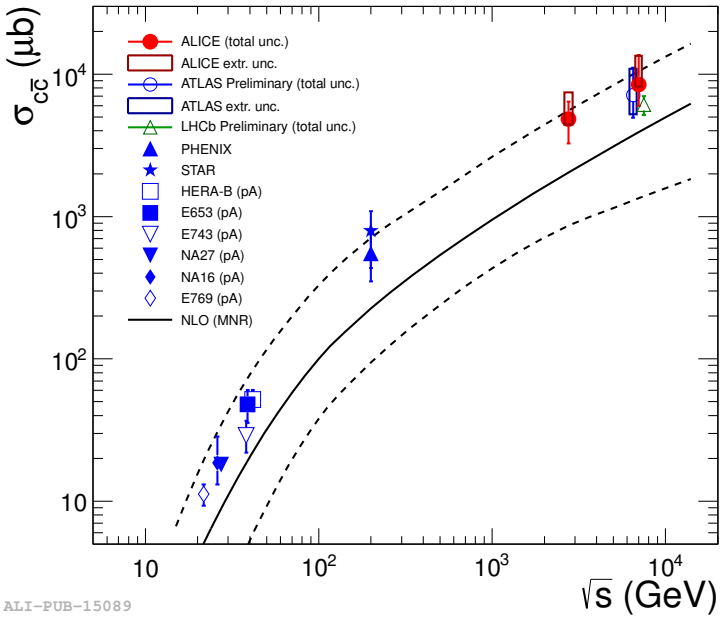

FIGURE 2.2: Energy dependence of the total charm production cross section compared with pQCD expectations. In case of proton–nucleon (pA) or deuteron–nucleus (dA) collisions, the measured cross sections have been divided by the number of binary nucleon–nucleon collisions [39–42, 44–46].

average number $\langle N_{\rm coll} \rangle$ of inelastic NN collisions (binary scaling):

$$\mathrm{d}^2 N^{\mathrm{H}_Q}_{\mathrm{AA(pA)}}/\mathrm{d}p_{\mathrm{T}}\mathrm{d}y = \langle N_{\mathrm{coll\ AA(pA)}} \rangle \times \mathrm{d}^2 N^{\mathrm{H}_Q}_{\mathrm{pp}}/\mathrm{d}p_{\mathrm{T}}\mathrm{d}y\,. \tag{2.2}$$

Several effects can determine a departure from binary scaling. They are usually divided in two classes:

- **Initial-state effects**, such as the modification of the parton distribution functions in the nucleus. Partons can also suffer initial state radiation or experience momentum broadening due to multiple soft scattering before the hard process. These effects can be addressed at the LHC by comparing the charm production in p–Pb to that in pp collisions and they will be explained in more detail in Section 2.4.

- **Final-state effects** due to the interaction of the produced hard partons with the hot and dense medium formed in the AA collision. Partonic energy loss in the medium is an example of such an effect. Charm and beauty quarks are qualitatively different probes with respect to light partons since QCD predicts different in-medium energy loss of massive partons with respect to that of light quarks and gluons. The study of the difference in the attenuation of light and massive probes allows to investigate the quenching effects in a deconfined medium. Heavy quarks with low momentum can also reach thermal equilibrium with the medium and

participate in the collective expansion of the system. These effects will be treated in detail in the next section (Section 2.3).

2.3 Heavy Quarks as QGP Probes

Heavy quarks are produced in the early stage of the Pb–Pb collisions at the LHC on a temporal and spatial scale proportional to the inverse of the large virtuality $\mathcal{Q}$ of the process, $\Delta\tau \sim \Delta r \sim 1/\mathcal{Q}$, thus, sufficiently small for the production to be unaffected by the properties of the QGP that is formed in the collision. In fact, the minimum virtuality $\mathcal{Q}_{\rm min} = 2m_Q$ in the production of a $Q\overline{Q}$ pair implies a space-time scale of $\sim 1/(2m_Q) \simeq 1/2.4$ GeV$^{-1} \simeq 0.1$ fm (for charm), to be compared with the formation time $\tau_0 \simeq 1$ fm and the lifetime ($\simeq 10$ fm) of the thermalized QGP. Thus, heavy quarks experience the full evolution of the system and can be studied to investigate the properties of the medium. In particular, they are expected to lose energy interacting with the constituents of the medium, while their multiplicity is not expected to change. The energy lost by a particle in the medium (ΔE) depends on the characteristics of the particle traversing it (energy, mass and colour charge) and provides fundamental information on the plasma properties, like the gluon density, particle–medium interaction coupling, temperature and thickness.

Low-momentum heavy quarks could also participate, through interactions with the medium, in the collective expansion of the system and eventually reach thermal equilibrium with the medium constituents.

Through the measurement of charm and beauty meson production at low and high momentum, it is also possible to investigate whether the hadronization mechanisms take place in the medium or via fragmentation in the vacuum, respectively. Hadronization via recombination in the medium would occur if a quark and an antiquark (or three quarks) close by in the phase space, thus with similar velocities (direction and magnitude), combine together to form a meson (or a baryon). In this case the momentum of the hadron is equal to the sum of the momenta of the original quarks [47]. Instead, in case of hadronization via fragmentation of a high-momentum parton in the vacuum, the hadron carries a fraction of the original momentum of the parton. A possible hadronization via recombination of the charm quark with the partons in the medium would affect the $\rm D_s^+$ meson production: the medium created in heavy-ion collisions presents an enhanced multiplicity of strange quarks [48], and if c quarks recombine in the medium, an enhancement of $\rm D_s^+/D$ with respect to pp collisions is expected [49, 50]. Recombination can also be responsible of an enhanced charmed baryon (e.g. Λ_c^+) production relative to D mesons.

2.3.1 In-Medium Energy Loss

The interactions of particles inside a medium are characterized by the following, closely related, variables:

- *mean free path* $\lambda = 1/(\rho\sigma)$ related to the medium density ρ and to the cross section of the particle-medium interaction σ;
- *opacity* $N = L/\lambda$ or number of scatterings experienced by the particle in a medium of thickness L;
- *Debye mass* m_D is the inverse of the screening length of the colour fields in the plasma. It is related to the temperature of the medium ($m_D(T) \sim gT$, with g equal to the coupling parameter) and characterizes the typical momentum exchanges with the medium;
- *transport coefficient* $\hat{q}$, which encodes the scattering power of the medium through the average transverse momentum squared transferred to the traversing particle per unit path length. It combines both thermodynamical and dynamical properties of the medium:
$$\hat{q} \equiv \frac{m_D^2}{\lambda} = m_D^2 \rho\sigma = \frac{\langle k_{\mathrm{T}}^2 \rangle}{\lambda}\,; \tag{2.3}$$
- *diffusion constant* D which characterizes the dynamics of heavy non-relativistic particles traversing the plasma.

QCD energy loss differs from QED energy loss mainly because of the non-Abelian nature of QCD, i.e. the fact that gluons can also interact with each other. The QCD coupling α_{s} runs faster that α_{em} and the scale $\mathcal{Q}$ at which $\alpha_{\mathrm{s}}(\mathcal{Q})$ is evaluated needs to be explicitly considered in all calculations of QCD energy loss. Moreover, it is crucial to take into account the different coupling of quarks and gluons with the medium. The relative strengths of the three distinct QCD vertices involved ($q \to qg$, $g \to gg$, and $g \to q\bar{q}$) are determined by the structure (Casimir factors) of the gauge $\mathrm{SU}(3)_{\mathrm{colour}}$ group. The probability for a gluon to radiate a gluon is proportional to the colour factor $C_A = 3$, while for a quark the same probability is proportional to $C_F = 4/3$. If the radiated gluons carry a small fraction of the original parton momentum, the average number of gluons radiated by a gluon is $C_A/C_F = 9/4$ higher than that radiated by a quark.

Depending on the kinematic region, a colour charge can lose energy[1] in a plasma with temperature T mainly by collisional and radiative mechanisms (Figure 2.3). Therefore, the total energy loss of a parton traversing a medium is the sum of two terms: $\Delta E = \Delta E_{coll} + \Delta E_{rad}$.

[1] If the energy of the particle is similar to the plasma temperature, $E \sim \mathcal{O}(T)$, the particle can also gain energy while traversing it.

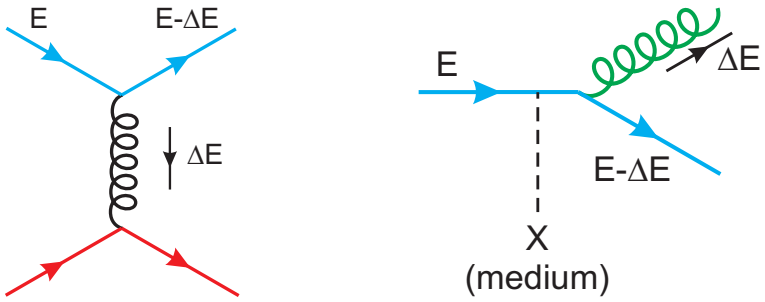

FIGURE 2.3: Diagrams for collisional (left) and radiative (right) energy losses of a quark of energy E traversing a quark-gluon medium.

Collisional energy loss

Collisional energy loss is due to elastic scatterings with the medium constituents (Figure 2.3, left) and dominates at low particle momentum. The average energy loss in one scattering (with cross section $\mathrm{d}\sigma/\mathrm{d}t$, where $t = \mathcal{Q}^2$ is the squared momentum transfer) in a medium of temperature T is:

$$\langle \Delta E_{coll}^{1scatt} \rangle \approx \frac{1}{\sigma T} \int_{m_D^2}^{t_{max}} t \frac{\mathrm{d}\sigma}{\mathrm{d}t} \mathrm{d}t \,, \tag{2.4}$$

where t_{max} is the maximum squared momentum transfer, σ the integrated particle-medium interaction cross section and m_D the Debye mass. If one considers the momentum-transfer integral limits given by the QGP Debye mass squared $t_{min} = m_D^2(T) \sim 4\pi\alpha_s T^2(1+n_f/6)$ and $t_{max} = s \sim ET$ and as the dominant contribution to the parton-parton t-differential elastic cross section

$$\frac{\mathrm{d}\sigma}{\mathrm{d}t} \approx C_i \frac{4\pi\alpha_s^2(t)}{t^2} \,, \tag{2.5}$$

where $C_i = 9/4, 1, 4/9$ are the colour factors for gg, gq and qq scatterings respectively, one obtains for a parton of energy E inside a QGP of temperature T (for $E \gg m_q^2/T$) [51]:

- Light quark, gluon: $-\left.\frac{\mathrm{d}E_{coll}}{\mathrm{d}l}\right|_{q,g} = \frac{1}{4} C_R \alpha_s(ET) m_D^2 \ln\left(\frac{ET}{m_D^2}\right)$,
- Heavy quark: $-\left.\frac{\mathrm{d}E_{coll}}{\mathrm{d}l}\right|_{Q} = -\left.\frac{\mathrm{d}E_{coll}}{\mathrm{d}l}\right|_{q} - \frac{2}{9} C_R \pi T^2 \left[\alpha_s(m_Q^2)\alpha_s(ET) \ln\left(\frac{ET}{m_Q^2}\right)\right]$,

with $C_R = 4/3$ (3) being the quark-gluon (gluon-gluon) coupling. $-\frac{\mathrm{d}E}{\mathrm{d}l} = \frac{\langle \Delta E^{tot} \rangle}{L}$ is defined as the energy loss per unit length or stopping power. For incoherent scatterings one has: $\Delta E^{tot} = N \cdot \Delta E^{1scatt}$. The energy loss per unit length reduces to $-\mathrm{d}E/\mathrm{d}l = \langle \Delta E^{1scat} \rangle / \lambda$. The amount of ΔE_{coll} is linear with the medium thickness and it has a logarithmic dependence on the initial parton energy.

The fact that heavy-quark masses are well above the typical temperature of the system, $m_Q \gg T$, allows also a diffusion treatment of their elastic interactions with the medium which can be parametrized in terms of Brownian motion of a heavy test particle in a bath of light-particle fluid. Non-relativistically, the typical thermal momentum transfer of a heavy quark is $p_{\rm th} \simeq 3m_Q T \gg T^2$, and therefore much larger than the typical momentum transfer from the medium, $\mathcal{Q}^2 \sim T^2$. This allows to expand the Boltzmann equation in momentum transfer to arrive at a Fokker-Planck description of heavy-quark diffusion in the QGP, which directly yields the pertinent transport coefficients, as will be explained in the following. The transport coefficients are related to the underlying (elastic) scattering matrix elements on light partons in the QGP which allow for direct comparisons of microscopic models of the heavy-quark interaction.

The starting point for the derivation of the Fokker-Plank equation is the Boltzmann equation for the heavy-quark phase-space distribution, f_Q,

$$\left[\frac{\partial}{\partial t} + \frac{\mathbf{p}}{\omega_{\mathbf{p}}}\frac{\partial}{\partial \mathbf{x}} + \mathbf{F}\frac{\partial}{\partial \mathbf{p}}\right] f_Q(t,\mathbf{x},\mathbf{p}) = C[f_Q]\,, \tag{2.6}$$

where $\omega_{\mathbf{p}} = \sqrt{m_Q^2 + \mathbf{p}^2}$ denotes the energy of a heavy quark with 3-momentum $\mathbf{p}$, $\mathbf{F}$ is the mean-field force on the test particle due to an external (in-medium) potential, and $C[f_Q]$ summarizes the collision integral induced by scattering off particles in the heat bath. Neglecting mean-field effects, and assuming an uniform medium, by integration over the fireball volume, Equation (2.6) simplifies to an equation for the distribution function, f_Q, of the heavy quark in momentum space determined by the collisions term:

$$\frac{\partial}{\partial t} f_Q(t,\mathbf{p}) = C[f_Q]\,. \tag{2.7}$$

The collision integral $C[f_Q]$ encodes the transition rate for collisions of a heavy quark with heath-bath particles. The relevant momentum transfers to the heavy quark can be considered much smaller than the heavy-quark momentum $\mathbf{p}$, and Equation (2.7) is approximated by the Fokker-Plank equation

$$\frac{\partial}{\partial t} f_Q(t,\mathbf{p}) = \frac{\partial}{\partial p_i}\Big\{A_i(\mathbf{p}) f_Q(t,\mathbf{p}) + \frac{\partial}{\partial p_j}[B_{ij}(\mathbf{p}) f_Q(t,\mathbf{p})]\Big\}\,. \tag{2.8}$$

The transport coefficients A_i and B_{ij} depend on the transition rate. A_i encodes the average momentum change of the heavy quark per unit time and thus describes the friction in the medium, while B_{ij} represents the average momentum broadening per unit time, i.e. the diffusion in momentum-space. For an isotropic medium (in thermal equilibrium) in a non-relativistic regime the transport coefficients can be reduced to two constants γ and D, further simplifying the Fokker-Plank equation. Solving this new equation one sees that γ determines the relaxation rate of the average momentum

to its equilibrium value, it is a drag or friction coefficient ($\gamma = \tau_{\rm therm}^{-1}$, where $\tau_{\rm therm}$ is the thermal relaxation time). D is the momentum-diffusion constant, describing the momentum fluctuations. Moreover, since in thermal equilibrium the heavy quarks have to obey an equilibrium distribution with the temperature T of the bath, the drag and diffusion coefficients should satisfy the Einstein dissipation-fluctuation relation,

$$D = m_Q \gamma T \,. \tag{2.9}$$

The spatial diffusion coefficient, D_s, which describes the broadening of the spatial distribution with time, is related to the drag and momentum-diffusion coefficients through

$$D_s = \frac{T}{m_Q \gamma} = \frac{T^2}{D} \,. \tag{2.10}$$

The heavy-quark friction and diffusion coefficients in the QGP have been calculated with several microscopic approaches. A perturbative expansion of the elastic scattering off thermal partons shows poor convergence for coupling constants believed to be relevant for a QGP as formed in heavy-ion collisions ($\alpha_{\rm s} \sim 0.1$). Thus, alternative methods have been investigated:

- perturbative QCD with running coupling constant at low momentum transfer or reduced screening mass;
- non-perturbative calculations implementing resonance-like correlations in the QGP using heavy-quark effective theory, in-medium T-matrices with heavy-quark potentials estimated from thermal lattice QCD;
- evaluations based on the strong-coupling limit of conformal field theory (CFT) using a conjectured correspondence to string theory in Anti-de-Sitter (AdS) space.

In Figure 2.4 the transport coefficients for charm quark, obtained with the different approaches mentioned before, are reported as a function of temperature for $p = 0$. As can be observed in the left panel (Figure 2.4(a)), close to the critical temperature T_c, the $T-$matrix approach, the pQCD calculation with running $\alpha_{\rm s}$ and the AdS/CFT correspondence matched to QCD are not much different and share overlap around $\gamma \simeq 0.2$ c/fm. Figure 2.4(b) shows the dimensionless quantity $2\pi T D_s$ for leading order pQCD, leading order pQCD with running coupling, effective resonance model and $T-$matrix approach. The former three are fairly constant as a function of temperature while $T-$matrix approach exhibits a significant increase with temperature, indicating maximal interaction strength close to T_c. This originates from the increasing potential strength (decrease in colour screening) with decreasing temperature, enhancing resonance correlations at lower temperature.

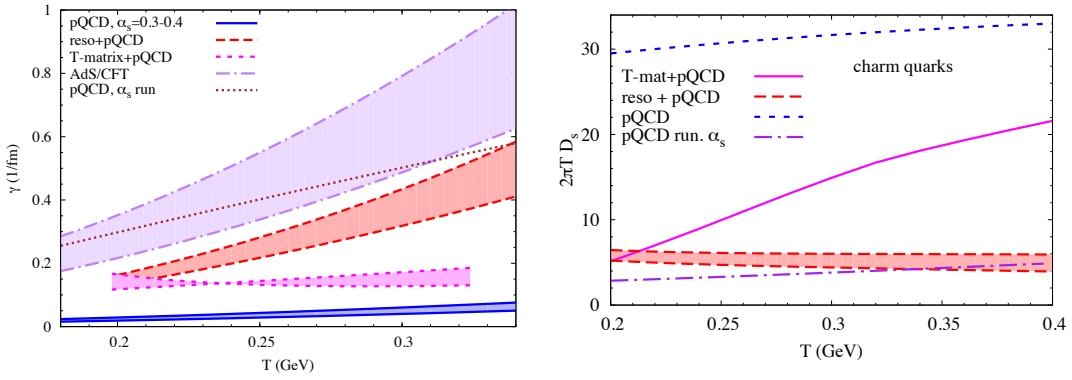

(a) (b)

FIGURE 2.4: (a) Charm-quark friction coefficient γ in the QGP as a function of temperature for LO-pQCD with fixed $\alpha_s = 0.4$ [52], $T-$matrix plus LO-pQCD for gluons [53], pQCD with running α_s [54, 55], and from AdS/CFT correspondence matched to QCD [56]. (b) Charm spatial diffusion coefficient D_s in the QGP for: LO-pQCD with fixed $\alpha_s = 0.4$ [52], effective resonance model plus LO-pQCD, $T-$matrix approach plus LO-pQCD for gluons [53], and pQCD with running α_s [54, 55].

Radiative energy loss

The dominant mechanism of energy loss of a fast parton in a QCD environment is of radiative nature: a parton traversing a QGP loses energy mainly by medium-induced multiple gluon emission (Figure 2.3, right). This loss can be determined from the corresponding single- or double-differential gluon Bremsstrahlung spectrum ($\omega \mathrm{d}I_{rad}/\mathrm{d}\omega$ or $\omega \mathrm{d}I_{rad}/\mathrm{d}^2\omega \mathrm{d}k_{\mathrm{T}}^2$, where ω, k_{T} are the energy and transverse momentum of the radiated gluon, respectively):

$$\langle \Delta E_{rad}^{1scatt} \rangle = \int^{E} \omega \frac{\mathrm{d}I_{rad}}{\mathrm{d}\omega} \mathrm{d}\omega, \quad \text{or} \quad \langle \Delta E_{rad}^{1scatt} \rangle = \int^{E} \int^{k_{\mathrm{T}},max} \omega \frac{\mathrm{d}^2 I_{rad}}{\mathrm{d}\omega \mathrm{d}k_{\mathrm{T}}^2} \mathrm{d}\omega \mathrm{d}k_{\mathrm{T}}^2 \,. \quad (2.11)$$

As an example, the general concepts of the BDMPS model [57, 58] are reported here. An energetic parton produced in a hard collision undergoes, along its path in the dense medium, multiple scatterings in a Brownian-like motion with mean free path λ, which decreases as the medium density increases. The medium is modeled with static scattering centres, which implies that in the multiple scattering process the gluons in the parton wave function pick up transverse momentum k_{T} with respect to its direction and they may eventually decohere and be radiated. The scale of the energy loss is set by the characteristic energy of the radiated gluons, which depends on L and on the properties of the medium:

$$\omega_c = \hat{q} L^2 / 2 \,, \quad (2.12)$$

where $\hat{q}$ is the transport coefficient of the medium. In the case of a static medium, the distribution of energy ω of the radiated gluons (for $\omega \ll \omega_c$) is of the form:

$$\omega \frac{\mathrm{d}I_{rad}}{\mathrm{d}\omega} \simeq \frac{2\alpha_{\mathrm{s}} C_R}{\pi} \sqrt{\frac{\omega_c}{2\omega}} \,. \tag{2.13}$$

The average energy loss of the parton is thus:

$$\langle \Delta E_{rad}^{1scatt} \rangle = \int_0^{\omega_c} \omega \frac{\mathrm{d}I_{rad}}{\mathrm{d}\omega} \mathrm{d}\omega \;\propto\; \alpha_{\mathrm{s}} C_R \omega_c \;\propto\; \alpha_{\mathrm{s}} C_R \hat{q} L^2 \,. \tag{2.14}$$

The average energy loss is: proportional to $\alpha_{\mathrm{s}} C_R$ and, thus, larger by a factor $9/4 = 2.25$ for gluons than for quarks; proportional to the transport coefficient of the medium; proportional to L^2; independent of the initial parton energy E.

For heavy quarks, because of their large mass, the radiative energy loss should be lower than for light quarks. Heavy quarks with moderate energy, i.e. $m_Q/E \gg 0$, propagate with a velocity $\beta = \sqrt{1-(m_Q/E)^2}$ significantly smaller than the velocity of light, $\beta = 1$. As a consequence, in the vacuum, gluon radiation at angles Θ smaller than the ratio of their mass to their energy $\Theta_0 = m_Q/E$ is suppressed. The relatively depopulated cone around the heavy-quark direction with $\Theta < \Theta_0$ is called the dead cone. The dead-cone effect is assumed to characterize also in-medium gluon radiation, and the energy distribution of the radiated gluons, for heavy quarks, is estimated to be suppressed by a factor

$$\omega \left.\frac{\mathrm{d}I}{\mathrm{d}\omega}\right|_{\mathrm{Heavy}} / \omega \left.\frac{\mathrm{d}I}{\mathrm{d}\omega}\right|_{\mathrm{Light}} = \left[1 + \frac{\Theta_0^2}{\Theta^2}\right]^{-2} = \left[1 + \left(\frac{m_Q}{E}\right)^2 \sqrt{\frac{\omega^3}{\hat{q}}}\right]^{-2} \equiv F_{\mathrm{H/L}}(m_Q/E, \hat{q}, \omega) \,, \tag{2.15}$$

where the expression for the characteristic gluon emission angle $\Theta \simeq (\hat{q}/\omega^3)^{1/4}$ has been used. The dead-cone suppression factor $F_{\mathrm{H/L}}$ increases (less suppression) as the heavy-quark energy E increases (the mass becomes negligible) and it decreases at large ω, indicating that the high-energy part of the gluon radiation spectrum is drastically suppressed by the dead-cone effect [59].

Due to the aforementioned hierarchy of flavour-dependent collisional and radiative energy losses, the medium effects are expected to be larger for gluons and light quarks than for c and b quarks: $\Delta E(g) > \Delta E(q) > \Delta E(c) > \Delta E(b)$ (Figure 2.5).

Jet Quenching

Medium-induced parton energy loss in nucleus–nucleus collisions results in various consequences, mostly observed through comparison with proton–proton collisions.

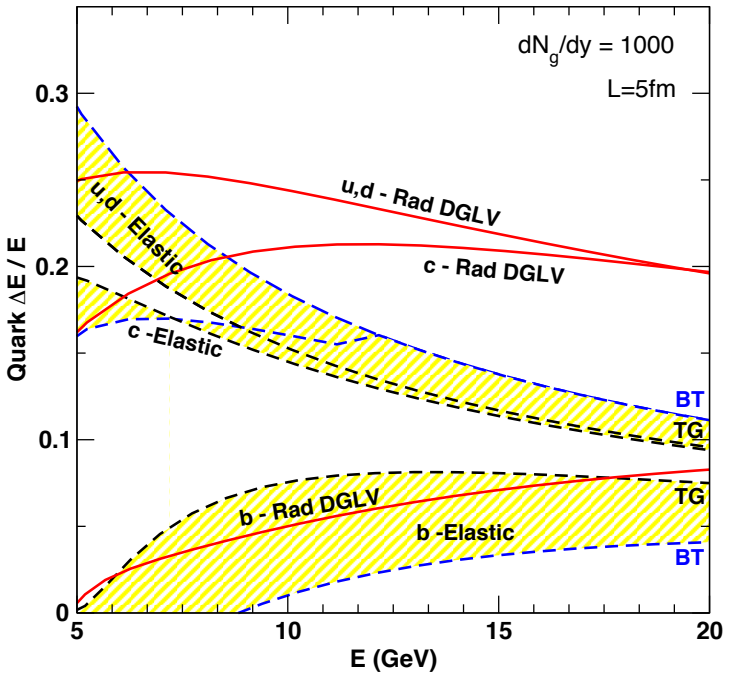

FIGURE 2.5: Average relative energy loss, $\Delta E/E$, for u, c and b quarks as a function of the energy in a longitudinally expanding QGP with fixed path length $L = 5$ fm, initial gluon density $\mathrm{d}N_g/\mathrm{d}y = 1000$ and fixed $\alpha_\mathrm{s} = 0.3$. Solid lines indicate radiative energy loss while collisional (elastic) energy loss is indicated with dashed bands [52].

The modification of fully reconstructed jets, formed by fragmentation of high p_T partons and propagating through the medium, is an example of these observables. Measuring the energy of fully reconstructed jets allows one to distinguish between energy redistribution among leading parton and the remainder of the jet, and energy dissipation out of the jet into the thermal medium. The energy dissipation into the medium can be studied by measuring the asymmetry in p_T of dijets in heavy-ion collisions as a function of centrality and by comparing them to data from pp collisions. Similarly, the measurement of the relative azimuthal angle of the two jet axes gives information about the degree of scattering of partons as they traverse the medium.

The measurement of the dijet asymmetry $A_J = (p_\mathrm{T1} - p_\mathrm{T2})/(p_\mathrm{T1} + p_\mathrm{T2})$, where "1" and "2" refer to the leading and subleading jet, respectively, was performed by ATLAS [60] and CMS [61] at the LHC. The most striking observation is the large centrality-dependent increase of the imbalance in the energy of the two jets as reported in Figure 2.6. While their energies are very different, the two jets are observed to be very close to back-to-back in the azimuthal plane, implying little or no angular scattering of the partons during their traversal of the medium.

In-medium parton energy loss changes the momentum of the partons, modifying the spectrum of high-p_T hadrons compared to pp collisions. This effect can be quantified

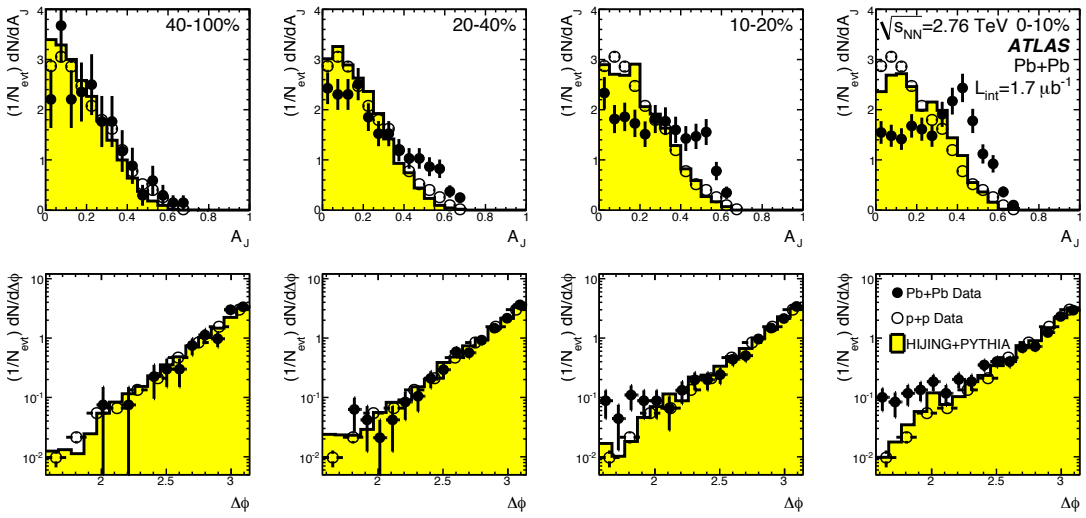

FIGURE 2.6: Dijet asymmetry (top) and azimuthal angle between the leading and subleading jets (bottom) as a function of collision centrality (from peripheral to central) for pp and Pb–Pb collisions [60].

through the nuclear modification factor R_{AA}. This observable is defined as the ratio of particle production measured in nucleus–nucleus to that expected from the proton–proton spectrum scaled by the average number of binary nucleon–nucleon collisions $\langle N_{\mathrm{coll}} \rangle$ occurring in the AA collision. Using the nuclear overlap function, defined as the convolution of the nuclear density profiles of the colliding ions in Section 1.5.1, the nuclear modification factor of the transverse momentum distribution can be expressed as:

$$R_{\mathrm{AA}}(p_{\mathrm{T}}) = \frac{\mathrm{d}N_{\mathrm{AA}}/\mathrm{d}p_{\mathrm{T}}}{\langle T_{\mathrm{AA}} \rangle \mathrm{d}\sigma_{\mathrm{pp}}/\mathrm{d}p_{\mathrm{T}}}\,, \tag{2.16}$$

where the AA spectrum corresponds to a given collision-centrality class and $\langle T_{\mathrm{AA}} \rangle$ is the average nuclear overlap function for that centrality class (proportional to $\langle N_{\mathrm{coll}} \rangle$). In-medium energy loss determines a suppression, $R_{\mathrm{AA}} < 1$, of hadrons at moderate-to-high transverse momentum. The transport approach for heavy-quark diffusion in the QGP predicts a reduction of the R_{AA} with an increasing of the interaction strength, thus a decreasing spatial diffusion coefficient.

The measurement of the D^0 meson nuclear modification factor in Au–Au collisions at $\sqrt{s_{\mathrm{NN}}} = 200$ GeV at RHIC shows no suppression in peripheral collisions, but a strong suppression, at the level of $R_{\mathrm{AA}} \sim 0.5$, in the most central collisions for $p_{\mathrm{T}} > 3$ GeV/c [62] (Figure 2.7). This observation suggests a significative energy loss of charm quarks in the hot medium. The enhancement in the intermediate-p_{T} region is consistent with model calculations including strong charm–medium interactions and hadronization via coalescence (recombination with other quarks from the medium) at intermediate p_{T}.

The R_{AA} measurement for charged particles, charged pions and D mesons in the

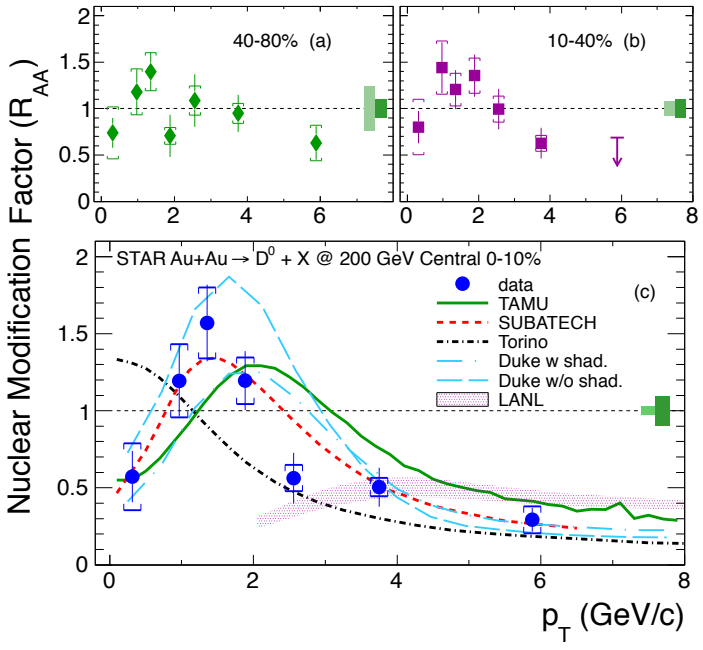

FIGURE 2.7: D^0 R_{AA} measured by STAR for peripheral 40–80% (a) and semi-central 10–40% (b) collisions. (c) D^0 R_{AA} for 0–10% most central events compared with model calculations [62].

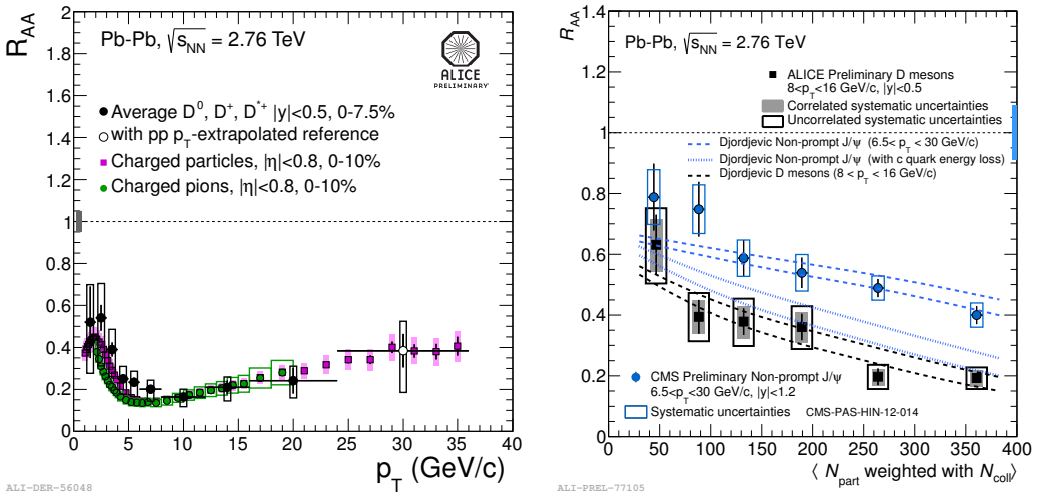

(a) (b)

FIGURE 2.8: (a) Nuclear modification factor R_{AA} as a function of p_T for D mesons, charged particles and charged pions measured in the central rapidity region for the most central Pb–Pb collisions [63]. (b) Centrality dependence of the R_{AA} of prompt D mesons [63] and of J/ψ from B meson decay [64] compared with a pQCD model including mass dependent radiative and collisional energy loss.

most central Pb–Pb collisions at $\sqrt{s_{NN}} = 2.76$ TeV at LHC is shown in Figure 2.8(a). The D meson R_{AA} is almost as strongly suppressed as inclusive charged particles and pions [63]. This observation seems in contrast to the expectation that gluons, which are

the dominant source of inclusive charged particles at LHC, should undergo larger energy loss than c quarks. The expected energy loss hierarchy, however, does not translate directly in a $R_{\rm AA}$ hierarchy, because other aspects, such as the $p_{\rm T}$ distribution and the fragmentation function of the different partons, play a role in the resulting final state hadron spectra. The comparison of the centrality dependence of the $R_{\rm AA}$ of D mesons measured by ALICE [63] and of J/ψ from B meson decays measured by CMS [64] is displayed in Figure 2.8(b). The $p_{\rm T}$ range was chosen for D mesons in order to have a similar average transverse momentum (about 10 GeV/c) to that of B mesons decaying in a J/ψ in the measured $p_{\rm T}$ interval. The result shows an indication for a stronger high-$p_{\rm T}$ suppression for charm than for beauty in central Pb–Pb collisions. The two measurements are described by the predictions based on a pQCD model including mass-dependent radiative and collisional energy loss [65]. In this model the difference in $R_{\rm AA}$ of charm and beauty mesons is mainly driven by the mass dependence of the charm and beauty energy loss, as shown by the curve in which the non-prompt J/ψ $R_{\rm AA}$ is calculated assuming charm quark energy loss.

In order to draw a more quantitative statement about the in-medium energy loss of charm (and beauty) quarks from the measurement of the nuclear modification factors of final state heavy mesons in Pb–Pb collisions, a deeper knowledge of the initial state effects induced by cold nuclear matter is required. These aspects can be addressed by measuring charm production in p–Pb collisions, as it will be explained in Section 2.4.

2.3.2 Azimuthal Anisotropy

The collective expansion of bulk matter created in nucleus–nucleus collisions exhibits various possible patterns: there can be an isotropic expansion as well as a non-isotropic component. The collective expansion is usually called flow and the underlying physics is conveniently pictured in terms of pressure gradients. Flow refers to a collective phenomenon which affects all (or almost all) particles in a given event. In that sense, it signals the presence of multiple interactions between the outgoing particles which contribute to the appearance of an overall pattern; this should be contrasted to nucleon–nucleon collisions where such effects are absent.

In central nucleus–nucleus collisions, the initial state is, on average, symmetric in azimuth. This implies that the azimuthal distribution of the final state particles is isotropic as well. Under such conditions, any pressure gradient will cause an azimuthally symmetric collective flow of the outgoing particles, which is called radial flow.

The nuclear overlap region in collisions with non-zero impact parameter is not azimuthally symmetric but has an almond shape whose deformation changes with centrality. Consequently, the pressure gradients between the centre of the overlap zone and its periphery in an average collision vary with azimuth, being strongest in the direction

of the reaction plane Ψ_{RP}, which coincides with the direction of the minor axis of the almond. The developing collective flow is proportional to the pressure gradient and therefore strongest towards the reaction plane, leading to an anisotropic distribution $\mathrm{d}N/\mathrm{d}\varphi$ of particles. Anisotropic particle distributions represent a signal of collective flow in ultra-relativistic heavy-ion collisions and the flow pattern is usually quantified via a Fourier expansion:

$$\frac{\mathrm{d}^2N}{\mathrm{d}\varphi \mathrm{d}p_{\mathrm{T}}} = \frac{\mathrm{d}N}{2\pi \mathrm{d}p_{\mathrm{T}}} \left[1 + 2\sum_{n=1}^{\infty} v_n(p_{\mathrm{T}}) \cos n(\varphi - \Psi_n)\right]. \tag{2.17}$$

The Fourier (or flow) coefficients v_n depend on p_{T} and are given by $v_n(p_{\mathrm{T}}) = \langle \cos[n(\varphi - \Psi_n)] \rangle$, where the brackets denote an average over particles in a given p_{T} interval and over events in a given centrality class. In the above equations, n is the order of the harmonic, φ is the azimuthal angle of the particle, and Ψ_n is the angle of the spatial plane of symmetry of harmonic n, the plane which maximizes the expectation value of v_n in each event, and coincides with the reaction-plane direction Ψ_{RP} in absence of fluctuations of the matter distribution.

The second coefficient v_2, usually called elliptic flow, is directly linked to the almond shape overlap region and is related to the hydrodynamic properties of the QGP like the equation of state and transport coefficient, and the kinematic viscosity, defined as the shear viscosity over entropy ratio (η/s). If the QGP is similar to a weakly-interacting gas of quarks and gluons, as might be argued on the basis of asymptotic freedom and colour Debye screening, the mean free path of particles in the medium is large, which implies a large viscosity. A direct consequence of a large viscosity is that the system will not develop strong collective expansion. A large flow, instead, is theoretically predicted in the framework of relativistic viscous hydrodynamic models, which explain the buildup of a large elliptic flow assuming that the system is, very quickly after the collision, in local equilibrium and forms a strongly-coupled quark-gluon liquid. This liquid behaves as an almost ideal or inviscid fluid, which has almost no resistance to shear stress. The lower bound for the ratio η/s calculated using gauge gravity duality for a strongly-coupled theory is equal to $1/4\pi$ (in natural units). This value turned to be the lower bound for all fluids (the KSS bound) [66]. Therefore, a fluid with $\eta/\mathrm{s} = 1/4\pi$ is called a perfect fluid.

Assuming a smooth matter distribution in the colliding nuclei, the plane of symmetry is the reaction plane and the odd Fourier coefficients are zero by symmetry. However, due to fluctuations in the matter distribution, including contributions from fluctuations in the positions of the participating nucleons in the nuclei, the plane of symmetry fluctuates event-by-event around the reaction plane. This plane of symmetry is determined by the participating nucleons. Event-by-event fluctuations of the spatial asymmetry generate

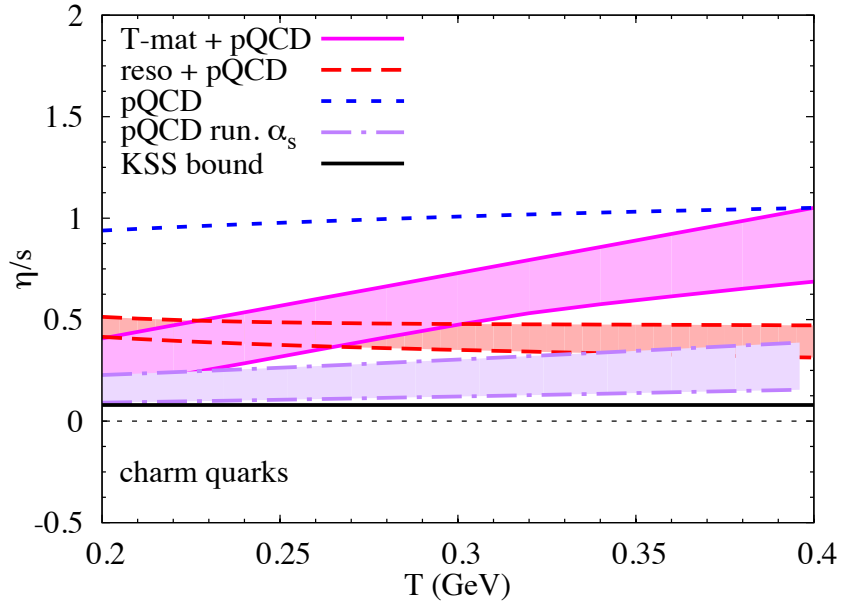

FIGURE 2.9: Ratio of shear viscosity to entropy density η/s estimates using charm-quark diffusion constants based on schematic LO pQCD elastic scattering ($\alpha_s = 0.4$) in the weakly-interacting limit (dashed line), pQCD elastic scattering with running coupling constant (band enclosed by dash-dotted lines using the weak- and strong-coupling limits), the effective resonance plus pQCD model in the strong-coupling limit (band enclosed by long-dashed lines), and the LQCD potential based $T-$matrix approach with pQCD scattering off gluons (band enclosed by solid lines constructed from weak- and strong-coupling limits.)

additional odd harmonic symmetry planes, which are predicted to give rise to the odd harmonics like v_3 and v_5. The magnitude and the transverse momentum dependence of these odd coefficients are also expected to be sensitive to the kinematic viscosity of the QGP and provides strong constraints on the initial density fluctuations of the collisions.

Heavy quarks quenched by in-medium energy loss are shifted towards low momenta and, while participating in the collective expansion, they may ultimately thermalize in the system. Low-momentum heavy quarks could also hadronize via the mechanism of recombination with other quarks in the medium, leading to a v_2 of the final state charmed hadrons arising from the v_2 of their light quark component. High-momentum heavy quarks should not thermalize in the medium and, thus, they should not acquire the large elliptic flow induced by collective pressure effects. Their azimuthal anisotropy in non-central collisions should instead be mainly determined by the path-length dependence of parton energy loss in the geometrically-asymmetric dense medium.

Heavy-quark transport calculations in the QGP show an increase of the elliptic flow as the spatial diffusion coefficient decreases and, thus, with increasing interaction strength. The η/s ratio is also related to the heavy-quark diffusion constant:

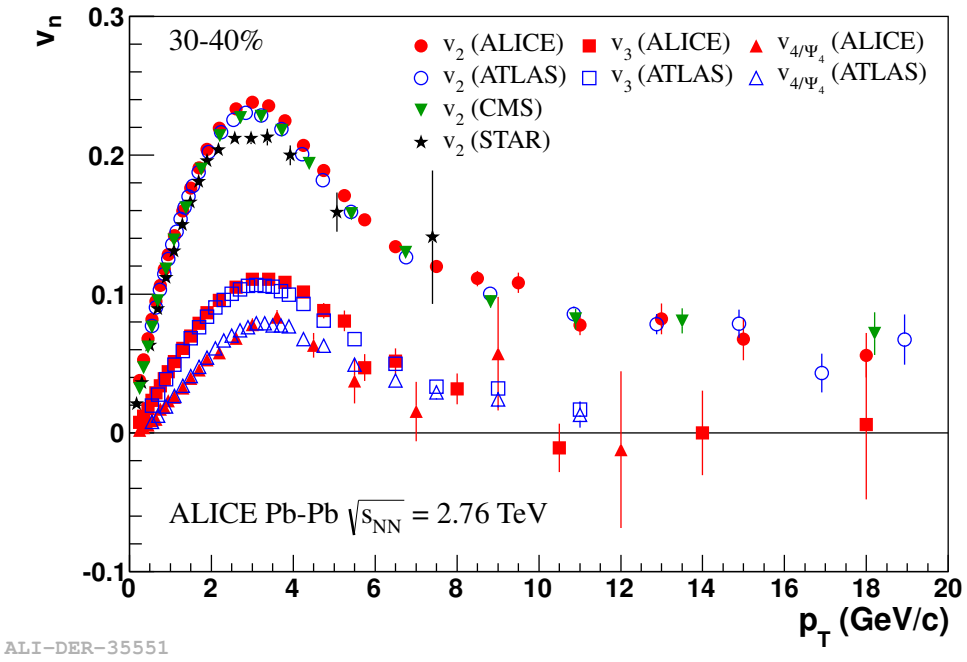

FIGURE 2.10: Comparison of the ALICE results on $v_n(p_{\mathrm{T}})$ to the analogous measurements from ATLAS and CMS collaborations, as well as v_2 measurements by STAR [67–70].

$\eta/s \propto D_s(2\pi T)$. The behaviour of the shear viscosity to entropy ratio as a function of temperature, as obtained considering different diffusion calculations, is reported in Figure 2.9. A different behaviour is only found for the $T-$matrix+pQCD model, which suggests a strongly-coupled regime close to T_c and a relatively weak coupling above $\sim 2T_c$. The increase of η/s with temperature is related to colour Debye screening of the LQCD-based potentials, which entails a gradual melting of the dynamically generated resonances in the heavy-light quark $T-$matrix.

Elliptic Flow

The anisotropic flow coefficients are usually estimated from measured correlations between the observed particles. The anisotropic flow coefficients of charged particles were measured at LHC for Pb–Pb collisions at $\sqrt{s_{\mathrm{NN}}} = 2.76$ TeV (Figure 2.10). The elliptic (v_2), triangular (v_3) and v_4 flow coefficients as a function of p_{T} for non-central Pb–Pb collisions are consistent among the LHC experiments [67–69]. v_2 at top RHIC energy has a peak value about 10% lower than at LHC although it is very similar in shape [70]. The elliptic flow coefficient rises approximately linearly with p_{T} to a maximum of $v_2 \approx 0.23$ around 3 GeV/c. The coefficient then decreases, but stays finite out of the highest p_{T} measured. Also the triangular flow coefficient is very significant out to about 10 GeV/c and similar in shape, reaching about half the value of v_2 at the maximum. The transverse

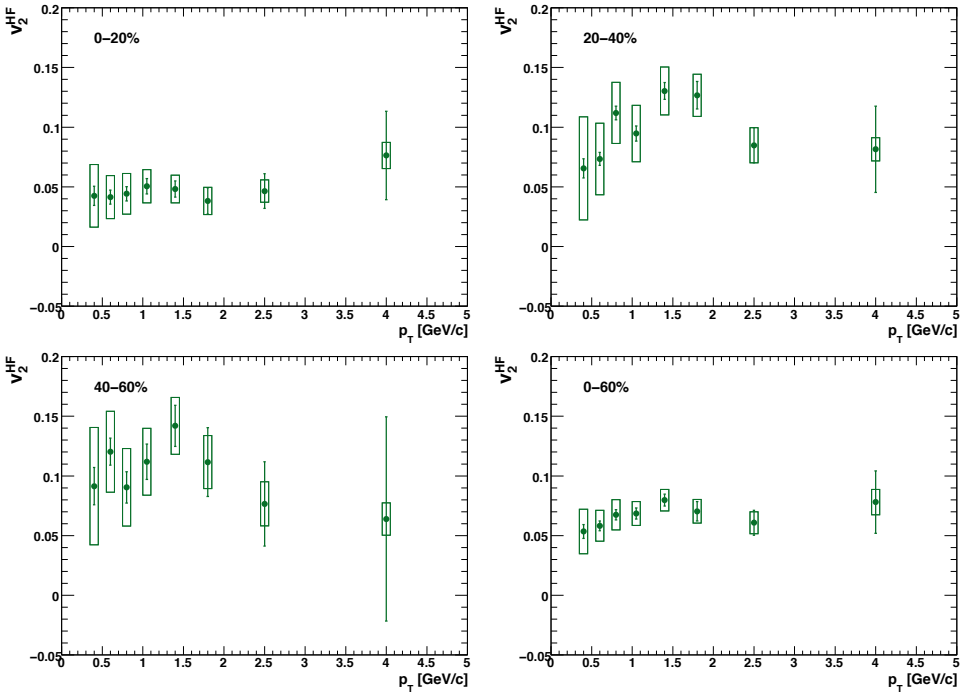

FIGURE 2.11: Elliptic flow v_2 of electrons coming from semileptonic decays of heavy-flavour mesons measured in Au–Au collisions at $\sqrt{s_{NN}}$ = 200 GeV by PHENIX for different collision centralities [44].

momentum dependence of v_2 and v_3 are described by hydrodynamical model calculations with small value of the shear viscosity to entropy ratio η/s. The centrality dependence of the elliptic and triangular flow was also investigated, and a significant difference was observed. v_3 does not depend strongly on centrality while v_2 increases from central to peripheral collisions. The strong change in v_2 and the small change in v_3 as a function of centrality, in particular for the most central collisions, follow the centrality dependence of the corresponding spatial anisotropies [71].

In the heavy-flavour sector, an azimuthal anisotropy in the production was observed in Au–Au collisions at RHIC with v_2 values of up to about 0.13 for electrons from heavy-flavour decays, as shown in Figure 2.11 [44]. The results obtained at the LHC by ALICE on D meson azimuthal anisotropy, which is one of the main goals of this thesis, will be presented in Chapter 7.

2.4 Initial-State Effects and the Role of pA Collisions

A complete understanding of the nucleus–nucleus results requires an understanding of the nuclear effects in the initial state, which can be accessed by studying proton–nucleus collisions.

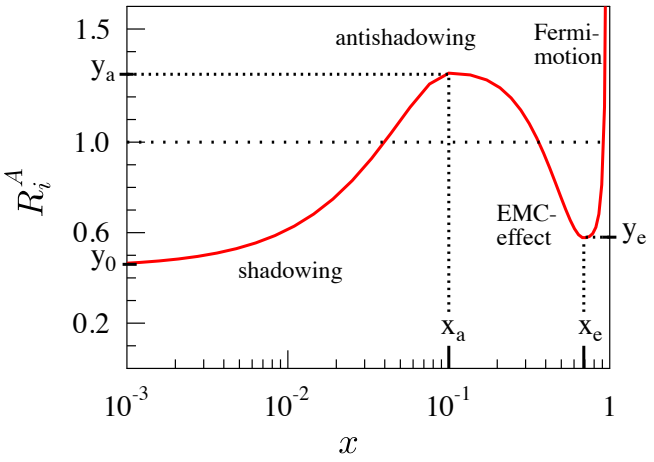

FIGURE 2.12: Illustration of the nuclear modification of bound nucleons.

Nuclear Modification of Parton Densities

The colliding nuclei do not behave as a mere incoherent superposition of their constituent nucleons. In the initial state, the nuclear environment affects the quark and gluon distributions, which are modified in bound nucleons depending on the parton fractional momentum x and the atomic mass number A.

The bound nucleon PDFs $f_i^A(x, \mathcal{Q}^2)$ for each parton flavour i are usually expressed by

$$f_i^A(x, \mathcal{Q}^2) \equiv R_i^A(x, \mathcal{Q}^2) f_i(x, \mathcal{Q}^2)\,, \tag{2.18}$$

where $R_i^A(x, \mathcal{Q}^2)$ denotes the nuclear modification to the free nucleon PDF $f_i(x, \mathcal{Q}^2)$. Experiments of deep inelastic scattering (DIS) with nuclei have measured different nuclear effects associated to different ranges of x, illustrated in Figure 2.12: 1) *shadowing* for the suppression observed at small x ($x \lesssim 0.05$); 2) *antishadowing* for the enhancement at moderate values of x ($0.05 \lesssim x \lesssim 0.3$); *EMC effect* for the suppression observed in the region $0.3 \lesssim x \lesssim 0.7$; and 4) *Fermi motion* for the enhancement when $x \to 1$ [72]. As in the case of the free proton, the sets of nuclear PDFs are obtained by global fits to several sets of experimental data. In Figure 2.13 a few sets for the ratios of PDFs of protons inside a lead nucleus over those in a free proton are shown. The ratios are rather similar for valence quarks, well constrained by the DIS data except at small x, and sea quarks, constrained by DIS and Drell-Yan data except for very small and large x. In the case of the gluons very different parametrizations lead to similar descriptions of the available DIS and Drell-Yan data. The EPS09 [73] global fit analysis includes also the results on pion production in d–Au and pp collisions at RHIC, which are sensitive to the gluon distribution, and provides evidence for shadowing and EMC-effect also in the nuclear gluons.

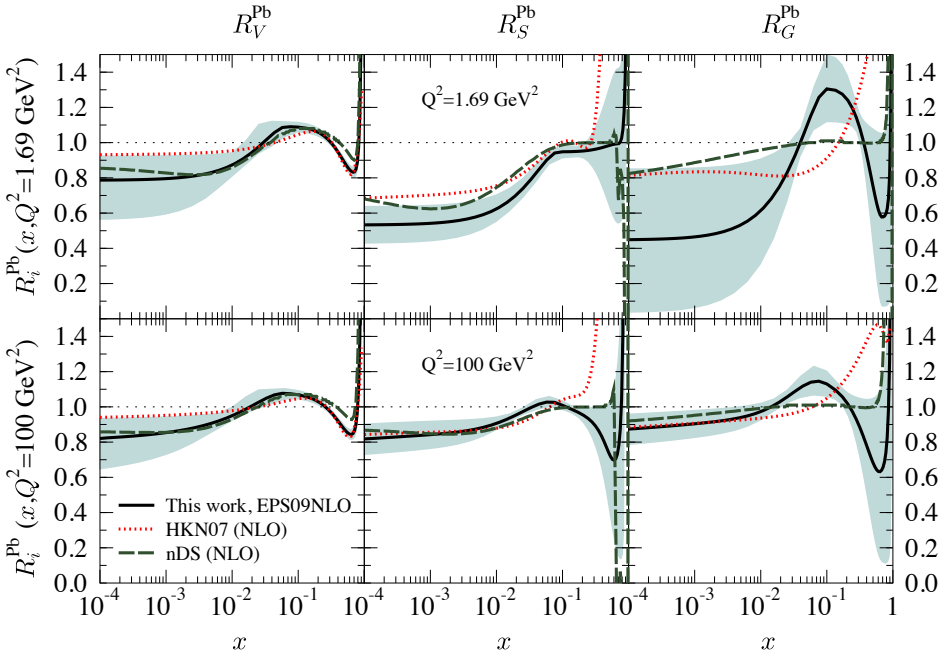

FIGURE 2.13: Comparison of the average valence and sea quark, and gluon modifications at $\mathcal{Q}^2 = 1.69$ GeV^2 and $\mathcal{Q}^2 = 100$ GeV^2 for Pb nucleus from different global fits [73–75].

A direct consequence of shadowing is the reduction of hard-scattering cross sections in the phase-space region characterized by small x incoming partons, hence, at midrapidity, low-p_{T} outgoing partons. Charm and beauty production cross sections would also be affected, in particular reduced, by this effect and the measurement of the nuclear modification factor of the D meson p_{T} distribution in p–Pb collisions at the LHC is a sensitive tool to probe nuclear PDFs.

Nuclear-modified parton distribution functions allow to account for high-density effects at small x within the framework of perturbative QCD collinear factorization. However, factorization is expected to break down when the gluon density is large enough and the gluon phase-space becomes saturated. In these conditions, partons in the nuclear wave function at small x would act coherently, not independently as assumed with factorization, and they may form a Color Glass Condensate (CGC). The relevant parameter in the CGC is the saturation scale $\mathcal{Q}_{\mathrm{s}}^2(x)$, determined by the parton density per unit transverse area, and thus growing with the nuclear mass number A as $\mathcal{Q}_{\mathrm{s}}^2(A) \sim A/R_A^2 \sim A^{1/3}$, at fixed x. For a Pb nucleus probed at LHC energy, the estimated saturation scale at $x \sim 10^{-4}$–10^{-5} is $\mathcal{Q}_{\mathrm{s}}^2 \sim 2$–$3$ GeV^2 [76]. It has been argued that charm-quark production in the kinematic domain corresponding to transverse masses smaller than the saturation scale, $m_{\mathrm{T},c} \lesssim \mathcal{Q}_{\mathrm{s}} \sim 1.5$–$2$ GeV, would be strongly affected by the presence of the CGC. In particular, since the mean intrinsic transverse momentum of partons in the CGC is of

the order $\mathcal{Q}_s$, rather than of the order $\Lambda_{QCD} \sim 0.2$ GeV as assumed in collinear factorization, the fact that $\mathcal{Q}_s \ll \Lambda_{QCD}$ would lead to significantly harder transverse momentum distributions for charm quarks in p–Pb than in pp collisions, and to a suppression of the production for $m_T < \mathcal{Q}_s$ [77–80].

Initial State Multiple Scattering and Energy Loss

Partons can also lose energy in the initial stages of the collision via initial state radiation, thus modifying the centre-of-mass energy of the partonic system, or experience transverse momentum broadening due to multiple soft collisions before the $c\bar{c}$ pair is produced.

It was first observed in 1987 [81] that high-p_T hadrons in pA collisions are produced copiously in the range of $p_T \lesssim 2$ GeV/c. This effect is know as Cronin effect and is usually explained in terms of multiple interactions within the nucleus. The mechanism of multiple interaction changes with energy. At low energies a high-k_T parton is produced off different nucleons incoherently, while at high energies it becomes a coherent process. This is controlled by the coherence length

$$l_c = \frac{\sqrt{s}}{m_N k_T}\,, \tag{2.19}$$

where k_T is the transverse momentum of the parton produced at midrapidity and then hadronizing into the detected hadron with transverse momentum p_T. If the coherence length is shorter than the typical nucleon–nucleon separation, the projectile interacts incoherently with individual nucleons and the Cronin effect is due to soft multiple interactions. If the coherence length is longer than the nuclear radius all amplitudes interfere coherently and result in a collective parton distribution of the nucleus. In this regime hard partons originate mainly from radiated gluons and the gluon shadowing is responsible of a reduction of the Cronin effect [82–84].

Parton energy loss in nuclear matter shows a linear dependence on the path length and on the energy for finite nuclei in the case of few interactions. The destructive interference of gluons results to be less effective than in a hot medium in reducing the total radiative energy loss with respect to a sum of single gluon emissions. In AA collisions the final state energy loss is expected to be dominant with respect to initial state one, due to the large density of the QGP, e.g. $\hat{q}_{cold} \simeq 0.05$ GeV^2/fm, $\hat{q}_{hot} \simeq 10$ GeV^2/fm [85].

Possible Effects of Final State Flow

Recent studies on long-range correlations of charged hadrons in p–Pb collisions [86–89], the measured species-dependent nuclear modification factor of pions, kaons, and protons in d–Au collisions [90], and the larger suppression observed for the ψ' meson with respect

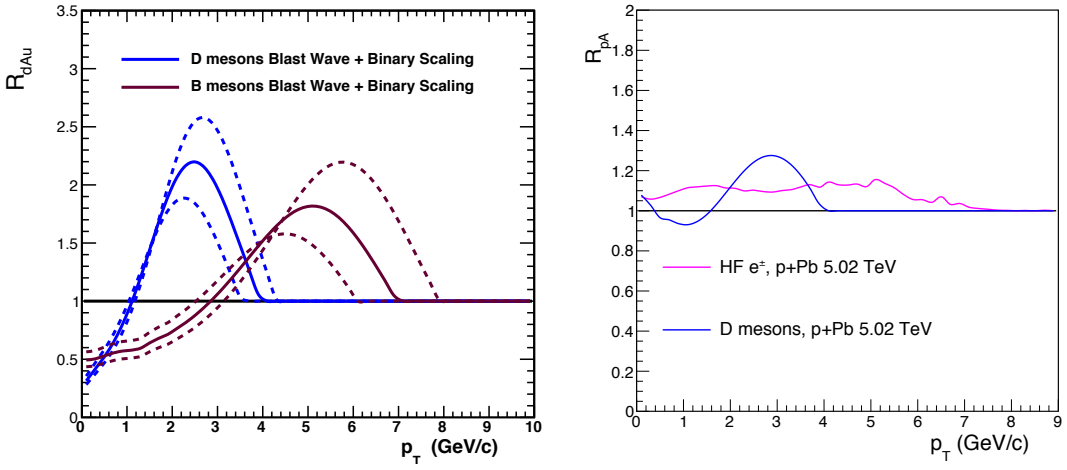

(a) (b)

FIGURE 2.14: (a) R_{dA} obtained from the comparison of the blast-wave and FONLL [34–36] D and B meson p_{T} distributions with binary scaling. The dashed lines show the changes in the blast-waves expectations from the uncertainties on the blast-wave parameters. (b) R_{pA} predicted for p–Pb collisions at $\sqrt{s_{\mathrm{NN}}} = 5.02$ TeV. Blast-wave fit results from the 5% highest multiplicity p–Pb collisions [95] and FONLL [34–36] heavy-meson spectra have been used to generate these results [93].

to the J/ψ in both d–Au [91] and p–Pb [92] collisions, suggest the presence of final state effects in small collision systems. These observations can be described in terms of an hydrodynamically expanding medium. Some of them can also be described with a Color Glass Condensate model. A possible hydrodynamic behaviour of heavy quarks in d–Au and p–Pb collisions has been investigated using a blast-wave model [93]. This model assumes thermalization and expansion with a common velocity field to describe the p_{T} distributions of particles. The parameters of the blast-wave (flow velocity β, and freeze-out temperature) were extracted from the fits to the identified particle p_{T} distributions measured in d–Au [94] and p–Pb collisions [95], then the heavy-flavour meson spectra were determined using the extracted parameters and the D and B meson masses. In order to quantify the nuclear modification factor for heavy mesons expected from the blast wave, the nuclear modification factor with respect to the FONLL [34–36] p_{T} distribution was calculated.

Figure 2.14 shows the nuclear modification factors R_{dA} and R_{pPb} that result from the model. A large enhancement of D mesons, approximately of a factor two, is observed at $p_{\mathrm{T}} \approx 2$ GeV/c in d–Au collisions. A smaller enhancement (of a factor of about 1.8) is observed for B mesons at $p_{\mathrm{T}} \approx 5$ GeV/c (Figure 2.14(a)). The prediction for p–Pb collisions at $\sqrt{s_{\mathrm{NN}}} = 5.02$ TeV is obtained using the blast-wave parameters extracted from the 5% highest multiplicity events [95]. The D meson enhancement reaches a maximum of approximately 20% at $p_{\mathrm{T}} \sim 3$ GeV/c and the electrons from heavy-flavour decays are enhanced by 10–15%, nearly independently of p_{T} over the range 1–6 GeV/c

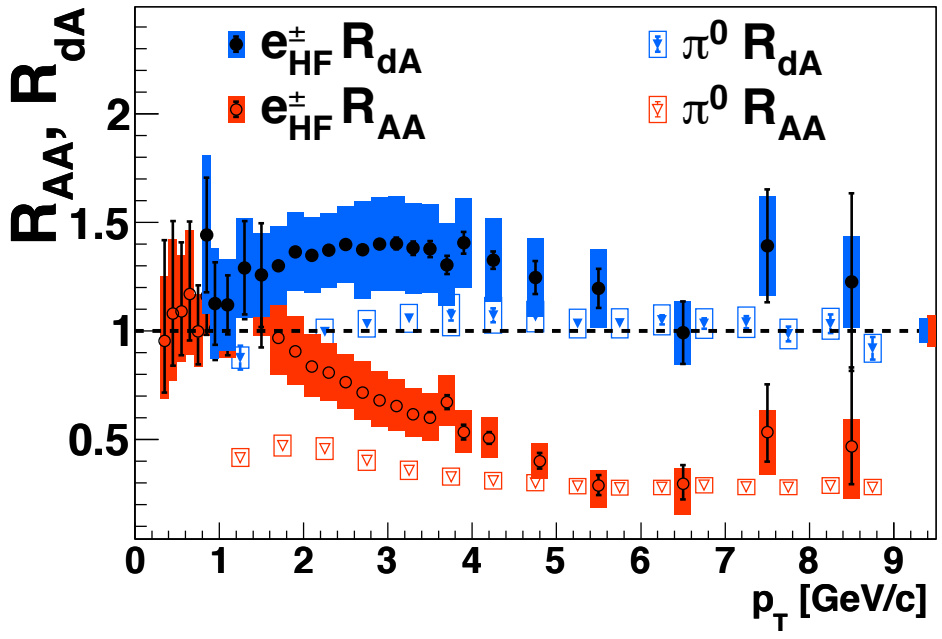

FIGURE 2.15: The nuclear modification factors for minimum-bias d–Au and Au–Au collisions for π^0 and heavy-flavour electrons [96].

(Figure 2.14(b)). Because of the harder D and B meson p_{T} distributions at the higher collision energy, this calculation results in a smaller enhancement of heavy-flavour mesons at LHC energy than at RHIC energy, despite the larger maximal velocity extracted from the blast-wave fit.

Measurement of Heavy-Flavour Production in d–Au Collisions at RHIC

Initial state effects, due to cold nuclear matter, in heavy-flavour production were investigated at RHIC by measuring the production of electrons from heavy-flavour hadron decays in d–Au collisions at $\sqrt{s_{\mathrm{NN}}} = 200$ GeV. PHENIX measured an enhancement of about 40% of the heavy-flavour decay electrons in the 20% most central d–Au collisions with respect to pp collisions out to $p_{\mathrm{T}} \approx 5$ GeV/c [96]. This enhancement suggests a p_{T} broadening of the D spectral shape, which depends on the mass of the particle (pions which are much lighter than heavy-flavour mesons are less enhanced).

The nuclear matter effects are expected to be present also in the initial state of AA collisions, however, combined with final state effects induced by the hot medium. The comparison of the nuclear modification factor measured at RHIC in d–Au and Au–Au collisions for electrons coming from heavy-flavour decays suggests that the suppression observed in AA collisions is mainly due to hot medium effects, as can be argued from

Figure 2.15 [96]. At the LHC, initial state effects in charm production were investigated in p–Pb collisions at $\sqrt{s_{\rm NN}} = 5.02$ TeV, and the measurement is presented in Chapter 8 as one of the main results of this thesis.

2.5 Objective of the Thesis

Heavy quarks are valuable probes of the medium produced in ultra-relativistic collisions of heavy nuclei. The fact that their masses are well above the typical temperature of the system has at least three important implications, which allow to investigate different aspects of their interaction with the medium:

1. The heavy-quark production process is restricted to primordial nucleon–nucleon collisions and can be described with a perturbative QCD approach. Re-interactions in the subsequently evolving medium are not expected to change the multiplicity of heavy quarks.

2. The thermal relaxation time of heavy quarks is predicted to be larger than the QGP lifetime, thus, they are not expected to reach thermal equilibrium, but their interactions should modify the initial momentum spectrum. The final heavy-quark spectra may therefore encode a memory of the interaction history throughout the evolving fireball.

3. The energy loss of heavy quarks in the QGP is expected to be different with respect to the one of light quarks and gluons. In particular, gluon bremsstrahlung is predicted to be suppressed at small angles reducing the energy lost by a charm (beauty) quark with respect to a light quark. Collisional (elastic) processes can be related to the transport coefficients of the medium through a Brownian motion treatment.

The results obtained on heavy-flavour production in pp, pA and AA collisions at RHIC and LHC colliders, using D mesons and leptons from heavy-flavour semileptonic decays have shown that:

- The production cross section in pp collisions is described by models implementing the factorization approach with perturbative hard parton–parton interaction description.

- The QGP formation induces a modification of the transverse momentum spectrum of final state particles, in particular heavy-flavour mesons yields are suppressed at high $p_{\rm T}$ in Pb–Pb collisions with respect to pp collisions, consistently with a mass dependent energy loss in the medium.

- Electrons from heavy-flavour meson decays show a non-zero elliptic flow in Au–Au collisions which gives an indication that not only light partons but also heavy quarks retain memory of the collective expansion of the medium. In d–Au collisions heavy-flavour electrons yields are enhanced with respect to pp collisions.

In this thesis the measurement of the azimuthal anisotropy of the D meson production in Pb–Pb collisions is presented. This provides further information to the open question of whether low-momentum heavy quarks participate in the collective expansion of the system and whether they can reach thermal equilibrium with the medium constituents (Chapter 7).

Furthermore, the D meson production in p–Pb collisions is measured and compared with pp collisions in order to investigate initial state effects due to cold nuclear matter, which are also present in Pb–Pb collisions. This measurement will allow to assess whether the suppression observed in Pb–Pb collisions at high p_{T} is entirely due to charm quark energy loss in the hot medium (Chapter 8).

3

The ALICE Experiment at the LHC

A Large Ion Collider Experiment (ALICE) is one of the four large experiments at the Large Hadron Collider (LHC), the accelerator built at CERN where protons and Pb ions are accelerated to the highest energies ever reached. This chapter is devoted to the description of ALICE, which is the experiment dedicated to the study of the Quark-Gluon Plasma. In Section 3.1 the LHC main features are introduced, together with some parameters of the proton and heavy-ion beams that are relevant for the study presented in this thesis. An overview of the ALICE setup is given in Section 3.2, focusing on the detectors that are used for the reconstruction of D meson decays. Section 3.3 and Section 3.4 are devoted to the description of the ALICE tracking strategy and of the particle identification signals and techniques which allow to deal with the extremely-high multiplicity environment of Pb–Pb collisions. In Section 3.5 one of the most important variables for the reconstruction of heavy-flavour particles, the track impact parameter, is described.

3.1 The LHC Accelerator

The LHC is a superconducting accelerator and collider for hadrons with a circumference of approximately 27 km. It is made of two rings with counter-rotating beams. It was built to produce the highest energy proton–proton collisions ever performed, with the aim of the discovery of the Higgs boson, which was actually announced the 4^{th} of July 2012 by the two experiments ATLAS [97] and CMS [98], and of the search of rare events beyond the Standard Model. In addition to the proton beams, the LHC accelerates also heavy-ion beams in order to study QCD matter created in ultra-relativistic heavy-ion collisions. The LHC design energies are $\sqrt{s} = 14$ TeV for pp collisions and $\sqrt{s_{\rm NN}} = 5.5$ TeV for Pb–Pb collisions [99].

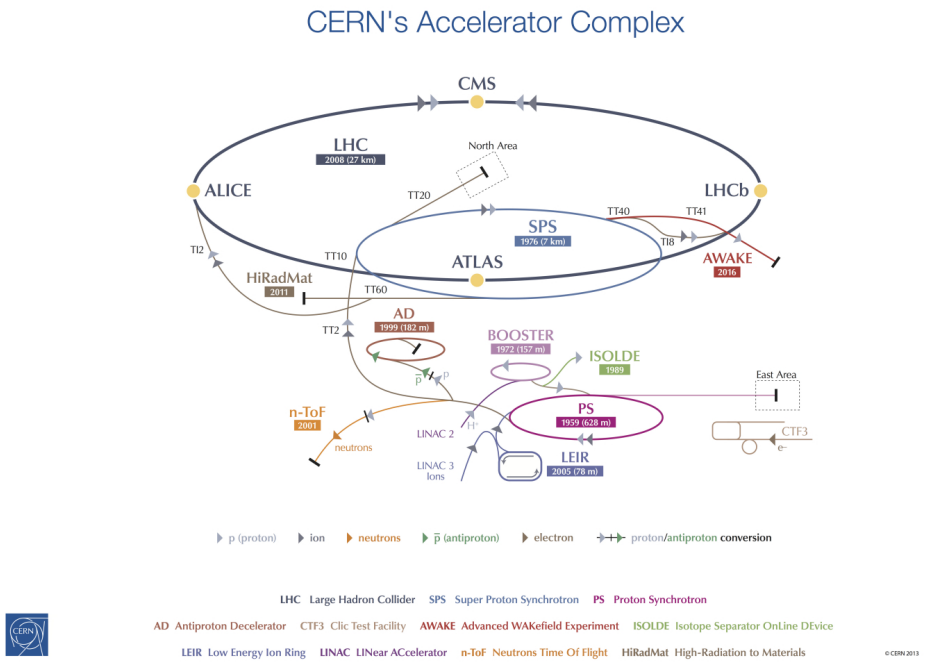

FIGURE 3.1: The CERN's accelerator complex.

3.1.1 Acceleration Chain

The LHC is supplied with protons and Pb ions from a complex system of accelerators, which is represented in Figure 3.1. Each machine boosts the energy of a beam of particles, before injecting the beam into the next machine in the sequence. The proton source is a tank of hydrogen gas. The hydrogen is passed through an electric field to strip off its electrons, leaving only protons to enter the accelerator. Linear Accelerator 2 (Linac 2), the first accelerator in the chain, accelerates protons to the energy of 50 MeV. The beam is then injected into the Proton Synchrotron Booster (PSB), which accelerates protons to 1.4 GeV, followed by the Proton Synchrotron (PS), which pushes the beam to 25 GeV. Protons are then sent to the Super Proton Synchrotron (SPS) where they are accelerated to 450 GeV. The proton are finally transferred to the two beam pipes of the LHC where the beams have been accelerated up to 4 TeV up to now (2012) [99].

Lead ions for the LHC start from a source of vaporized lead and enter Linear Accelerator 3 (Linac 3) before being collected and accelerated in the Low Energy Ion Ring (LEIR). They then follow the same route to maximum energy (of 1.38 TeV per nucleon up to now) as the protons [99].

The two beams are brought into collision inside the four experiments which are installed on the LHC ring. ATLAS and CMS are the two experiments designed to investigate a wide range of physics, including the search for the Higgs boson, extra dimensions, and particles that could make up dark matter. The LHCb experiment is

specialized in investigating CP-violation mainly through B physics channels. ALICE is the dedicated heavy-ion experiment and it is designed to study strongly-interacting matter at extreme energy density, namely the QGP formation and properties.

3.1.2 pp, p–Pb and Pb–Pb Collisions

Since the main objective of the LHC physics programme is the exploration of rare events, the main requirement of the machine is to deliver a large number of collisions. The number of events per second (rate R) generated in the LHC collisions is given by:

$$R = \mathcal{L}\sigma_{\text{event}} \,, \tag{3.1}$$

where σ_{event} is the cross section for the event under study and $\mathcal{L}$ the machine luminosity. The machine luminosity depends only on the beam parameters and can be written for a Gaussian beam distribution as:

$$\mathcal{L} = \frac{N_{\text{b}}^2 n_{\text{b}} f_{\text{rev}} \gamma_r}{4\pi\epsilon_n \beta^*} F \,, \tag{3.2}$$

where N_{b} is the number of particles per bunch, n_{b} the number of bunches per beam, f_{rev} the revolution frequency, γ_r the relativistic gamma factor, ϵ_n the normalized transverse emittance[1], β^* the beta function[2] at the collision point and F the geometric luminosity reduction factor due to the crossing angle at the interaction point:

$$F = \left(1 + \left(\frac{\theta_c \sigma_z}{2\sigma^*}\right)\right)^{-1/2} \,, \tag{3.3}$$

where θ_c is the full crossing angle at the interaction point, σ_z the RMS bunch length, and σ^* the transverse RMS beam size at the interaction point. The investigation of rare phenomena in the LHC collisions therefore requires both high beam energies and high beam intensities. The LHC design foresees 2802 bunches per beam in the ring with 25 ns spacing between them. The nominal intensity is of around 10^{11} protons per bunch.

ATLAS and CMS are the two high luminosity experiments, aiming in proton–proton collisions at a peak luminosity of 10^{34} cm^{-2}s^{-1}. LHCb aims at a peak luminosity 10^{32} cm^{-2}s^{-1}, and ALICE at a peak luminosity of 10^{27} cm^{-2}s^{-1} for nominal lead-lead operation [99].

[1] The emittance measures the average spread of particle coordinates in position and momentum phase space. A low emittance particle beam is a beam where the particles are confined to a small distance and have nearly the same momentum. The emittance is inversely proportional to the beam momentum: increasing the momentum of the beam reduces the emittance and hence the physical size of the beam. It is often more useful to consider the normalized emittance $\epsilon_n = \beta\gamma\epsilon$, which does not change as a function of energy.

[2] The amplitude function $\beta(z)$ describes the single-particle motion and determines the variation of the beam envelope as a function of the coordinate along the the beam orbit, z. β^* denotes the value of the beta function at the interaction point.

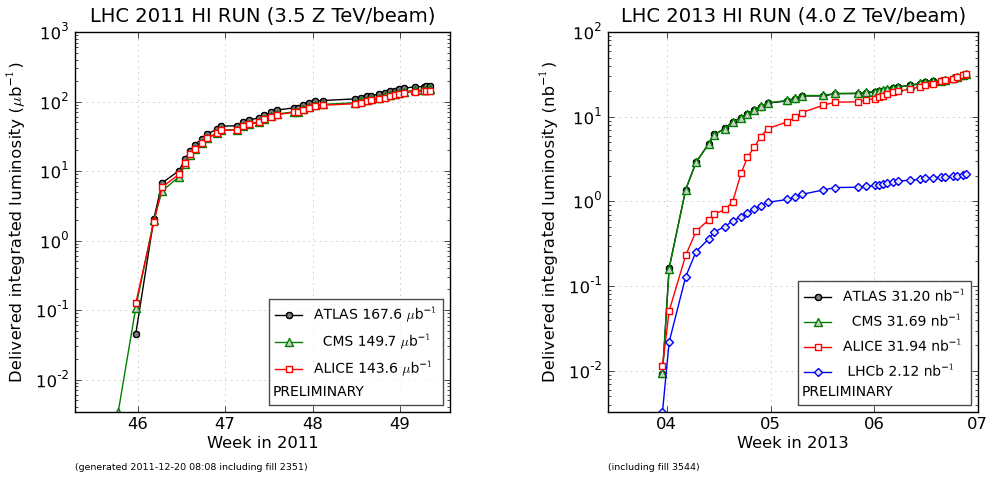

(a) (b)

FIGURE 3.2: LHC delivered integrated luminosity to the experiments during 2011 Pb–Pb run (a) and during 2013 p–Pb run [100].

The luminosity in the LHC is not constant over a physics run but decays due to the degradation of intensities and emittances of the circulating beams. The main cause for the luminosity decay for nominal LHC performance are the collisions themselves.

The integral of the luminosity over time is called integrated luminosity and represents a measurement of the collected data size.

The LHC started its operation, the LHC Run 1, at the beginning of 2010 colliding proton beams at the energy of $\sqrt{s} = 7$ TeV. Pb–Pb collisions were also delivered at the energy of $\sqrt{s_{\mathrm{NN}}} = 2.76$ TeV per nucleon pair. The centre-of-mass energy for a nucleon–nucleon collision, when two beams of nuclei (Z_1, A_1) and (Z_2, A_2) are accelerated with the same magnetic rigidity, is obtained from the formula

$$\sqrt{s_{\mathrm{NN}}} = \sqrt{\frac{Z_1 Z_2}{A_1 A_2}}\sqrt{s}\,. \tag{3.4}$$

In 2011 the proton and lead beam energy remained at 3.5 TeV and 1.38 TeV, respectively. The Pb–Pb run was characterized by a factor 10 higher peak luminosity with respect to the 2010 value, which translates to an integrated luminosity of about 150 $\mu\mathrm{b}^{-1}$ for ALICE, ATLAS, and CMS (Figure 3.2(a)) [100]. An increase in proton beam energy to 4 TeV marked the start of operations in 2012. LHC Run 1 was completed with a successful proton-lead run at the beginning of 2013 with beams of energy of 4 TeV and 1.58 TeV, respectively. ATLAS, CMS, and ALICE were able to collect 31 nb^{-1} of integrated luminosity, as reported in Figure 3.2(b) [100].

The results presented in this thesis were obtained with data samples collected during the 2011 Pb–Pb run and 2013 p–Pb run. While pp and Pb–Pb are symmetric collisions for which the centre-of-mass frame coincides with the laboratory frame, p–Pb collisions

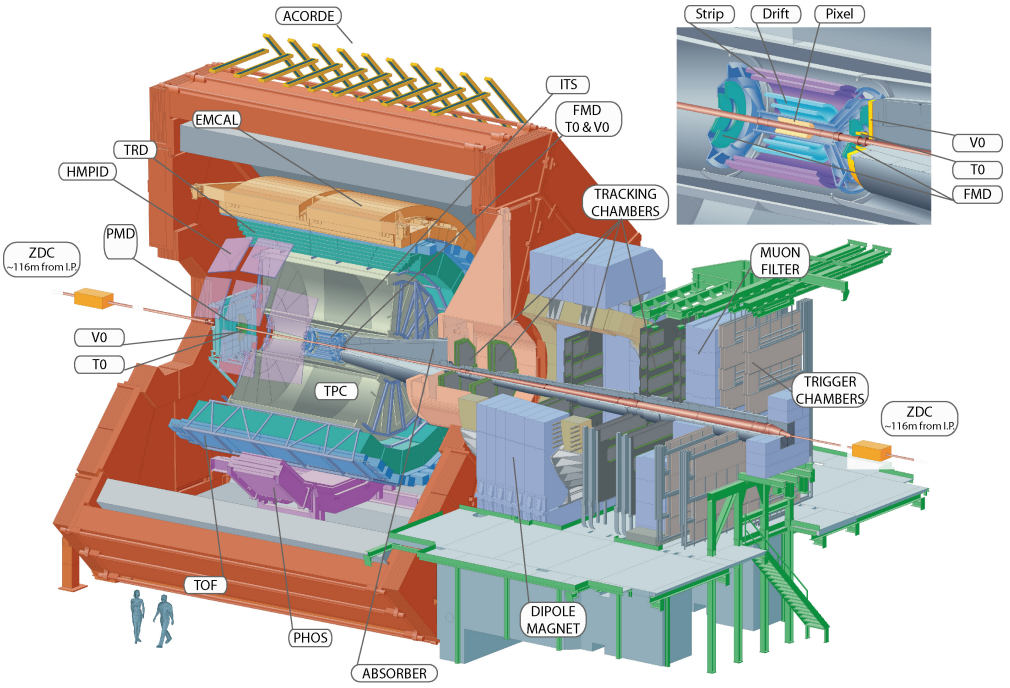

FIGURE 3.3: The ALICE experiment at the CERN LHC. The central-barrel detectors are embedded in a solenoid with magnetic field $B = 0.5$ T and address particle production at midrapidity. The cosmic-ray trigger detector ACORDE is positioned on top of the magnet. Forward detectors are used for triggering, event characterization, and multiplicity studies. The Muon Spectrometer covers $-4.0 < \eta < -2.5$.

are asymmetric due to the different energies per nucleon of the proton and the lead beams. The nucleon–nucleon centre-of-mass system moves with a longitudinal rapidity $y_{\mathrm{CM}} = 0.465$ in the proton beam direction. The rapidity shift is obtained from the expression:

$$y_{\mathrm{CM}} = \frac{1}{2} \ln \left(\frac{Z_1 A_2}{Z_2 A_1} \right) , \tag{3.5}$$

where $(Z_1, A_1) = (1, 1)$ and $(Z_2, A_2) = (82, 208)$ are the atomic and mass numbers of the proton and lead nucleus, respectively.

3.2 The ALICE Apparatus

The ALICE design has been chosen to perform precise measurements of the properties of strongly-interacting matter that is formed in nucleus–nucleus collisions at extreme values of temperature and energy density.

3.2.1 General Detector Layout

The ALICE apparatus, sketched in Figure 3.3, has overall dimensions of $16 \times 16 \times 26$ m^3 and a total weight of about 10000 t. It was designed to cope with the particle densities

expected in central Pb–Pb at the LHC and, thus, has a high detector granularity, a low momentum threshold $p_{\mathrm{T}}^{\mathrm{min}} \approx 0.1$ GeV/c, and good particle identification capabilities up to 20 GeV/c. The experiment is composed of seventeen detector systems, which can be classified in three categories: central-barrel detectors, forward detectors, and the muon spectrometer. Table 3.1 summarizes the acceptance and location of the various detector systems [101].

The ALICE coordinate system is a right-handed orthogonal Cartesian system: the origin is at the LHC Interaction Point 2, the z axis is parallel to the mean beam direction at the Interaction Point 2 and points along the LHC Beam 2 (i.e. LHC anticlockwise), the x axis is horizontal and points approximately towards the center of the LHC, the y axis, consequently, is approximately vertical and points upwards.

The Central-Barrel Detectors

The central-barrel detectors are the Inner Tracking System (ITS), the Time Projection Chamber (TPC), the Transition Radiation Detector (TRD), the Time Of Flight (TOF), the Photon Spectrometer (PHOS), the Electromagnetic Calorimeter (EMCal), and the High Momentum Particle Identification Detector (HMPID). They are embedded in a solenoid magnet with $B = 0.5$ T. The first four detectors cover the full azimuth at midrapidity ($|\eta| \lesssim 0.9$). The ITS and the TPC are the main detectors of ALICE for the tracking of charged particles. The ITS is composed of six tracking layers, two Silicon Pixel Detectors (SPD), two Silicon Drift Detectors (SDD), and two Silicon Strip Detectors (SSD). The TPC has a 90 m^3 drift volume filled with Ne–Co_2 and is divided into two parts by the central cathode, which is kept at -100 kV. The end plates are equipped with multiwire proportional chambers (MWPC). In addition to tracking, SDD, SSD and TPC provide charged-particle identification via measurement of the specific ionization energy loss dE/dx. The TRD detector consists of six layers of MWPCs filled with Xe–CO_2, with a fiber/foam radiator in front of each chamber. It is used for charged-particle tracking and for electron identification via transition radiation and dE/dx. The TOF detector is used for charged particle identification at intermediate momenta. It is based on Multigap Resistive Plate Chamber (MRPC) technology. Finally, the cylindrical volume outside TOF is shared by two electromagnetic calorimeters with thickness of $\sim 20\ X_0$ (radiation lengths) and $\sim 1\ \lambda_{int}$ (nuclear interaction length), the high resolution PHOS and the large-acceptance EMCal, along with the ring-imaging Cherenkov detector HMPID, which has a liquid C_6F_14 radiator and a CsI photo-cathode for charged-hadron identification at intermediate momenta.

TABLE 3.1: Summary of the ALICE detector subsystems. The acceptance in η is calculated from the nominal interaction point and is 360° in azimuth, unless noted otherwise. The position is the approximate distance from the interaction point to the face of the detector and corresponds to the radius for barrel detectors (inner and outer radius for the TPC and TRD) or the position along the beam (z coordinate) for the others. The dimension corresponds to the total area covered by active detector elements. The total number of independent readout channels is also indicated. In case the detector is subdivided, the numbers refer to the individual components [101].

Detector	Acceptance (η, φ)	Position (m)	Dimension (m^2)	Channels
ITS layer 1,2 (SPD)	± 2, ± 1.4	0.039, 0.076	0.21	9.8 M
ITS layer 3,4 (SDD)	± 0.9, ± 0.9	0.150, 0.239	1.31	133000
ITS layer 5,6 (SSD)	± 0.97, ± 0.97	0.380, 0.430	5.0	2.6 M
TPC	± 0.9 at $r = 2.8$	0.848, 2.466	readout 32.5 m^2	557568
	± 1.5 at $r = 1.4$ m		Vol. 90 m^3	
TRD	± 0.84	2.90, 3.68	716	1.2 M
TOF	± 0.9	3.78	141	157248
HMPID	± 0.6, $1.2° < \varphi < 58.8°$	5.0	11	161280
PHOS	± 0.12, $220° < \varphi < 320°$	4.6	8.6	17920
EMCal	± 0.7, $80° < \varphi < 187°$	4.36	44	12672
ACORDE	± 1.3, $-60° < \varphi < 60°$	8.5	42	120
Muon Spectrometer				
Tracking station 1	$-4.0 < \eta < -2.5$	-5.36	4.7	1.08 M
Tracking station 2		-6.86	7.9	
Tracking station 3		-9.83	14.4	
Tracking station 4		-12.92	26.5	
Tracking station 5		-14.22	41.8	
Trigger station 1	$-4.0 < \eta < -2.5$	-16.12	64.6	21000
Trigger station 2		-17.12	73.1	
ZDC:ZN	$\lvert\eta\rvert < 8.8$	± 116	2×0.0049	10
ZDC:ZP	$6.5 < \eta < 7.5$	± 116	2×0.027	10
	$-9.7° < \varphi < 9.7°$			
ZDC:ZEM	$4.8 < \eta < 5.7$	7.25	2×0.0049	2
	$-16° < \varphi < 16°$ and			
	$164° < \varphi < 196°$			
PMD	$2.3 < \eta < 3.7$	3.64	2.59	2221184
FMD disc 1	$3.62 < \eta < 5.03$	inner: 3.2		
FMD disc 2	$1.7 < \eta < 3.68$	inner: 0.834	0.266	51200
		outer: 0.752		
FMD disc 3	$-3.4 < \eta < -1.7$	inner: -0.628		
		outer: -0.752		
VZERO-A	$2.8 < \eta < 5.1$	3.4	0.548	32
VZERO-C	$-3.7 < \eta < -1.7$	-0.897	0.315	32
T0A	$4.61 < \eta < 4.92$	3.75	0.0038	12
T0C	$-3.28 < \eta < -2.97$	-0.727	0.0038	12

The Forward Detectors

The ALICE forward detectors include the preshower/gas-counter Photon Multiplicity Detector (PMD) and the silicon Forward Multiplicity Detector (FMD), which are dedicated to the measurement of photons and charged particles around $\eta \approx 3$, respectively. The quartz Cherenkov detector T0 delivers the time and the longitudinal position of the interaction. It consists of two arrays of Cherenkov counters positioned at opposite sides of the interaction point at $-3.28 < \eta < -2.97$ and $4.61 < \eta < 4.92$. The plastic scintillator detector VZERO measures charged particles at $-3.7 < \eta < -1.7$ and $2.8 < \eta < 5.1$, and it is mainly used for triggering and for the determination of centrality and event-plane angle in Pb–Pb collisions. The centrality can also be measured with the Zero Degree Calorimeter (ZDC). The ZDC consists of two tungsten-quartz neutron (ZN) and two brass-quartz proton (ZP) calorimeters, placed symmetrically on both sides of the interaction point and used to count spectator nucleons.

The Muon Spectrometer

The Muon Spectrometer is used to measure heavy-flavour quarkonium and light vector meson production in a region $-4.0 < \eta < -2.5$. It is also used to measure high-p_{T} muons which predominantly come from the decay of W bosons. The Muon Spectrometer is made of a hadron absorber of about $10\lambda_{int}$, a dipole magnet of 3 Tm, and five tracking stations with two pad chambers each (Muon Chambers, MCH). Single-muon and muon-pair triggers with an adjustable transverse momentum threshold are provided by two further stations (Muon Trigger, MTR) placed behind an additional $7\lambda_{int}$ absorber.

The D mesons are reconstructed in the central rapidity region exploiting the tracking and particle identification capabilities of the ALICE central-barrel detectors. The relevant detectors for the D meson analysis are the ITS, the TPC and the TOF: their main features are described below.

3.2.2 ITS

The main tasks of the ITS are to localize the primary vertex with a resolution better than 100 μm, to reconstruct the secondary vertices from the decays of hyperons and D and B mesons, to track and identify particles with momentum below 200 MeV/c, to improve the momentum and angle resolution for particles reconstructed by the TPC and to reconstruct particles traversing dead regions of the TPC.

The ITS surrounds the beam pipe, which is a 800 μm-thick beryllium cylinder of 6 cm outer diameter, coaxial with the ITS detector layers. The ITS consists of six

cylindrical layers of silicon detectors, located at radii between 3.9 and 43 cm. It covers the rapidity range of $|\eta| < 0.9$ for all vertices located within the length of the interaction diamond ($\pm 1\sigma$, i.e. ± 5.3 cm along the beam direction).

The two innermost layers, with average radii of 3.9 cm (about 1 cm from the beam vacuum tube) and 7.6 cm, are equipped with Silicon Pixel Detectors, comprising 9.8×10^6 pixels of size $50(r\varphi) \times 425(z)$ μm^2, with intrinsic spatial resolution of $12(r\varphi) \times 100(z)$ μm^2. The signals of the 1200 SPD readout chips provide a fast trigger through a programmable logic. The two intermediate layers, at radii of 15.0 and 23.9 cm, are made of Silicon Drift Detectors. The intrinsic spatial resolution of the third and fourth layers is of 35 μm in $r\varphi$ direction and 25 μm in z direction. The two outermost layers are made of Silicon Strip Detectors, located at radii of 38.0 and 43.0 cm, consisting of double-sided silicon strip sensor modules, with an intrinsic spatial resolution of $20(r\varphi) \times 830(z)$ μm^2. The alignment of the ITS sensor modules is crucial for the precise space point reconstruction needed for heavy-flavour analysis. It was performed using survey information, cosmic-ray tracks and pp data. The effective spatial resolution along the most precise direction, $r\varphi$, is about 14, 40 and 25 μm for SPD, SDD and SSD, respectively [101].

The momentum and impact parameter (i.e. the distance of closest approach of the track to the primary interaction vertex) resolution for low-momentum particles are dominated by multiple scattering effects in the material of the detector; therefore the amount of material in the active volume has been kept to a minimum. The total material budget of the ITS is on average 7.7% of radiation length for tracks crossing the ITS perpendicularly to the detector surfaces ($\eta = 0$).

3.2.3 TPC

The TPC is the main tracking detector of the central barrel and is optimized to provide, together with the other central-barrel detectors, charged-particle momentum measurements with good two-track separation, particle identification, and vertex determination. The phase space covered by the TPC in pseudorapidity is $|\eta| < 0.9$ for tracks with full radial track length; for reduced track length (at reduced momentum resolution) an acceptance up to about $|\eta| < 1.5$ is accessible. The TPC covers the full azimuth (with the exception of the dead zones). A large p_{T} range is covered from low p_{T} of about 0.1 GeV/c up to 100 GeV/c with good momentum resolution.

The TPC has a cylindrical shape; the active volume has an inner radius of about 85 cm, an outer radius of about 250 cm, and an overall length along the beam direction of 500 cm.

The detector is made of a cylindrical field cage, filled with 90 m^3 of $Ne/CO_2/N_2$ (90/10/5), in which the primary electrons are transported over a distance of up to 2.5 m on either side of the central electrode to the end plates. Multi-wire proportional

chambers with cathode pad readout are mounted into 18 trapezoidal sectors at each end plate.

Charged-particle tracks are reconstructed and identified with up to 159 3-dimensional space points. The TPC also provides particle identification capabilities through the measurement of the specific energy deposition $\mathrm{d}E/\mathrm{d}x$, with up to 159 samples. Using cosmic-ray muons and data taken in pp collisions, the relative $\mathrm{d}E/\mathrm{d}x$ resolution was measured to be about 5.5% for tracks that cross the entire detector [101].

3.2.4 TOF

The TOF detector is a large area array that covers the central pseudorapidity region ($|\eta| < 0.9$) for Particle IDentification (PID) in the intermediate momentum range, below about 2.5 GeV/c for pions and kaons, up to 4 GeV/c for protons, with a π/K and K/p separation better than 3σ.

TOF is based on the Multi-gap Resistive-Plate Chambers in a cylindrical configuration at radius 370–399 cm from the beam axis, with readout consisting of 152928 sensitive pads of dimension 2.5×3.5 cm^2.

The TOF provides an arrival time measurement for charged tracks with an overall resolution, including the measurement of the event start time, of about 80 ps for pions and kaons at $p_{\mathrm{T}} = 1$ GeV/c [101]. The particle identification is based on the difference between the measured time-of-flight and its expected value, computed for each mass hypothesis from the track momentum and length.

3.3 Central-Barrel Tracking

The procedure of track finding in the central barrel starts with the clusterization step, in which the detector data are converted into "clusters" characterized by positions, signal amplitudes, signal times, etc., and their associated errors. The clusterization is performed separately for each detector. The next step is a first reconstruction of the interaction vertex using clusters in the first two ITS layers (SPD). Subsequently, track finding and fitting is performed in TPC and ITS using the Kalman filter technique [102]. The found tracks are matched to the outer central-barrel detectors and fitted. The final interaction vertex is determined using the reconstructed tracks.

3.3.1 Interaction Vertex Reconstruction with SPD

Tracking in the central barrel starts with the determination of the interaction vertex using the two innermost layers (SPD) of the ITS. It is found as a space point to which

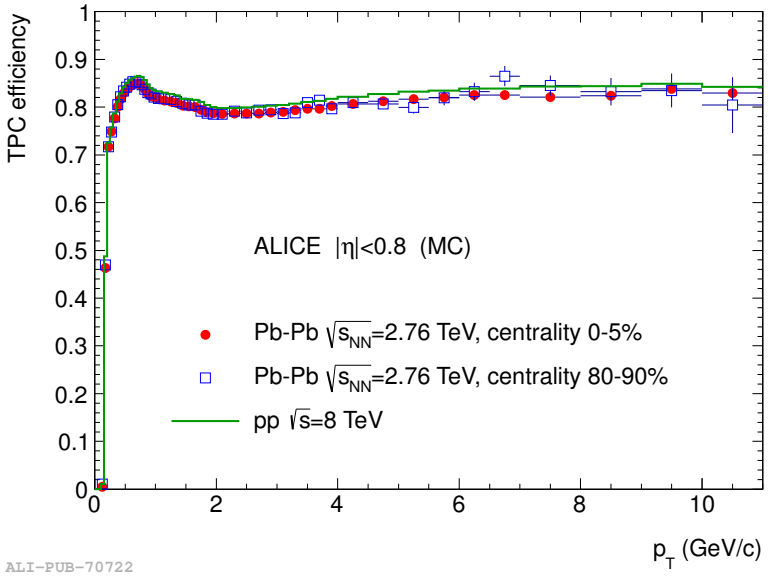

FIGURE 3.4: TPC track finding efficiency for primary particles in pp and Pb–Pb collisions (simulation). The efficiency does not depend on the detector occupancy [103].

a maximum number of tracklets[3] converge. In pp collisions, where interaction pileup is expected, the algorithm is repeated several times, discarding at each iteration those clusters which contributed to already-found vertices. By construction, the first vertex found has the largest number of contributing tracklets and is assumed to be the primary one. When a single convergence point is not found (in particular in low-multiplicity events) the algorithm performs a one-dimensional search of the maximum in the z-distribution of the points of closest approach of tracklets to the nominal axis.

3.3.2 Track Reconstruction

Track finding and fitting is performed in three stages, following an inward-outward-inward scheme. The first inward stage starts with finding tracks in the TPC. The TPC readout chambers have 159 tangential pad rows and thus a track can, ideally, produce 159 clusters within the TPC volume. The track search in the TPC starts at a large radius. Track seeds are built first with two TPC clusters and the vertex point, then with three clusters and without the vertex constraint. The seeds are propagated inward and, at each step, updated with the nearest cluster provided that fulfils a proximity cut. Only those tracks that have at least 20 clusters (out of maximum 159 possible) and that miss no more than 50% of the clusters expected for a given track position are accepted. These are propagated inwards to the inner TPC radius. The tracking efficiency, defined as the ratio between the reconstructed tracks and generated primary particles in the simulation, is shown in Figure 3.4 as a function of transverse momentum. The drop

[3]Tracklets are defined as the lines which connect a pair of clusters, one cluster in each SPD layer.

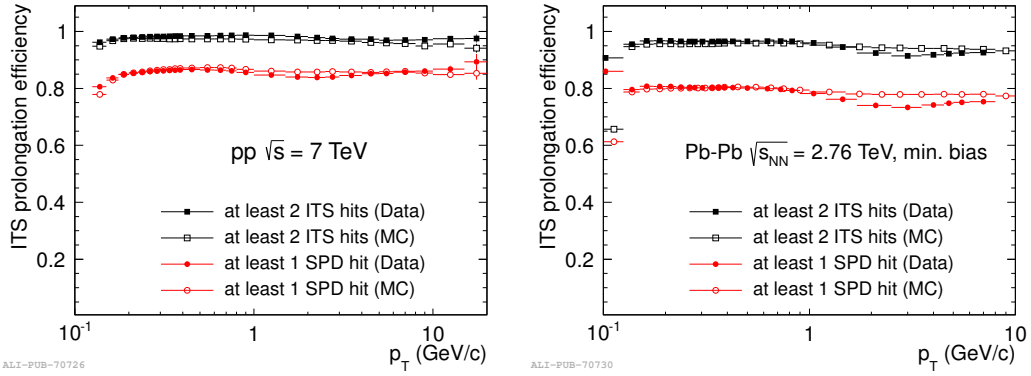

(a) (b)

FIGURE 3.5: ITS-TPC matching efficiency vs. p_T for data and Monte Carlo for pp (a) and Pb–Pb (b) collisions [103].

below a transverse momentum of about 0.5 GeV/c is caused by the energy loss and multiple scattering in the detector material and the shape at larger p_T is determined by the loss of clusters in the p_T-dependent fraction of the track trajectory projected on the dead zone between readout sectors. The efficiency is almost independent of the occupancy in the detector: even in the most central Pb–Pb collisions the contamination by tracks with more than 10% wrongly associated clusters does not exceed 3% [103].

The reconstructed TPC tracks are propagated to the outermost ITS layer and become the seeds for track finding in the ITS. The seeds are propagated inward and are updated at each ITS layer by all clusters within a proximity cut, which takes into account positions and errors. In order to account for detector inefficiency, seeds without an update at a given layer are also used for further track finding. The χ^2 of such seeds takes into account the missing cluster unless the seed extrapolation happened to be in the dead zone of the layer, in which case no cluster should be expected. Each TPC track produces a set of track hypothesis in the ITS. This seeding procedure is performed in two steps, with and without vertex constraint, as in the case in TPC. Once the complete tree of prolongation candidates for the TPC track is built, the candidate are sorted according to the reduced χ^2. The candidates with the highest quality from each tree are checked for cluster sharing among each other. If shared clusters are found, an attempt is made to find alternative candidates in the involved trees. In the case of a failure to completely resolve the conflict between two tracks, the worse of the two acquires a special flag for containing potentially incorrectly matched (fake) clusters. Finally, the highest quality candidate from each hypothesis tree is added to the reconstructed event. Figure 3.5 shows the TPC track prolongation efficiency to ITS in pp and Pb–Pb collisions as a function of track transverse momentum, with different requirements of ITS layer contributions. The fraction of tracks with at least one fake cluster in the ITS in the most central Pb–Pb collisions reaches about 30% at $p_T < 0.2$ GeV/c, decreases to

about 7% at 1 GeV/c, and drops below 2% at 10 GeV/c [103].

A standalone ITS reconstruction is performed with those clusters that were not used in the ITS-TPC tracks. The algorithm adopted enables the tracking of particles with transverse momenta down to about 80 MeV/c.

Once the reconstruction in the ITS is complete, all tracks are extrapolated to their point of closest approach to the preliminary interaction vertex, and the outward propagation starts. The tracks are refitted by the Kalman filter in the outward direction using the clusters found at the previous stage. At each outward step, the track length integral, as well as the time of flight expected for various particle species are updated for subsequent particle identification. Once the track reaches the TRD, an attempt is made to match it with the TRD tracklet (track segment within a TRD layer) in each of the six TRD layers. Similarly, the tracks reaching the TOF detector are matched to TOF clusters. The track length integration and time-of-flight calculation are stopped at this stage. The tracks are then propagated further for matching with signals in EMCal, PHOS, and HMPID. The detectors at a radius larger than that of TPC are currently not used to update the measured track kinematics, but their information is stored in the track object for the purposes of particle identification.

At the final stage of the track reconstruction, all tracks are propagated inwards starting from the outer radius of the TPC. In each detector (TPC and ITS), the tracks are refitted with the previously found clusters. The track's position, direction, inverse curvature, and its associated covariance matrix are determined.

Figure 3.6 shows the transverse momentum resolution for TPC standalone tracks and ITS-TPC combined tracks extracted from the track covariance matrix. The effect of constraining the tracks to the primary vertex is shown as well. The inverse-p_{T} resolution is connected to the relative transverse momentum resolution via

$$\frac{\sigma_{p_{\mathrm{T}}}}{p_{\mathrm{T}}} = p_{\mathrm{T}}\sigma_{1/p_{\mathrm{T}}} \,. \tag{3.6}$$

Figure 3.6 is relative to the data taken in the recent p–Pb run, in central Pb–Pb collisions, the p_{T} resolution is expected to deteriorate by about 10% at high p_{T} due to the loss (or reduction) of clusters sitting on the ion tails, cluster overlap, and fake cluster attached to the tracks [103]. Heavy-flavour analysis make use of the track parameters not constrained to the primary vertex.

3.3.3 Final Reconstruction of the Interaction Vertex

The interaction vertex is found using global tracks reconstructed in TPC and ITS. This method provides a better precision than the usage of SPD tracklets alone. By extrapolating the tracks to the point of closest approach to the nominal beam line and

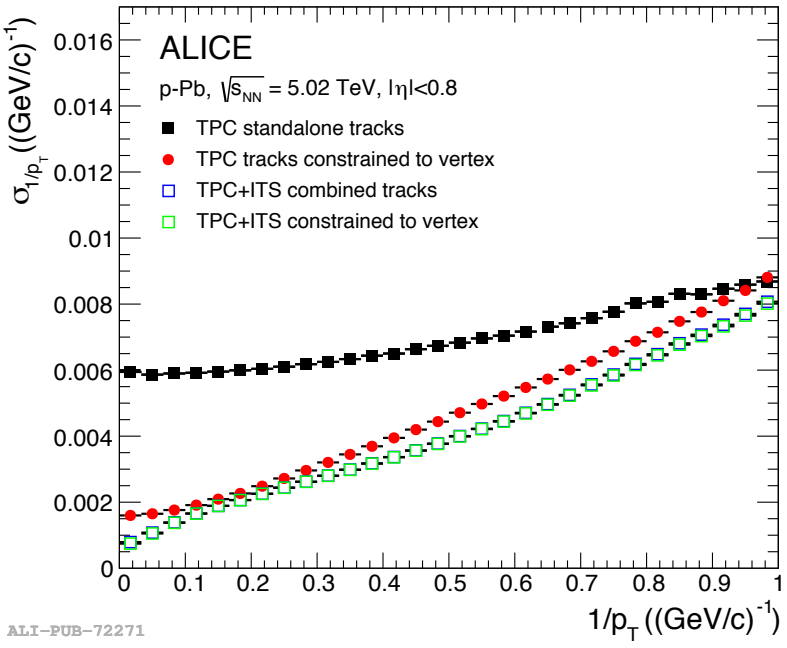

FIGURE 3.6: The p_{T}-resolution for standalone TPC and ITS-TPC matched tracks with and without constraint to the vertex. The vertex constraint significantly improves the resolution of TPC standalone tracks. For ITS-TPC tracks, it has no effect (green and blue squares overlap) [103].

removing far outliers, the approximate point of closest approach of validated tracks is determined. Then the precise vertex fit is performed using track weighting to suppress the contribution of any remaining outliers. In order to improve the transverse vertex position precision in low-multiplicity events, the nominal beam position is added in the fit as an independent measurement with errors corresponding to the transverse size of the luminous region[4]. Figure 3.7 shows the profiles (x Figure 3.7(a) and z Figure 3.7(b)) of the luminous region obtained from reconstructed vertices in pp and Pb–Pb collisions. The transverse resolution of the preliminary interaction vertices found with SPD and of the final ones, found with global tracks, are shown in Figure 3.8. Both resolutions scale with the inverse of the square root of the number of contributing tracks (tracklets), which is proportional to the charged-particle multiplicity, $\mathrm{d}N_{\mathrm{ch}}/\mathrm{d}\eta$.

3.4 Particle Identification

3.4.1 PID in the TPC

Particle identification in the TPC is performed by simultaneously measuring the specific energy loss ($\mathrm{d}E/\mathrm{d}x$), charge, and momentum of each particle traversing the detector gas.

[4]The interaction region, or beam size, is defined as the convolution of the two particles distributions in the two colliding bunches: the interaction vertex lies in a luminous region with dimensions $\sigma_q^{\text{lumi reg}} = \sigma_q^{\text{beam}}/\sqrt{2}$ with $q = x, y, z$.

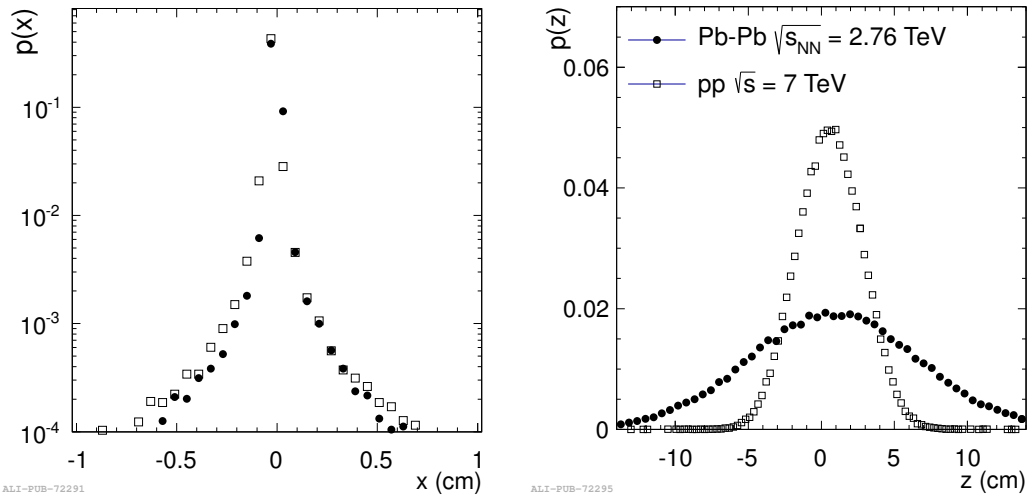

(a) (b)

FIGURE 3.7: The x (a) and z (b) projections of the luminous region obtained from reconstructed vertices in pp and Pb–Pb collisions (folded with vertex resolution) [103].

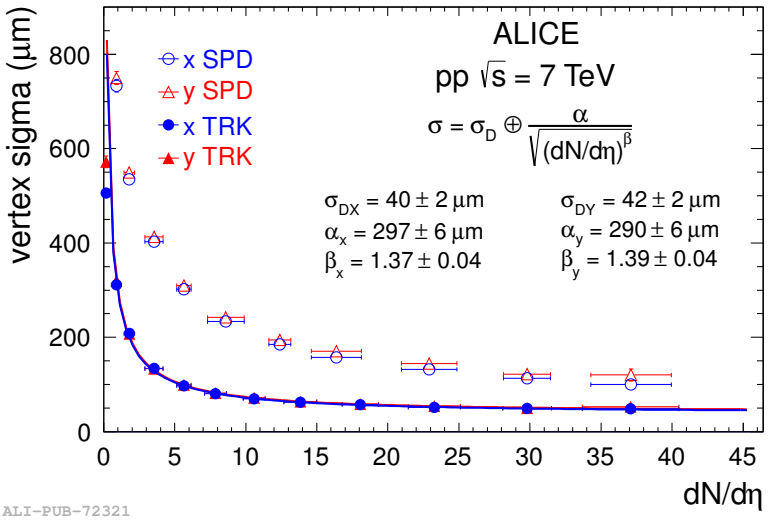

FIGURE 3.8: Transverse width of the final vertex distribution (solid points), decomposed into the finite size of the luminous region σ_D and the vertex resolution $\alpha/\sqrt{(\mathrm{d}N_{\mathrm{ch}}/\mathrm{d}\eta)^{\beta}}$. The widths of preliminary (SPD) interaction vertices are shown as open points [103].

The energy loss, described by the Bethe-Bloch formula, is parametrized by the function

$$f(\beta\gamma) = \frac{P_1}{\beta^{P_4}}\left(P_2 - \beta^{P_4} - \ln\left(P_3 + \frac{1}{(\beta\gamma)^{P_5}}\right)\right), \tag{3.7}$$

where β is the particle velocity, γ is the Lorentz factor, and P_{1-5} are fit parameters. Figure 3.9 shows the measured $\mathrm{d}E/\mathrm{d}x$ as a function of particle momentum in the TPC, demonstrating the clear separation between the different particle species. The lines

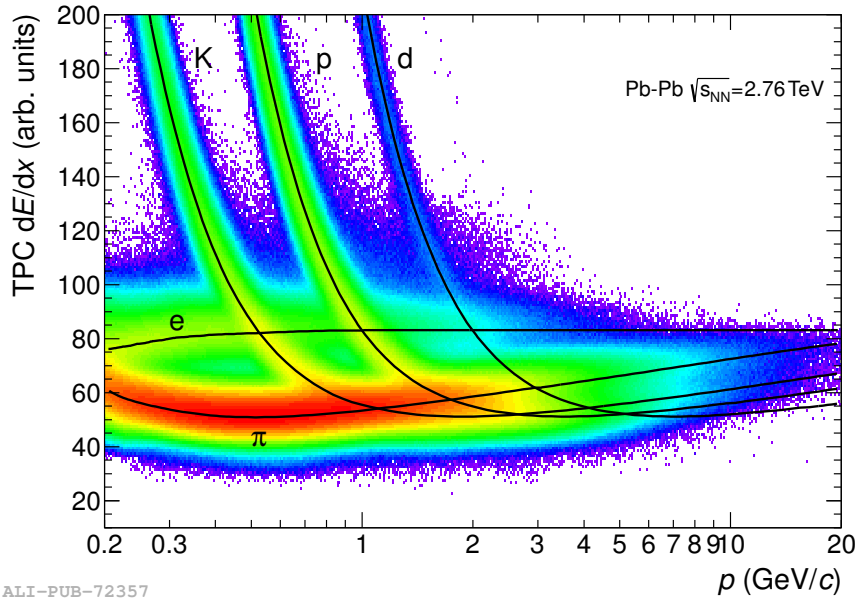

FIGURE 3.9: Specific energy loss ($\mathrm{d}E/\mathrm{d}x$) in the TPC vs. particle momentum in Pb–Pb collisions at $\sqrt{s_{\mathrm{NN}}} = 2.76$ TeV. The lines show the parametrization of the expected mean energy loss [103].

correspond to the parametrization. At low momenta ($p \lesssim 1$ GeV/c) particles can be identified on a track-by-track basis. At higher momenta particles can still be separated on a statistical basis via multi-Gaussian fits.

In the relativistic rise region, the $\mathrm{d}E/\mathrm{d}x$ exhibits a nearly constant separation for the different particle species over a wide momentum range. Due to a $\mathrm{d}E/\mathrm{d}x$ resolution of about 5.2% in pp collisions and 6.5% in the 0–5% most central Pb–Pb collisions, particle ratios can be measured at a p_{T} of up to 20 GeV/c [103].

3.4.2 PID in the TOF

The overall TOF time resolution in Pb–Pb collisions, in the centrality range 0–70%, is 80 ps for pions with a momentum around 1 GeV/c. This value includes the intrinsic detector resolution, the contribution from electronics and calibration, the uncertainty on the start time of the event, and the tracking and momentum resolution. TOF provides PID in the intermediate momentum range, up to 2.5 GeV/c for pions and kaons, and up to 4 GeV/c for protons.

The start time for the TOF measurement is provided by the T0 detector. The time resolution of the detector is 20-25 ps in Pb–Pb collisions and about 40 ps in pp collisions. The start time of the event is also estimated using the particle arrival times at the TOF detector if at least three particles reach it. The method is particularly useful for events

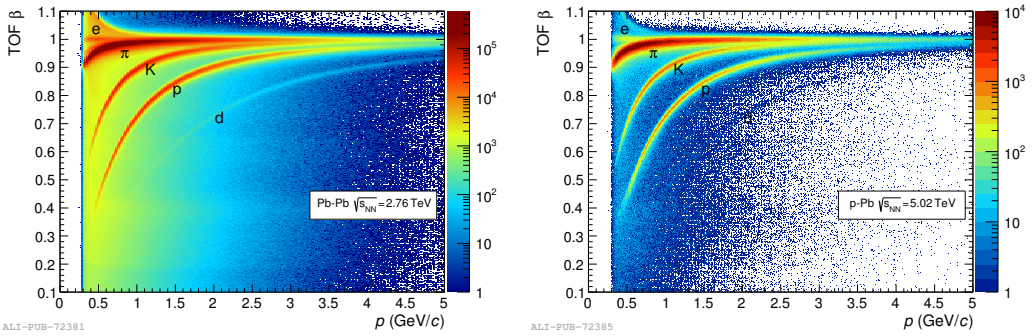

(a) (b)

FIGURE 3.10: Distribution of β as measured by the TOF detector as a function of momentum for particles reaching TOF in Pb–Pb interaction (a) and in p–Pb interactions (b). The background of mismatched tracks is lower in p–Pb than in higher occupancy Pb–Pb collisions [103].

in which the T0 signal is not present. If neither of these two methods is available an average TOF start time for the run is used instead.

Figure 3.10 illustrates the performance of the TOF detector by showing the measured velocity β distribution as a function of the momentum (measured by the TPC). The background is due to tracks that are incorrectly matched to TOF hits in high-multiplicity collisions. The background is larger in Pb–Pb collisions (Figure 3.10(a)) while the distribution is cleaner in p–Pb collisions (Figure 3.10(b)), showing that the background is not related to the resolution of the TOF detector, but is rather an effect of track density and the fraction of mismatched tracks. The fraction of mismatched tracks above 1 GeV/c in Pb–Pb events is closely related to the TOF occupancy. With 10^4 hits at TOF (corresponding to a very central Pb–Pb event) the TOF pad occupancy is 6.7% and the fraction of mismatched hits is about 6.5% [103].

The resolution can be studied in a given narrow momentum interval by computing the difference between the time of flight measured by TOF and the pion time expectation. The distribution is fitted with a Gaussian whose width is the convolution of the intrinsic time resolution of the TOF detector and the resolution of the event time. In the limit of high track multiplicity the width becomes equal to the intrinsic resolution of the TOF detector and has a value of 80 ps (Figure 3.11) [103].

3.5 Impact Parameter Resolution

Weakly-decaying particles, such as those containing strangeness, charm or beauty, are recognized through the secondary vertices in the event. The most effective constraint for the selection of such particles is the presence of one or more tracks displaced from the interaction vertex. The displacement of a track is evaluated through its impact

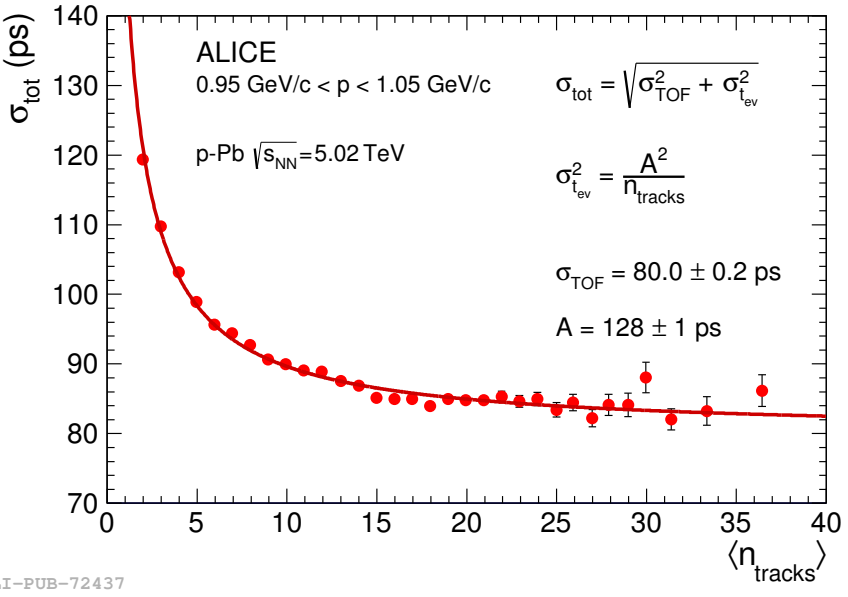

FIGURE 3.11: Time resolution of pion track with $0.95 < p < 1.05$ GeV/c as a function of the number of tracks used to define the start time of the collision t_{ev}. The data are from p–Pb collisions [103].

parameter, which is defined as the distance of closest approach of the reconstructed particle trajectory to the primary vertex. The two projections of the impact parameter in the transverse plane and along the beam direction are, respectively:

$$d_0(r\varphi) = \rho - \sqrt{(x_V - x_0)^2 + (y_V - y_0)^2} \qquad \text{and} \qquad d_0(z) = z_{track} - z_V \,, \tag{3.8}$$

where ρ and (x_0, y_0) are the radius and the centre of the track projection in the transverse plane, (x_V, y_V, z_V) is the position of the primary vertex, and z_{track} is the z position of the track after the propagation to the point of closest approach in the transverse plane.

The impact parameter resolution is estimated in data by fitting the inclusive distribution of d_0 in intervals of p_T (see Figure 3.12). The fit function is the sum of a Gaussian, that accounts for the component due to prompt particles produced at the primary vertex, and two exponential functions, that account for secondary particles, mainly from weak decays of strange hadrons. The width σ of the Gaussian provides an estimate of the d_0 resolution, which for both $r\varphi$ and z projections includes the resolution of the track parameters and of the primary vertex position.

Figure 3.13 shows the transverse momentum dependence of the $r\varphi$ impact parameter resolution for ITS-TPC tracks in three collision systems. An improvement of the resolution is observed going from pp to Pb–Pb collisions thanks to the more precise vertex determination for higher-multiplicity events.

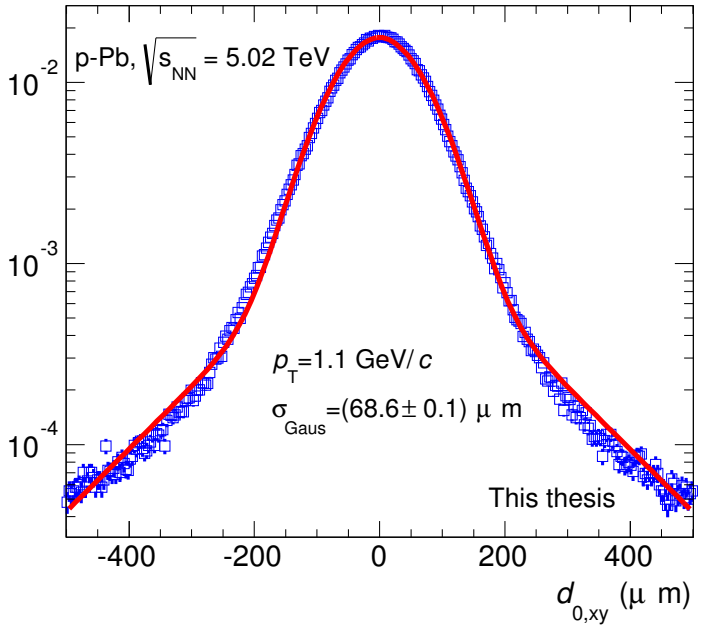

FIGURE 3.12: Fit to the distribution of the $r\varphi$ component of the impact parameter for tracks of $p_{\mathrm{T}} = 1.1$ GeV/c in p–Pb collisions. The fit function (red) is the sum of a Gaussian and two exponential funtions. The width of the Gaussian, which is indicated, represents the estimate of the d_0 resolution at that p_{T}.

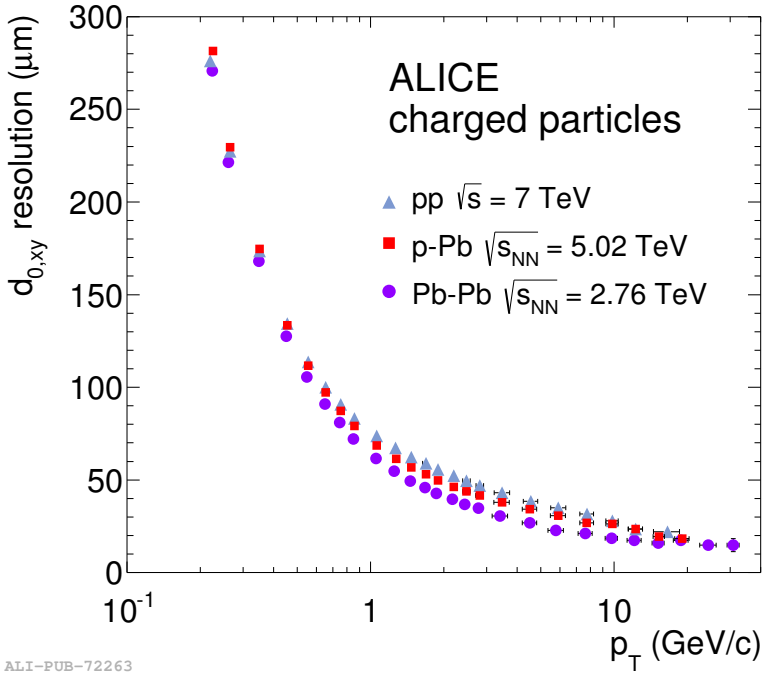

FIGURE 3.13: Resolution of the $r\varphi$ projection of the impact parameter for ITS-TPC tracks. The contribution from the vertex resolution is included [103].

4

Experimental Observables

This chapter introduces the experimental observables that were studied for this thesis. The two quantities that were used to investigate the azimuthal anisotropy of the D^0 production in semi-peripheral Pb–Pb collisions, namely the elliptic flow v_2 and the nuclear modification factor azimuthal dependence, are defined in Section 4.1. Section 4.2 is devoted to the definition of the observables that were measured to study the D^0 production in minimum-bias p–Pb collisions: the p_T- and y-differential cross sections and the nuclear modification factor R_{pPb}. The observables used to investigate the dependence of the D^0 production on event activity are also defined.

The strategy to obtain the D^0 proton–proton cross section at the proper energy, which is used to compute the nuclear modification factor both in Pb–Pb and p–Pb collisions, is described in the last part of the chapter (Section 4.3).

4.1 Azimuthal Anisotropy of D^0 Production in Pb–Pb Collisions

The azimuthal anisotropy of the D^0 production was studied by measuring two observables: the elliptic flow v_2 and the azimuthal dependence of the nuclear modification factor R_{AA}. Both measurements were performed for Pb–Pb collisions in the centrality class 30-50%. The D^0 v_2 was measured also in the 0–10% and 10–30% centrality classes.

4.1.1 Event-Plane Definition

The basic quantity that is needed to study azimuthal anisotropy is the estimate of the reaction-plane angle, which is defined by the vector of the impact parameter and the beam direction. The reaction-plane angle can not be directly measured, but can be estimated from the particle azimuthal distribution event-by-event. Anisotropic flow can

fluctuate event to event, both in magnitude and direction even at fixed impact parameter. One of the important sources of flow fluctuations are fluctuations in the initial geometry of the overlapping region due to random nature of the interaction between constituents of the two nuclei. The principal axis of the participant region can deviate from the reaction plane inducing flow fluctuations [104].

The orientation of the reaction plane or, in case of flow fluctuations, the n^{th}-harmonic collision symmetry plane is estimated with the n^{th}-harmonic event-plane angle, ψ_n. For a given harmonic n, one constructs the two-dimensional event-plane vector $\mathbf{Q}_n$ from the measured azimuthal distribution of particles produced in the event as follows:

$$\mathbf{Q}_n = (Q_{n,x}, Q_{n,y}) = \left(\sum_i w_i \cos n\varphi_i, \sum_i w_i \sin n\varphi_i, \right) . \tag{4.1}$$

The sums run over all reconstructed tracks in the case of the TPC, or segments of detectors with azimuthal segmentation like VZERO, FMD, ZDC, or PMD. The angle φ_i is the azimuthal emission angle of the particle i or the azimuthal coordinate of the detector element i, respectively. For TPC tracks the weight w_i can be unity or a specific function of p_{T}. For segmented detectors, w_i is the signal observed in the detector element i. Using the components of the $\mathbf{Q}$-vector one can calculate the ψ_n. The azimuthal angle of the $\mathbf{Q}_2$-vector

$$\psi_2 = \frac{1}{2} \arctan 2(Q_{2,y}, Q_{2,x}) \tag{4.2}$$

is an estimate of the second harmonic symmetry plane Ψ_2 and it is used to determine the second harmonic coefficient elliptic flow, v_2.

The measured flow coefficients need to be corrected for the finite event-plane angle resolution. The resolution correction factor is close to unity (zero) for perfect (poor) reconstruction of the collision symmetry plane. The event-plane resolution for the second harmonic is given by:

$$R_2 = \langle \cos[2(\psi_2 - \Psi_2)] \rangle \, , \tag{4.3}$$

where the angle brackets $\langle\rangle$ denote an average over a large event sample.

The resolution correction factor can be calculated using the two- or three-(sub-) detector correlation technique. In case of two (sub-)detectors A and B the subevent resolution is defined as

$$R_2^{\text{sub}} = \sqrt{\langle \cos[2(\psi_2^A - \psi_2^B)] \rangle} \, , \tag{4.4}$$

where ψ_2^A and ψ_2^B are the event-plane angles of the two subevents, and the angle brackets denote the average over an ensemble of the events.

In case of (sub-)detectors with different kinematic coverages, such as VZERO-A and VZERO-C, a three-detector subevent technique can be used. In this case, the resolution

for a given detector can be defined from the correlation between each detector pair

$$R_2^A = \sqrt{\frac{\langle \cos[2(\psi_2^A - \psi_2^C)]\rangle \langle \cos[2(\psi_2^A - \psi_2^B)]\rangle}{\langle \cos[2(\psi_2^B - \psi_2^C)]\rangle}}\,, \tag{4.5}$$

where ψ_2^A is the event-plane angle for which the resolution is calculated, and B and C are any other two (sub-)detectors. One can get the resolution for each of the three detectors by permutation of the event-plane angles. Variations in the event-plane resolution calculated with different methods indicate differences in their sensitivity to the correlations unrelated to reaction plane (non-flow) and/or flow fluctuations.

4.1.2 Elliptic Flow

The D^0 elliptic flow was measured with the event-plane method. The event-plane angle ψ_2 was determined event-by-event as explained in Section 4.1.1 and the D^0 yields were measured in two 90°-wide orthogonal azimuthal regions:

1. in-plane, $-\frac{\pi}{4} < \Delta\varphi \leq \frac{\pi}{4}$ and $\frac{3\pi}{4} < \Delta\varphi \leq \frac{5\pi}{4}$,
2. out-of-plane, $\frac{\pi}{4} < \Delta\varphi \leq \frac{3\pi}{4}$ and $\frac{5\pi}{4} < \Delta\varphi \leq \frac{7\pi}{4}$,

where $\Delta\varphi = \varphi_{\mathrm{D}} - \psi_2$, with φ_{D} defined as the azimuthal angle of the D^0 meson momentum vector at the primary vertex. The v_2 can be expressed in terms of the in-plane ($N_{\mathrm{in-plane}}$) and out-of-plane ($N_{\mathrm{out-of-plane}}$) yields as:

$$v_2\{\mathrm{EP}\} = \frac{1}{R_2}\frac{\pi}{4}\frac{N_{\mathrm{in-plane}} - N_{\mathrm{out-of-plane}}}{N_{\mathrm{in-plane}} + N_{\mathrm{out-of-plane}}}\,. \tag{4.6}$$

This expression is obtained by integrating Equation (2.17) in the two azimuthal regions and includes already the correction for the event-plane resolution $1/R_2$. The contribution of higher harmonics to the v_2 value calculated with this equation can be evaluated by integrating the corresponding terms of the Fourier series. All the odd harmonics, as well as v_4 and v_8, induce the same average contribution to $N_{\mathrm{in-plane}}$ and $N_{\mathrm{out-of-plane}}$ due to symmetry, and therefore they do not affect v_2 calculated with Equation (4.6). The contribution of v_6, v_{10} and higher harmonics was assumed to be negligible based on the values measured for light-flavour hadrons [68, 105].

4.1.3 R_{AA} Azimuthal Dependence

The azimuthal dependence of the nuclear modification factor was studied by measuring the R_{AA} of prompt[1] D^0 mesons in the in-plane and out-of-plane regions defined in

[1] Prompt D^0 are the mesons coming directly from the fragmentation of the c quarks. The D^0 which results from beauty meson decays are defined as "feed-down D^0".

Section 4.1.2. It is defined as:

$$R_{\mathrm{AA}}^{\mathrm{in(out)}}(p_{\mathrm{T}}) = \frac{2 \cdot \mathrm{d}N_{\mathrm{AA}}^{\mathrm{in(out)}}/\mathrm{d}p_{\mathrm{T}}}{\langle T_{\mathrm{AA}} \rangle \cdot \mathrm{d}\sigma_{\mathrm{pp}}/\mathrm{d}p_{\mathrm{T}}} \,. \tag{4.7}$$

$\mathrm{d}N_{\mathrm{AA}}^{\mathrm{in(out)}}/\mathrm{d}p_{\mathrm{T}}$ are the D^0 meson yields, integrated over the two 90°-wide intervals used to determine v_2 with the event-plane method. The factor 2 in Equation (4.7) accounts for the fact that the D meson yields for Pb–Pb collisions were integrated over half of the full azimuth. The average value of the nuclear overlap function in the centrality class 30–50% is $\langle T_{\mathrm{AA}} \rangle = 3.87 \pm 0.18\ \mathrm{mb}^{-1}$ [16]. $\mathrm{d}\sigma_{\mathrm{pp}}/\mathrm{d}p_{\mathrm{T}}$ is the proton–proton reference cross section, that will be described in Section 4.3.

The yields of prompt D^0 mesons in the two azimuthal intervals were obtained as:

$$\left.\frac{\mathrm{d}N^{\mathrm{D}^0}}{\mathrm{d}p_{\mathrm{T}}}\right|_{|y|<0.5} = \frac{1}{\Delta y \Delta p_{\mathrm{T}}} \frac{f_{\mathrm{prompt}}(p_{\mathrm{T}}) \cdot \left.\frac{1}{2} N_{\mathrm{raw}}^{\mathrm{D}^0+\overline{\mathrm{D}^0}}(p_{\mathrm{T}})\right|_{|y|<y_{\mathrm{fid}}} \cdot c_{\mathrm{refl}}(p_{\mathrm{T}})}{(\mathrm{Acc} \times \epsilon)_{\mathrm{prompt}}(p_{\mathrm{T}}) \cdot \mathrm{BR} \cdot N_{\mathrm{events}}} \,. \tag{4.8}$$

The raw yields $N_{\mathrm{raw}}^{\mathrm{D}^0+\overline{\mathrm{D}^0}}$ were divided by a factor of two to obtain the charge (particle and antiparticle) averaged yields. The factor $c_{\mathrm{refl}}(p_{\mathrm{T}})$ was introduced to correct the raw yields for the contribution of signal candidates that are counted both as a particle (D^0) and an antiparticle ($\overline{\mathrm{D}^0}$) (see Section 5.5). To correct for the contribution of B meson decay feed-down, the raw yields were multiplied by the prompt factor f_{prompt}. Furthermore, they were divided by the product of prompt D meson acceptance and efficiency $(\mathrm{Acc} \times \epsilon)_{\mathrm{prompt}}$, normalized by the decay channel branching ratio (BR), the transverse momentum (Δp_{T}) and rapidity ($\Delta y = 2y_{\mathrm{fid}}$) interval widths and the number of events (N_{events}). The normalization by Δy gives the corrected yields in one unity of rapidity $|y| < 0.5$.

The procedure applied to obtain the elements needed to compute the corrected yield will be described in detail in Chapter 5.

4.2 D^0 Production in p–Pb Collisions

The D^0 production was studied in p–Pb collisions as a function of the transverse momentum and of the rapidity of the mesons. The p_{T}-differential production cross section was used to calculate the nuclear modification factor R_{pPb} for prompt D^0 mesons.

Furthermore, the multiplicity dependence of the D^0 production was investigated with two different analysis observables: the nuclear modification factor was measured in different event-activity classes and the D^0 invariant yields were studied as a function of the charged-particle multiplicity.

4.2.1 Production Cross Section and R_{pPb}

The total cross section for hard processes $\sigma_{\mathrm{pA}}^{\mathrm{hard}}$ in proton–nucleus collisions can be derived from the expression of the inelastic cross section of a pA collision $\sigma_{\mathrm{pA}} = \int \mathrm{d}^2b \left[1 - e^{\sigma_{\mathrm{NN}}(s)T_{\mathrm{A}}(b)}\right]$ considering the first term of the expansion in orders of $\sigma_{\mathrm{NN}}^{\mathrm{hard}} T_{\mathrm{A}}(b)$:

$$\sigma_{\mathrm{pA}}^{\mathrm{hard}} \approx \int \mathrm{d}^2b \sigma_{\mathrm{NN}}^{\mathrm{hard}} T_{\mathrm{A}}(b)\,, \tag{4.9}$$

where $\sigma_{\mathrm{NN}}^{\mathrm{hard}}$ is the corresponding cross section in nucleon–nucleon collisions, and $T_{\mathrm{A}}(b)$ is the nuclear thickness function of the nucleus A at impact parameter b, normalized so that $\int \mathrm{d}^2 T_{\mathrm{A}}(b) = A$ [106]. Thus, integrating Equation (4.9) over impact parameter one gets the minimum-bias cross section for a given hard process in pA collisions relative to the same cross section in pp collisions:

$$(\sigma_{\mathrm{pA}}^{\mathrm{hard}})_{\mathrm{MB}} = A \cdot \sigma_{\mathrm{NN}}^{\mathrm{hard}}\,. \tag{4.10}$$

Therefore, the nuclear modification factor for prompt D mesons in minimum-bias p–Pb collisions, R_{pPb}, is given by:

$$R_{\mathrm{pPb}} = \frac{\left(\frac{\mathrm{d}\sigma}{\mathrm{d}p_{\mathrm{T}}}\right)_{\mathrm{pPb}}}{A \cdot \left(\frac{\mathrm{d}\sigma}{\mathrm{d}p_{\mathrm{T}}}\right)_{\mathrm{pp}}} = \frac{\left(\frac{\mathrm{d}N}{\mathrm{d}p_{\mathrm{T}}}\right)_{\mathrm{pPb}}}{\langle T_{\mathrm{pPb}} \rangle \cdot \left(\frac{\mathrm{d}\sigma}{\mathrm{d}p_{\mathrm{T}}}\right)_{\mathrm{pp}}}\,. \tag{4.11}$$

The D^0 production cross section $\left(\frac{\mathrm{d}\sigma}{\mathrm{d}p_{\mathrm{T}}}\right)_{\mathrm{pPb}}$ was obtained as:

$$\left.\frac{\mathrm{d}\sigma^{\mathrm{D}^0}}{\mathrm{d}p_{\mathrm{T}}}\right|_{|y_{\mathrm{lab}}|<0.5} = \frac{1}{\Delta y \Delta p_{\mathrm{T}}} \frac{f_{\mathrm{prompt}}(p_{\mathrm{T}}) \cdot \frac{1}{2}\, N_{\mathrm{raw}}^{\mathrm{D}^0+\overline{\mathrm{D}^0}}(p_{\mathrm{T}})\Big|_{|y_{\mathrm{lab}}|<y_{\mathrm{fid}}} \cdot c_{\mathrm{refl}}(p_{\mathrm{T}})}{(\mathrm{Acc} \times \epsilon)_{\mathrm{prompt}}(p_{\mathrm{T}}) \cdot \mathrm{BR} \cdot L_{\mathrm{int}}}\,. \tag{4.12}$$

The integrated luminosity L_{int} was computed as $N_{\mathrm{pPb,MB}}/\sigma_{\mathrm{pPb,MB}}$ where $N_{\mathrm{pPb,MB}}$ is the number of p–Pb collisions passing the minimum-bias trigger condition and $\sigma_{\mathrm{pPb,MB}}$ is the cross section of the minimum-bias trigger which was measured with the p–Pb van der Meer scan and results 2.09 b $\pm$ 3.7% (syst.) [107].

The p_{T}- and y-differential cross section for prompt D^0 was obtained by applying the same formula used for the p_{T}-differential cross section, Equation (4.12), but considering the yield, the efficiency, and f_{prompt} extracted in intervals of y_{lab}.

4.2.2 Nuclear Modification Factor in Classes of Event Activity: Q_{pPb}

The D^0 nuclear modification factor was studied as a function of the centrality of p–Pb collisions defined with several event-activity estimators:

- CL1: the number of reconstructed clusters in the outer layer of the SPD, $|\eta| < 1.4$;
- V0A: the amplitude measured by the VZERO hodoscopes in the A-side (the Pb-going side), $2.8 < \eta < 5.1$;
- ZNA: the energy deposited in the neutron calorimeter on the A-side (the Pb-going side).

For a centrality selected event sample, we define Q_{pPb} as

$$Q_{\mathrm{pPb}}(p_{\mathrm{T}};\mathrm{cent}) = \frac{\mathrm{d}N^{\mathrm{pPb}}_{\mathrm{cent}}/\mathrm{d}p_{\mathrm{T}}}{\langle N^{\mathrm{Glauber}}_{\mathrm{coll}}\rangle \mathrm{d}N^{\mathrm{pp}}/\mathrm{d}p_{\mathrm{T}}} = \frac{\mathrm{d}N^{\mathrm{pPb}}_{\mathrm{cent}}/\mathrm{d}p_{\mathrm{T}}}{\langle T^{\mathrm{Glauber}}_{\mathrm{pPb}}\rangle \mathrm{d}\sigma^{\mathrm{pp}}/\mathrm{d}p_{\mathrm{T}}}\,, \tag{4.13}$$

with $\langle T^{\mathrm{Glauber}}_{\mathrm{pPb}}\rangle = \langle N^{\mathrm{Glauber}}_{\mathrm{coll}}\rangle/\sigma^{\mathrm{inel}}_{\mathrm{NN}}$ and $\sigma^{\mathrm{inel}}_{\mathrm{NN}} = (70 \pm 5)$ mb at $\sqrt{s_{\mathrm{NN}}} = 5.02$ TeV [108]. In contrast to minimum-bias collisions, where $\langle N_{\mathrm{coll}}\rangle = 6.9$ is fixed by the ratio of the pN and the p–Pb cross sections times the mass number A, in general, $\langle N^{\mathrm{Glauber}}_{\mathrm{coll}}\rangle$ for a given centrality in p–Pb, and thus Q_{pPb}, is influenced by potential biases from the centrality estimators, depending on the pseudorapidity range they cover. The bias is mainly due to multiplicity fluctuations in p–Pb collisions [108]. In p–Pb collisions, the range of multiplicities used to select a centrality class is of similar magnitude as the fluctuations, with the consequence that a centrality selection based on multiplicity may select a sample of nucleon–nucleon collisions which is biased compared to a sample defined by cuts in the impact parameter b. By selecting high (low) multiplicity one chooses not only large (small) average N_{coll}, but also positive (negative) multiplicity fluctuations leading to deviations from the binary scaling of hard processes.

The D^0 Q_{pPb} were calculated in four centrality classes defined by dividing the visible cross section according to the three event-activity estimators described above.

For the CL1 and V0A estimators the values of $\langle N_{\mathrm{coll}}\rangle$ were determined by fitting the measured multiplicity distribution with a distribution obtained from the Glauber model combined with a simple model for particle production.

An alternative hybrid method that aims at providing an unbiased centrality estimator was developed on the basis of two assumptions:

1. the event selection performed using the ZNA signal is expected to be free from a bias on the bulk multiplicity or high-p_{T} particle yields,
2. N_{coll} obtained on the basis of particular scaling for particle multiplicity.

The centrality selection based on the energy measurement with the ZDC is expected to introduce almost no bias on the binary scaling of hard processes owing to its large η-separation from the central part of ALICE. One option to calculate $\langle N_{\rm coll}\rangle$ is to consider that the charged-particle multiplicity at midrapidity is proportional to the number of participants ($N_{\rm part} = N_{\rm coll} + 1$) [109]. Therefore, the average number of binary NN collisions in each centrality interval, was obtained by scaling the minimum-bias value of $\langle N_{\rm part}\rangle_{\rm MB} = 7.9$ [110] accordingly to the multiplicity at midrapidity:

$$\langle N_{\rm part}\rangle_i^{\rm mult} = \langle N_{\rm part}\rangle_{\rm MB} \cdot \left(\frac{\langle {\rm d}N/{\rm d}\eta\rangle_i}{\langle {\rm d}N/{\rm d}\eta\rangle_{\rm MB}}\right)_{-1<\eta<0} \tag{4.14}$$

$$\langle N_{\rm coll}\rangle_i^{\rm mult} = \langle N_{\rm part}\rangle_i^{\rm mult} - 1\,. \tag{4.15}$$

The $\rm D^0$ $Q_{\rm pPb}$ calculated with the CL1 and V0A estimators and $\langle T_{\rm pPb}^{\rm Glauber}\rangle$, as well as with the hybrid method, will be presented in Chapter 8.

4.2.3 Self-normalized Yields

The second approach used to investigate the multiplicity dependence of the $\rm D^0$ production in p–Pb collisions was the measurement of the $\rm D^0$ yield as a function of the multiplicity of produced charged particles. The results will be given in Chapter 8 in terms of the relative yields with respect to the yields in minimum-bias events:

$$\frac{({\rm d}^2N^{\rm D^0}/{\rm d}y{\rm d}p_{\rm T})^j}{\langle {\rm d}^2N^{\rm D^0}/{\rm d}y{\rm d}p_{\rm T}\rangle} = \left(\frac{1}{N_{\rm event}^j}\frac{N_{\rm raw\ D^0}^j}{\epsilon_{\rm prompt\ D^0}^j}\right) \Bigg/ \left(\frac{1}{N_{\rm MB\ trigger}/\epsilon_{\rm MB\ trigger}}\frac{\langle N_{\rm raw\ D^0}\rangle}{\langle \epsilon_{\rm prompt\ D^0}\rangle}\right), \tag{4.16}$$

where the index j identifies the multiplicity interval, $N_{\rm raw\ D^0}^j$ are the raw yields for each multiplicity and $p_{\rm T}$ interval, $\epsilon_{\rm prompt\ D^0}^j$ the reconstruction and selection efficiencies and $N_{\rm events}^j$ the number of events analyzed in the considered multiplicity interval. Equation (4.16) holds under the assumption that the relative contribution to the D meson raw yield due to the feed-down from B hadron decays does not depend on the multiplicity of the event, and is therefore canceling in the ratio to the multiplicity-integrated values. The acceptance correction, defined as the fraction of $\rm D^0$ mesons within a given rapidity and $p_{\rm T}$ interval that decay into pairs of particles within the detector coverage, cancels in this ratio. The number of events used for the normalization of the multiplicity integrated yield has to be corrected for the fraction of inelastic events not seen by the minimum-bias trigger condition, and it is therefore expressed as $N_{\rm MB\ trigger}/\epsilon_{\rm MB\ trigger}$, with $\epsilon_{\rm MB\ trigger} = (96.4 \pm 2.2)\%$. It was verified with PYTHIA 6.4.21 Monte Carlo simulations that the minimum-bias trigger is 100% efficient for D mesons in the kinematic range of the measurement meaning that the number of $\rm D^0$ in the minimum-bias triggered events is the same as in the sample of inelastic events.

The charged-particle multiplicity intervals were defined considering two alternative estimators. The first experimental estimator is the number of SPD tracklets in $|\eta| < 1.0$, $N_{\rm tracklets}$. As will be shown in Chapter 5, Monte Carlo simulations have demonstrated that $N_{\rm tracklets}$ is proportional to the pseudorapidity density of the generated charged primary particles, $\mathrm{d}N_{\rm ch}/\mathrm{d}\eta$. Primary particles are defined as prompt particles produced in the collision, including their decay products, except those from weak decays of strange particles. The results obtained with the $N_{\rm tracklets}$ multiplicity estimator are presented as a function of the relative charged-particle multiplicity at midrapidity, $(\mathrm{d}N_{\rm ch}/\mathrm{d}\eta)^{j}/\langle \mathrm{d}N_{\rm ch}/\mathrm{d}\eta\rangle$, with $\langle \mathrm{d}N_{\rm ch}/\mathrm{d}\eta\rangle = 17.64 \pm 0.01$ (stat.) ± 0.15 (syst.) as measured in inelastic p–Pb collisions producing at least one charged particle in $|\eta| < 1$ [109, 110].

The analysis of D^0 production was also performed as a function of the charged-particle multiplicity in the region $2.8 < \eta < 5.1$, as measured with the charge collected by the A side of the VZERO scintillator counters, $N_{\rm V0A}$, reported in units of the minimum-ionizing-particle charge. The advantage of this estimator is that the event multiplicity and the D meson yields are evaluated in different pseudorapidity ranges, avoiding any possible auto-correlation. Monte Carlo simulations demonstrate that $N_{\rm V0A}$ is proportional to the charged-particle multiplicity in that pseudorapidity interval. The D^0 relative yields per event will be reported as a function of the relative uncorrected multiplicity in the VZERO-A detector, $N_{\rm V0A}/\langle N_{\rm V0A}\rangle$.

4.3 Proton–Proton Reference

The reference proton–proton cross section, which is needed to calculate the nuclear modification factors in Pb–Pb and p–Pb collisions, was obtained by means of a pQCD-based energy scaling of the $p_{\rm T}$-differential cross section measured at $\sqrt{s} = 7$ TeV [38]. The $p_{\rm T}$-dependent scaling factors were defined as the ratio of the cross sections obtained from FONLL calculations [34–36] at $\sqrt{s} = 2.76$ TeV (or at $\sqrt{s} = 5.02$ TeV) and 7 TeV.

The scaled D^0 meson $p_{\rm T}$-differential cross section in $2 < p_{\rm T} < 16$ GeV/c is consistent with that measured at $\sqrt{s} = 2.76$ TeV using a smaller statistics data sample [39]. The D^0 cross section measured at 7 TeV in this $p_{\rm T}$ range had smaller uncertainties with respect to the measurement at 2.76 TeV and thus the scaled result from 7 TeV was used as pp reference for the $R_{\rm AA(pA)}$ calculation. The D^0 cross section in pp collisions in the interval $1 < p_{\rm T} < 2$ GeV/c was measured at 7 and 2.76 TeV with similar uncertainty, both results were scaled to 5.02 TeV, and averaged considering their relative statistical uncertainties as weights.

The maximum $p_{\rm T}$ reached by the current available ALICE pp measurement is limited to $p_{\rm T} = 16$ GeV/c. To obtain the pp reference for the p–Pb measurements in the $16 < p_{\rm T} < 24$ GeV/c interval, the measured pp cross section was extrapolated to higher $p_{\rm T}$ using the spectrum predicted by FONLL [34–36] scaled to match pp data in

$5 < p_{\mathrm{T}} < 16$ GeV/c. Then the D^0 cross section at 7 TeV in $16 < p_{\mathrm{T}} < 24$ GeV/c was scaled to 5.02 TeV.

5

$D^0 \to K^-\pi^+$ Decay Reconstruction

The chapter is devoted to the description of the D^0 analysis in Pb–Pb and p–Pb collisions. The aim of the analysis is to extract the elements that are needed to measure the elliptic flow in Pb–Pb collisions, the production cross section and nuclear modification factor in both Pb–Pb and p–Pb collisions.

In the first part of the chapter, Section 5.1, the Pb–Pb and p–Pb data samples are described. In Section 5.2 the event-plane determination for the azimuthal anisotropy measurement is explained. Section 5.3 is devoted to the description of the reconstruction and selection strategy for D mesons. The strategy exploits the displacement (from the primary vertex) of the secondary vertices originating from the weak decay of the D mesons. The variables allowing to select the $D^0 \to K^-\pi^+$ topology will be introduced, together with the particle identification procedure to improve the rejection of the combinatorial background. A description of the invariant mass analysis used to extract the yields is given in Section 5.4. The invariant mass distributions together with the fits performed to obtain the raw signals are shown for both Pb–Pb and p–Pb systems. Section 5.5 describes the study of the D^0 reflections, defined as the signal candidates that pass the cuts both as D^0 and $\overline{D^0}$. The last two sections, 5.6 and 5.7, are devoted to the description of the efficiency calculation and feed-down correction, respectively.

5.1 Data Samples

Pb–Pb Collisions

The D^0 azimuthal anisotropy analysis was performed on the data sample of Pb–Pb collisions recorded in November and December 2011 at the centre-of-mass energy per nucleon–nucleon collision of $\sqrt{s_{\rm NN}} = 2.76$ TeV. The events were collected with an interaction trigger based on the information from the VZERO detector, which required

coincident signals in the detectors at forward and backward pseudorapidities. Events were further selected offline to remove background from parasitic beam interactions by using the time information provided by the VZERO and the neutron ZDC detectors. Only events with a reconstructed primary vertex within ±10 cm from the centre of the detector along the beam line were used for the analysis.

Collisions were classified in centrality classes, determined from the sum of the amplitudes of the signal in the VZERO detector and defined in terms of percentiles of the total hadronic Pb–Pb cross section. The centrality classes were related to the collision geometry by fitting the VZERO summed amplitudes by a model based on the Glauber approach for the geometrical description of the nuclear collision [15] complemented by a two-component model for particle production [16], following the procedure explained in Section 1.5.1. The centrality distribution of the collected events was flat in the 30–50% centrality class. In order to obtain an uniform centrality distribution also in the 0–10% and 10–30% classes, a small fraction of events were randomly rejected in the regions 0–10% and 10–12%. The results presented in this thesis are obtained from 16.0×10^6 events in the centrality class 0–10% and 9.5×10^6 events in the centrality classes 10–30% and 30–50%. The corresponding integrated luminosities are $L_{\rm int} = (20.9 \pm 0.7)\ \mu{\rm b}^{-1}$ in 0–10% and $L_{\rm int} = (6.2 \pm 0.2)\ \mu{\rm b}^{-1}$ in the 10–30% and 30–50% centrality classes.

p–Pb Collisions

The data sample analyzed to measure the production of the $\rm D^0$ mesons in proton–nucleus collisions was collected during the p–Pb run of LHC that took place at the beginning of 2013. The energy of the collisions was $\sqrt{s_{\rm NN}} = 5.02$ TeV and data were collected with a minimum-bias trigger that required the arrival of the bunches from both directions and coincident signals in both scintillator arrays of the VZERO detector. Events were selected offline using the timing information of the VZERO and ZDC to remove background due to beam-gas interactions. Also in this case, only events with a primary vertex reconstructed within ±10 cm from the centre of the detector along the beam line were considered. About 10^8 events passed the selection criteria, corresponding to an integrated luminosity $L_{\rm int} = (48.6 \pm 1.6)\ \mu{\rm b}^{-1}$.

5.2 Event-Plane Determination in Pb–Pb Collisions

The event-plane angle was estimated starting from the **Q** vector, as explained in Section 4.1.1. The charged-particle tracks (reference particles) used for the **Q** vector determination were selected with the following criteria:

- at least 50 associated space points in the TPC,

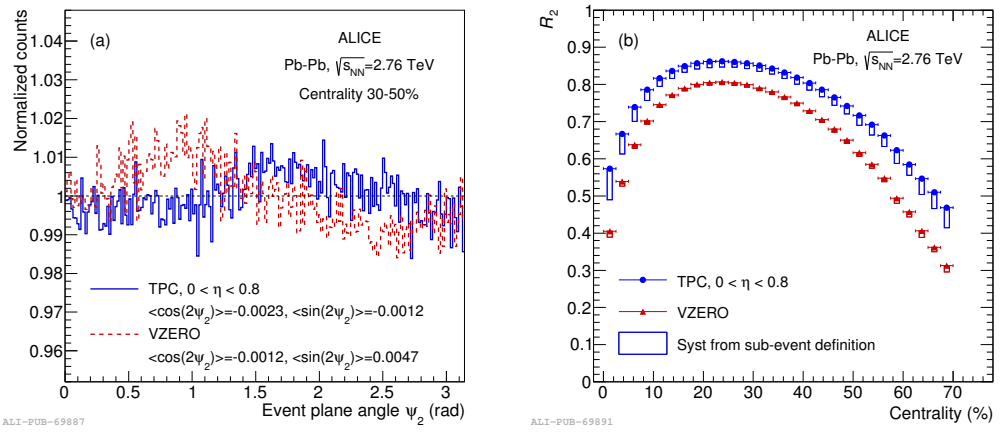

(a) (b)

FIGURE 5.1: (a) Distribution of event-plane angle ψ_2, estimated from TPC tracks with $0 < \eta < 0.8$ (solid line) or with the VZERO detector signals (dashed line) in the centrality range 30–50%. The distributions are normalized by their integral [111]. (b) Event-plane resolution correction factor R_2 as a function of centrality for the TPC and VZERO detectors. The boxes represent the systematic uncertainties estimated from the variation of R_2 when changing the subevents used for its determination [111].

- $\chi^2/\mathrm{ndf} < 2$ for the momentum fit in the TPC,
- a distance of closest approach to the primary vertex smaller than 3.2 cm in z and 2.4 cm in the (x, y) plane,
- $p_\mathrm{T} > 150$ MeV/c.

The pseudorapidity interval was limited to the positive region $0 < \eta < 0.8$, where the TPC acceptance and efficiency were more uniform as a function of the azimuthal angle for the analyzed data set. The remaining azimuthal non-uniformity was corrected for using as weights w_i in Equation (4.1) the inverse of the φ distribution of charged particles used for the $\mathbf{Q}$ vector determination, $1/(\mathrm{d}N/\mathrm{d}\varphi_i)$, multiplied by a function $f(p_\mathrm{T}) = \begin{cases} p_\mathrm{T}/\ \mathrm{GeV}/c, & p_\mathrm{T} < 2\ \ \mathrm{GeV}/c \\ 2, & p_\mathrm{T} \geq 2\ \ \mathrm{GeV}/c \end{cases}$. This function mimics the p_T dependence of the charged-particle v_2 and it improves the estimate of Ψ_2 by enhancing the contribution of particles with a stronger flow signal. To avoid auto-correlations between the D meson candidates and the event-plane angles, the $\mathbf{Q}$ vector was calculated for each candidate excluding from the set of reference particles the tracks used to form that particular candidate.

The distribution of the event-plane angle ψ_2 obtained for this set of reference particles is shown in Figure 5.1(a), for the centrality range 30–50%. The distribution, divided by its integral, exhibits a residual non-uniformity below 1% [111].

An additional study was performed with the $\mathbf{Q}$ vector determined from the azimuthal distribution of signals in the segments of the VZERO detectors, which are

sensitive to particles produced at forward and backward rapidities. Also with this procedure the residual non-uniformity in the event-plane distribution is of about 1% (Figure 5.1(a)) [111].

The event-plane resolution correction factor R_2 was computed with the two- or three-subevent methods for both strategies adopted to estimate the event-plane angle. For the event plane computed using TPC tracks, R_2 was determined from the correlation of the event-plane angles reconstructed in the two sides of the TPC, $-0.8 < \eta < 0$ and $0 < \eta < 0.8$, i.e. two samples of tracks with similar multiplicity and v_2. R_2 is shown in Figure 5.1(b) as a function of collision centrality. The average R_2 value in the centrality class 30–50% is 0.8059 [111]. The statistical uncertainty is negligible ($\sim 10^{-4}$). The systematic uncertainty was estimated by using a three-subevent method considering the event planes reconstructed in the TPC ($0 < \eta < 0.8$), VZERO-A ($2.8 < \eta < 5.1$) and VZERO-C ($-3.7 < \eta < -1.7$).

The resolution of the event plane determined from the VZERO detector is also shown in Figure 5.1(b). In this case, R_2 was measured with three subevents, namely the signal in the VZERO detector and the tracks in the positive and negative η region of the TPC. The event-plane determination has a poorer resolution with the VZERO detector than with the TPC tracks, thus, the v_2 measurement is expected to be more precise with the TPC event plane [111].

5.3 D^0 Reconstruction and Selection

The reconstruction of charm mesons is performed with a common strategy within the ALICE experiment. The lowest-mass charm hadron states, D^0 and D^+ (and antiparticles), can decay only through weak processes and they have proper decay lengths of a few hundred microns: $c\tau = 122.9$ μm for the D^0 and $c\tau = 311.8$ μm for the D^+ [7]. Therefore, the distance between the interaction point (primary vertex) and their decay point (secondary vertex) is measurable. The D meson detection strategy is based on an invariant mass analysis of fully reconstructed topologies originating from secondary vertices.

The results presented in this thesis are based on the reconstruction and selection of the D^0 hadronic decay channel, $D^0 \to K^-\pi^+$ ($\overline{D^0} \to K^+\pi^-$), with branching ratio B.R.$= (3.88 \pm 0.05)\%$ [7]. A sketch of the decay is shown in Figure 5.2. The main feature of this topology is the presence of two tracks displaced from the primary vertex and originating from a common point.

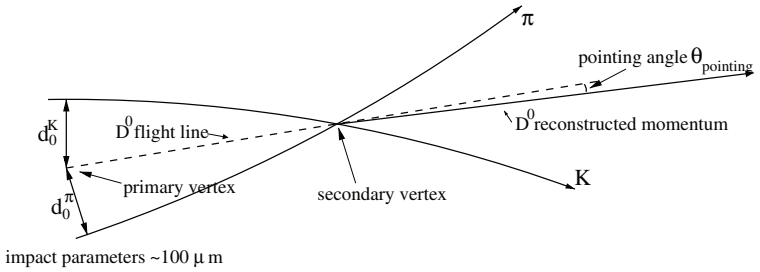

FIGURE 5.2: Schematic representation of the $D^0 \to K^-\pi^+$ decay with the impact parameters (d_0) and the pointing angle (θ_{pointing}).

5.3.1 Secondary Vertex Reconstruction

The knowledge of the momenta of the decay tracks and of the position of the secondary vertex allows the complete reconstruction of the momentum of the particle that has decayed.

The secondary vertex is reconstructed for a given pair of opposite-sign tracks by a minimization of the distance in space between the two helices representing the tracks. Once the minimum segment between the tracks is found, the position of the vertex on this segment is defined keeping into account the different spatial precisions of the two tracks, which are estimated by the track covariance matrix. The track with the largest momentum has better precision (see Figure 3.13) and, therefore, the vertex is usually estimated to be closer to this track than to the lower-momentum one.

The resolution on the secondary vertex position is strongly correlated to the impact parameter resolution: it is better in the bending plane (x and y) than along z and, for $p_{\mathrm{T}} < 2$–3 GeV/c, it improves as p_{T} increases. At low p_{T}, the decay tracks are affected by multiple scattering and the resolution deteriorates, while at high p_{T} the worsening is due to the fact that the angle between the decay tracks becomes smaller as the p_{T} of the D^0 increases and, thus, the determination of the crossing point becomes less precise. For intermediate p_{T} (~ 2 GeV/c) the resolution is of about 70 μm [112].

5.3.2 Topological Selection Strategy

The reconstructed tracks are grouped in pairs following the charge ordering of the decay channel, defining the D^0 candidates. For each candidate the secondary vertex is computed, and the candidates are selected on the basis of typical kinematical and geometrical properties that characterize the single tracks and the reconstructed secondary vertex. The high tracking spatial precision provided by the ITS detector allows to reconstruct the primary vertex position with high precision and, then, to tag displaced tracks with distances to the interaction point of few tens of microns. In order to select signal

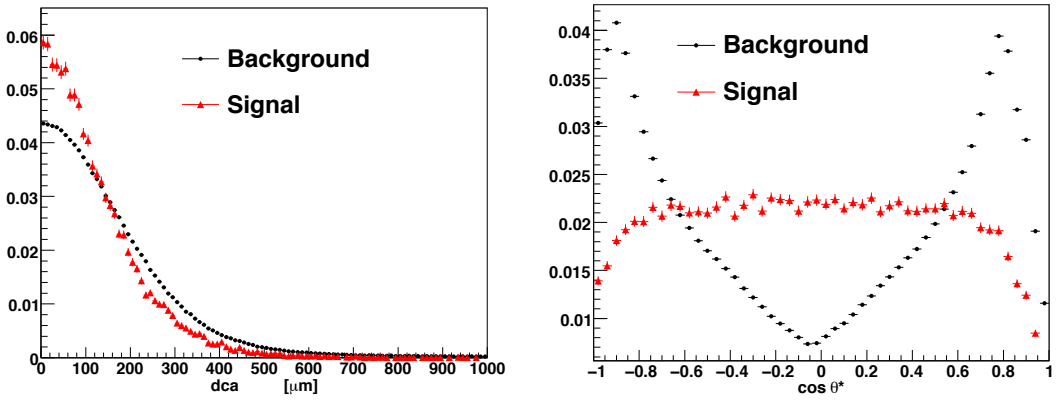

(a) (b)

FIGURE 5.3: (a) Distance of closest approach (dca) of signal (red) and background (black) D^0 candidates obtained with a pp PYTHIA simulation. (b) Distribution of the θ^* angle for signal and background candidates. For signal the distribution is almost flat due to the isotropic emission of the pion and the kaon in the centre-of-mass system.

candidates among the huge number of those obtained by combinatorial association, the key point is to measure the separation between the primary and the secondary vertices.

Several variables are used to reject background candidates and to select as much signal as possible. The variables used to enhance the signal-to-background ratio can be subdivided into two classes: single track variables and candidate variables.

The track selection criteria are:

- pseudorapidity within the TPC fiducial acceptance ($|\eta| < 0.8$),
- the number of space points in the TPC ($N_{\rm cl} > 70$),
- the quality of the momentum fit in the TPC ($\chi^2/{\rm ndf} < 2$),
- at least one hit in either of the two layers of the SPD (helps in rejecting secondaries).

The selection of tracks with $|\eta| < 0.8$ introduces a steep drop in the acceptance of D mesons for rapidities larger than 0.7–0.8, depending on $p_{\rm T}$. A D meson fiducial acceptance region was, therefore, defined as $|y| < y_{\rm fid}(p_{\rm T})$, with $y_{\rm fid}(p_{\rm T})$ increasing from 0.5 to 0.8 in $0 < p_{\rm T} < 5$ GeV/c and taking a constant value of 0.8 for $p_{\rm T} > 5$ GeV/c.

Cuts are applied on the *impact parameter* (the projection on the transverse plane $d_0(r\varphi)$) with respect to the primary vertex and on the track *transverse momentum*. The impact parameter resolution in Pb–Pb and p–Pb collisions is about 60 μm and 70 μm, respectively, for tracks with $p_{\rm T} = 1$ GeV/c, as shown is Section 3.5. A lower limit on the impact parameter of the tracks reduces the number of primary tracks, while an upper cut allows to reject those with large displacement, e.g. from strange-hadron decays and electrons coming from photon conversions in the detector material.

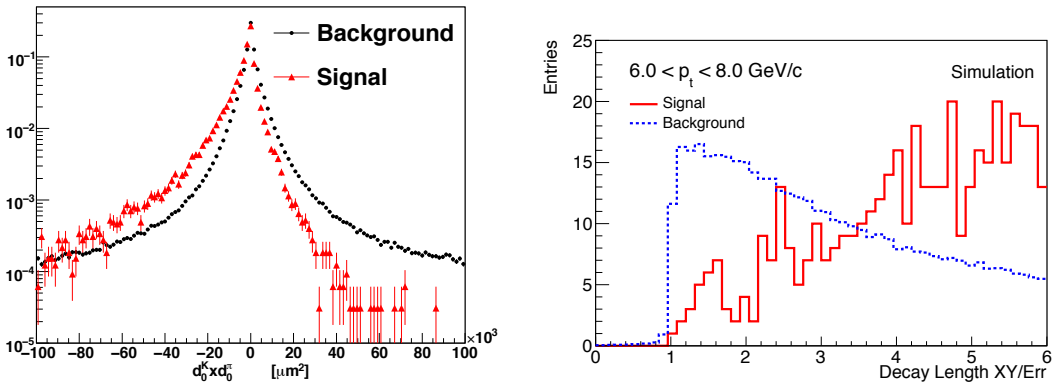

(a) (b)

FIGURE 5.4: (a) Distributions of the product of the impact parameters $d_0^{\mathrm{K}} \times d_0^{\pi}$ of signal and background candidates measured in pp Monte Carlo. The signal candidates are characterized by an symmetric distribution (red). (b) Normalized decay length distributions for signal (red) and background (blue) candidates measured in Pb–Pb Monte Carlo simulation.

The candidate variables involve the properties of the tracks that are paired to form a D^0 candidate. The *distance of closest approach (dca)* between two tracks is the length of a segment minimizing the distance between the two track trajectories. Two tracks with a common vertex should have $dca = 0$. The measured dca is determined by the resolution on the track position (see Figure 5.3(a)).

In the reference frame of the decaying D^0, the θ^* angle is defined as the angle between the pion momentum and the D^0 flight line. In this reference frame the pion and the kaon are emitted isotropically with three-momenta of equal magnitude and opposite direction, thus, the $\cos\theta^*$ distribution for signal pairs is almost flat. The background, instead, accumulates at $\cos\theta^* = \pm 1$ and it can be reduced by accepting only pairs with $|\cos\theta^*| < \cos\theta^*_{\mathrm{max}} \approx 0.8$ (see Figure 5.3(b)).

The projection of the impact parameter in the bending plane allows to define a sign for the impact parameter. The sign is positive or negative depending on the position of the track projection with respect to the primary vertex. The tracks originating from a D^0 decaying far from the primary vertex will then have impact parameters of opposite sign and large in absolute value. The product of the two transverse projections of the impact parameters, $d_0^{\mathrm{K}} \times d_0^{\pi}$, is an appropriate variable for the selection of D^0 candidates. For true decays this quantity should tend to be negative and large in absolute value, while for background it is symmetric with respect to zero (see Figure 5.4(a)).

Further improvement is obtained by exploiting the reconstructed secondary vertex, requiring that the candidate momentum direction points back to the primary vertex. This condition is imposed by a cut on the pointing angle $\theta_{\mathrm{pointing}}$, which is the angle between the reconstructed momentum vector (sum of the reconstructed momenta of the decay tracks) of the D^0 candidate and the line connecting the primary and secondary

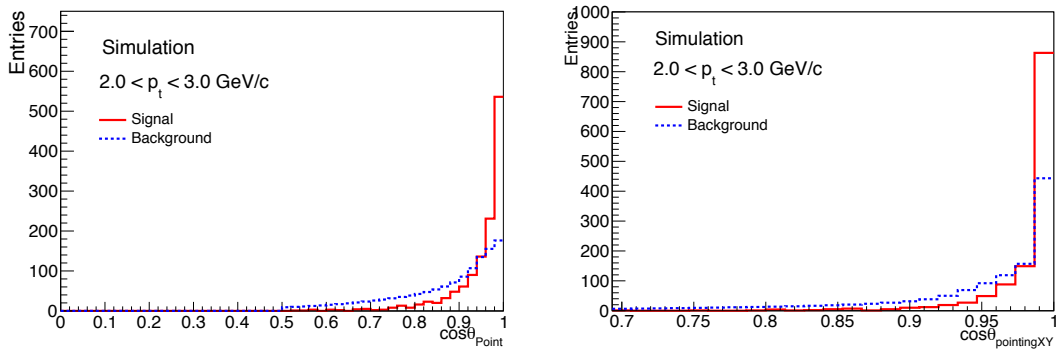

(a) (b)

FIGURE 5.5: (a) Distribution of the cosine of the pointing angle $\cos\theta_{\rm pointing}$ for signal (red) and background (blue) candidates in Pb–Pb Monte Carlo. (b) Distribution of the cosine of the pointing angle measured in the transverse plane $\cos\theta^{xy}_{\rm pointing}$ for signal and background candidates measured in a HIJING charm enriched Monte Carlo.

vertex (D^0 flight line). For background pairs there is no correlation between the reconstructed momentum and the reconstructed flight line, so that the $\cos\theta_{\rm pointing}$ is almost uniformly distributed. The signal, instead, is characterized by a distribution peaked at +1 (see Figure 5.5(a)).

The pointing angle can be defined in 3D space, or also considering only the transverse plane, where the tracking and the primary vertex resolutions are better. A new cut variable can, thus, be introduced to better separate background candidates with respect to signal ones. The distribution of the $\cos\theta^{xy}_{\rm pointing}$ is more peaked close to 1 with respect to the pointing angle in three dimensions, and is used in the Pb–Pb analysis to cope with the larger background (see Figure 5.5(b)).

The last selection variable, used only in the Pb–Pb analysis, is the normalized decay length in the transverse plane L_{xy}. It is obtained by dividing (normalizing) the decay length (distance between the reconstructed primary and secondary vertex) in the transverse plane by the uncertainty on its measurement. The background is characterized by small normalized decay length, as can be seen in Figure 5.4(b).

The values used as selection cuts were chosen in order to reject as much background as possible without losing too much signal, and, in general for Pb–Pb analysis the cuts are tighter with respect to p–Pb due to the larger combinatorial background. The values of the selection cuts applied in Pb–Pb and p–Pb are reported in the next section (Section 5.4).

5.3.3 Particle Identification

For the D^0 analysis, the Particle Identification (PID) is mainly used to identify the kaon in the candidate and remove the high combinatorial background from pairs of

pions. Kaons (and pions) are identified via the specific energy loss ($\mathrm{d}E/\mathrm{d}x$) in the TPC (Section 3.4.1) and the time of flight measurements in the TOF (Section 3.4.2). These two detectors can separate kaons and pions from other particles in different momentum ranges. With both detectors a track can be identified on the basis of the difference, expressed in units of resolution (σ), between the measured signal and that expected for the considered particle species ($n\sigma$ cut method). For the D^0, the PID selection is aimed at reducing the background while preserving most of the signal.

The same PID strategy was applied for Pb–Pb and p–Pb analysis.

In order to assign the kaon or pion mass to the decay tracks, compatibility cuts were applied to the difference between the measured and the expected TPC and TOF signals. For both $\mathrm{d}E/\mathrm{d}x$ and time of flight, a 3σ compatibility cut was used for all momenta (a track is not excluded as a pion or kaon in the TPC (TOF) if its signal is within 3σ from the expected $\mathrm{d}E/\mathrm{d}x$ (time of flight) for the pion or kaon hypothesis). Tracks without a TOF signal were identified using only the TPC information, and tracks with incompatible TOF and TPC indications were considered to be compatible with both pion and kaon.

In the TPC, a 2σ cut was applied to identify both pions and kaons. If the track energy loss signal is between 2 and 3σ from the expected value, the track is used both as pion and kaon. In the momentum interval $0.6 < p < 0.8$ GeV/c, the selection band is tightened to 1σ, since the pion and kaon expectations become closer.

If the track reaches the TOF, a 3σ cut is applied on its expected arrival time. Kaons are identified up to $p = 2$ GeV/c, and for larger momenta, particles are used both as pion and kaon since the signal bands of pions and kaons start to overlap and the contamination effect is not negligible anymore.

Two-prong candidates were accepted (as D^0, $\overline{\mathrm{D}^0}$, or both) or rejected on the basis of their compatibility with the $\mathrm{K}^{\mp}\pi^{\pm}$ final state. If a true D^0 candidate is compatible with both D^0 and $\overline{\mathrm{D}^0}$ hypotheses, the "wrong" one, which can not be rejected on a candidate by candidate basis, is called "reflection" (Section 5.5).

5.4 Yield Extraction

The D^0 raw yields were extracted in several p_{T} intervals from an invariant mass analysis of the candidates that pass the topological cuts and the PID requirements. For each D^0 candidate the invariant mass is calculated as $M(\mathrm{K}\pi) = \sqrt{(E_{\mathrm{K}} + E_{\pi})^2 - (\vec{p}_{\mathrm{K}} + \vec{p}_{\pi})^2}$ starting from the reconstructed information of the corresponding pair of tracks. The $\mathrm{K}^{\pm}\pi^{\mp}$ invariant mass distribution can be considered as the sum of a Gaussian function representing the D^0 signal and the background, that is described with an exponential

TABLE 5.1: Summary table of the D^0 analysis cuts applied in Pb–Pb collisions in the centrality class 30–50%.

p_T (GeV/c)	dca (μm)<	$\lvert\cos\theta^*\rvert$ <	$d_0^K \times d_0^\pi$ (μm^2)<	$\cos\theta_{pointing}$ >	$\cos\theta^{xy}_{pointing}$ >	$L_{xy}/\sigma_{L_{xy}}$ >
2 – 3	250	0.8	−40000	0.95	0.991	5
3 – 4	250	0.8	−36000	0.95	0.993	5
4 – 5	250	0.8	−27000	0.95	0.994	5
5 – 6	250	0.8	−21000	0.92	0.998	5
6 – 8	270	0.8	−14000	0.88	0.998	5
8 – 12	300	0.8	−5000	0.85	0.995	5
12 – 16	350	1	0	0.83	0.995	4

function. Therefore the distribution is fitted to the expression:

$$f(M) = \frac{P_1(P_0 - P_2)}{\exp(-P_1 M_{\min}) - \exp(-P_1 M_{\max})} \exp(-P_1 M) + \frac{P_2}{\sqrt{2\pi} P_4} \exp\left[-\frac{(M - P_3)^2}{2P_4^2}\right], \tag{5.1}$$

where $[M_{\min}, M_{\max}]$ is the fit range, P_0 is the integral of the distribution in the fit range, which is known (sum of the bin contents) and fixed, P_1 is the slope of the exponential background and P_2, P_3, P_4 are, respectively, the integral (S), the centroid and the σ of the Gaussian. The fit is performed in two steps using the Minuit package [113]. The first step consists of a fit of the side-bands of the distribution with an exponential to determine a first approximation of the slope parameter, P_1; then, with the second step, the whole distribution is fitted to determine P_1 and the three parameters of the Gaussian at the same time. The amount of signal (S) and background (B) are extracted from the fit parameters together with their errors, and the statistical significance $S/\sqrt{S+B}$ can be computed. The quality of the fits are evaluated on the basis of the statistical significance, requiring values larger than 3, which means a statistical error on the signal of at most 33%.

In the following, the invariant mass distributions and fits obtained with Pb–Pb and p–Pb data samples will be presented, together with the cut values that allow to obtain a good statistical significance in all the p_T intervals considered for the analysis.

5.4.1 Pb–Pb

Invariant Mass Distributions

The topological cuts applied for D^0 selection in Pb–Pb collisions in the 30–50% centrality class are reported in Table 5.1. In addition, the single tracks were required to have a minimum p_T equal to 0.5 for D^0 in the p_T interval $2 < p_T < 3$ GeV/c or 0.7 in $3 < p_T < 16$ GeV/c, and an impact parameter significance in the xy plane $|d_0/\sigma_{d_0}| > 0.5$. The cuts are in general tighter at low p_T to reject the higher combinatorial background and become loser as the transverse momentum increases due to the decreasing background.

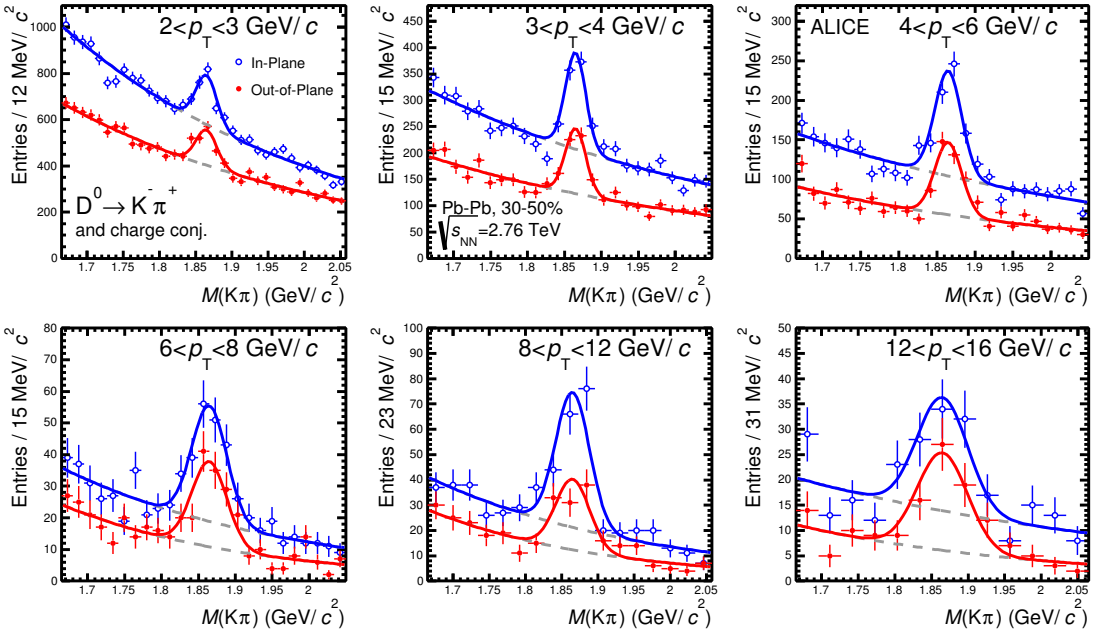

FIGURE 5.6: Distributions of the invariant mass for D^0 in the two $\Delta\varphi$ intervals, for Pb–Pb collisions in the 30–50% centrality class [111].

TABLE 5.2: Summary table of the D^0 raw yield (S) and significance extracted in each p_T interval in-plane and out-of-plane in Pb–Pb collisions in the centrality class 30–50%.

p_T (GeV/c)	S		Significance	
	In-plane	Out-of-plane	In-plane	Out-of-plane
$2-3$	739 ± 66	526 ± 55	11.2	9.6
$3-4$	452 ± 36	297 ± 28	12.5	10.6
$4-6$	429 ± 33	276 ± 25	13	11
$6-8$	150 ± 18	115 ± 15	8.3	7.7
$8-12$	195 ± 19	77 ± 14	10.3	5.5
$12-16$	56 ± 13	76 ± 11	4.3	6.9

The D^0 meson yield was extracted in the in-plane and the out-of-plane regions defined in Section 4.1.2. The invariant mass distributions for the D^0 meson are shown in Figure 5.6 in six p_T intervals for the 30–50% centrality class, along with the fits used for the yield estimation [111]. The raw signal, background and significance extracted in each p_T interval are reported in Table 5.2. When fitting the invariant mass distribution in the two $\Delta\varphi$ intervals, the centroid and the width of the Gaussian functions were fixed to those obtained from a fit to the invariant mass distribution integrated over φ, where the statistical significance of the signal is larger. The centroids for the φ-integrated distributions were found to be in agreement with the D^0 meson world-average [7] mass value and with the values from the simulation, confirming that the background fluctuations were not causing a distortion in the signal line shape.

TABLE 5.3: Summary table of the D^0 analysis cuts applied in minimum-bias p–Pb collisions.

p_T (GeV/c)	dca (μm)<	$\lvert\cos\theta^*\rvert$ <	$d_0^K \times d_0^\pi$ (μm^2)<	$\cos\theta_{pointing}$ >
1 – 2	300	0.8	−35000	0.90
2 – 3	300	0.8	−30000	0.90
3 – 4	300	0.8	−30000	0.90
4 – 5	300	0.8	−15000	0.90
5 – 6	300	0.8	−10000	0.90
6 – 7	300	0.8	−8000	0.85
7 – 8	300	0.8	−8000	0.85
8 – 12	300	0.9	−5000	0.85
12 – 16	300	1	10000	0.85
16 – 24	300	1	10000	0.85

5.4.2 p–Pb

Invariant Mass Distributions for Minimum-Bias Events

In Table 5.3 the topological cuts applied to select the D^0 candidates in the p–Pb data sample are reported. In case of p–Pb, the cuts on $\cos\theta^{xy}_{pointing}$ and on the normalized decay length were not applied, since the combinatorial background is lower than in Pb–Pb collisions, due to the lower charged-particle multiplicity. In addition, only tracks with minimum p_T equal to 0.4 for D^0 in the p_T interval $1 < p_T < 2$ GeV/c or 0.7 in $2 < p_T < 24$ GeV/c were accepted, and an impact parameter significance in the xy plane $|d_0/\sigma_{d_0}| > 0.5$ was required.

The D^0 raw yields were extracted in 10 p_T intervals from the fit to the invariant mass distributions shown in Figure 5.7. For all p_T intervals the statistical significance is larger than 6 and the values of the centroid and width of the Gaussian are compatible with those obtained in the simulation. Table 5.4 summarizes the values for the raw signal, background and significance obtained in each p_T interval.

The D^0 production in p–Pb collisions was studied also as a function of rapidity for three p_T intervals. The sample of selected D^0 candidates was divided in five intervals of rapidity of the candidate (y_{lab}) in the laboratory reference system. The invariant mass distributions and the fits used to extract the signal are shown in Figure 5.8 for $2 < p_T < 5$ GeV/c, Figure 5.9 for $5 < p_T < 8$ GeV/c, and Figure 5.10 for $8 < p_T < 16$ GeV/c.

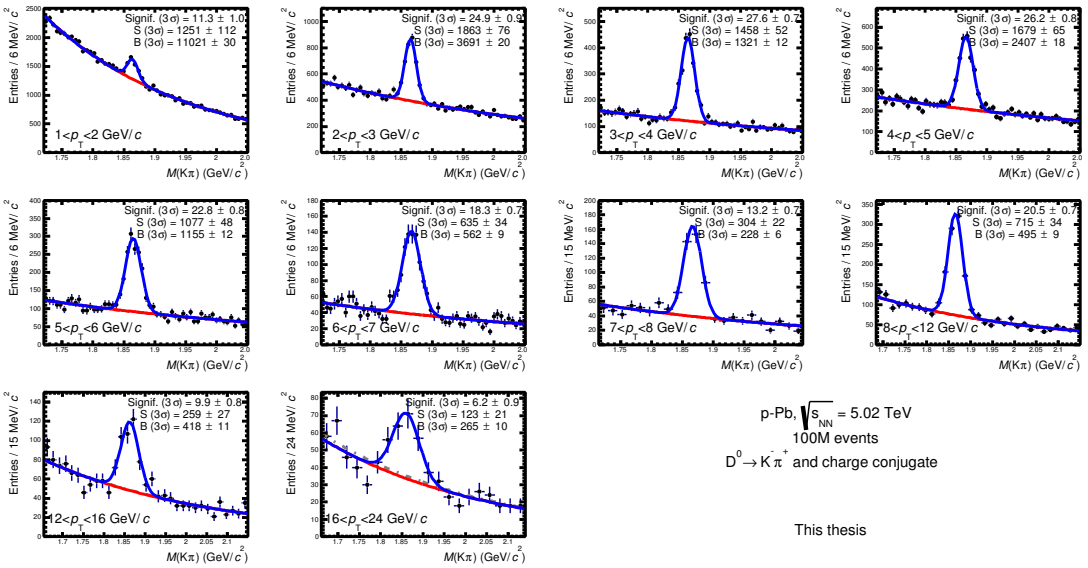

FIGURE 5.7: D^0 invariant mass distributions in p–Pb collisions. The signal was extracted in 10 p_T intervals in the range $1 < p_T < 24$ GeV/c.

TABLE 5.4: Summary table of the D^0 raw yield (S), background (B) and significance extracted in each p_T interval in minimum-bias p–Pb collisions.

p_T (GeV/c)	S	B	Significance
$1-2$	1251 ± 112	11021 ± 30	11.3
$2-3$	1863 ± 76	3691 ± 20	24.9
$3-4$	1458 ± 52	1321 ± 12	27.6
$4-5$	1679 ± 65	2407 ± 18	26.2
$5-6$	1077 ± 48	1155 ± 12	22.8
$6-7$	635 ± 34	562 ± 9	18.3
$7-8$	304 ± 22	228 ± 6	13.2
$8-12$	715 ± 34	495 ± 9	20.5
$12-16$	259 ± 27	418 ± 11	9.9
$16-24$	123 ± 21	265 ± 10	6.2

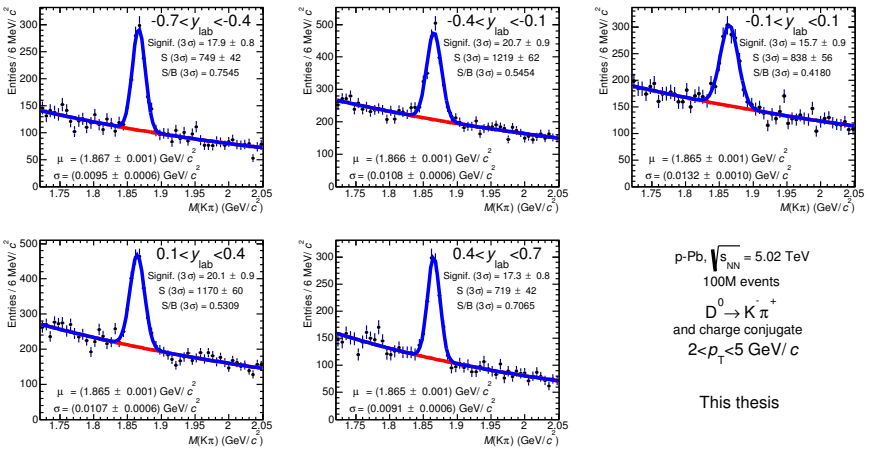

FIGURE 5.8: Distributions of the invariant mass of D^0 candidates in p–Pb collisions in five rapidity intervals for $2 < p_{\mathrm{T}} < 5$ GeV/c.

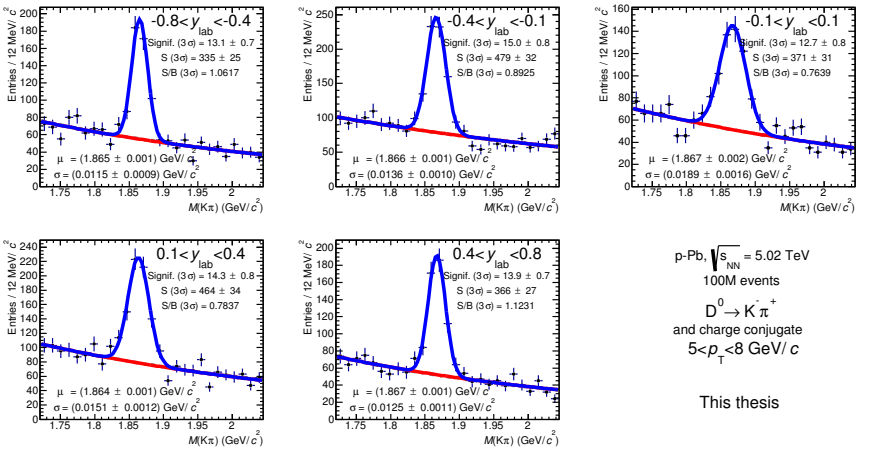

FIGURE 5.9: Distributions of the invariant mass of D^0 candidates in p–Pb collisions in five rapidity intervals for $5 < p_{\mathrm{T}} < 8$ GeV/c.

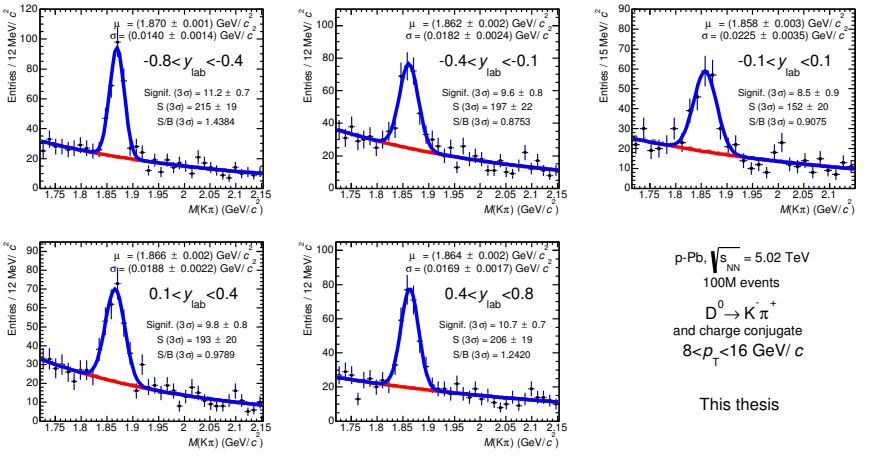

FIGURE 5.10: Distributions of the invariant mass of D^0 candidates in p–Pb collisions in five rapidity intervals for $8 < p_{\mathrm{T}} < 16$ GeV/c.

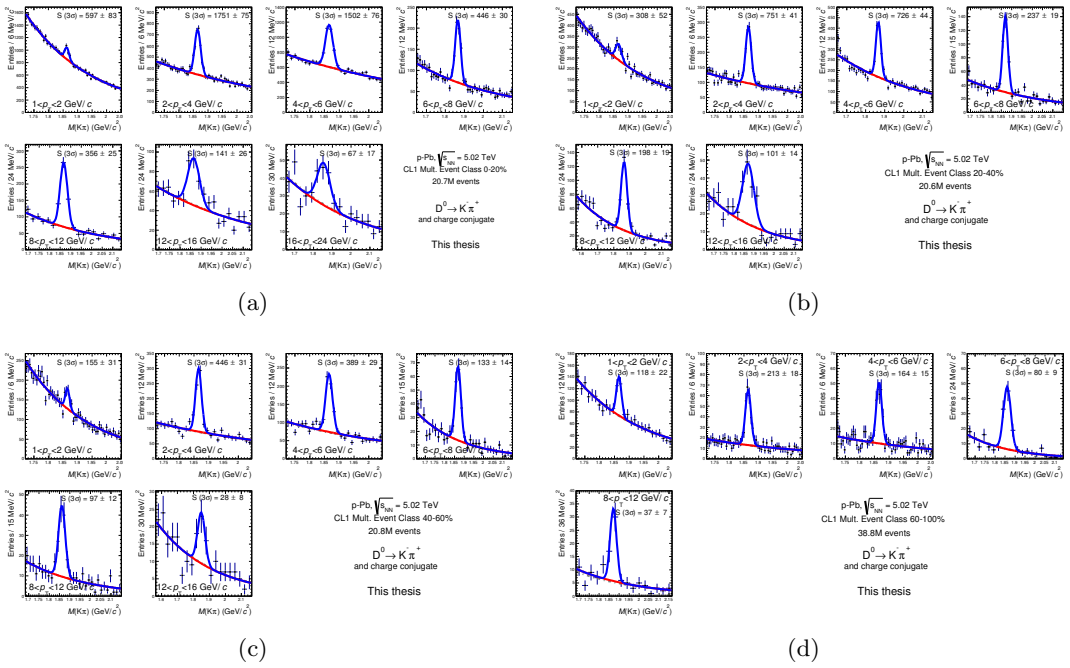

FIGURE 5.11: D^0 invariant mass distributions for 0–20% (a), 20–40% (b), 40–60% (c), and 60–100% (d) event-activity classes defined with the CL1 estimator.

Invariant Mass Distributions in Event-Activity Classes

The multiplicity dependence of the D^0 production was investigated with two different methods, as explained in Section 4.2.

The Q_{pPb} measurement was performed in four event-activity classes determined with the three different estimators introduced in Section 4.2.2, as percentiles of the total cross section: 0–20%, 20–40%, 40–60%, and 60–100%. The first three classes contain about 20×10^6 events each, while in 60–100% about 40×10^6 were analyzed. The invariant mass distributions are shown in Figures 5.11, 5.12, and 5.13 for the CL1, V0A and ZNA estimators, respectively. Only the p_{T} intervals where the signal significance is larger than 3 are shown.

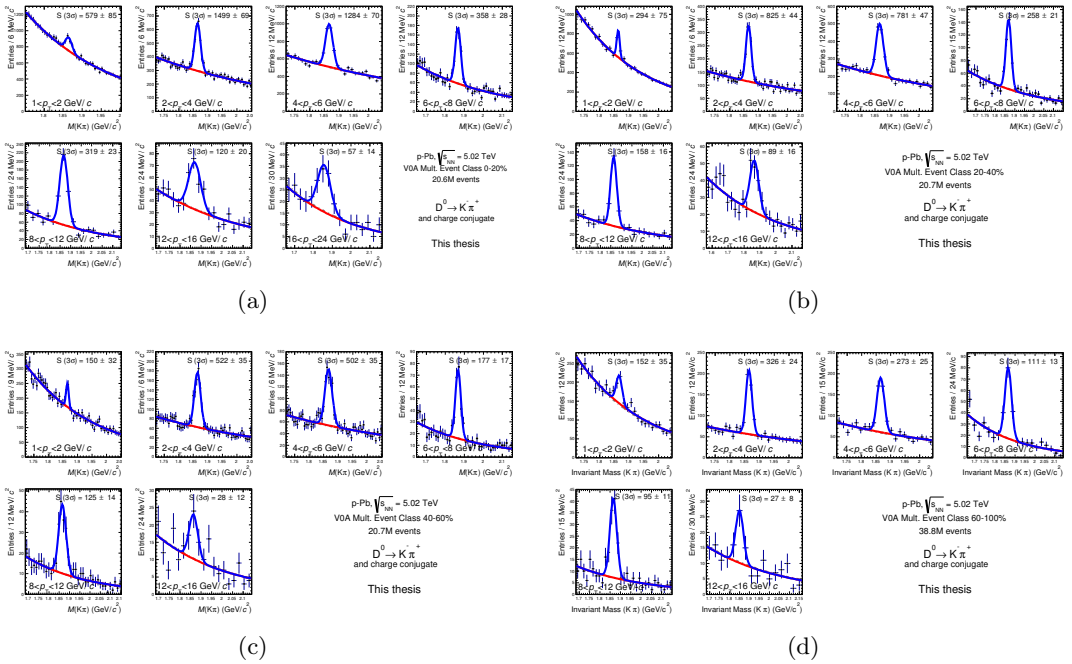

FIGURE 5.12: D^0 invariant mass distributions for 0–20% (a), 20–40% (b), 40–60% (c), and 60–100% (d) event-activity classes defined with the V0A estimator.

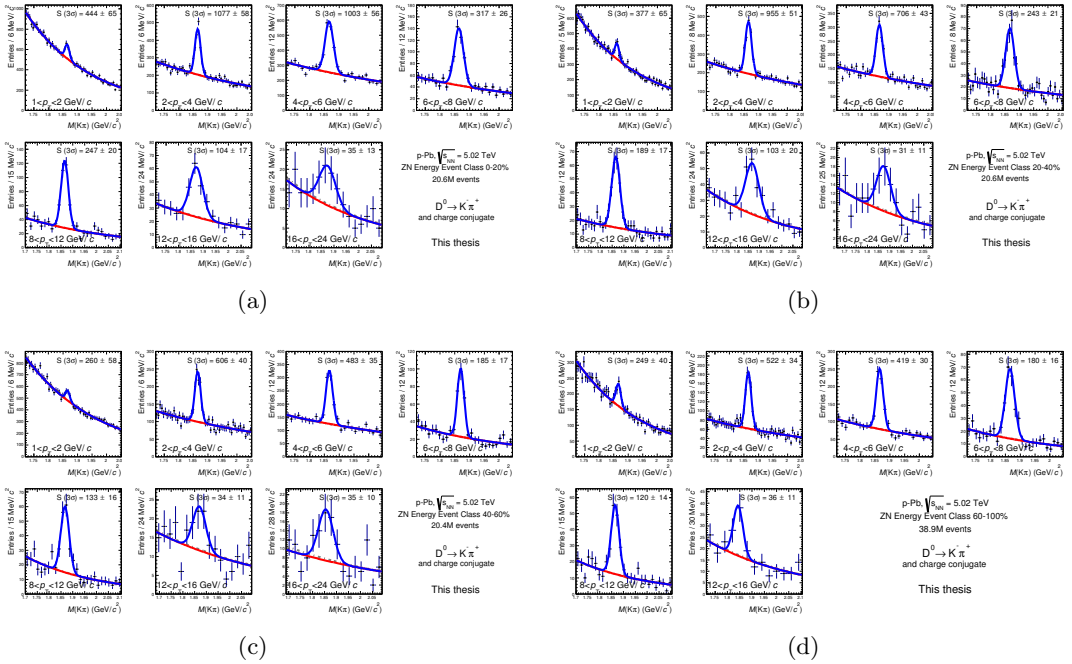

FIGURE 5.13: D^0 invariant mass distributions for 0–20% (a), 20–40% (b), 40–60% (c), and 60–100% (d) event-activity classes defined with the ZNA estimator.

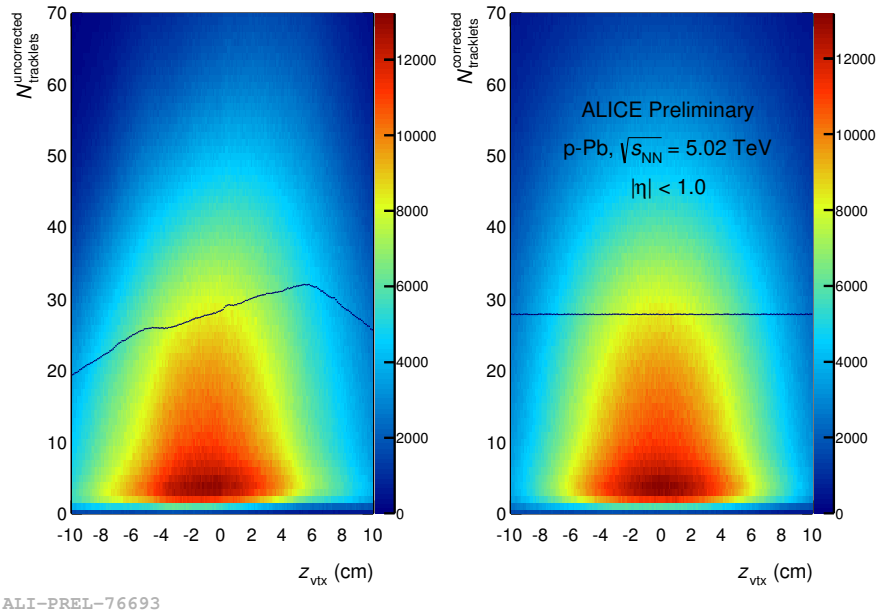

FIGURE 5.14: z_{vtx} distributions of multiplicity estimated with $N_{\text{tracklets}}$ in $|\eta| < 1$. In the left panel is reported the raw distribution which demonstrates the variation of the SPD acceptance with time and z_{vtx}. In the right panel the corrected distribution is shown.

Invariant Mass Distributions in Multiplicity Intervals

The second observable used to investigate the multiplicity dependence of the D^0 production (Section 4.2.3) requires the extraction of the raw yields in charged-particle multiplicity intervals. The number of tracklets in $|\eta| < 1.0$ measured with the SPD detector was used to define the multiplicity intervals. The pseudorapidity acceptance of the SPD depends on the position of the interaction vertex along the beam line, z_{vtx}. In addition, it varied during the data taking due to the variation of the number of inactive channels. The detector response was equalized by means of a data-driven correction, which was applied on an event-by-event basis depending on z_{vtx} and time. The variation of the SPD acceptance as a function of z_{vtx} can be verified with the two-dimensional distribution of the number of tracklets ($N_{\text{tracklets}}$) as a function of the position of the primary vertex along the z direction, shown in Figure 5.14. The profile of the distribution, defined as the mean $N_{\text{tracklets}}$ as a function of z_{vtx}, is shown as a black line. The raw profile, shown in the left panel, was applied event-by-event, in order to correct the multiplicity distribution. The formula used for the correction was:

$$N_{\text{tracklets}}^{\text{corrected}}(z_{\text{vtx}}) = \frac{\langle N_{\text{tracklets}}^{\text{ref}} \rangle}{\langle N_{\text{tracklets}}^{\text{uncorrected}}(z_{\text{vtx}}) \rangle} \cdot N_{\text{tracklets}}^{\text{uncorrected}}(z_{\text{vtx}}) \,, \tag{5.2}$$

where $\langle N_{\text{tracklets}}^{\text{ref}} \rangle$ is the mean number of tracklets in a given z_{vtx} interval chosen as reference. $N_{\text{tracklets}}^{\text{uncorrected}}(z_{\text{vtx}})$ is the number of tracklets for events with vertex at a given value

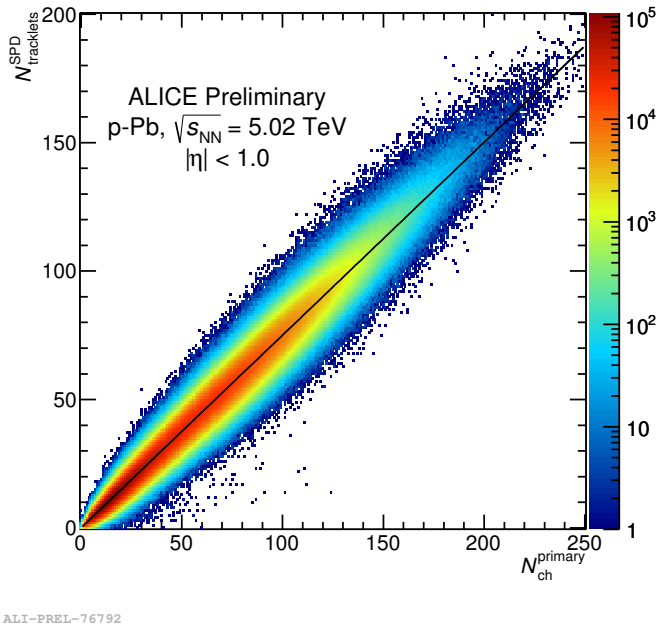

FIGURE 5.15: SPD $N_{\text{tracklets}}$ multiplicity as a function of the primary charged-particle multiplicity in Monte Carlo simulations. The black line indicates the profile of the distribution: linear proportionality was found with a factor of 0.75.

of z for the data taking period under consideration, and $\langle N_{\text{tracklets}}^{\text{uncorrected}}(z_{\text{vtx}})\rangle$ its mean value. In the correction procedure, the Poisson statistics is employed to get an integer value for $N_{\text{tracklets}}^{\text{corrected}}(z_{\text{vtx}})$ starting from the value of $(\langle N_{\text{tracklets}}^{\text{ref}}\rangle / \langle N_{\text{tracklets}}^{\text{uncorrected}}(z_{\text{vtx}})\rangle) \cdot N_{\text{tracklets}}^{\text{uncorrected}}(z_{\text{vtx}})$. The resulting $N_{\text{tracklets}}^{\text{corrected}}$ distribution, reported in the right panel of Figure 5.14, is uniform in z_{vtx}, with an average $N_{\text{tracklets}}^{\text{ref}}$ value being set at the predetermined reference multiplicity.

The multiplicity intervals were defined on the basis of the corrected $N_{\text{tracklets}}$ distributions and then converted to intervals of relative charged-particle multiplicity, $(\mathrm{d}N_{\text{ch}}/\mathrm{d}\eta)/\langle \mathrm{d}N_{\text{ch}}/\mathrm{d}\eta\rangle$. The conversion was done exploiting the proportionality of the number of reconstructed tracklets to the generated charged primary particles $N_{\text{ch}}^{\text{primary}}$ observed in the simulations for $|\eta| < 1.0$. It was found that there is a linear relation between $N_{\text{tracklets}}$ and $N_{\text{ch}}^{\text{primary}}$, with a factor of proportionality $(N_{\text{tracklets}}/N_{\text{ch}}^{\text{primary}}) = 0.75$ (Figure 5.15). The $N_{\text{tracklets}}$ values were divided by the proportionality factor to convert to $N_{\text{ch}}^{\text{primary}}$, and then by a further factor of two (the width of the pseudorapidity range studied) to give $\mathrm{d}N_{\text{ch}}/\mathrm{d}\eta$. The average pseudorapidity density of charged particles in the considered range, $\langle \mathrm{d}N_{\text{ch}}/\mathrm{d}\eta\rangle$, used to obtain the relative multiplicity in each $N_{\text{tracklets}}$ interval, is 17.64 ± 0.01 (stat.) $\pm$ 0.15 (syst.), as measured in inelastic p–Pb collisions producing at least one charged particle in $|\eta| < 1$ [109, 110]. The considered $N_{\text{tracklets}}$ intervals and the corresponding relative charged-particle multiplicity ranges are summarized in Table 5.5.

TABLE 5.5: Description of the considered intervals as defined by the number of reconstructed tracklets $N_{\text{tracklets}}$, the average charged-particle multiplicity $\langle \mathrm{d}N_{\text{ch}}/\mathrm{d}\eta \rangle$, and the relative charged-particle multiplicity $\mathrm{d}N_{\text{ch}}/\mathrm{d}\eta / \langle \mathrm{d}N_{\text{ch}}/\mathrm{d}\eta \rangle$. The number of events analyzed in the various multiplicity ranges are reported.

$N^i_{\text{tracklets}}$	$\langle N_{\text{tracklets}} \rangle^i$	$\left(\frac{\mathrm{d}N_{\text{ch}}}{\mathrm{d}\eta}\right)^i$	$\left\langle \frac{\mathrm{d}N_{\text{ch}}}{\mathrm{d}\eta} \right\rangle^i$	$\frac{(\mathrm{d}N_{\text{ch}}/\mathrm{d}\eta)^i}{\langle \mathrm{d}N_{\text{ch}}/\mathrm{d}\eta \rangle}$	$\left\langle \frac{(\mathrm{d}N_{\text{ch}}/\mathrm{d}\eta)^i}{\langle \mathrm{d}N_{\text{ch}}/\mathrm{d}\eta \rangle} \right\rangle$	$N_{\text{events}}/10^6$
$[1, 24]$	12.11	$0.7 - 16.4$	8.09	$0.04 - 0.93$	0.46	51.86
$[25, 44]$	33.58	$16.4 - 29.7$	22.43	$0.93 - 1.69$	1.27	28.35
$[45, 59]$	51.17	$29.7 - 39.8$	34.19	$1.69 - 2.25$	1.94	11.32
$[60, 74]$	65.95	$39.8 - 49.8$	44.07	$2.25 - 2.82$	2.50	5.32
$[75, 99]$	83.54	$49.8 - 66.5$	55.82	$2.82 - 3.77$	3.16	2.67
$[100, 199]$	110.75	$66.5 - 133.0$	74.00	$3.77 - 7.54$	4.20	0.45

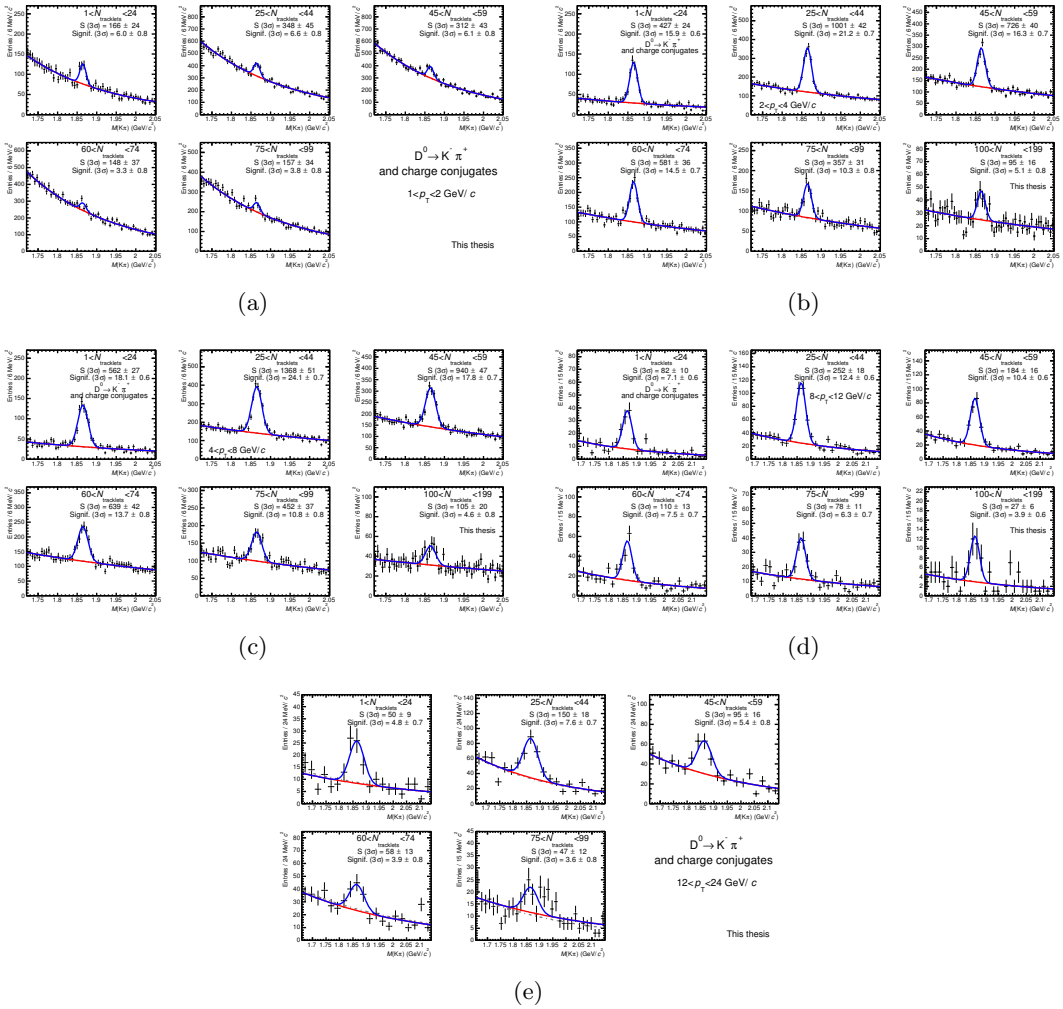

FIGURE 5.16: D^0 invariant mass distributions as a function $N_{\text{tracklets}}$ for the five p_{T} intervals considered for the analysis.

The D^0 meson yields were extracted in each multiplicity interval for several p_{T} intervals. The invariant mass distributions are shown in Figure 5.16.

The raw yields were also extracted as a function of the multiplicity at forward

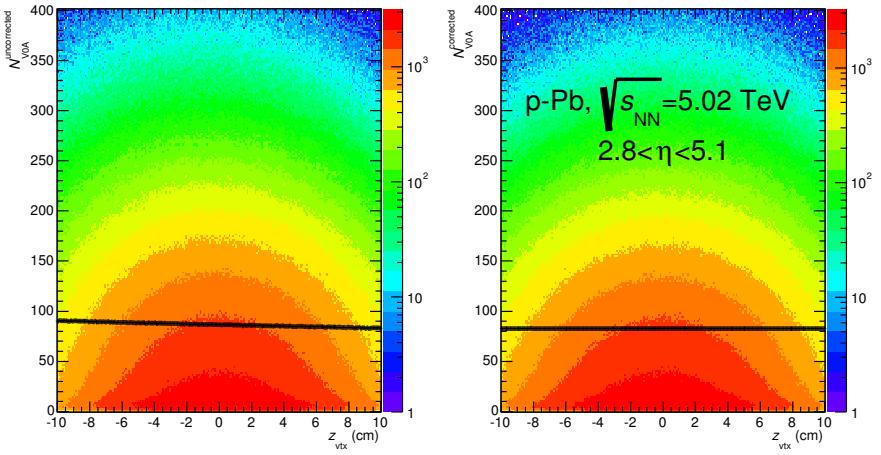

FIGURE 5.17: $z_{\rm vtx}$ distributions of multiplicity estimated with $N_{\rm V0A}$ in $2.7 < \eta < 5.1$. In the left panel is reported the raw distribution which demonstrates the variation of the VZERO-A acceptance with time and $z_{\rm vtx}$. In the right panel the corrected distribution is shown.

TABLE 5.6: Description of the considered intervals defined by $N_{\rm V0A}$ estimator. The number of events analyzed in the various multiplicity ranges are reported.

$N^i_{\rm V0A}$	$\langle N_{\rm V0A}\rangle^i$	$\frac{\langle N_{\rm V0A}\rangle^i}{\langle N_{\rm V0A}\rangle}$	$N_{\rm events}/10^6$
$[1, 90]$	39.96	0.48	58.46
$[91, 131]$	109.48	1.32	15.28
$[132, 172]$	150.04	1.81	10.04
$[173, 225]$	195.51	2.36	7.11
$[226, 798]$	272.53	3.29	4.88
$[173, 797]$	225.33	2.72	11.99

rapidity ($2.7 < \eta < 5.1$). The intervals were defined in terms of the $N_{\rm V0A}$ estimator defined in Section 4.2.3. The detector response was equalized as a function of $z_{\rm vtx}$ and time applying the same data-driven procedure used for the $N_{\rm tracklets}$ estimator. Figure 5.17 shows the two-dimensional distributions and the profile distributions of $N_{\rm V0A}$ as a function of $z_{\rm vtx}$ before and after the equalization. Table 5.6 summarizes the $N_{\rm V0A}$ intervals considered for the analysis.

The $\rm D^0$ meson yields were extracted in each $N_{\rm V0A}$ interval for several $p_{\rm T}$ intervals. The invariant mass distributions are shown in Figure 5.18.

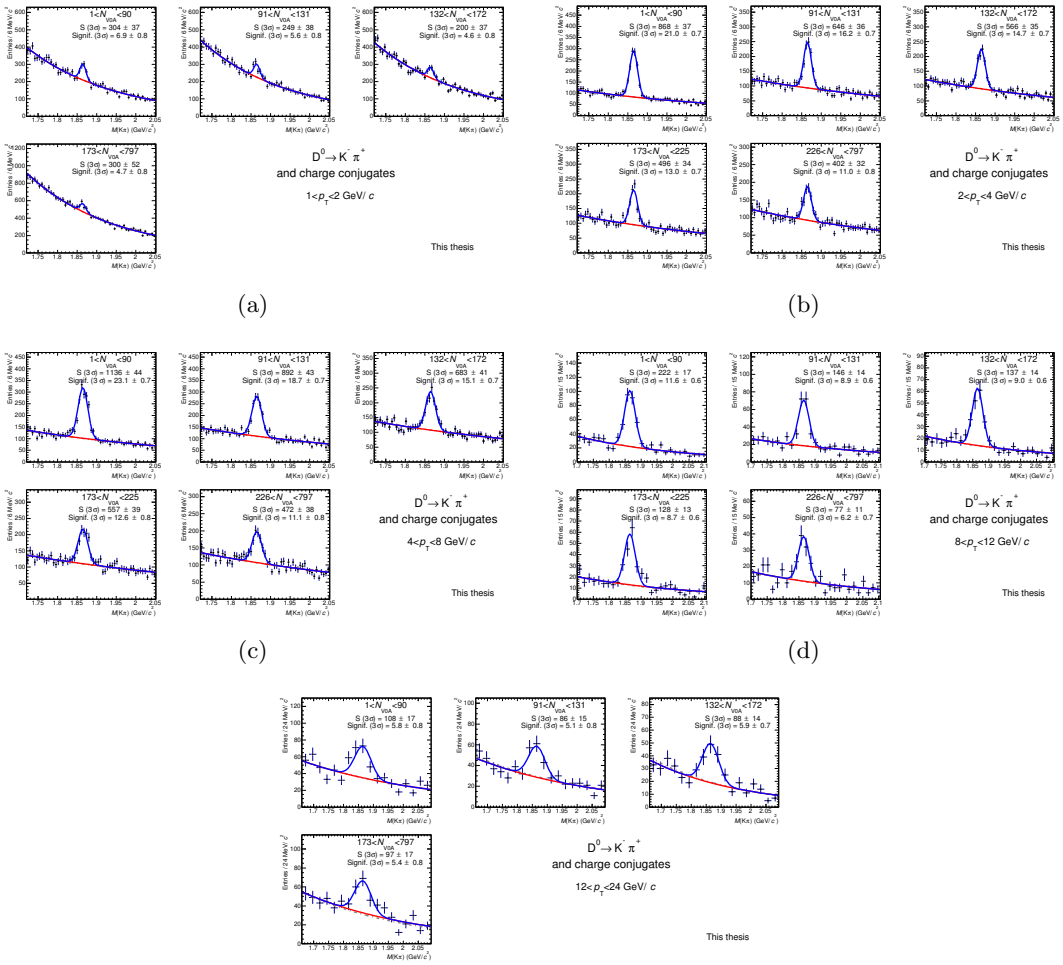

FIGURE 5.18: D^0 invariant mass distributions as a function N_{V0A} for the five p_{T} intervals considered for the analysis.

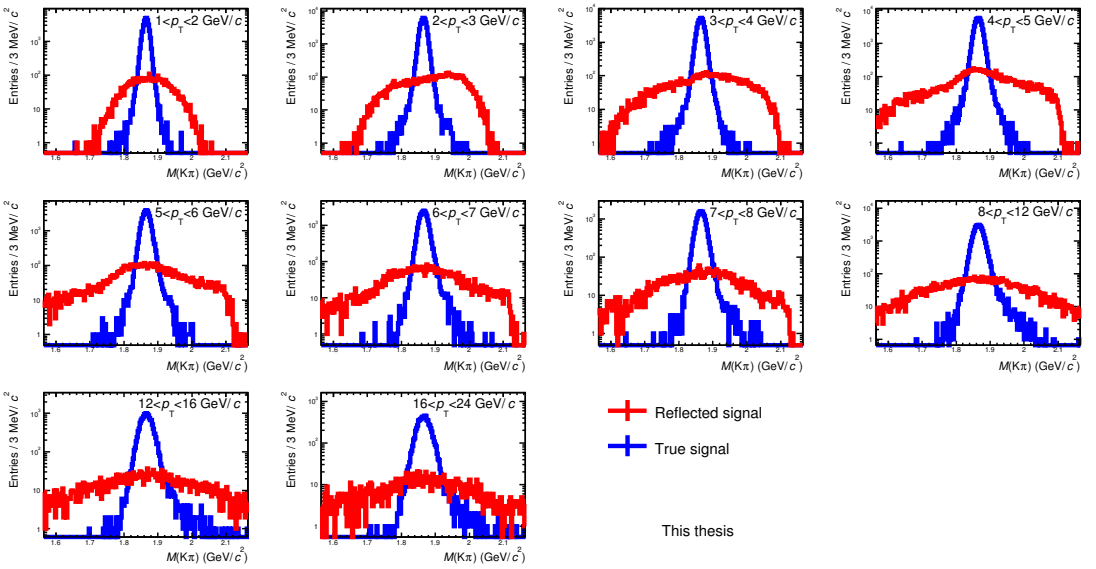

FIGURE 5.19: Invariant mass distributions of the simulated true and reflected signal in p–Pb collisions.

5.5 Study of the "Reflected" Signal

The invariant mass distributions were obtained including the candidates that pass the selections as $\mathrm{D}^0 \to \mathrm{K}^-\pi^+$ or as $\overline{\mathrm{D}^0} \to \mathrm{K}^+\pi^-$. The candidates were also kept if compatible with both decays. In the case of signal (a true D^0 decay), one of the two combinations, e.g. $\mathrm{K}^-\pi^+$ and $\pi^-\mathrm{K}^+$, enters with the wrong mass hypothesis assignment for the decay tracks and it is called "signal reflection". The invariant mass distribution of reflections has a centroid close to the D^0 mass and a typical r.m.s. value of about 100 MeV/c^2, as observed from the simulation (see Figure 5.19). In data, the case with the wrong mass hypothesis can not be distinguished from the correct one, and the reflection contribution can modify the background shape and affect the signal extraction enlarging the width of the Gaussian peak. Particle identification limits the probability that a true $\mathrm{K}^-\pi^+$ can be also compatible with the $\pi^-\mathrm{K}^+$ mass hypothesis, but a residual reflection contribution is expected due to the conservative PID selection applied and to the partial superposition of the kaon and pion TPC bands in the low p_{T} region of the analysis.

An example of the p–Pb simulated reflection invariant mass distributions is shown in Figure 5.20 for three different PID strategies. The amount of reflections is largest when PID is not applied (green line). If the PID selection is extended to all tracks, requiring the compatibility of the TOF and TPC signal with expectation for kaons and pions within 3σ (blue line), the reflections are suppressed (Pb–Pb R_{AA} azimuthal dependence and p–Pb analysis). If the TPC and TOF compatibility is required only for tracks with

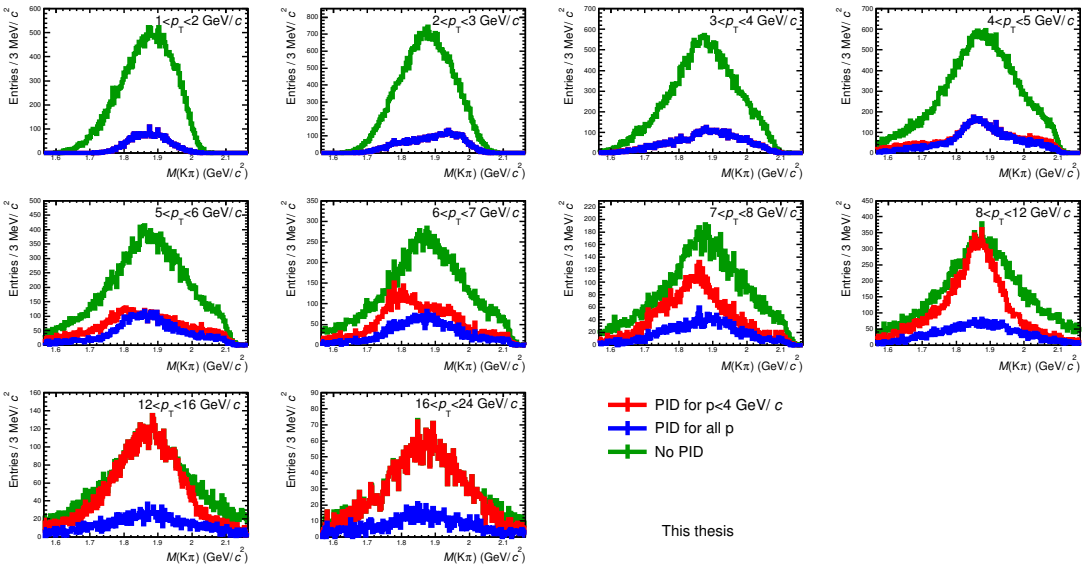

FIGURE 5.20: Invariant mass distributions of the simulated reflections in p–Pb collisions. The distributions are reported for three different PID selections: PID not applied (green lines), PID applied only for tracks with momentum $p < 4$ GeV/c (red lines), and PID applied for all the tracks (blue lines).

momentum $p < 4$ GeV/c (red line), the reflection distributions tend to the no PID case as the $p_{\rm T}$ of the $\rm D^0$ increases (v_2 analysis).

The effect of the reflected signal candidates on the signal extraction was studied quantitatively in each $p_{\rm T}$ interval considered for the Pb–Pb and p–Pb analysis with two different methods. Both methods provide an estimate of the so called R-factor, which allows to estimate the relative bias, due to reflections, of the signal extracted from the fit of the invariant mass distributions if no special treatment for reflections is applied, and it is defined as:

$$R(p_{\rm T}) = \frac{S_{\rm true}(p_{\rm T}) - S_{\rm fit}(p_{\rm T})}{S_{\rm true}(p_{\rm T})}\,. \tag{5.3}$$

The first method is based on a Monte Carlo procedure from which the R-factor is obtained for each $p_{\rm T}$ interval by the comparison of the "true" signal and the signal extracted when reflections are included in the invariant mass distribution. An "artificial" invariant mass distribution was built for each $p_{\rm T}$ interval as the sum of background, signal, and reflections invariant mass distributions. The background distributions were parametrized by the fit functions obtained from data invariant mass distributions, while the signal and reflection distributions were obtained from the simulation. The signal distributions were normalized to the yields measured in data. The reflection invariant mass distributions were normalized to the signal yields extracted from data multiplied by the ratio of the integrals of the simulated distributions of reflections and true signal. Poissonian smearings were applied independently for background, signal and reflection

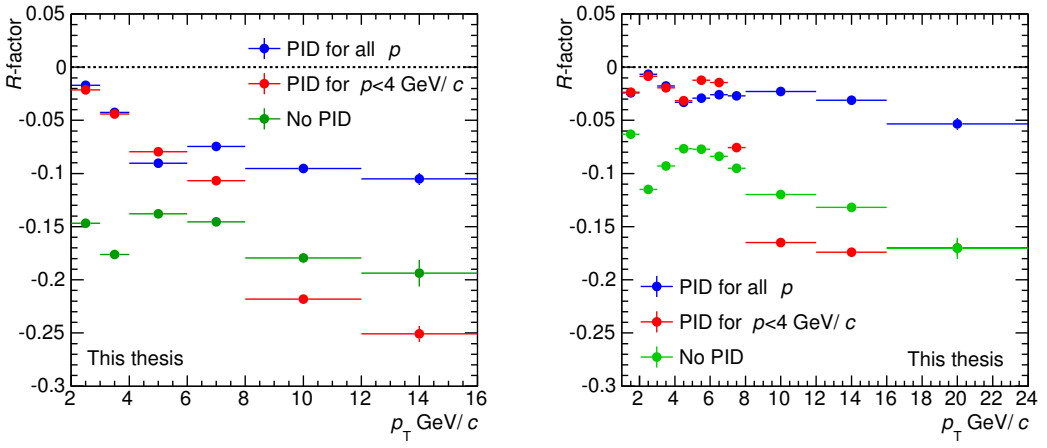

FIGURE 5.21: R-factor as a function of D^0 p_T obtained with Monte Carlo method for Pb–Pb collisions in the 30–50% centrality class (a) and for minimum-bias p–Pb collisions (b) for three PID strategies: TPC and TOF 3σ compatibility band for all tracks (blue points), for tracks with $p < 4$ GeV/c (red points), and PID selection not applied.

distributions in each bin of the invariant mass distributions to simulate statistical fluctuations. The signal yields were extracted applying the same fit procedure used in data and compared with true signal injected in the invariant mass distribution. The procedure was iterated 1000 times. The mean of the distribution of $(S_{\rm true} - S_{\rm fit})/S_{\rm true}$ estimates the R-factor. The obtained R-factors as a function of p_T in Pb–Pb and p–Pb collisions are shown in Figure 5.21 for three PID strategies. In Pb–Pb (left panel) if PID selection is not applied (green points) the signal bias is of about 15–20% for all p_T intervals, while if the PID is applied to all the tracks the bias is within 5% up to $p_T = 4$ GeV/c and of about 10% from 4 to 16 GeV/c (blue points). If the PID selection is applied only for tracks with $p < 4$ GeV/c (red points), the bias is similar to the case with PID for all tracks at low p_T, while it increases starting from $p_T = 6$ GeV/c, reaching 25% at high p_T. In p–Pb (Figure 5.21(b)), a similar behaviour is observed for the three PID strategies, but the bias stays within 5% if the PID is applied to all tracks, while reaches at most 17% at high p_T if PID is not used or an upper momentum cut is introduced in the PID selection. The signal bias is minimum if PID is applied for all the tracks (blue points); the residual bias is smaller in p–Pb than in Pb–Pb due to the better separation of the kaon and pion signals in the TPC in p–Pb. The method was validated by computing the R-factors without adding the reflection contributions to the invariant mass distributions: the obtained values were compatible with zero within the uncertainties.

With the second method the R-factor was estimated directly from the data invariant mass distributions. A template of the distribution of reflected signal candidates, which was obtained from the simulation for each p_T interval, was included in the invariant

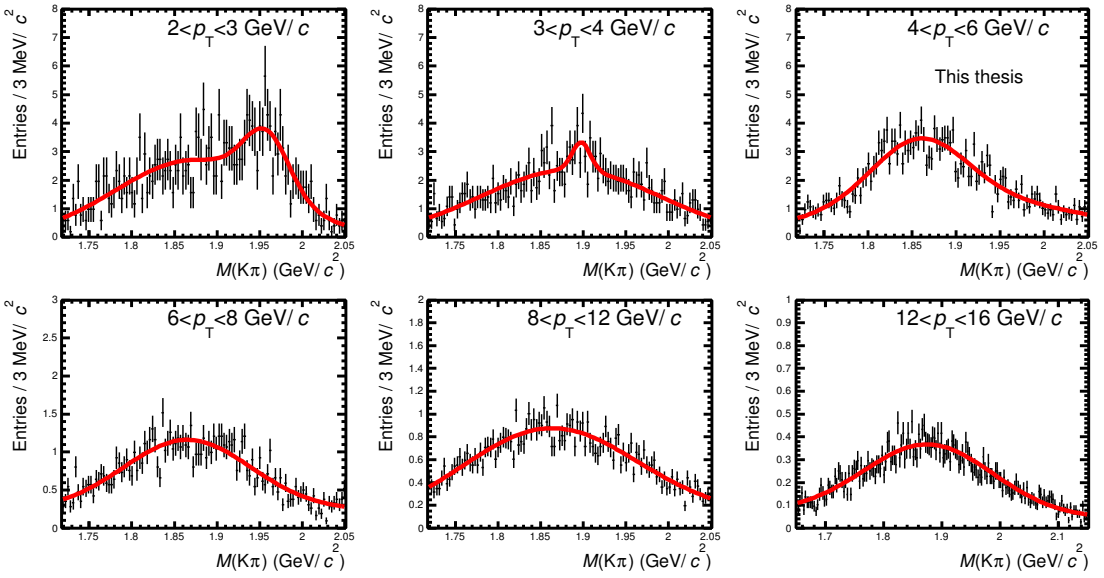

FIGURE 5.22: Double gaussian fit to the simulated invariant mass distributions of reflections in Pb–Pb collisions in the 30–50% centrality class. The obtained fit functions (red lines) were included as templates of the reflected signal in the invariant mass fit procedure on data.

mass fit procedure. The signal extracted from the fit including the reflection template is assumed to be the true signal, to be compared with the "biased" signal that is extracted from the fit without template.

The templates were obtained by parametrizing the reflection distributions from the simulation with the sum of two Gaussians (see Figure 5.22). In the fit with the template, the ratio of the integrals of the total distribution of reflections and of the Gaussian used for the signal were fixed to the value obtained from the simulation. Figure 5.23 shows an example of the fits without (a) and with (b) template for the interval 4–6 GeV/c in Pb–Pb collisions in the centrality class 30–50% [111]. The bias of the raw signal obtained including the template in the fit is shown in Figure 5.24 for the two collisions systems. The bias obtained with the template method was in good agreement with the result provided through the simulated invariant mass distribution, both for Pb–Pb and p–Pb (see Figure 5.24).

For the v_2 analysis, the PID selection was used only for tracks with $p < 4$ GeV/c. Since the contribution of the reflections does not depend on the angle relative to the event plane, it is not necessary to apply a correction for v_2. For the $R_{\rm AA}$ analysis, the reflections bias in the raw signal needs to be taken into account. In order to minimize the correction, the PID selection was extended to tracks with $p > 4$ GeV/c. The correction factor $c_{\rm refl}$, introduced in Equation (4.8), was determined as the ratio of the signal yield from the fit including the reflections template and the signal yield from the

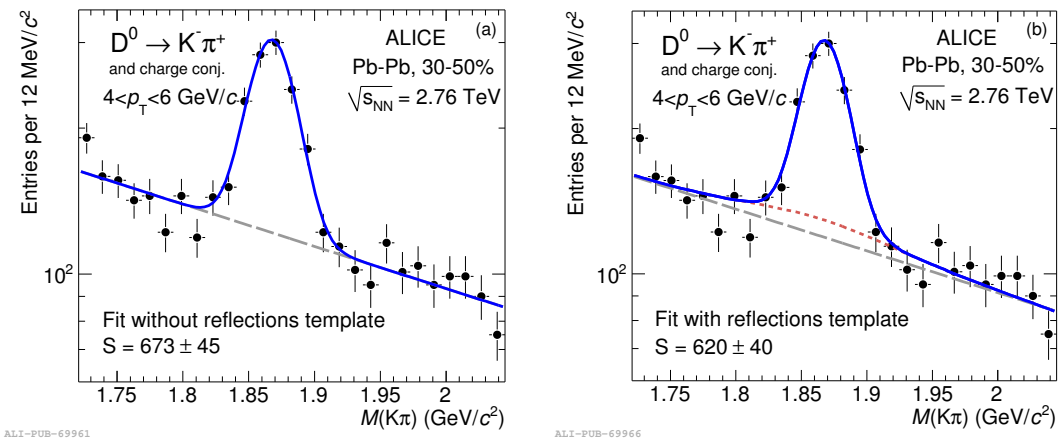

(a) (b)

FIGURE 5.23: Invariant mass distribution of D^0 candidates with $4 < p_T < 6$ GeV/c in Pb–Pb collisions in the centrality class 30–50%: (a) fit without template for reflections and (b) with template for reflections (dotted lines). The raw yield obtained as integral of the signal Gaussian is reported [111].

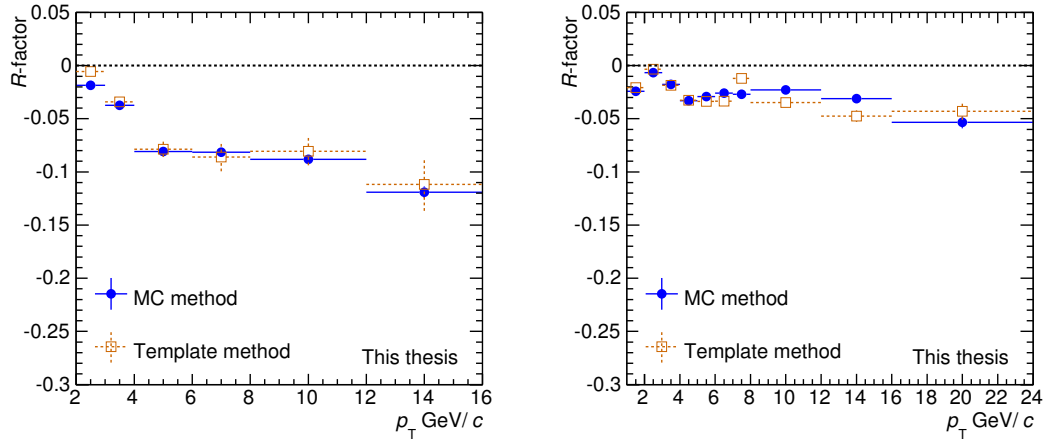

(a) (b)

FIGURE 5.24: R-factor as a function of D^0 p_T obtained with Monte Carlo (blue) and template fit (orange) methods for Pb–Pb collisions in the 30–50% centrality class (a) and for minimum-bias p–Pb collisions (b). The comparison is shown for the case with PID selection applied for all momenta.

fit without the template. It was computed using the sum of the in-plane and out-of-plane invariant mass distributions, in order to have a more precise value, and it was multiplied to both the in-plane and out-of-plane yields extracted with the fit procedure described in Section 5.4. The numerical value of c_{refl} ranges from 0.98 in the interval $2 < p_T < 3$ GeV/c to 0.90 in the interval $4 < p_T < 16$ GeV/c.

For the p–Pb analysis the PID selection was applied also for tracks with $p > 4$ GeV/c, and given the small values of the resulting R-factor (maximum of 4% at high p_T), the

signal yields were not corrected for reflections, but the bias was taken into account as an additional source of systematic uncertainty in the yield extraction (see Chapter 6).

The estimate of the bias due to reflected signal candidates was performed also for the pp 2010 data sample. The D meson production cross section measured with this data sample is used to obtain the $R_{\rm AA}$ and $R_{\rm pPb}$ pp reference (Section 4.3). The measurement of the D meson cross section in pp at $\sqrt{s} = 7$ TeV was performed applying the PID selection up to high momenta of the tracks, and the signal bias induced by reflections was estimated to be within 5% in all $p_{\rm T}$ intervals, thus smaller than the systematic uncertainties due to the extraction of the yields from the fit. When the nuclear modification factor is computed the residual bias that is present in the p–Pb yields partially cancels in the ratio with the pp references.

5.6 Efficiency Corrections

The raw yield extracted from the invariant mass analysis $N^{\rm D^0}_{\rm raw}(p_{\rm T})$ is only a fraction of the total number of $\rm D^0$ produced in the collisions. $\rm D^0$ may not be reconstructed for different reasons, such as the limited detector acceptance, vertex and track reconstruction inefficiencies, and selection cuts on the candidates. The total yield is derived through the correction for the reconstruction and selection efficiency using Monte Carlo simulations.

The generated $\rm D^0 \to K^-\pi^+$ decays are propagated along the simulation, reconstruction and analysis chain. The two latter steps are exactly the same as for data.

The efficiency correction (Acc $\times$ ϵ), introduced in Equations (4.8) and (4.12), is calculated as the ratio of the number of $\rm D^0$ mesons after the reconstruction and selection to the number of generated $\rm D^0$ for which all decay products are in the fiducial acceptance region, $|y| < y_{\rm fid}(p_{\rm T})$.

Since charm production has low cross section, in the Monte Carlo sample used to compute the efficiencies, the charm production is enhanced and D mesons are forced to decay in the channels under study.

The simulations were configured with a detailed description of the ALICE apparatus geometry and detector response. The simulations were tuned to reproduce the position and width of the interaction vertex distribution, the number of active electronic channels and the accuracy of the detector calibration, as well as their time evolution within the Pb–Pb or p–Pb data taking periods. The generated particles were transported through the ALICE detector using GEANT3 [114].

Pb–Pb

The HIJING v1.383 [115] generator was used to simulate Pb–Pb collisions at $\sqrt{s_{\rm NN}} =$ 2.76 TeV, prompt and feed-down $\rm D^0$ meson signals were added using pp events from the

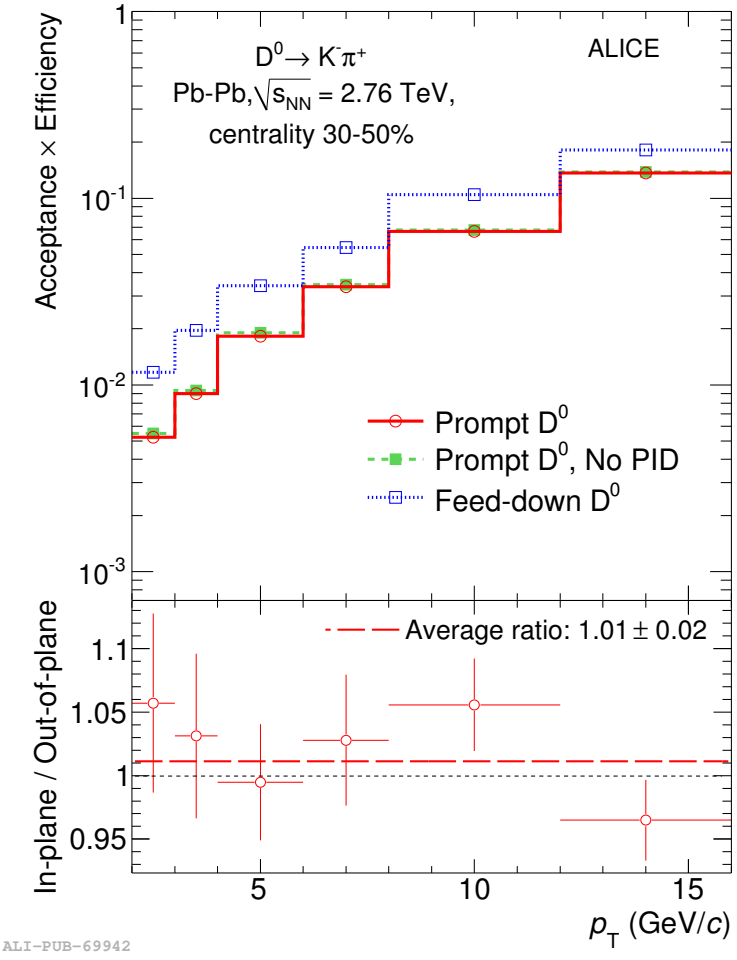

FIGURE 5.25: Product of acceptance and efficiency for D^0 mesons in Pb–Pb collisions for 30–50% centrality class (upper panel). The values for prompt (solid line) and feed-down (dotted line) D^0 mesons are shown. The dashed line stands for the values obtained without PID selection. The lower panel shows the ratio of the efficiencies for prompt D^0 in the in-plane and the out-of-plane regions used for the analysis. The ratio was estimated using simulation samples with a difference in particle multiplicity similar to that observed in data for the two azimuthal regions [111].

PYTHIA v6.4.21 [116] event generator with the Perugia-0 tune [117]. Each simulated pp event contained a $c\bar{c}$ or $b\bar{b}$ pair with a D^0 meson decaying into the $K^-\pi^+$ channel. Out of all the particles produced in these PYTHIA pp events, only the heavy-flavour decay products were kept and transported through the detector simulation together with the particles produced by HIJING.

The efficiencies were evaluated from simulated events that had the same p_T shape and average charged-particle multiplicity, corresponding to the same detector occupancy, as observed in data in the centrality class 30–50%. Figure 5.25 shows (Acc × ϵ) for prompt and feed-down D^0 mesons within the rapidity interval $|y| < y_{\rm fid}$. The magnitude of (Acc × ϵ) increases with p_T, starting from about 1% and reaching about 10–15% at

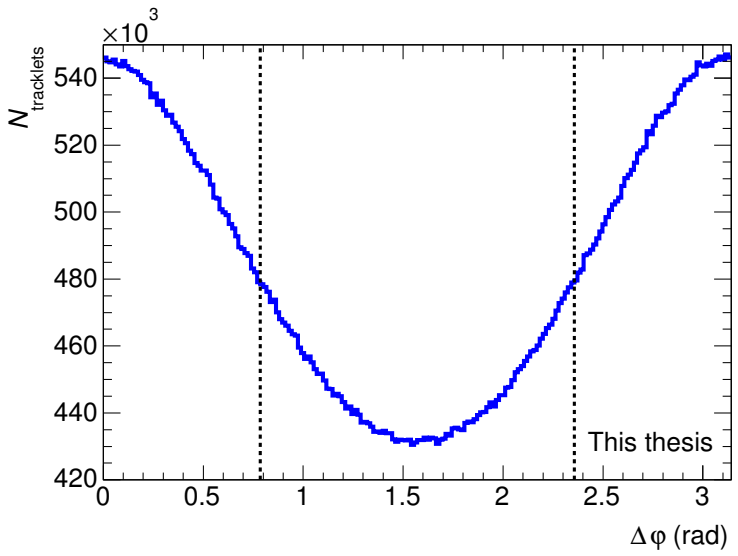

FIGURE 5.26: Distributions of the number of SPD tracklets ($N_{\text{tracklets}}$) in $|\eta| < 1.6$ as a function of $\Delta\varphi$ in 30–50% Pb–Pb collisions. The in-plane and the out-of-plane regions are indicated.

high p_{T}. The values of (Acc $\times$ ϵ) are also shown for the case where the PID selection was not applied. The relative difference with respect to the (Acc $\times$ ϵ) obtained using also the PID selection is about 5%, thus illustrating the high efficiency of the applied PID strategy. The D^0 mesons from B decays have larger (Acc $\times$ ϵ) than prompt D^0's (by a factor of about 1.5), because the decay vertices of the feed-down D mesons are more displaced from the primary vertex and, therefore, more efficiently selected by the topological cuts.

A possible difference in the reconstruction and selection efficiency between in-plane and out-of-plane D^0 mesons was investigated using simulations. The difference could arise from the variation of the particle density, and consequently of the detector occupancy, induced by the azimuthal anisotropy of bulk particle production. The difference in occupancy was estimated in data using the multiplicity of SPD tracklets, which measures the multiplicity of charged particles with $p_{\mathrm{T}} > 50$ MeV/c and $|\eta| < 1.6$, in the two considered azimuthal regions. The SPD tracklet multiplicity in the 30–50% centrality class was found to be larger in-plane than out-of-plane by about 12% (mean variation, see Figure 5.26). In order to study the efficiency variation, two samples of simulated events with 12% difference in average multiplicity were used. The ratio of the efficiencies obtained from these two data sets was found to be consistent with unity (see lower panel of Figure 5.25) and therefore no correction was applied.

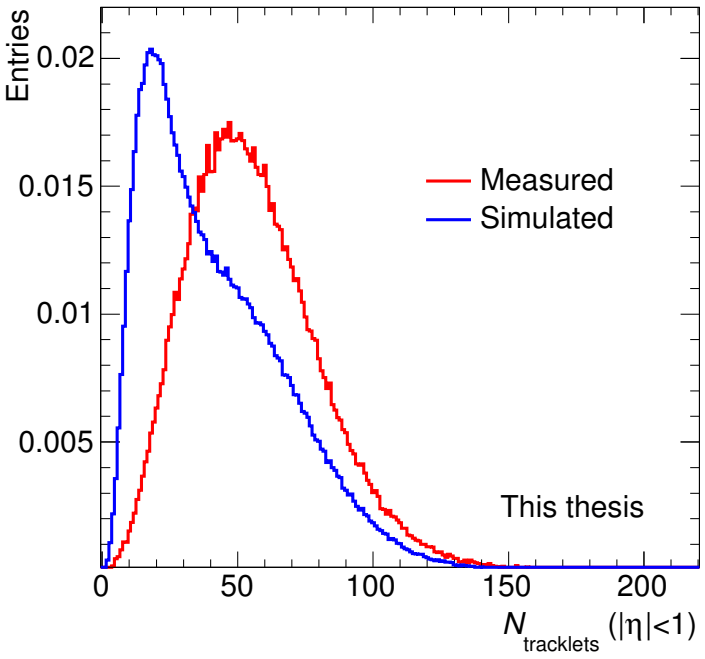

FIGURE 5.27: Distributions of the number of SPD tracklets ($N_{\text{tracklets}}$) in $|\eta| < 1$ obtained from data (red) and from simulation (blue). The two distributions are normalized to their integral.

p–Pb

Proton–lead events were generated starting from a pp PYTHIA event with forced D meson production (as described for the Pb–Pb case). For each event, a N_{coll} value was sampled from a minimum-bias distribution obtained from a Glauber Monte Carlo simulation. If the sampled number of binary collisions was larger than 1, a HIJING (v1.36 version) p–Pb event was added as underlying event.

The generated D meson p_{T} spectrum used to calculate the efficiencies was tuned to reproduce the shape given by FONLL calculations [34–36] at $\sqrt{s} = 5.02$ TeV, by means of a weighting procedure of the generated spectrum. The weight function was obtained from the ratio of the FONLL p_{T} distribution to the generated one.

The efficiency for D meson reconstruction and selection depends also on the multiplicity of particles produced in the collision, mainly because the vertex reconstruction efficiency and the resolution on the primary vertex position depend on the number of tracks used for its evaluation. In particular, the resolution on the primary vertex improves with increasing multiplicity. As a consequence, the resolution of the selection variables that make use of the primary vertex position (track impact parameter, D meson decay length, pointing angle) also improves with increasing multiplicity, inducing a multiplicity dependence in the topological selection efficiency.

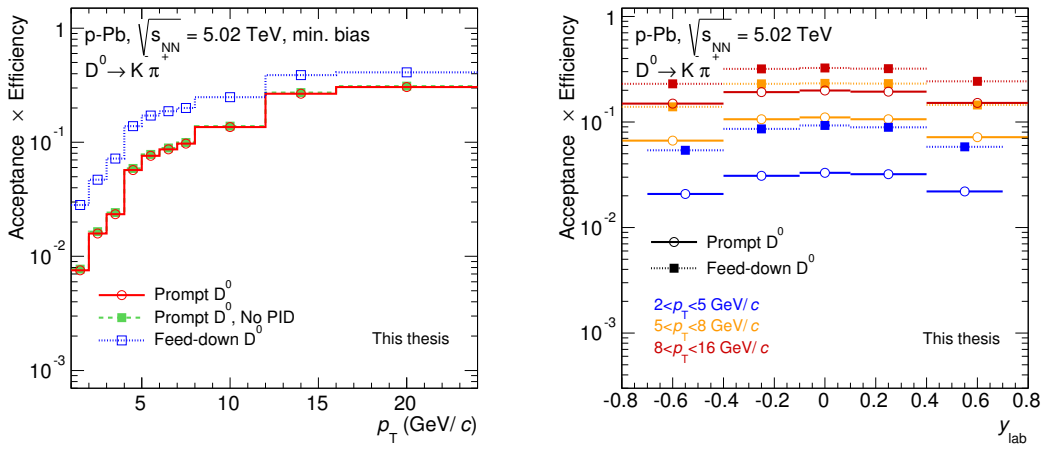

FIGURE 5.28: (a) $D^0 \to K^-\pi^+$ (Acc × ϵ) as a function of p_T for prompt (solid line) and feed-down (dotted line) D^0 in minimum-bias p–Pb collisions at $\sqrt{s_{NN}} = 5.02$ TeV. The values for prompt D^0 mesons obtained without PID selection (dashed line) are also displayed. (b) Product of acceptance and efficiency as a function of rapidity for D^0 mesons in p–Pb collisions. The values of (Acc × ϵ) for prompt (open circles) and feed-down (filled squares) D^0 are shown for three p_T intervals.

The Monte Carlo multiplicity distribution was observed to be different from that of data (see Figure 5.27), therefore the simulated distribution was tuned to reproduce the one measured in minimum-bias p–Pb collisions. The ratio of the distributions of the number of SPD tracklets ($N_{\text{tracklets}}$) obtained from data to that simulated was computed for events containing at least one D^0 candidate with an invariant mass compatible with D^0 mass within 20 MeV/c^2. This ratio was used as a weight function applied to the simulated events in order to reproduce the charged-particle multiplicity observed in data. The $D^0 \to K^-\pi^+$ (Acc × ϵ) for prompt and feed-down D^0 mesons in p–Pb collisions is shown in Figure 5.28 as a function of p_T and rapidity. As observed in the Pb–Pb case, the (Acc × ϵ) increases with transverse momentum of the D^0 because of the larger displacement of the decay vertex of high-p_T candidates due to the Lorentz boost. It varies from about 1% for $1 < p_T < 2$ GeV/c to 40% for $p_T > 12$ GeV/c. Similarly to the Pb–Pb (Acc × ϵ), also in p–Pb the values for feed-down D^0 are larger than for prompt mesons, and the efficiency of the PID selection is of about 95%.

In the simulation it was not possible to select the centrality classes using the same event-activity estimators considered in data because the particles produced at forward rapidities were not transported through the detector. Therefore, a weighting procedure was applied to obtain the (Acc × ϵ) factors in each event class defined with the three estimators considered (Chapter 4). Weight functions were used to reproduce in the simulation the multiplicity distributions measured in data for each event class. The $N_{\text{tracklets}}$ distributions at midrapidity ($|\eta| < 1$) were measured in data for each class

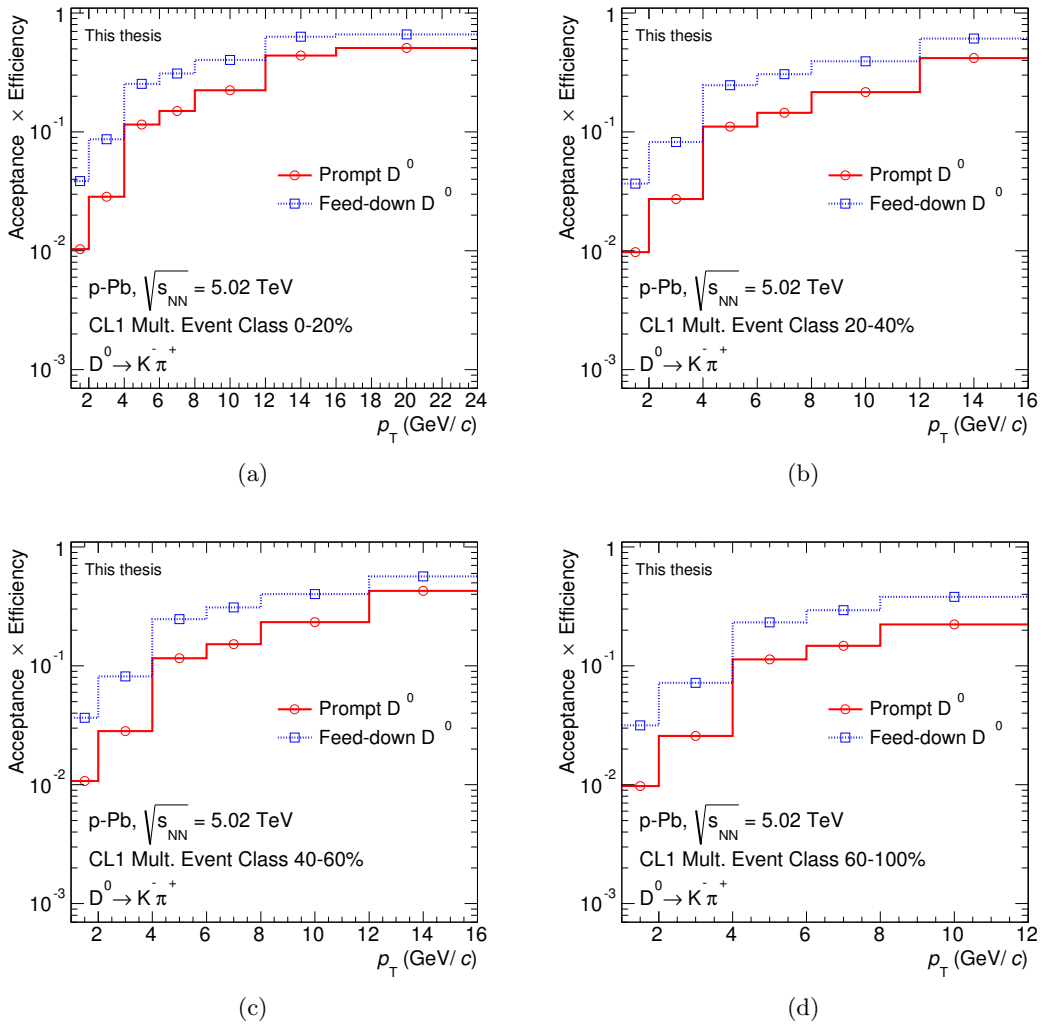

FIGURE 5.29: (Acc × ϵ) as a function of $p_{\rm T}$ for prompt (red) and feed-down (blue) $\rm D^0$ in 0–20% (a), 20–40% (b), 40–60% (c), and 60–100% (d) event-activity classes defined with the CL1 estimator.

(defined with CL1, V0A or ZNA) and divided by the simulated $N_{\rm tracklets}$ distribution to calculate the weights. The (Acc × ϵ) as a function of $p_{\rm T}$ were obtained for a given event-activity class using the relative weight function to tune the simulated multiplicity distribution.

The (Acc × ϵ) values as a function of $p_{\rm T}$ for prompt and feed-down $\rm D^0$ mesons are reported in Figures 5.29, 5.30, and 5.31 for the four event-activity classes defined with the CL1, V0A and ZNA estimators, respectively.

The Monte Carlo sample analyzed to estimate the efficiency correction for the minimum-bias analysis was used also to extract the efficiency factors for the study of the $\rm D^0$ production as a function of charged-particle multiplicity. The efficiencies ϵ^j for the correction of the yields in the different $N_{\rm tracklets}$ intervals were obtained after the weighting of the simulated multiplicity distribution on the basis of that observed in data.

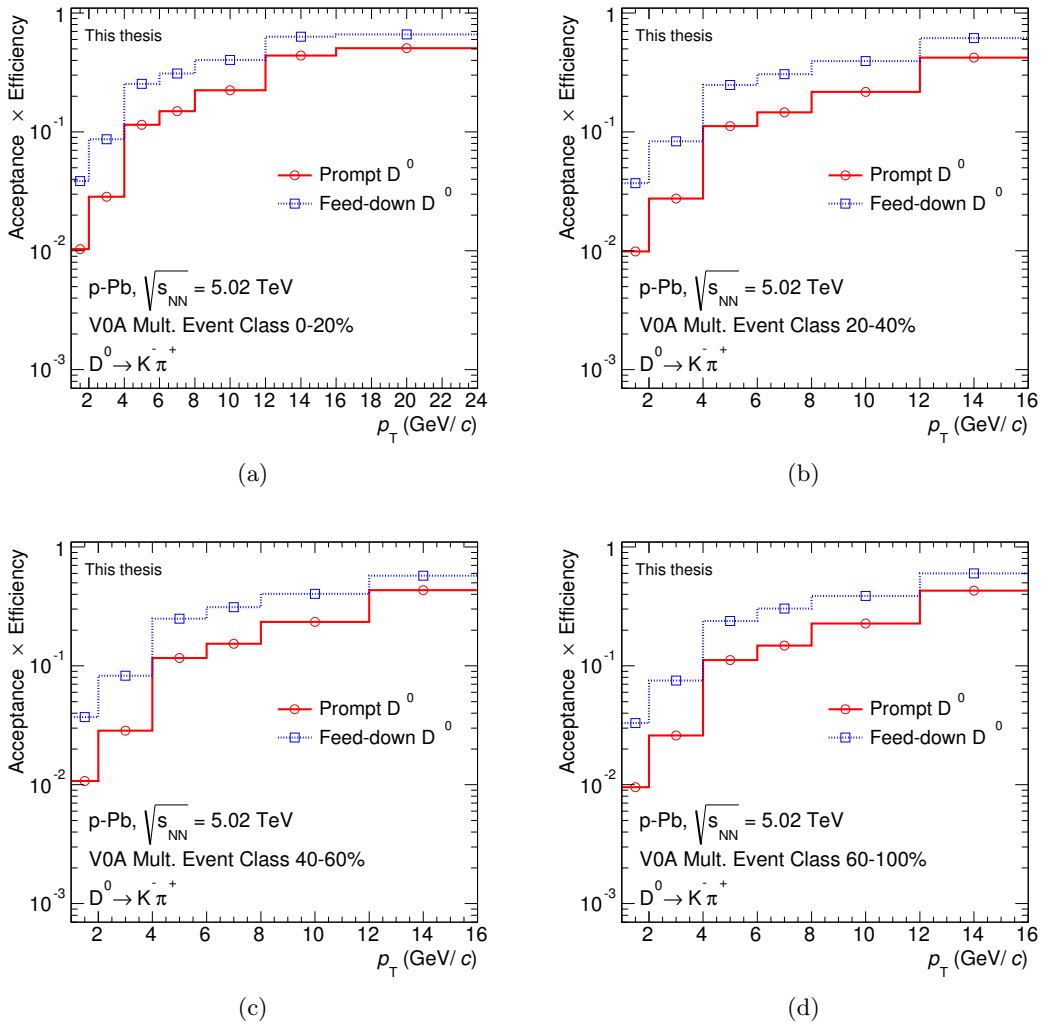

FIGURE 5.30: (Acc × ϵ) as a function of $p_{\rm T}$ for prompt and feed-down $\rm D^0$ in 0–20% (a), 20–40% (b), 40–60% (c), and 60–100% (d) event-activity classes defined with the V0A estimator.

Figure 5.32(a) shows the efficiencies for prompt $\rm D^0$ mesons as a function of $N_{\rm tracklets}$ for the five $p_{\rm T}$ intervals considered for the analysis. The values of ϵ increase as a function of $p_{\rm T}$ and also with increasing multiplicity, as expected. The efficiencies ϵ^j for the correction of the yields in the different $N_{\rm V0A}$ intervals were obtained by weighting the simulated $N_{\rm tracklets}$ distribution in order to reproduce the distributions measured in data for each $N_{\rm V0A}$ interval. Figure 5.32(b) shows the efficiencies for prompt $\rm D^0$ mesons as a function of $N_{\rm V0A}$ for the five $p_{\rm T}$ intervals considered for the analysis.

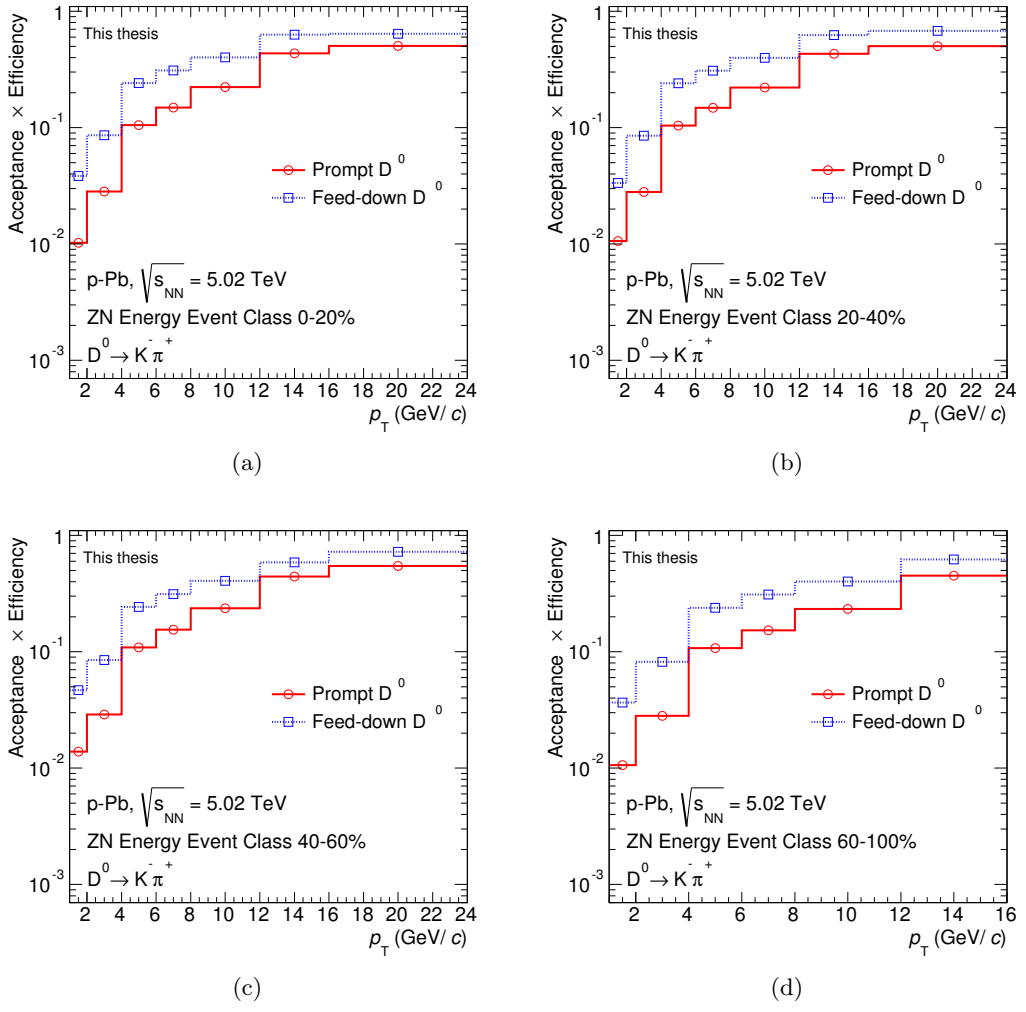

FIGURE 5.31: (Acc × ϵ) as a function of p_{T} for prompt and feed-down D^0 in 0–20% (a), 20–40% (b), 40–60% (c), and 60–100% (d) event-activity classes defined with the ZNA estimator.

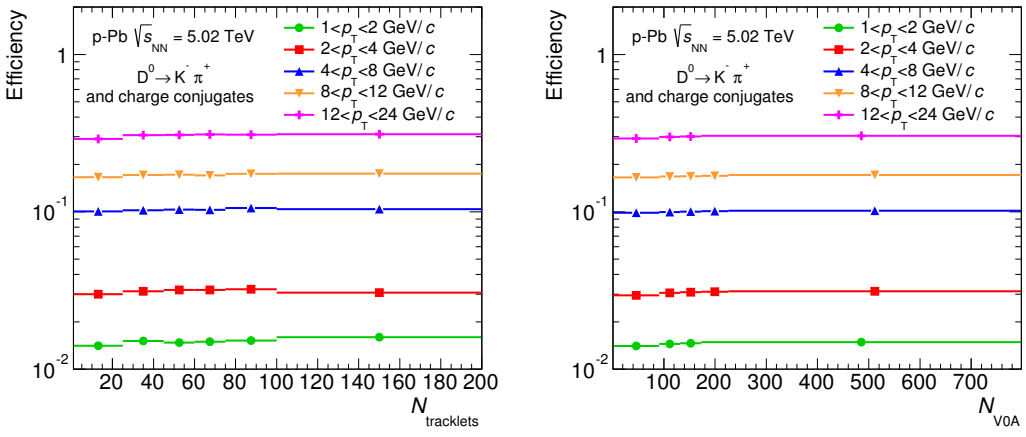

FIGURE 5.32: Efficiencies for prompt D^0 as a function of $N_{\mathrm{tracklets}}$ (a) and N_{V0A} (b) for the five p_{T} intervals considered for the analysis.

5.7 Correction for Feed-Down from B Decays

The prompt D^0 meson production yields $\mathrm{d}N/\mathrm{d}p_\mathrm{T}$ in Pb–Pb and p–Pb collisions were obtained by subtracting the contribution of D mesons from B decays.

The fraction f_prompt of D^0 coming from c quark hadronization, i.e. the correction factor that accounts for the feed-down from B meson (see Equations (4.8) and (4.12) in Chapter 4), was evaluated using the B production cross section from the FONLL pQCD calculation [34–36], and the $\mathrm{B} \to \mathrm{D}^0 + X$ kinematics from the EvtGen package [118]. The cross section for the feed-down component for the D^0 was computed at the energy of the collisions (2.76 TeV for Pb–Pb and 5.02 for p–Pb), scaled by the average nuclear overlap function $\langle T_\mathrm{AA} \rangle$ or $\langle T_\mathrm{pA} \rangle$, and used together with the Monte Carlo acceptance times efficiency $(\mathrm{Acc} \times \epsilon)_\mathrm{feed-down}$ for D mesons from B decays to compute the expected fraction of prompt D^0 in the measured yields:

$$\begin{aligned} f_\mathrm{prompt} &= 1 - \frac{N^{\mathrm{D}^0\ \mathrm{feed-down\ raw}}}{N^{\mathrm{D}^0\ \mathrm{raw}}} = \\ &= 1 - \langle T_\mathrm{AA(pA)} \rangle \times \left(\frac{\mathrm{d}^2\sigma}{\mathrm{d}y\mathrm{d}p_\mathrm{T}} \right)^\mathrm{FONLL}_\mathrm{feed-down} \times R^\mathrm{feed-down}_\mathrm{AA(pA)} \times \\ &\times \frac{(\mathrm{Acc} \times \epsilon)_\mathrm{feed-down} \cdot \Delta y \Delta p_\mathrm{T} \cdot \mathrm{BR} \cdot N_\mathrm{evt}}{N^{\mathrm{D}^0\ \mathrm{raw}}/2} . \end{aligned} \tag{5.4}$$

The symbol of the p_T-dependence (p_T) is omitted in the formulas, for brevity. The nuclear modification factor of the feed-down D^0 mesons, $R^\mathrm{feed-down}_\mathrm{AA(pA)}$, is related to the nuclear modification of beauty production, which has not been measured in the p_T interval of the analysis.

An alternative method to obtain the prompt fraction was considered. f_prompt is computed using the FONLL cross sections for prompt and feed-down D mesons (with $\mathrm{B} \to \mathrm{D} + X$) and their respective Monte Carlo efficiencies:

$$f_\mathrm{prompt} = \left(1 + \frac{(\mathrm{Acc} \times \epsilon)_\mathrm{feed-down}}{(\mathrm{Acc} \times \epsilon)_\mathrm{prompt}} \frac{\left. \frac{\mathrm{d}\sigma^\mathrm{FONLL}_\mathrm{feed-down}}{\mathrm{d}p_\mathrm{T}} \right|_{|y|<0.5}}{\left. \frac{\mathrm{d}\sigma^\mathrm{FONLL}_\mathrm{prompt}}{\mathrm{d}p_\mathrm{T}} \right|_{|y|<0.5}} \frac{R^\mathrm{feed-down}_\mathrm{AA(pA)}}{R^\mathrm{prompt}_\mathrm{AA(pA)}} \right)^{-1} . \tag{5.5}$$

The measured raw yield is multiplied by the $f_\mathrm{prompt}(p_\mathrm{T})$ correction factor to obtain the prompt D^0 cross section. Since the central value of the FONLL beauty cross section calculations describe better data at different energies and rapidities than the calculations of charm cross section, the central value of the $f_\mathrm{prompt}(p_\mathrm{T})$ calculation is taken from the first method, which does not depend on the FONLL charm calculation. The feed-down subtraction uncertainties were defined as the envelope of the uncertainties from both methods (see Chapter 6).

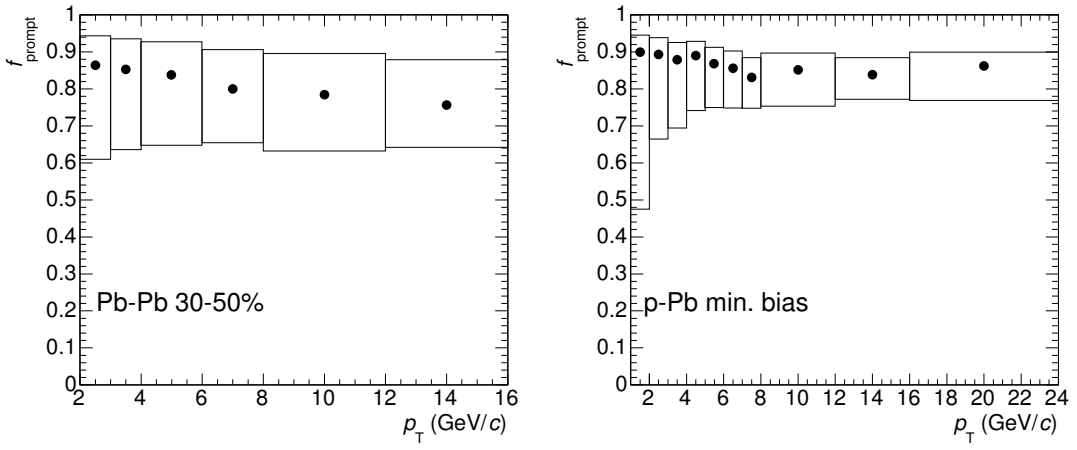

(a) (b)

FIGURE 5.33: (a) Fraction of prompt D^0 mesons obtained in Pb–Pb collisions in the 30–50% centrality class with the hypothesis $R_{\text{AA}}^{\text{feed-down}} = 2 \cdot R_{\text{AA}}^{\text{prompt}}$. (b) Fraction of prompt D^0 mesons obtained in p–Pb collisions with the hypothesis $R_{\text{pPb}}^{\text{feed-down}} = R_{\text{pPb}}^{\text{prompt}}$. The open boxes indicate the uncertainty (see Chapter 6) obtained considering the variation of the hypothesis and the two methods to calculate f_{prompt}

Pb–Pb Analysis

The comparison of the nuclear modification factor of prompt D mesons with that of J/ψ from B decays measured in the CMS experiment indicates that charmed hadrons are more suppressed than beauty hadrons (see Section 2.3.1). Therefore, for the Pb–Pb analysis, it was assumed that the ratio of the nuclear modification factors for feed-down and prompt D mesons lies in the range $1 < R_{\text{AA}}^{\text{feed-down}}/R_{\text{AA}}^{\text{prompt}} < 3$. The value $R_{\text{AA}}^{\text{feed-down}} = 2 \cdot R_{\text{AA}}^{\text{prompt}}$ was used to compute the correction, and the variation over the full range was used to assign a systematic uncertainty (see Chapter 6). With this assumption, the resulting f_{prompt} for D^0 mesons ranges from about 0.86 in the lowest transverse momentum interval ($2 < p_{\text{T}} < 3$ GeV/c) to about 0.75 at high p_{T} (Figure 5.33(a)).

The measured v_2 is a combination of the v_2 of promptly produced and feed-down D^0 mesons. The elliptic flow of prompt D^0, v_2^{prompt}, can be obtained from the measured v_2^{all} ($v_2\{\text{EP}\}$) as:

$$v_2^{\text{prompt}} = \frac{1}{f_{\text{prompt}}} v_2^{\text{all}} - \frac{1 - f_{\text{prompt}}}{f_{\text{prompt}}} v_2^{\text{feed-down}}, \tag{5.6}$$

where $v_2^{\text{feed-down}}$ is the elliptic flow of D^0 mesons from B decays, which depends on the dynamics of beauty quarks in the medium. It can be seen in Equation (5.6) that v_2^{all} coincides with v_2^{prompt} if $v_2^{\text{feed-down}} = v_2^{\text{prompt}}$, independent of f_{prompt}. Therefore, the assumption $v_2^{\text{feed-down}} = v_2^{\text{prompt}}$ was used to compute the central value of the results

for the prompt D^0 elliptic flow. Due to the larger mass of the b quark, the v_2 of B mesons is expected to be lower than that of D mesons. Therefore, the assumption made to calculate the central values results to be the most conservative for the observation of D meson $v_2 > 0$. The variation of $v_2^{\text{feed-down}}$ in the interval $0 \leq v_2^{\text{feed-down}} \leq v_2^{\text{prompt}}$ was considered to estimate the systematic uncertainty (see Chapter 6).

p–Pb Analysis

For the p–Pb analysis, the prompt fraction was calculated assuming $R_{\text{pPb}}^{\text{feed-down}} = R_{\text{pPb}}^{\text{prompt}}$, and the ratio of the nuclear modification factors was varied in the range $0.9 < R_{\text{pPb}}^{\text{feed-down}}/R_{\text{pPb}}^{\text{prompt}} < 1.3$ to evaluate the systematic uncertainty. The resulting f_{prompt} is shown as a function of p_{T} in Figure 5.33(b): it ranges from 0.9 in the lowest p_{T} interval ($1 < p_{\text{T}} < 2$ GeV/c) to about 0.85 at higher p_{T}. These assumptions were based on the study of the possible modification of the B hadron production due to initial state effects. The estimate of the influence of shadowing in the prompt and feed-down D^0 production was performed using NLO pQCD calculations (MNR [28]) including the EPS09 nuclear modification of the parton distribution functions. The resulting nuclear modification factor of the prompt D and B mesons is shown in Figure 5.34(a). The equivalent calculation of the R_{pPb} of the D^0 from B with EPS09 shadowing was obtained considering the EvtGen decayer for the D from B decays, see Figure 5.34(b). Their ratio is shown in Figure 5.34(c). The relative ratio is evaluated considering the uncertainties on the prompt and feed-down D to be correlated, i.e. only central/upper/lower bands of the calculations are taken into account when computing the ratio, and not their combination.

The calculation of f_{prompt} was also performed setting the central value of the ratio $R_{\text{pPb}}^{\text{feed-down}}/R_{\text{pPb}}^{\text{prompt}}$ to that of the calculation reported in Figure 5.34(c), and considering an interval of 3 times the uncertainty around the central value as range of variation of the hypothesis. The variation of the central values of the R_{pPb} obtained with the two hypotheses ($R_{\text{pPb}}^{\text{feed-down}}/R_{\text{pPb}}^{\text{prompt}} = 1$ and $R_{\text{pPb}}^{\text{feed-down}}/R_{\text{pPb}}^{\text{prompt}}$ as in Figure 5.34(c)) was found to be much smaller than the systematic uncertainty, which remained very similar as well. Therefore, the first, p_{T}-independent, option was chosen.

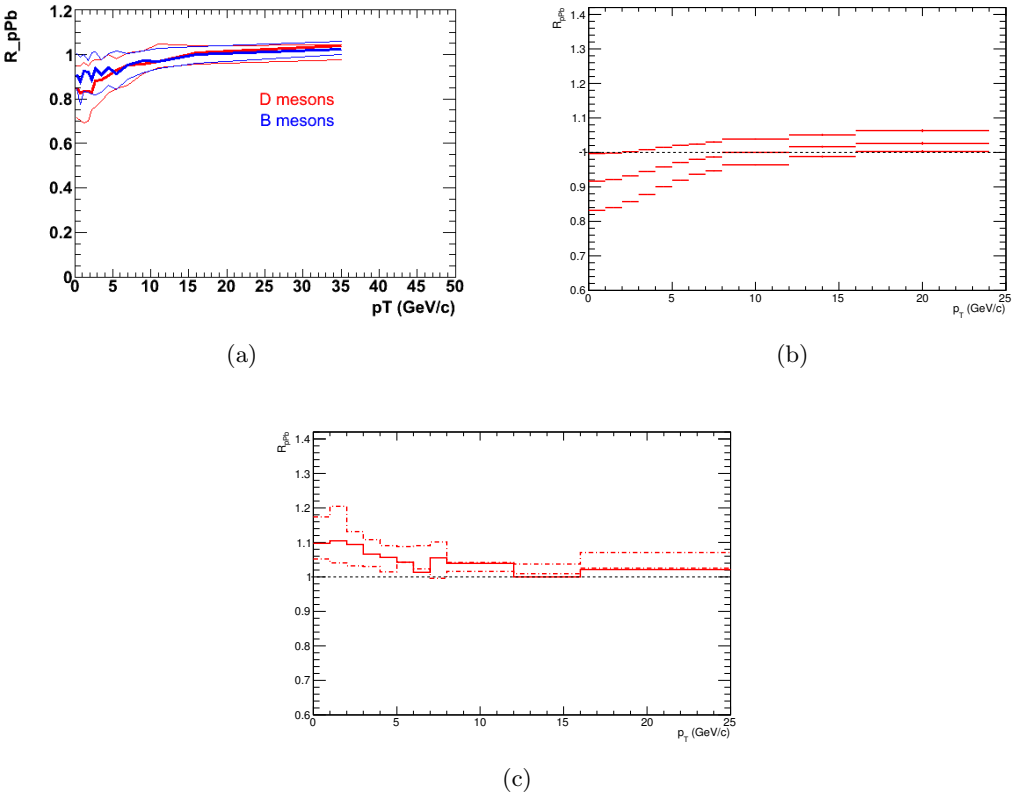

FIGURE 5.34: (a) Calculation of the D and B meson nuclear modification factor including EPS09 shadowing. (b) Nuclear modification factor of D^0 from B decays obtained with EvtGen decayer and including shadowing. (c) Ratio of D^0 from B and prompt D^0 nuclear modification factors.

6

Systematic Uncertainties

This chapter is devoted to the description of the systematic uncertainties that were studied for each observable in Pb–Pb and p–Pb collisions. The various sources of uncertainty are listed in Table 6.1. In the first part of the chapter, the methods applied to evaluate the "data systematics" (yield extraction, correction for reflections, tracking/-cut/PID efficiency and Monte Carlo p_{T} and multiplicity distributions) are presented. The description of the systematic uncertainty related to the B feed-down subtraction and to the scaling of the pp reference cross section needed to compute the nuclear modification factor are given in Sections 6.7 and 6.8, respectively. In the last four sections the values of the uncertainties for each measured observable are summarized, in particular: Section 6.9 is devoted to the D^0 v_2 measurement, Section 6.10 to the azimuthal dependence of the R_{AA}, Section 6.11 to the minimum-bias measurements in p–Pb collisions (namely the p_{T}-differential cross section and R_{pPb} and the p_{T}- and y-differential cross section), Section 6.12 to the multiplicity-dependent analysis carried out in p–Pb collisions (namely the Q_{pPb} and the relative yields as a function of multiplicity).

6.1 Yield Extraction

One of the main sources of systematic uncertainty originates from the D^0 yield extraction using a fit to the invariant mass distributions. This uncertainty was estimated by repeating the fits under different conditions and by using an alternative method for the yield determination. In general, the following variations to the fit procedure were considered:

- different fit range;
- different function to describe the background, in particular parabolic and linear functions were tested in addition to the exponential;

TABLE 6.1: Sources of systematic uncertainties studied for the observables that were measured. The ✓ symbol indicates a source of systematics that affects and was estimated for that particular observable. The × indicates a source that does not contribute to the systematics for a particular observable.

Measurement	v_2	R_{AA}	$\frac{\mathrm{d}\sigma}{\mathrm{d}p_{\mathrm{T}}}$	$\frac{\mathrm{d}\sigma}{\mathrm{d}p_{\mathrm{T}}\mathrm{d}y}$	R_{pPb}	Q_{pPb}	$\frac{\mathrm{d}^2N^{\mathrm{D}^0}/\mathrm{d}y\mathrm{d}p_{\mathrm{T}}}{\langle \mathrm{d}^2N^{\mathrm{D}^0}/\mathrm{d}y\mathrm{d}p_{\mathrm{T}}\rangle}$
Yield extraction	✓	✓	✓	✓	✓	✓	✓
Correction for reflections	×	✓	✓	✓	✓	✓	×
Tracking efficiency	×	✓	✓	✓	✓	✓	×
Cut efficiency	×	✓	✓	✓	✓	✓	×
PID efficiency	×	✓	✓	✓	✓	✓	×
D^0 p_{T} distribution in MC	×	✓	✓	✓	✓	✓	×
Mult. distribution in MC	×	×	×	×	×	✓	×
B feed-down yield	×	✓	✓	✓	✓	✓	✓
B feed-down v_2	✓	✓	×	×	×	×	×
R_2 correction	✓	✓	×	×	×	×	×
Normalization	×	✓	✓	✓	✓	✓	✓
pp reference	×	✓	✓	✓	✓	✓	×

- fixing the centroid and width and of the Gaussian to the values observed in simulations;
- changing the invariant mass bin width of the histogram;
- using a bin counting method based on counting the entries within a 3σ interval centred on the peak position, after subtraction of the background estimated from a fit to the side bands; the interval considered for the bin counting procedure was also varied in order to reduce the statistical fluctuations on the systematic uncertainties evaluation.

The v_2 analysis with the event-plane method was performed by fixing the Gaussian centroids and widths of the in-plane and out-of-plane invariant mass distributions to the values obtained from a fit to the φ-integrated distribution. Therefore, the analysis was repeated with free Gaussian parameters in the fit instead of fixing them to the values extracted from simulations. The systematic uncertainty due to the yield measurement was estimated as the maximum variation of the v_2 values obtained from the described tests. It amounts to 10–20% depending on p_{T}. For the analysis of the D^0 meson R_{AA} in-plane and out-of-plane, the uncertainty on the yield extraction was estimated using the φ-integrated invariant mass distributions, in order to reduce the statistical fluctuations. The resulting uncertainty is 7% for $2 < p_{\mathrm{T}} < 8$ GeV/c and 10% for $8 < p_{\mathrm{T}} < 16$ GeV/c. For this measurement a correction factor c_{refl} was applied to subtract the reflection contribution from the raw yields, as explained in Section 5.5. The systematic uncertainty

on this correction was estimated by changing by ±50% the ratio of the integral of the reflections over the integral of the signal obtained from the simulation and used in the invariant mass fit with the reflections template. In addition, the shape of the

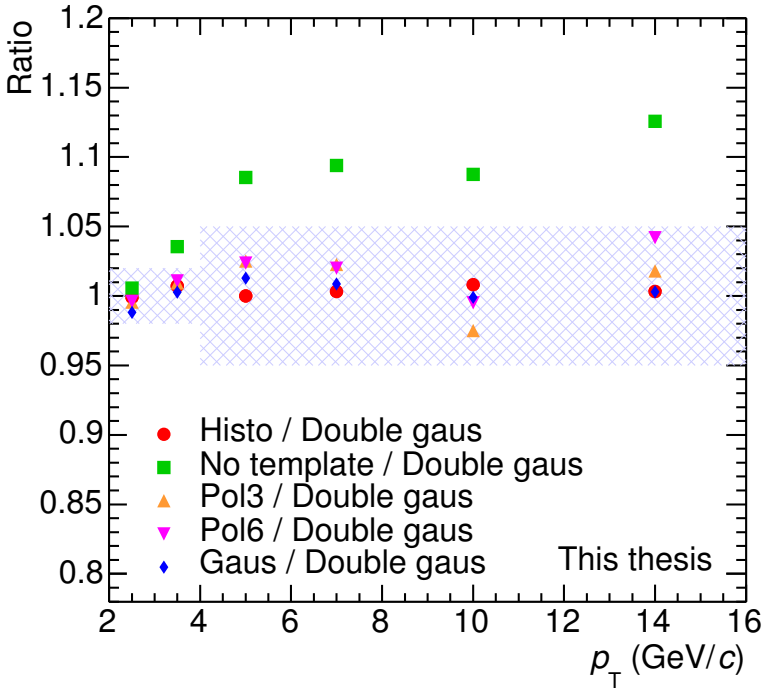

FIGURE 6.1: Raw yield ratios relative to the signal yield extracted with the double-Gaussian template for the reflection contribution in Pb–Pb collisions in the 30–50% centrality class. The green points are obtained without subtracting the reflected signal, thus represent the bias on the signal. The red points are obtained using the generated reflections distributions as templates, the orange, magenta and blue points indicate the variation of the raw signal when the template function is varied and were used to extract the systematic uncertainty on c_{refl} factor.

reflections templates was varied using a polynomial parametrization of the distribution from the simulation, instead of a double-Gaussian parametrization. A single-Gaussian parametrization and the templates obtained using the generated reflections distributions were also tested. These variations resulted in an uncertainty of 1–2% for $2 < p_{\mathrm{T}} < 4$ GeV/c and of 5% for $4 < p_{\mathrm{T}} < 16$ GeV/c on the c_{refl} factor (Figure 6.1).

For the minimum-bias p–Pb analysis the uncertainty was estimated from the ratio between the raw yield obtained with the default fit configuration and the yield extracted considering the variations listed above. In general, the systematic uncertainties were determined as the best estimate of the RMS of the results trying to disentangle the effect of statistical fluctuation and removing outliers on the basis of the quality of the fits. In some cases the background distribution was not properly reproduced by the fit variation, or the bin counting value was driven by the fluctuations of the background that are found when the statistics starts to be limited.

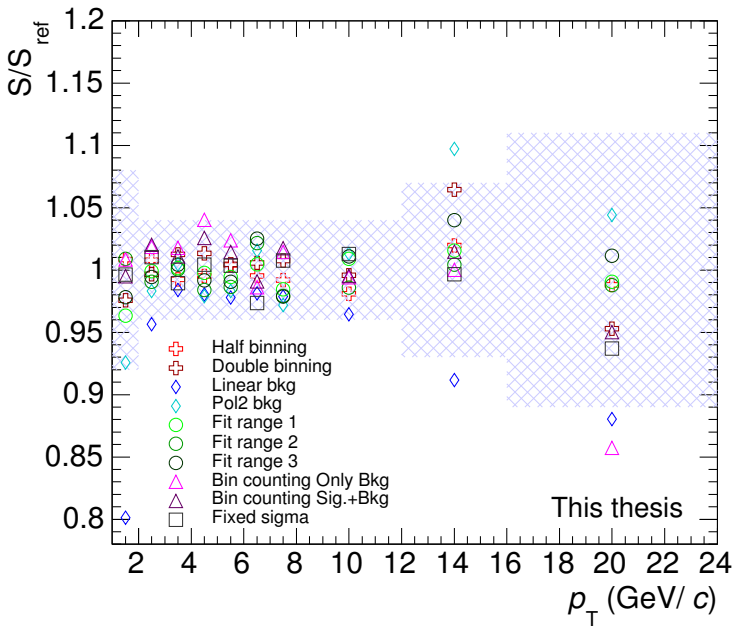

FIGURE 6.2: Raw yield ratios relative to the signal yield extracted with the default fit procedure as a function of p_{T} in p–Pb collisions. The shaded area indicates the assigned uncertainty due to yield extraction.

Figure 6.2 shows the relative ratios of the raw yields evaluated to estimate the uncertainty on the p_{T}-differential production cross section and the R_{pPb}.

Figure 6.3 shows the relative raw yield ratios from which the yield extraction systematics were evaluated for the y-dependent D^0 production cross section. For this study the peak widths were fixed to the values extracted from the y-integrated invariant mass fits. This was motivated by the fact that the simulations did not reproduce consistently the worsening of the p_{T} resolution from $y = 0.8$ to $y = 0$, which is due to the better space point resolution for smaller drift lengths in the TPC and to the crossing of the central TPC electrode.

For the Q_{pPb} analysis the yield extraction systematics were evaluated in each event-activity class for all the three estimators applying the same strategy as for the minimum-bias case. In Figures 6.4, 6.5, and 6.6 the results of the yield extraction studies are reported for the four event classes considered for the analysis, defined with the CL1, V0A, and ZNA event-activity estimators.

The systematic uncertainty from raw signal extraction on the relative yields as expressed in Equation (4.16) was obtained by testing the different approaches listed above to separate the signal from the combinatorial background. For this analysis, in the various multiplicity intervals, the peak position and width were fixed to the values obtained from the multiplicity-integrated distribution. Therefore, the case with peak

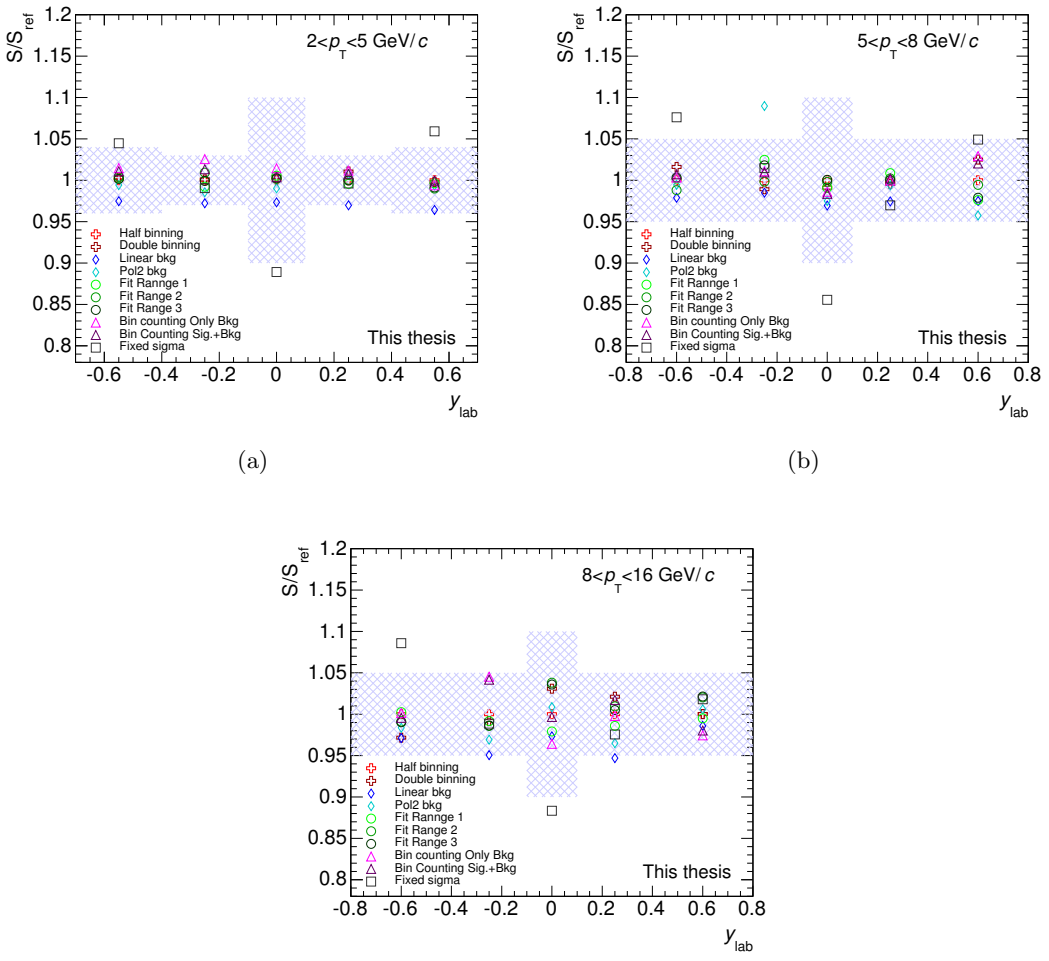

FIGURE 6.3: Raw yield ratios relative to the signal yield extracted with the default fit procedure as a function of $y_{\rm lab}$ for $2 < p_{\rm T} < 5$ GeV/c (a), $5 < p_{\rm T} < 8$ GeV/c (b), and $8 < p_{\rm T} < 16$ GeV/c (c) in p–Pb collisions. The shaded area indicates the assigned uncertainty due to yield extraction.

position and width left as free parameters in the fit was also tested. The uncertainty was estimated from the variation of the ratio of the raw yields $N^{j}_{\rm raw\ D^0}/\langle N_{\rm raw\ D^0}\rangle$, where the same raw yield extraction method was used in the multiplicity interval j and for the multiplicity-integrated result. The values of the ratio are reported in Figure 6.7 for the six different $N_{\rm tracklets}$ intervals considered for the analysis and defined in Table 5.5.

The values of the ratio are reported in Figure 6.8 for the $N_{\rm V0A}$ intervals considered for the analysis and defined in Table 5.6.

The systematic uncertainty due to the reflections in the p–Pb minimum-bias yields was estimated, as explained in Section 5.5, to be of 3% up to $p_{\rm T} = 12$ GeV/c and 4% in $12 < p_{\rm T} < 24$ GeV/c. The reflection contribution was not subtracted from the raw yields in any of the p–Pb analysis, but considered as a possible systematic effect

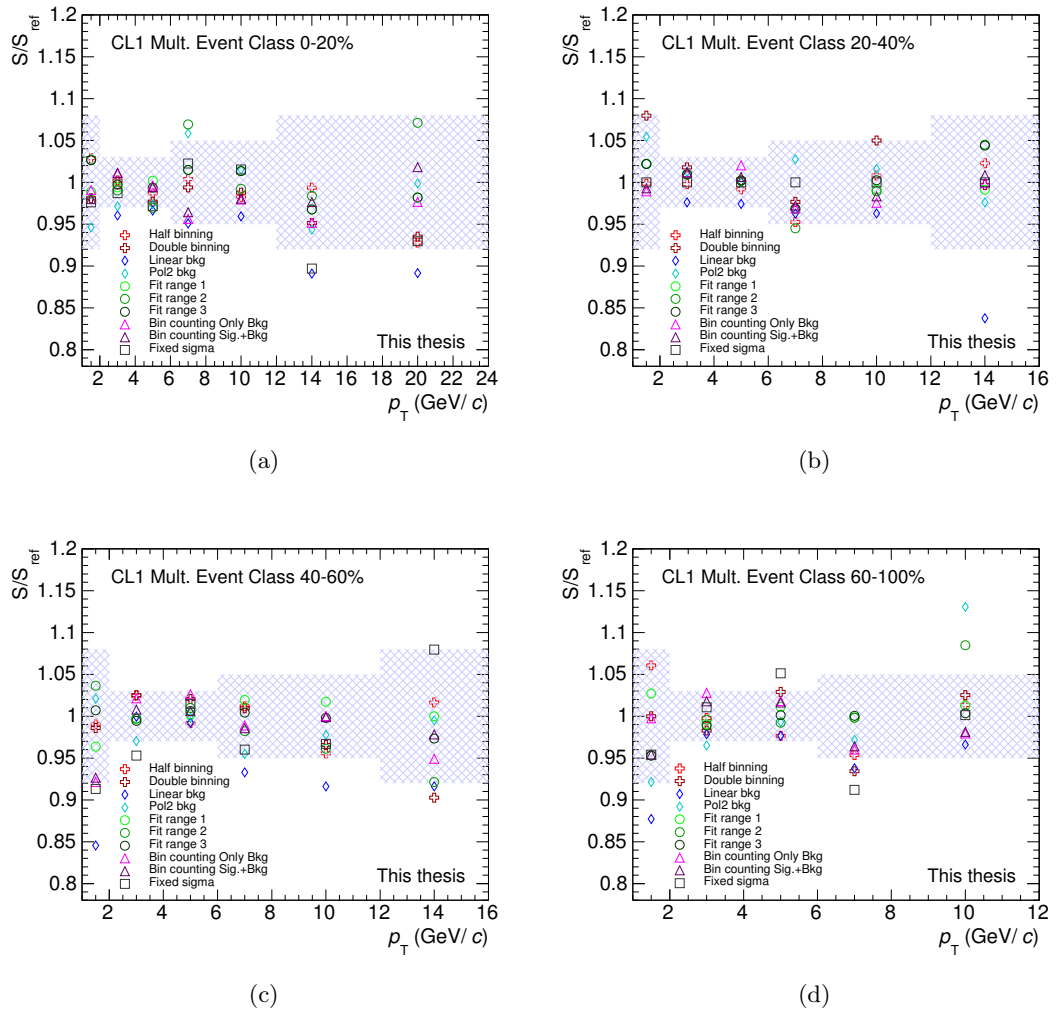

FIGURE 6.4: Raw yield ratios relative to the signal yield extracted with the default fit procedure as a function of p_T for 0–20% (a), 20–40% (b), 40–60% (c), and 60–100% (d) event-activity classes defined with the CL1 estimator in p–Pb collisions.

and added in quadrature to the yield extraction systematics. A similar study of the reflections effect was performed as a function of rapidity, providing similar results as those obtained for the y-integrated analysis. Moreover, the reflections contribution is not expected to depend on multiplicity since the PID performance is not expected to change in the considered range. Therefore, the same values as those obtained from the y- and multiplicity-integrated sample were considered as systematic uncertainty due to reflections for the y-differential cross section and the Q_{pPb}. No systematics due to reflections was considered for the analysis of the relative yields as a function of multiplicity, since the bias from reflections is expected to cancel in the ratio of the yields.

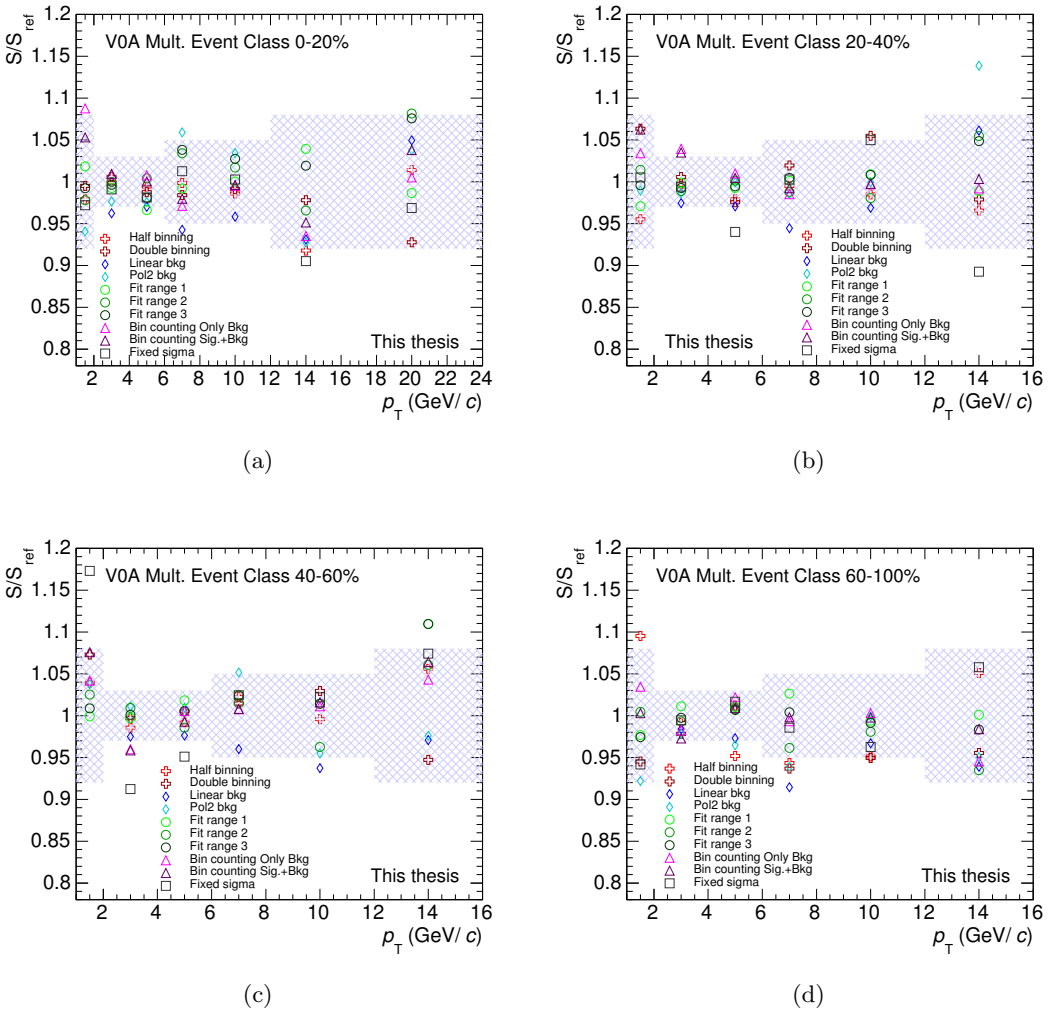

FIGURE 6.5: Raw yield ratios relative to the signal yield extracted with the default fit procedure as a function of p_{T} for 0–20% (a), 20–40% (b), 40–60% (c), and 60–100% (d) event-activity classes defined with the V0A estimator in p–Pb collisions.

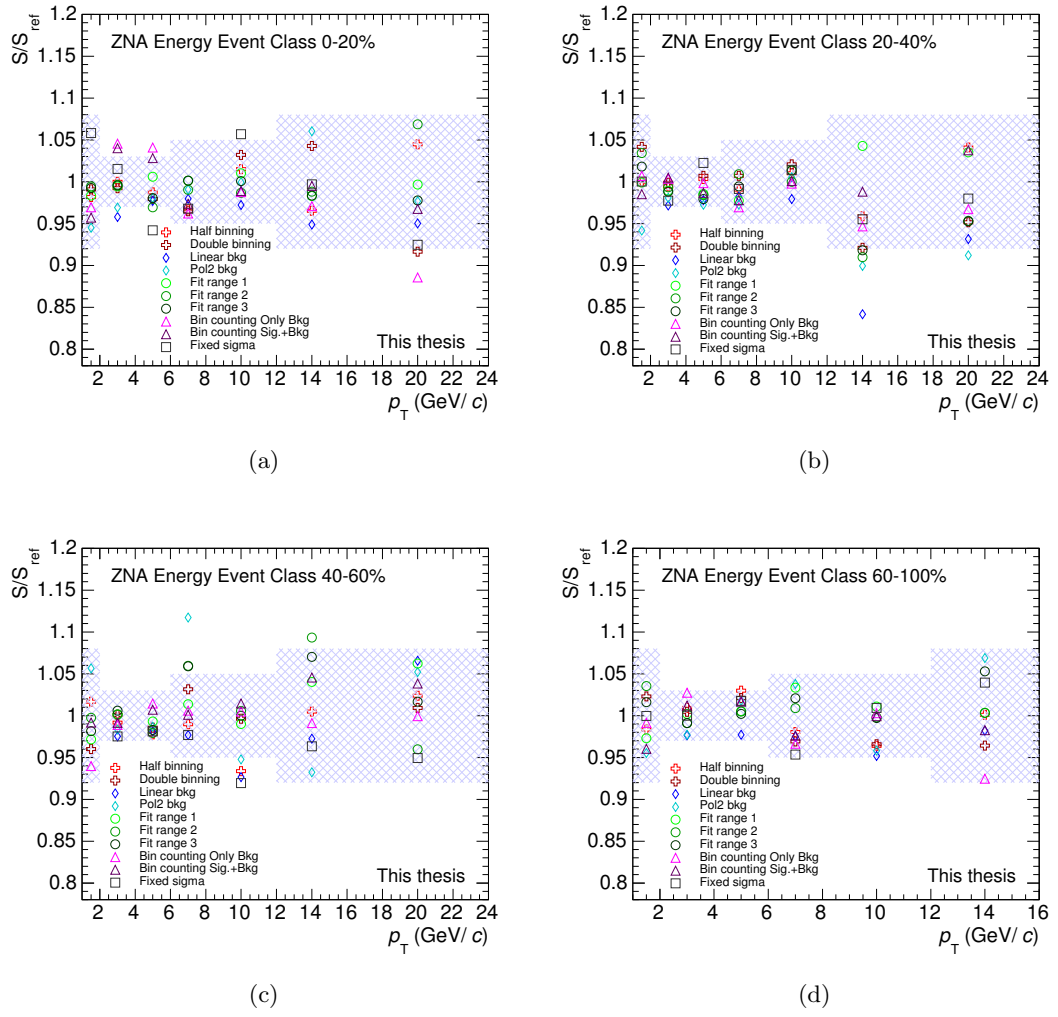

FIGURE 6.6: Raw yield ratios relative to the signal yield extracted with the default fit procedure as a function of p_{T} for 0–20% (a), 20–40% (b), 40–60% (c), and 60–100% (d) event-activity classes defined with the ZNA estimator in p–Pb collisions.

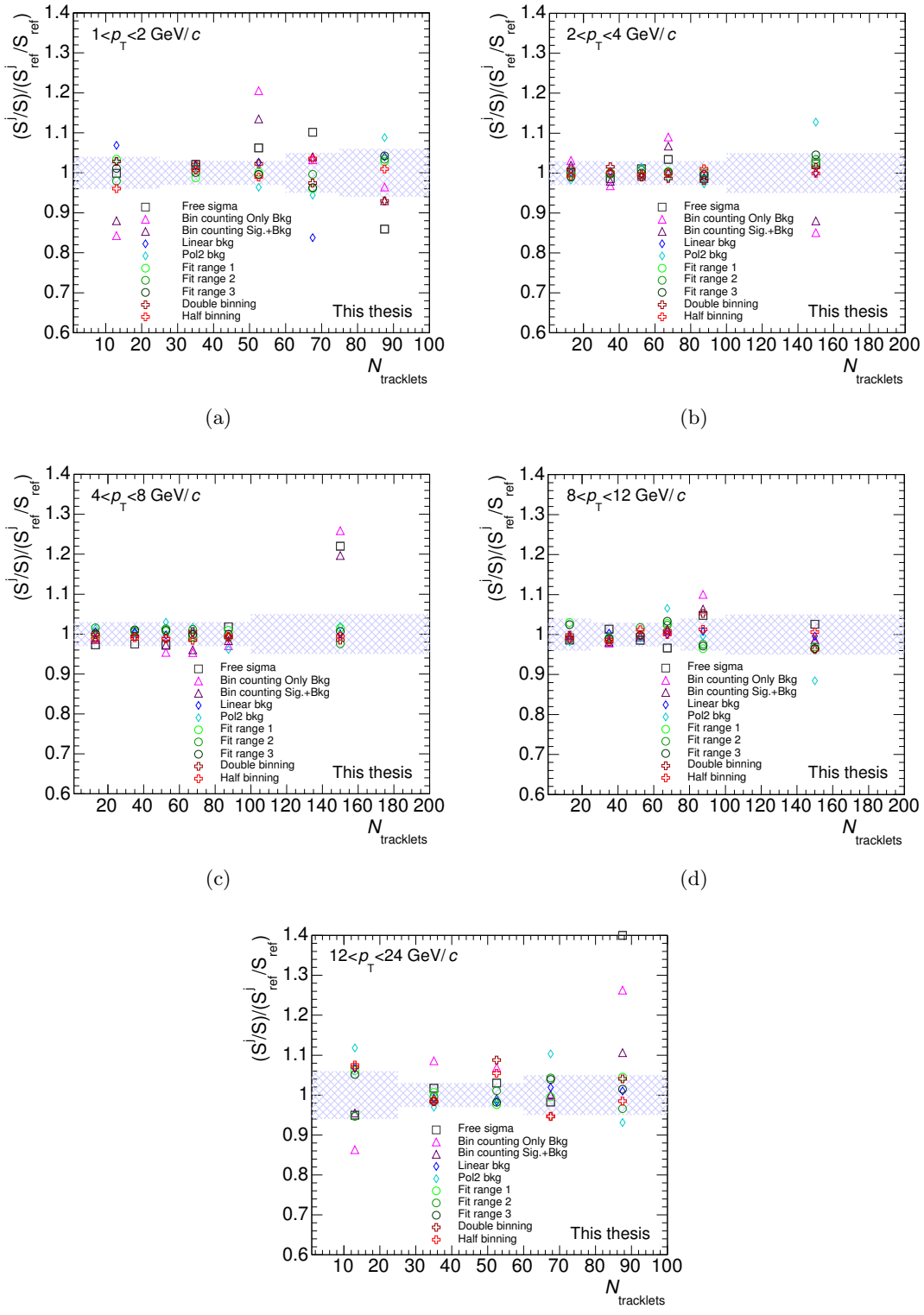

FIGURE 6.7: D^0 yield extraction systematics as a function of $N_{\text{tracklets}}$ for the five p_T intervals considered, in p–Pb collisions. The points represent the ratio of the relative yields extracted varying the fit procedure and the signal obtained with the standard fit procedure.

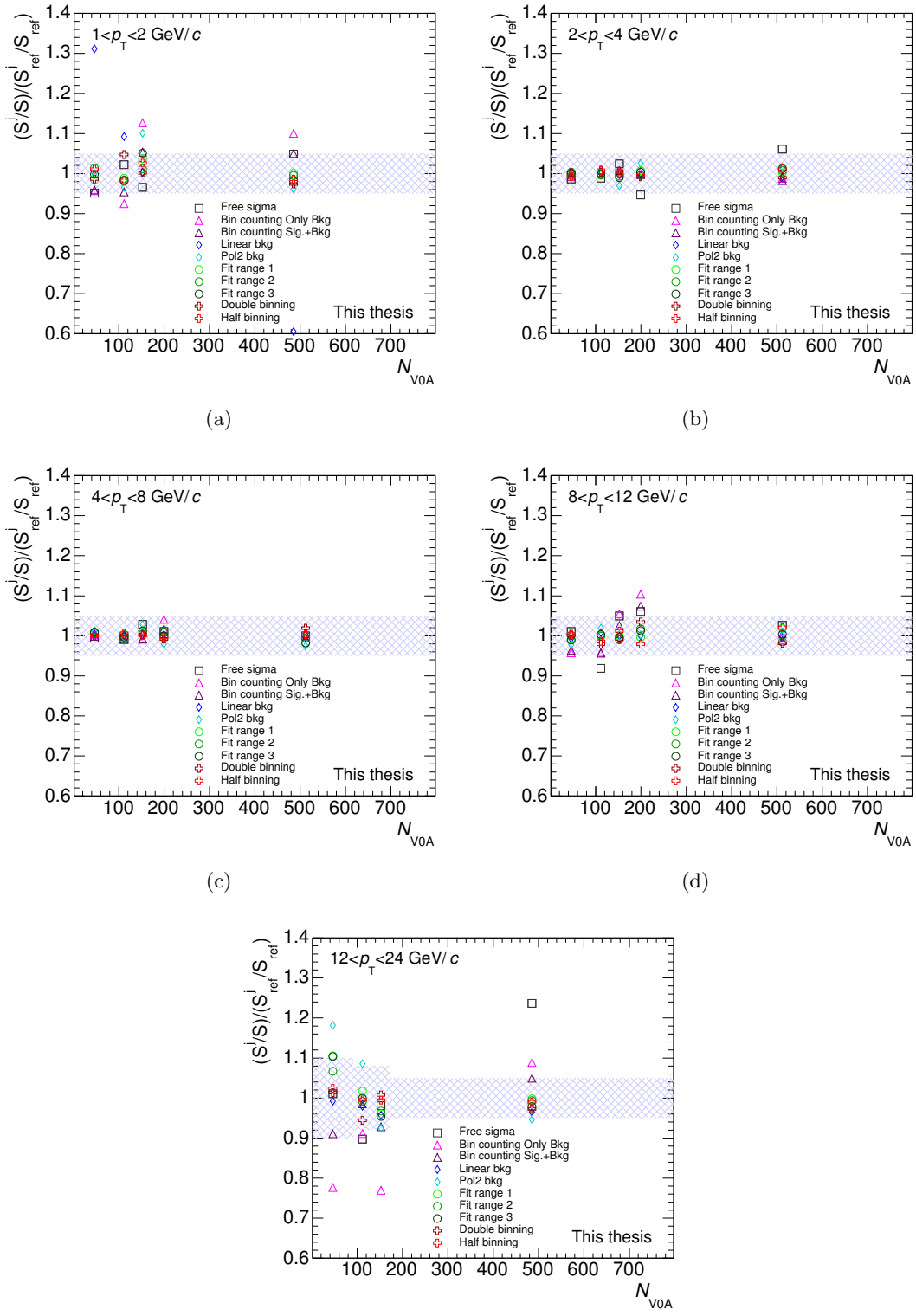

FIGURE 6.8: D^0 yield extraction systematics as a function of N_{V0A} for the five p_T intervals considered, in p–Pb collisions. The points represent the ratio of the relative yields extracted varying the fit procedure and the signal obtained with the standard fit procedure.

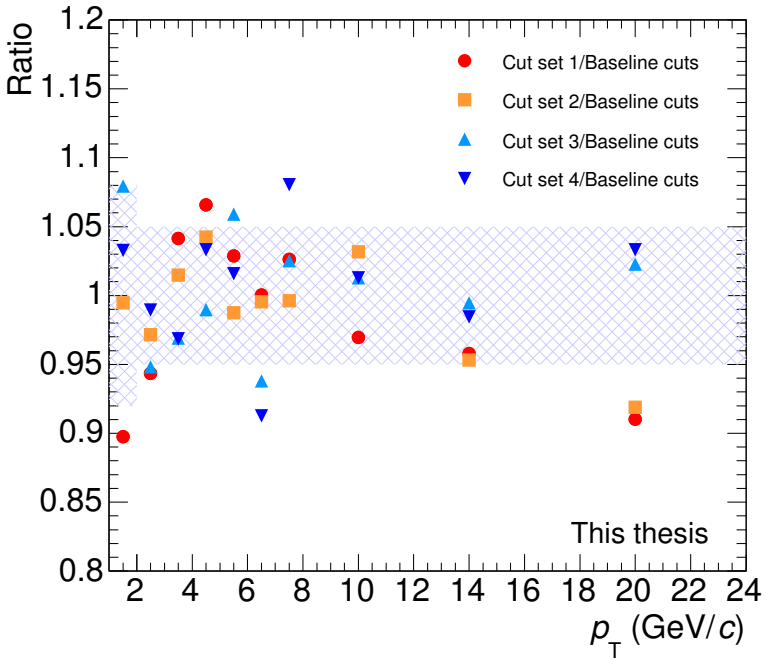

FIGURE 6.9: Ratios of the corrected yields obtained with different sets of cuts to those resulting with the baseline cuts in p–Pb collisions.

6.2 Cut Efficiency

A systematic effect can arise due to the residual discrepancies between data and simulation for the variables used to select the signal D^0 meson candidates. The uncertainty on the correction for the selection cut efficiencies was evaluated by repeating the analysis with different sets of cuts and was defined as the variation of the resulting corrected yields with respect to the value corresponding to the baseline cuts. The variation can be partially influenced by the yield extraction and by the statistical fluctuations of the background, therefore the uncertainties were evaluated excluding the outliers on the basis of the quality of the invariant mass fits. The cuts that were varied were those on the normalized decay length and the $\cos\theta^{xy}_{\mathrm{pointing}}$ in Pb–Pb and those on $d_0^{\mathrm{K}} \times d_0^{\pi}$ and $\cos\theta_{\mathrm{pointing}}$ in p–Pb, namely the most effective variables for the selection of the D^0 signal.

For the analysis of the D^0 R_{AA} in-plane and out-of-plane in Pb–Pb collisions the resulting variation was of 10% in the p_{T} intervals considered.

For the p–Pb analysis the variation was calculated as a function of p_{T} for the y-integrated analysis and also in the different rapidity intervals considered for the y-differential cross section measurement. Figure 6.9 shows the variation observed as a function of p_{T} considering the y-integrated sample, the resulting uncertainty estimated was 8% in $1 < p_{\mathrm{T}} < 2$ GeV/c and 5% in $2 < p_{\mathrm{T}} < 24$ GeV/c.

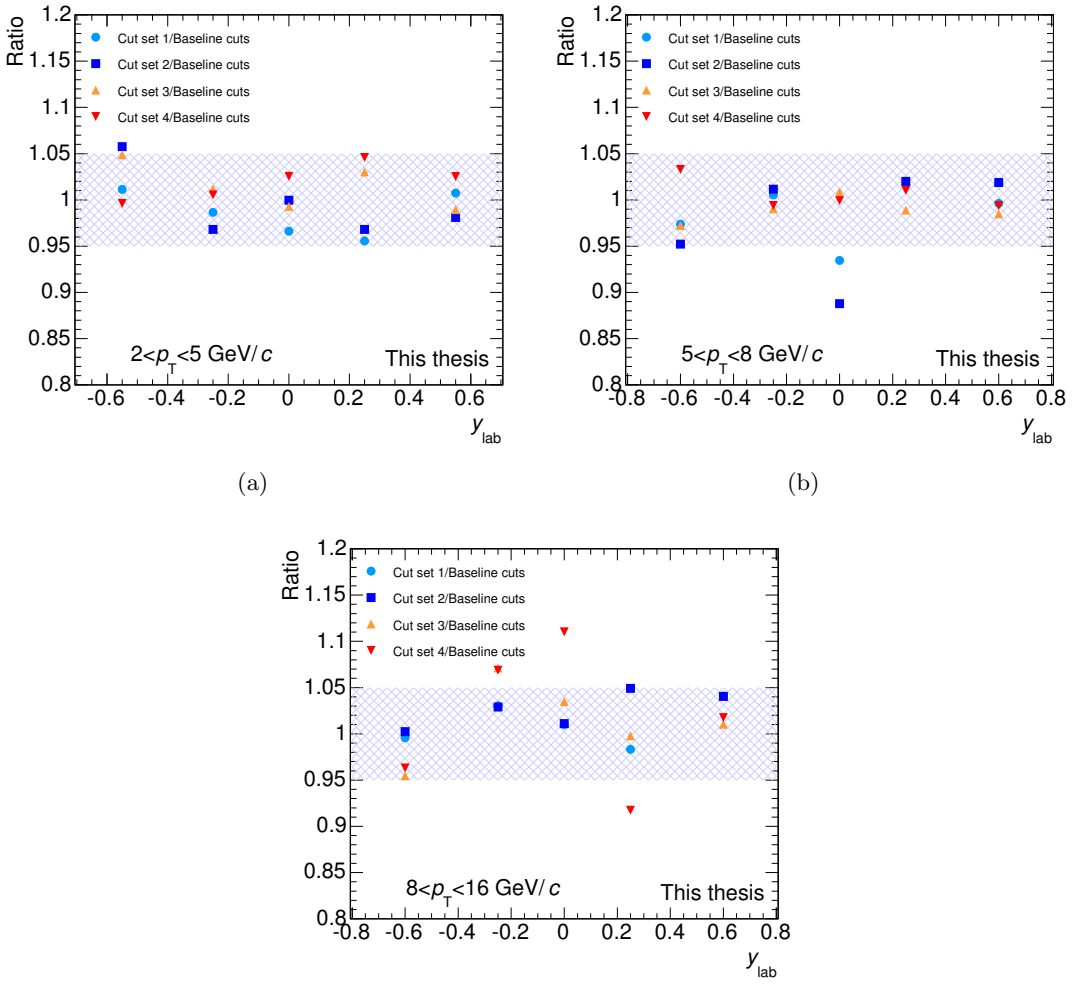

FIGURE 6.10: Ratios of the corrected yields obtained with different sets of cuts to those resulting with the baseline cuts in p–Pb collisions. The variations are presented as a function of $y_{\rm lab}$ for the three $p_{\rm T}$ intervals considered in the analysis.

The ratios of the corrected yields obtained as a function of rapidity in the three $p_{\rm T}$ intervals considered are shown in Figure 6.10. The cut efficiency systematics was also studied considering wider rapidity intervals to reduce the effect of statistical fluctuations. The merged intervals were those having similar efficiencies, i.e. $|y_{\rm lab}| < 0.4$ and $0.4 < |y_{\rm lab}| < 0.8$. The resulting uncertainty was in agreement with that obtained for the y-integrated analysis (5%).

The systematic uncertainty due to the cut efficiency was studied also in the different event-activity classes because the baseline cut values were changed with respect to those applied for the minimum-bias analysis, in order to optimize the signal extraction for the lower statistics in each class. The baseline cuts were equal for the CL1 analysis and the V0A one, while slightly different when the ZNA estimator was used.

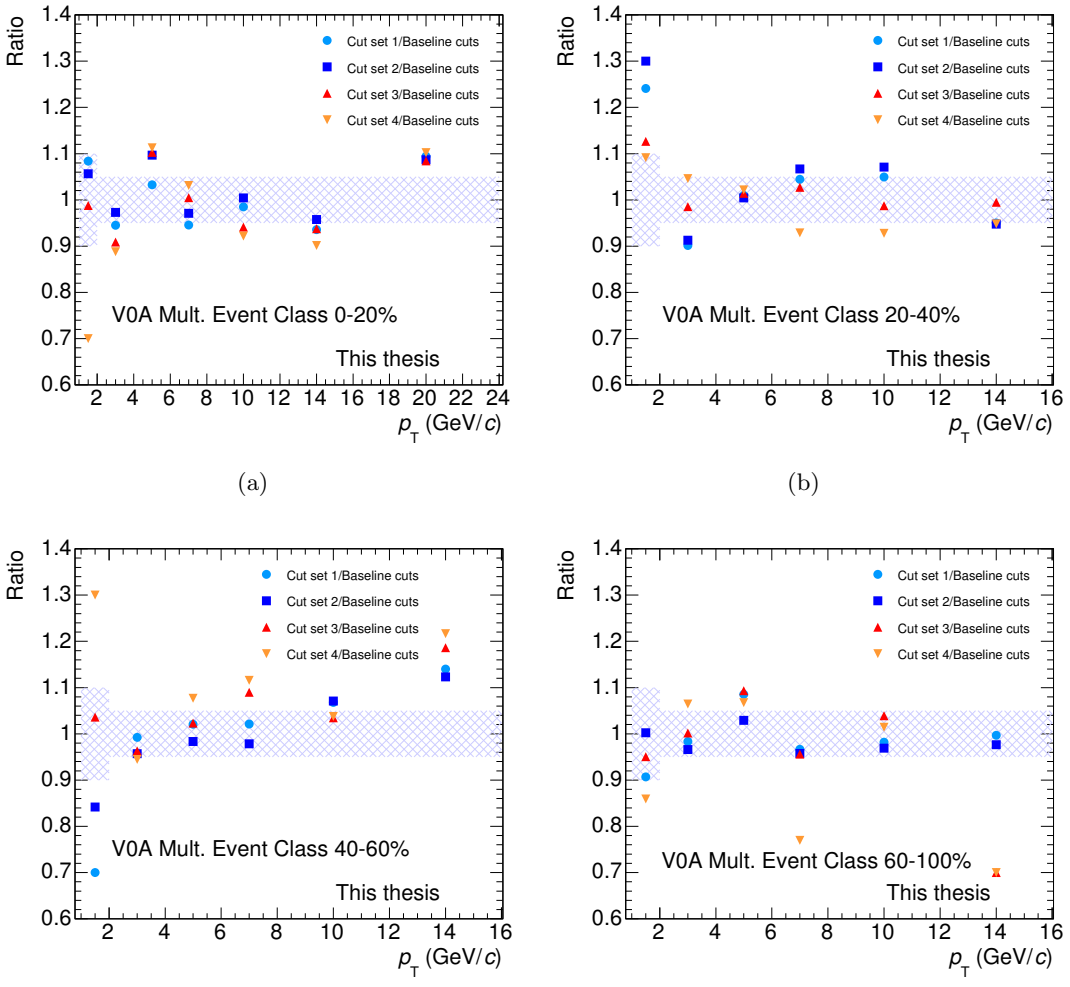

FIGURE 6.11: Ratios of the corrected yields obtained with different cuts to those obtained with the baseline cut values as a function of p_{T} for 0–20% (a), 20–40% (b), 40–60% (c), and 60–100% (d) event-activity classes defined with the V0A estimator in p–Pb collisions.

Figures 6.11 and 6.12 report the variations of the corrected yields for the four event-activity classes defined with V0A and ZNA, respectively. The estimated uncertainty was 10% in $1 < p_{\mathrm{T}} < 2$ GeV/c and 5% in $2 < p_{\mathrm{T}} < 24$ GeV/c.

Also the analysis of the relative yields as a function of multiplicity was repeated with different sets of topological selection criteria. It was verified that the relative yields as defined in Equation (4.16) are not sensitive to this variation. This confirms that the systematic uncertainty related to the topological selection description in the Monte Carlo cancels in the ratio, and therefore no additional systematic uncertainty has to be assumed.

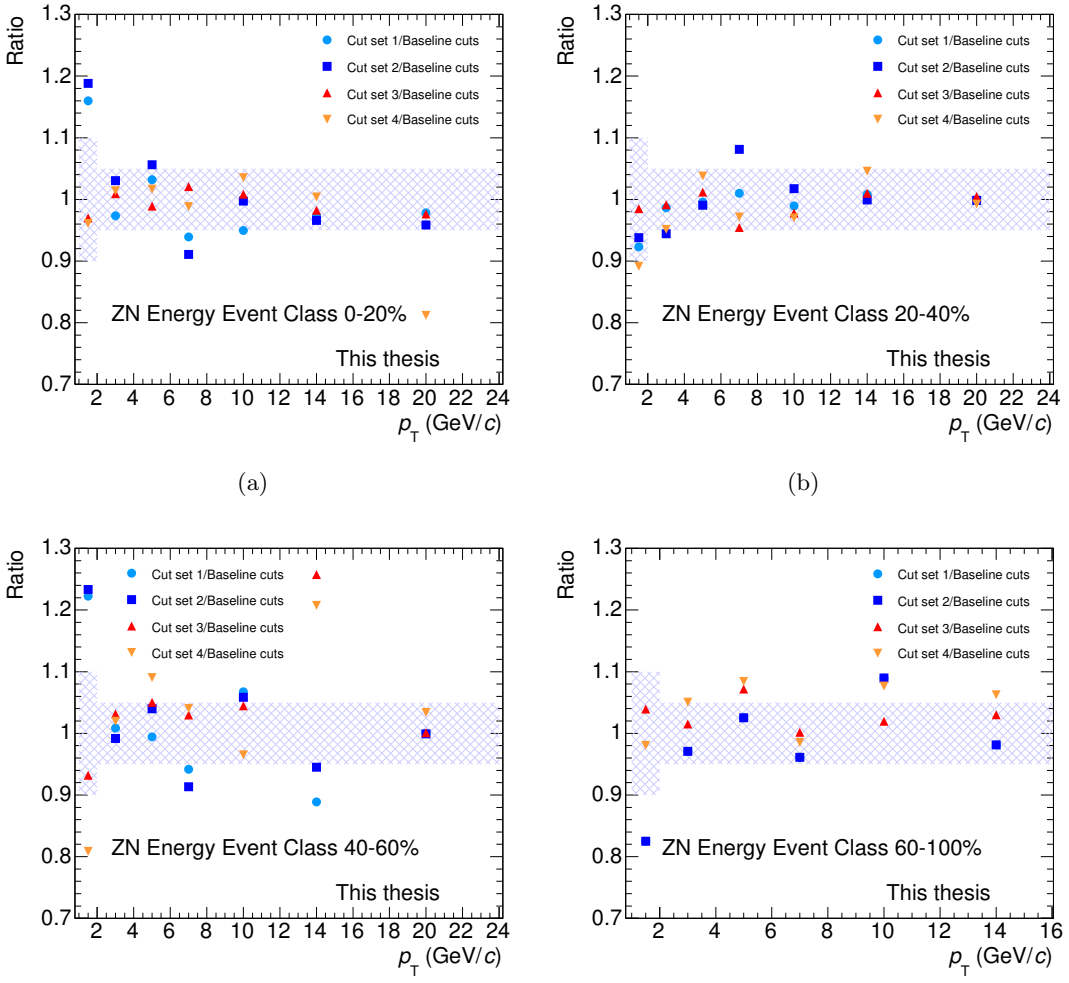

FIGURE 6.12: Ratios of the corrected yields obtained with different cuts to those obtained with the baseline cut values as a function of p_{T} for 0–20% (a), 20–40% (b), 40–60% (c), and 60–100% (d) event-activity classes defined with the ZNA estimator in p–Pb collisions.

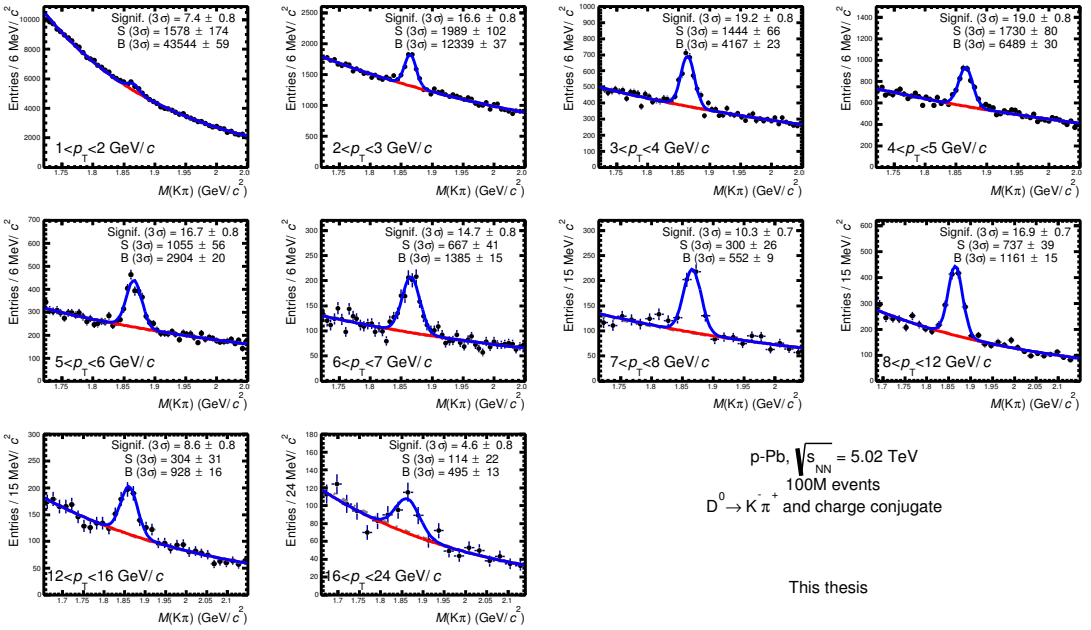

FIGURE 6.13: Distributions of the invariant mass for D^0 in p–Pb collisions obtained without applying PID selection. The raw signals include the reflection contribution.

6.3 PID Efficiency

The uncertainty arising from the PID selection was estimated by comparing the corrected yields obtained with and without this selection. In both cases, the bias on the raw signal induced by reflections was calculated and taken into account.

In Pb–Pb, the corrected yields resulting without PID selection were found to be consistent within 5% with those obtained with the PID selection. Therefore, a systematic uncertainty of 5% was assigned for the PID efficiency correction in the simulation.

In p–Pb, the difference between the corrected yields obtained with and without PID selection was negligible and, thus, no uncertainty was assigned. Figure 6.13 shows the invariant mass distributions obtained in minimum-bias p–Pb collisions when PID selection is not applied. In this case, the background is larger with respect to the case with PID selection applied.

For the relative yields as a function of multiplicity in p–Pb, no multiplicity-dependent influence of the PID is expected. The TPC response is stable up to an occupancy of 300–400 tracks, so there is no expected variation of the response in the range of multiplicity considered in this analysis. For what concerns the TOF information, a small effect on the resolution and start time information could be expected. Increasing the event multiplicity, the fraction of events with TOF or T0 start time changes, and the TOF PID resolution is slightly better. However, the efficiency is expected to remain unchanged.

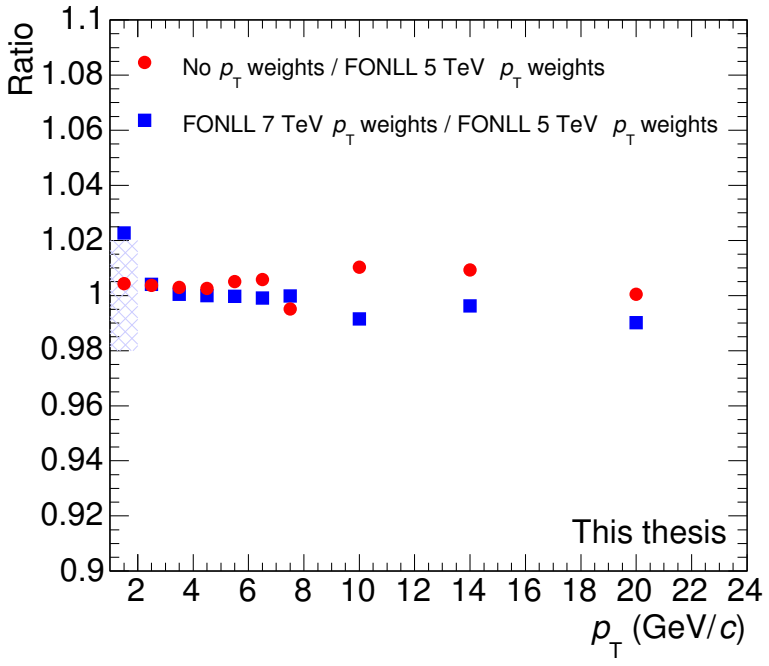

FIGURE 6.14: Rapidity integrated efficiencies ratios as a function of p_{T} calculated to estimate the systematic uncertainty due to the simulated D^0 momentum distribution in p–Pb collisions.

6.4 Monte Carlo p_{T} Shape

The uncertainty on the efficiencies arising from the difference between the real and simulated D^0 meson momentum distributions depends on the width of the p_{T} intervals and on the variation of the efficiencies within them.

The mean efficiency in a given p_{T} interval in Pb–Pb collisions was computed by re-weighting the simulated D^0 meson yield according to the p_{T} distribution measured for D^0 mesons in central Pb–Pb collisions [63]. The systematic uncertainty was defined as the difference with respect to the efficiency computed using the p_{T} distribution from a FONLL calculation multiplied by the R_{AA} value from one of the models that closely describe the central value of the measurement [119–121]. This uncertainty is of 2% in the interval $2 < p_{\mathrm{T}} < 3$ GeV/c, where the efficiency increases steeply with p_{T} (see Figure 5.25), and below 1% for $p_{\mathrm{T}} > 3$ GeV/c.

The efficiency correction in p–Pb was obtained considering as p_{T} distribution of generated D^0 mesons the one calculated with FONLL at $\sqrt{s} = 5.02$ TeV. The systematic uncertainty was evaluated from the variation of the Monte Carlo efficiencies with respect to those obtained without re-weighting the simulated p_{T} distribution, and those resulting when a weight function obtained by considering the p_{T} distribution from FONLL at $\sqrt{s} = 7$ TeV was used.

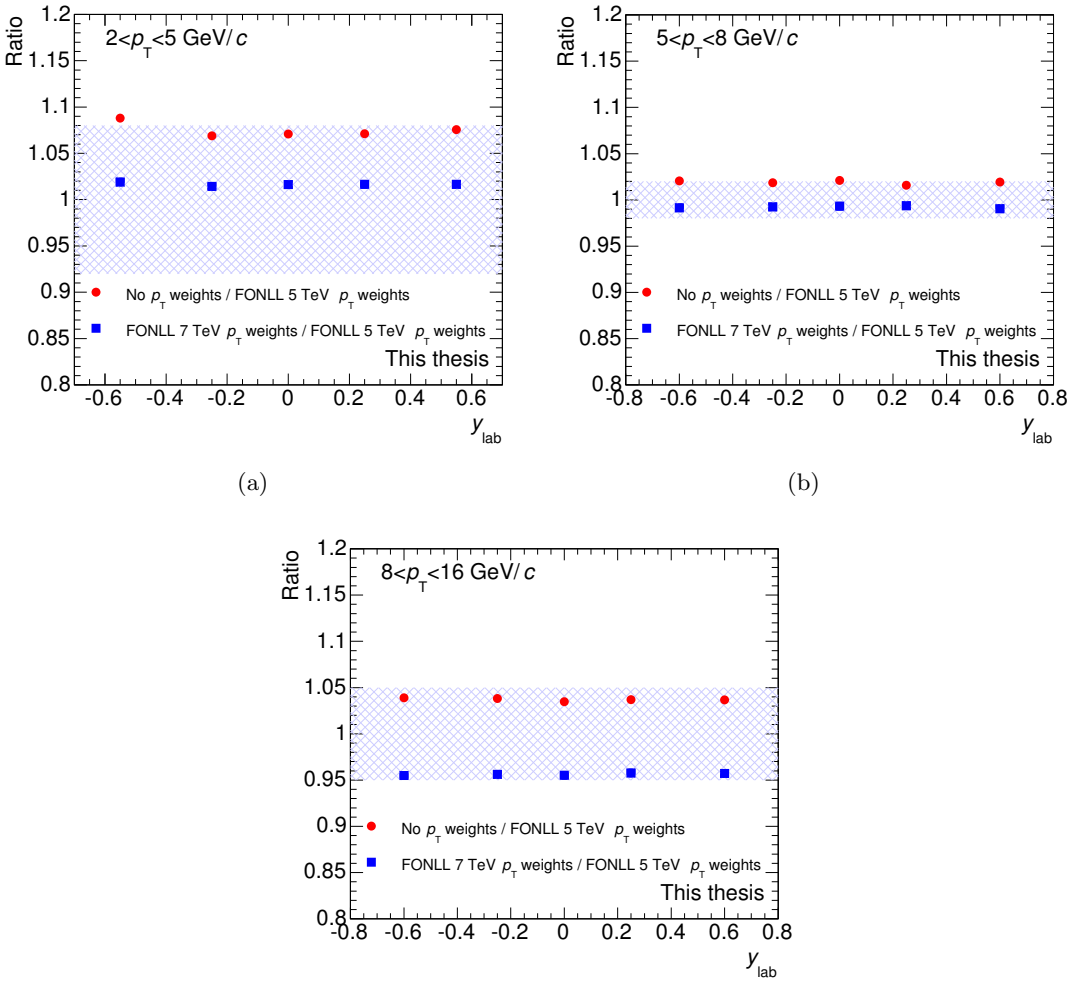

FIGURE 6.15: Efficiencies ratios as a function of $y_{\rm lab}$ for $2 < p_{\rm T} < 5$ GeV/c (a), $5 < p_{\rm T} < 8$ GeV/c (b), and $8 < p_{\rm T} < 16$ GeV/c (c) calculated to estimate the systematic uncertainty due to the simulated $\rm D^0$ momentum distribution in p–Pb collisions.

For the y-integrated analysis the uncertainty is of 2% in $1 < p_{\rm T} < 2$ GeV/c where the efficiencies increase steeply with $p_{\rm T}$, and negligible in $2 < p_{\rm T} < 24$ GeV/c (Figure 6.14). When larger $p_{\rm T}$ intervals are considered, e.g. for the cross section as a function of rapidity, the uncertainties are larger: 8% in $2 < p_{\rm T} < 5$ GeV/c, 2% in $5 < p_{\rm T} < 8$ GeV/c, and 5% in $8 < p_{\rm T} < 16$ GeV/c (Figure 6.15).

This systematic effect was verified to be negligible in the analysis of the relative yields as a function of multiplicity, since it cancels in the ratio of the corrected yields.

6.5 Monte Carlo Multiplicity Distribution

A systematic uncertainty due to the weighting procedure applied to obtain the (Acc $\times$ ϵ) factors in each event-activity class in p–Pb collisions, defined with the CL1, V0A,

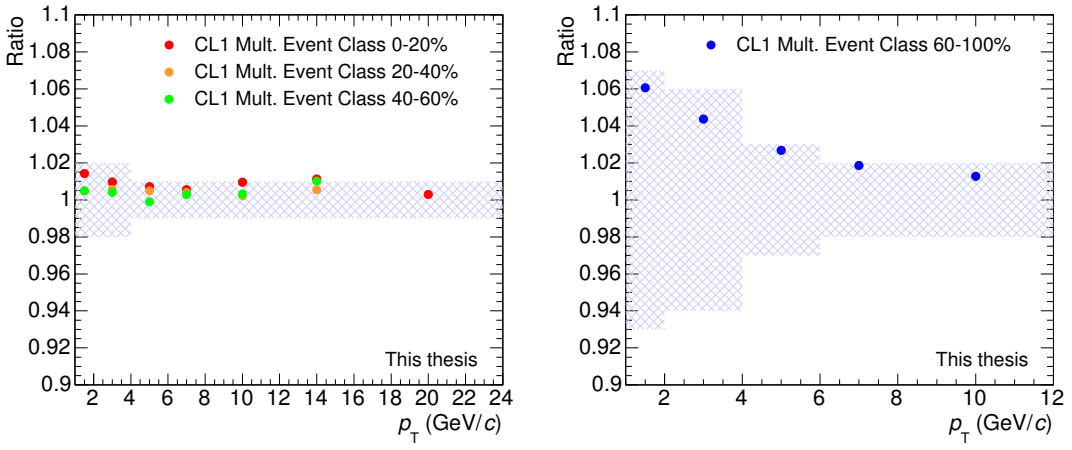

(a) (b)

FIGURE 6.16: Corrected yield ratios relative to the yield obtained with the reference $N_{\text{tracklets}}$ weight function as a function of p_{T} for 0–20%, 20–40%, 40–60% (a), and 60–100% (b) event-activity classes defined with the CL1 estimator in p–Pb collisions.

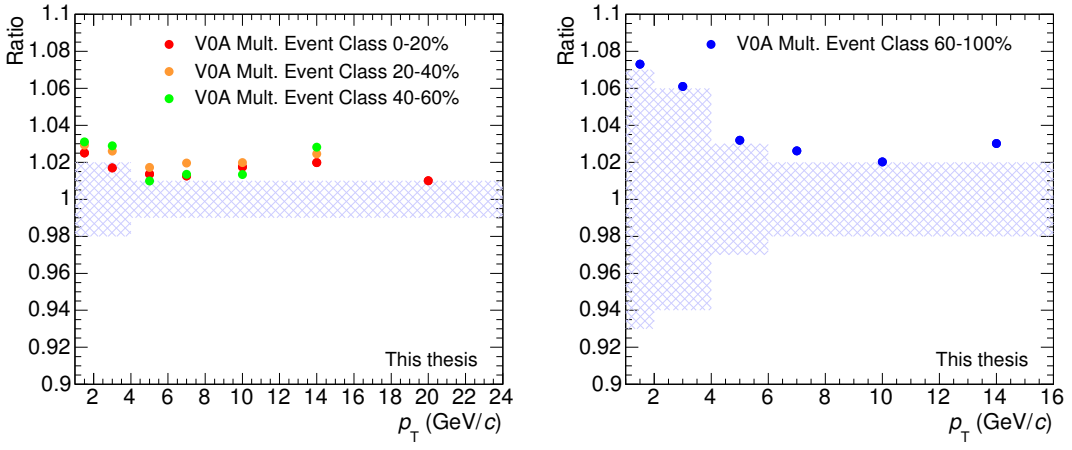

(a) (b)

FIGURE 6.17: Corrected yield ratios relative to the yield obtained with the reference $N_{\text{tracklets}}$ weight function as a function of p_{T} for 0–20%, 20–40%, 40–60% (a), and 60–100% (b) event-activity classes defined with the V0A estimator in p–Pb collisions.

and ZNA estimators (Section 5.6) was considered. The uncertainty was evaluated by comparing the corrected yields in each event-activity class obtained with the (Acc $\times$ ϵ) factors calculated by considering different weight functions with respect to those used as reference for the analysis. The weights used as reference were computed considering the events containing at least one D^0 candidate with an invariant mass compatible with D^0 mass within 20 MeV/c^2. The alternative weight functions were calculated considering the $N_{\text{tracklets}}$ distributions obtained for all the events selected for the analysis requiring the trigger condition, the pileup rejection, the event-activity selection, and $|z_{\text{vtx}}| < 10$ cm.

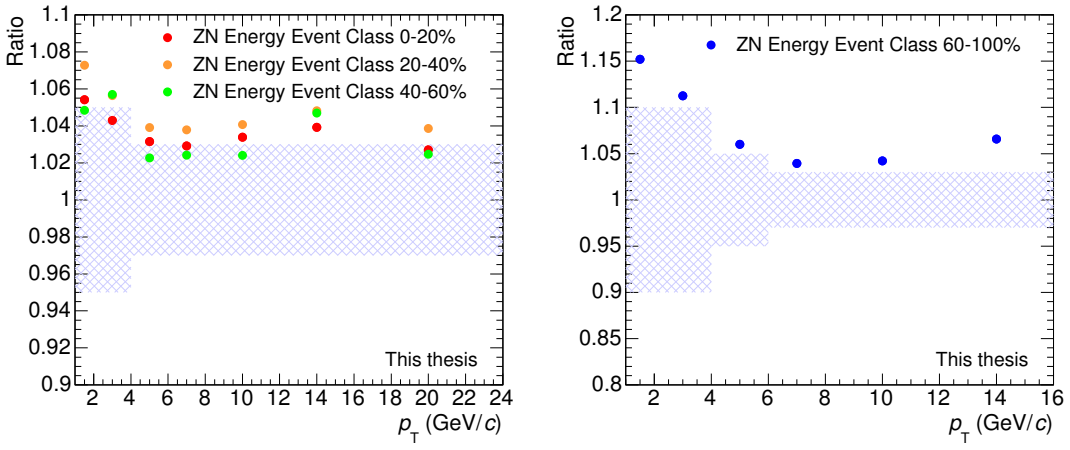

FIGURE 6.18: Corrected yield ratios relative to the yield obtained with the reference $N_{\text{tracklets}}$ weight function as a function of p_{T} for 0–20%, 20–40%, 40–60% (a), and 60–100% (b) event-activity classes defined with the ZNA estimator in p–Pb collisions.

Figures 6.16, 6.17 and 6.18 show the ratios of the corrected yields obtained with the three estimators, respectively, for the four event-activity classes considered. The corrected yields obtained when using the reference weights are always smaller with respect to the corrected yields obtained considering all the events selected. Requiring a D^0 in the mass region (events with large momentum transfer), events with larger multiplicity are selected and thus the reconstruction efficiency is larger. The ratio depends also on the width of the event-activity class, being larger in 60–100% with respect to 0–20%, 20–40%, and 40–60% where the same uncertainty was assigned. The same uncertainty was assigned in the event-activity classes defined with the CL1 and V0A estimators, while a larger uncertainty was considered for the ZNA estimator.

6.6 Tracking Efficiency

The systematic uncertainty related to the tracking efficiency was estimated by varying the track quality selection. The following single track cuts on TPC variables were considered one by one in addition to the default selection cuts:

- (number of TPC crossed rows[1]) $> 120 \times (p_{\text{T}}/5(\text{GeV}/c))$;
- (number of TPC clusters) $>$ (0.5 $\times$ number of TPC crossed rows);

[1]Each TPC sector contains 159 pad-rows. A charged particle traversing the TPC induces a signal on a given pad-row. If the charge in a search window of 5 pads in wire direction and 5 bins in time exceeds a certain threshold and fulfils all necessary quality criteria, it is called a cluster. Therefore the maximum number of clusters per track is 159, which corresponds to the total number of pad rows. Given the criteria required to define a cluster, a particle can traverse a pad row without generating a cluster (this is particularly true for long drift lengths and for particles in the minimum ionizing region).

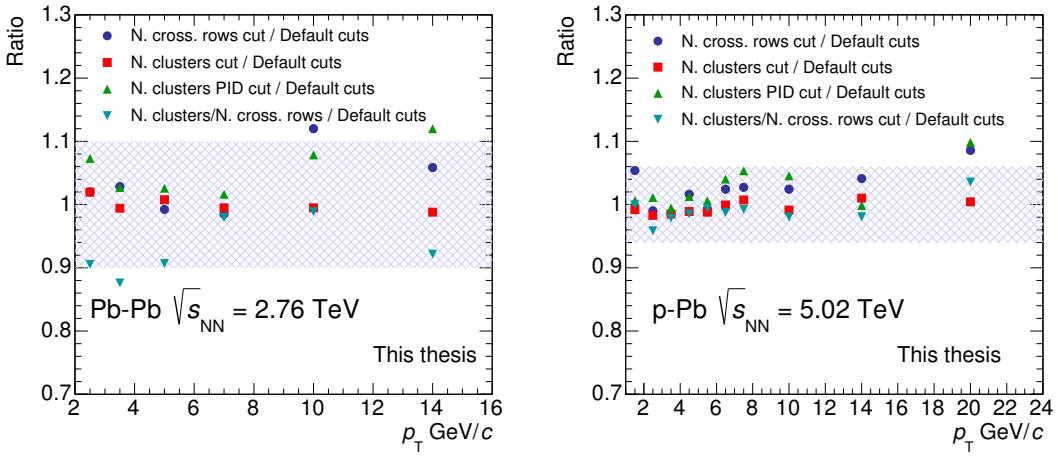

FIGURE 6.19: Ratio of the corrected yields obtained when applying different single track quality cuts to those obtained with default cuts for 30–50% Pb–Pb (a) and p–Pb collisions (b).

- (number of TPC clusters used for PID) $>$ (0.5 $\times$ number of TPC crossed rows);
- (number of TPC crossed rows)/(number of TPC findable clusters[2]) > 0.9.

The value of the systematic uncertainty was evaluated from the ratios of the corrected p_{T} distributions, computed with respect to the default track quality selection.

Figure 6.19 reports the ratios of the corrected yields. For Pb–Pb collisions the maximum observed deviation is of about 10% (Figure 6.19(a)). The resulting uncertainty was estimated to be 5% per decay track. In p–Pb collisions the assigned uncertainty was 3% per decay track on the basis of the values of the ratios obtained up to $p_{\mathrm{T}} = 16$ GeV/c (Figure 6.19(b)).

The tracking efficiency systematic uncertainty affects the R_{AA} in-plane and out-of-plane, the production cross section, R_{pPb} and Q_{pPb} measurements. In the R_{AA}, R_{pPb} and Q_{pPb} measurements the tracking efficiency systematic uncertainty does not cancel in the ratio because the yields are obtained from different data samples, namely Pb–Pb, p–Pb and pp, where the tracking performance was different. The tracking efficiency systematic uncertainty does not affect the v_2 and the relative yields, since it cancels in ratios of yields from the same data sample.

[2]The number of findable clusters is the number of geometrically possible clusters which can be assigned to a track. It takes into account the inactive zones due to chamber boundaries or the limited η-acceptance in which clusters are not findable.

6.7 Feed-down Correction

The systematic uncertainty arising from the subtraction of feed-down D^0 mesons has two contributions. The first contribution is due to the FONLL perturbative calculation of the cross sections and it was evaluated by varying the parameters of the calculation. The factorization and renormalization scales, μ_F and μ_R, were varied around their central values of $\mu_\mathrm{F} = \mu_\mathrm{R} = m_\mathrm{T} = \sqrt{p_\mathrm{T}^2 + m_c^2}$ over the range $0.5 \leq \mu_{\mathrm{R,F}}/m_\mathrm{T} \leq 2$, with the constraint $0.5 \leq \mu_\mathrm{R}/\mu_\mathrm{F} \leq 2$. The charm quark mass was varied within the range $1.3 \leq m_c \leq 1.7$ GeV/c^2, with a central value of 1.5 GeV/c^2, and the beauty quark mass was varied within the range $4.5 \leq m_b \leq 5$ GeV/c^2, with a central value of 4.75 GeV/c^2 [36]. f_prompt was calculated with both methods introduced in Section 5.7 and the full envelope of the uncertainty bands from the two methods obtained when varying the FONLL parameters was taken as a systematic uncertainty. This contribution partly cancels in the nuclear modification factor ratio, because these variations are done simultaneously for the Pb–Pb (p–Pb) yield and for the pp reference cross section.

The prompt fraction depends explicitly also on the ratio of nuclear modification factors of feed-down and prompt D mesons. The uncertainty introduced by the hypothesis on the value of the feed-down D meson R_AA was estimated from the variation of the ratio $R_\mathrm{AA}^\mathrm{feed-down}/R_\mathrm{AA}^\mathrm{prompt}$ in a given range.

The central values for the prompt D^0 elliptic flow, v_2^prompt, were obtained assuming $v_2^\mathrm{feed-down} = v_2^\mathrm{prompt}$ (see Section 5.7). The systematic uncertainty associated with this assumption on $v_2^\mathrm{feed-down}$ was estimated by varying it in the interval $0 \leq v_2^\mathrm{feed-down} \leq v_2^\mathrm{prompt}$. Considering this interval v_2^prompt ranges from v_2^all to $v_2^\mathrm{all}/f_\mathrm{prompt}$. For each p_T bin, a set of f_prompt values was computed by varying the heavy-quark masses and the perturbative scales in the FONLL calculation as indicated at the beginning of the section, and the ratio $R_\mathrm{AA}^\mathrm{feed-down}/R_\mathrm{AA}^\mathrm{prompt}$ in the range $1 < R_\mathrm{AA}^\mathrm{feed-down}/R_\mathrm{AA}^\mathrm{prompt} < 3$, based on the difference of the measured nuclear modification factor of prompt D meson to that of J/ψ from B decays. The smallest value of f_prompt was used to assign the uncertainty related to the B feed-down contribution to the elliptic flow of prompt D^0. The maximum relative uncertainty was about $^{+45}_{-0}$%.

For the R_AA azimuthal dependence analysis in Pb–Pb collisions, the systematic uncertainty due to feed-down correction was obtained varying the hypothesis on the ratio $R_\mathrm{AA}^\mathrm{feed-down}/R_\mathrm{AA}^\mathrm{prompt}$ in the range $1 < R_\mathrm{AA}^\mathrm{feed-down}/R_\mathrm{AA}^\mathrm{prompt} < 3$. The total uncertainty due to feed-down correction, which is in common to the in-plane and out-of-plane R_AA, ranges between $^{+9}_{-13}$% at low p_T and $^{+14}_{-12}$% at high p_T. The hypothesis on the value of v_2 for D^0 mesons from B decays ($0 \leq v_2^\mathrm{feed-down} \leq v_2^\mathrm{prompt}$) introduces an additional contribution to the systematic uncertainty, which is anti-correlated between $R_\mathrm{AA}^\mathrm{in-plane}$

and $R_{\rm AA}^{\rm out-of-plane}$. This uncertainty is typically of $^{+5}_{-0}$% for the in-plane and $^{+0}_{-5}$% for the out-of-plane $R_{\rm AA}$.

For the p–Pb analysis, the considered range was $0.9 < R_{\rm pPb}^{\rm feed-down}/R_{\rm pPb}^{\rm prompt} < 1.3$ taking into account the possible effect of shadowing on the prompt and feed-down D mesons nuclear modification factors (see Figure 5.34). The FONLL rapidity trend was evaluated to be flat within 4% in the rapidity range considered for the analysis ($|y| < 0.8$). Since further modifications of the rapidity shape due to shadowing or other cold nuclear matter effects are considered by the B meson nuclear modification hypothesis, no additional uncertainty to this trend was considered. The overall uncertainty due to feed-down subtraction was $^{+5}_{-47}$% in $1 < p_{\rm T} < 2$ GeV/c and $^{+4}_{-9}$% in $16 < p_{\rm T} < 24$ GeV/c on the cross section as a function of $p_{\rm T}$, $^{+1}_{-7}$% in $1 < p_{\rm T} < 2$ GeV/c and $^{+4}_{-11}$% in $16 < p_{\rm T} < 24$ GeV/c on the $R_{\rm pPb}$, and of about $^{+5}_{-20}$% in $2 < p_{\rm T} < 5$ GeV/c, $^{+5}_{-12}$% in $5 < p_{\rm T} < 8$ GeV/c, and $^{+5}_{-10}$% in $8 < p_{\rm T} < 16$ GeV/c on the cross section as function of rapidity. The $Q_{\rm pPb}$ uncertainties due to feed-down correction were evaluated considering the same procedure adopted for the minimum-bias analysis. The resulting uncertainties are, for example, $^{+1}_{-7}$% and $^{+1}_{-5}$% in $1 < p_{\rm T} < 2$ GeV/c in the 0–20% and 60–100% event-activity classes defined with the ZNA estimator, respectively.

The relative yields expressed as in Equation (4.16) assume that the relative contribution of B decays to the D yields in the different multiplicity intervals is constant and equal to that of the multiplicity integrated sample. With this assumption, $f_{\rm prompt}$ cancels in the ratio between the yield in a given multiplicity interval and that in the multiplicity integrated sample. However, the dependence of B hadrons and prompt D mesons with the charged-particle multiplicity could differ. In order to evaluate a systematic uncertainty due to this effect, a variation of the relative fraction of B/D hadrons with charged-particle multiplicity was considered. The $f_{\rm prompt}$ was calculated with the two methods for the multiplicity-integrated sample, then the fraction of the yield coming from B feed-down was computed as $f_{\rm B} = 1 - f_{\rm prompt}$. In each multiplicity interval $f_{\rm B}$ was varied by a factor increasing from 0.5 to 2 as a function of multiplicity, which parametrizes the variation of the B/D ratio, and a set of $f_{\rm prompt}$ was obtained using the relation $f_{\rm prompt} = 1 - f_{\rm B}$. The range of $f_{\rm prompt}$ was then converted in the uncertainty on the relative yields, in a given multiplicity interval j, by computing $f_{\rm prompt}^{j}/\langle f_{\rm prompt}\rangle$. The systematic uncertainties due to feed-down from B decays ranges from -20% to $+10$% depending on multiplicity interval.

6.8 Proton–Proton Reference

The uncertainty of the pp reference used for the calculation of the nuclear modification factors has two contributions.

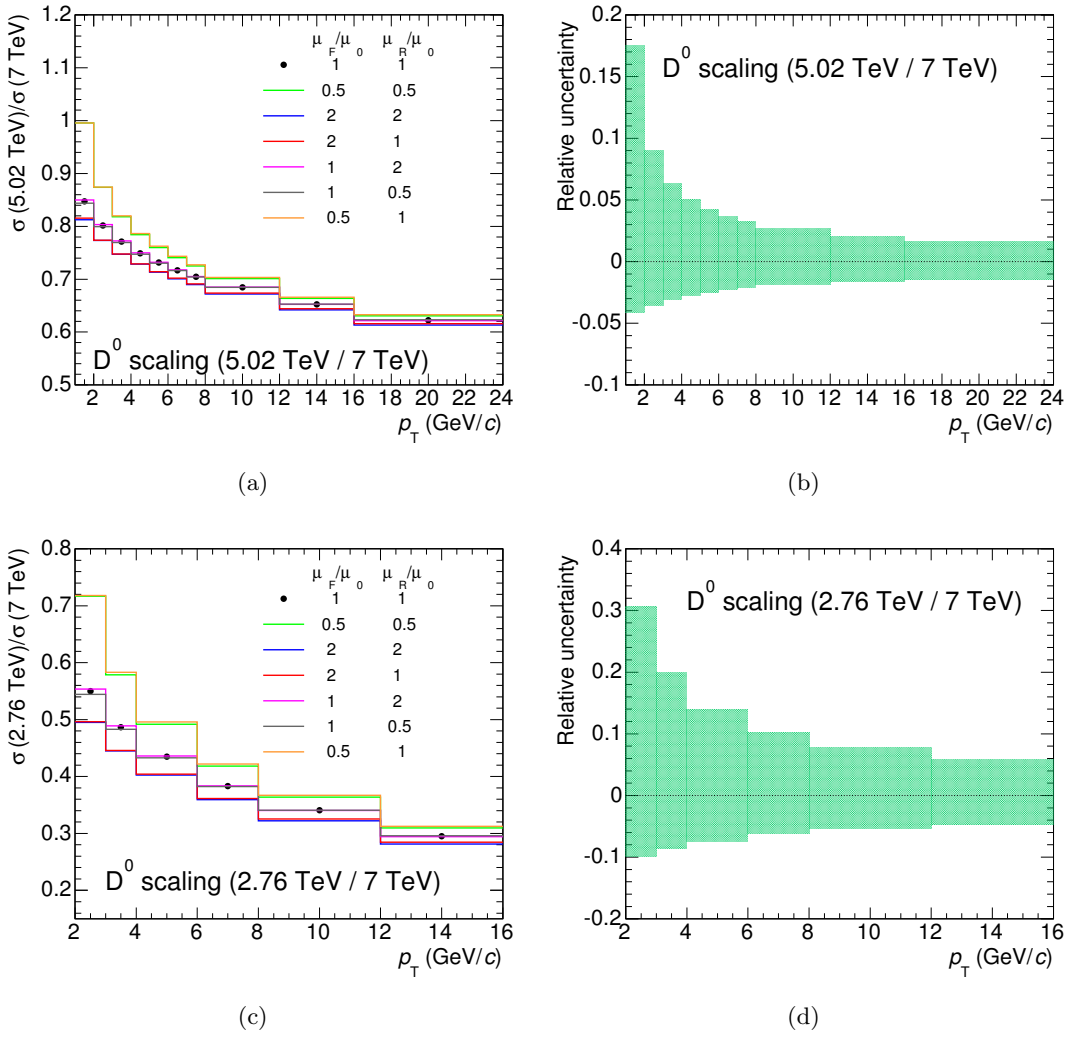

FIGURE 6.20: FONLL scaling factor from 7 TeV to 5.02 TeV (a) and its relative uncertainty (b), and from 7 TeV to 2.76 TeV (c) and its relative uncertainty (d).

The first is due to the systematic uncertainty of the measured D^0 meson p_T-differential cross section at $\sqrt{s} = 7$ TeV, which is of about 17%, approximately independent of p_T [38].

The second contribution is due to the scaling to $\sqrt{s} = 2.76$ TeV or $\sqrt{s} = 5.02$ TeV.

The scaling factors were obtained as explained in Section 4.3 from the ratio of the theoretical cross sections calculated at different energies. The uncertainty due to the scaling was determined by the envelope of the scaling factors obtained by varying the parameters of the FONLL calculation as described in Section 6.7.

The scaling factor from 7 TeV to 5.02 TeV and from 7 TeV to 2.76 TeV, and their associated uncertainty are shown in Figure 6.20. The uncertainty on the scaling factor ranges from $^{+31}_{-10}$% at low p_T to about 5% at high p_T for the Pb–Pb collision energy and from $^{+17.5}_{-4}$% at $p_\mathrm{T} = 1$ GeV/c to about 3% for $p_\mathrm{T} > 8$ GeV/c for the p–Pb collision energy.

TABLE 6.2: Systematic uncertainties on the D^0 v_2 measurement in the 0–10%, 10–30% and 30–50% centrality classes for the interval $4 < p_T < 6$ GeV/c.

Centrality class	0–10%	10–30%	30–50%
Yield extraction	37%	22%	9%
2 or 3 sub-ev. R_2	6.9%	2%	2.3%
R_2 centrality dependence	2%	0.5%	2%
Total (excl. B feed-down)	38%	22%	9%
B feed-down	$^{+50}_{-0}$%	$^{+45}_{-0}$%	$^{+48}_{-0}$%

In the interval $1 < p_T < 2$ GeV/c, the overall uncertainty on the cross section at $\sqrt{s} = 5.02$ TeV obtained by scaling the 2.76 TeV and the 7 TeV pp measurements were similar. The pp reference for this p_T interval was evaluated as the weighted average of these two results, considering their relative statistical and systematic uncertainties as weights. The uncertainty on the weighted average was obtained by propagating all the uncertainty sources.

6.9 Summary of Uncertainties on v_2

The observed v_2 was corrected for the event-plane resolution (Equation (4.6)). The uncertainty on the resolution correction factor R_2 was estimated with the two and three sub-event methods with an η-gap. The three sub-events were defined using the TPC tracks and the signals in the two VZERO detectors. The R_2 values estimated with these two methods differ by 2.3% in the 30–50% centrality class (see Figure 5.1(b)). A symmetric uncertainty equal to the relative difference between R_2 values obtained with the two and three sub-event methods was assigned to the D^0 v_2. The uncertainty due to the centrality dependence of the event-plane resolution was estimated from the difference between two ways to define the average resolution in the centrality class used in the analysis, starting from the resolutions in fine centrality intervals (see Figure 5.1(b)). The two ways considered were a plain arithmetic average and an average weighted with the D meson yield measured in smaller centrality classes (2.5% wide). The latter was estimated using D^0 meson raw yields in wide p_T intervals and the sum of the two $\Delta\varphi$ intervals, in order to reduce statistical fluctuations. The difference between these averages was found to be about 2% for the 30–50% centrality class. The resulting total uncertainty on R_2 amounts to 3%.

Table 6.2 reports a summary of the systematic uncertainties assigned to the D^0 v_2 measurement with the event-plane method in the interval $4 < p_T < 6$ GeV/c. The uncertainties are comparable in the other p_T intervals.

6.10 Summary of Uncertainties on $R_{\rm AA}$ In- and Out-Of-Plane

The $\rm D^0$ yields in the two azimuthal regions with respect to the event plane, obtained from Equation (4.8), were corrected for the event-plane resolution using the correction factor R_2 (Section 5.2) and the relation given in Equation (4.6). For example, the correction factor for the in-plane $R_{\rm AA}$ is $(1+R_2^{-1})/2+(N^{\rm out}/N^{\rm in})(1-R_2^{-1})/2$, where the $N^{\rm in(out)}$ is the $\rm D^0$ raw yield. The value $R_2=(0.8059\pm0.001)$ for the 30–50% centrality class and the typical $N^{\rm out}/N^{\rm in}$ magnitude result in a correction of approximately $+4(-6)\%$ for the in-plane (out-of-plane) yields. The uncertainty of 3% on the event-plane resolution correction factor R_2 in the 30–50% centrality class was also propagated to the $R_{\rm AA}$ observable, resulting in an uncertainty in the range 0.5–2%, depending on the $p_{\rm T}$ interval.

The uncertainties on the pp cross section normalization (3.5%) [38] and the average nuclear overlap function $\langle T_{\rm AA}\rangle$ (4.7%) were also included [16]. The contribution due to the 1.1% relative uncertainty on the fraction of the hadronic cross section used in the Glauber fit to determine the centrality class was obtained by estimating the variation of the D meson $\mathrm{d}N/\mathrm{d}p_{\rm T}$ when the limits of the centrality classes are shifted by $\pm1.1\%$. The resulting uncertainty, common to all $p_{\rm T}$ intervals, is 2% for the 30–50% centrality class. The total normalization uncertainty, computed as the quadratic sum of these three contributions, is 6.2%.

The systematic uncertainties of $R_{\rm AA}$ described in the previous sections were grouped in three categories, depending on their correlation between the in-plane and the out-of-plane measurements. The uncorrelated systematic uncertainties affect the two $R_{\rm AA}$ independently: this category includes only the yield extraction uncertainty. The correlated systematic uncertainties affect the two $R_{\rm AA}$ in the same way and do not change their relative difference. The uncertainties on the efficiency corrections (for track reconstruction and selection cuts, particle identification and $p_{\rm T}$ distribution in the simulation), as well as those on the pp reference, the variation of the pQCD scales and the $R_{\rm AA}^{\rm feed-down}$ hypothesis used for the feed-down subtraction were included in this category. Another correlated uncertainty is due to the normalization ($\langle T_{\rm AA}\rangle$ and centrality class definition), which was quoted separately. The anti-correlated systematics could shift the two $R_{\rm AA}$ in opposite directions, affecting their difference. This category includes the contribution from the unknown azimuthal anisotropy of feed-down D mesons (variation of $v_2^{\rm feed-down}$) and the contribution from the event-plane resolution correction factor. Within each category, the uncertainties from different sources were added in quadrature.

The summary of the systematic uncertainties assigned to the $\rm D^0$ $R_{\rm AA}$ in-plane and out-of-plane is reported in Table 6.3 for two $p_{\rm T}$ intervals: $2<p_{\rm T}<3$ GeV/c and

TABLE 6.3: Systematic uncertainties on the measurement of the D^0 R_{AA} in-plane and out-of-plane in the 30–50% centrality class for two p_T intervals. The uncertainties are grouped according to the type of correlation between the in-plane and out-of-plane cases.

p_T interval (GeV/c)	2–3	12–16
Uncorrelated uncertainties		
Yield extraction	7%	10%
Total uncorrelated	7%	10%
Correlated uncertainties		
Correction for reflections	1%	5%
Tracking efficiency	10%	10%
Cut efficiency	10%	10%
PID efficiency	5%	5%
D^0 p_T distribution in MC	2%	0
pp reference	$^{+20}_{-35}$%	18%
Data syst.	17%	17%
$\sqrt{s}$ scaling	$^{+10}_{-31}$%	$^{+5}_{-6}$%
B feed-down yield	$^{+9}_{-13}$%	$^{+14}_{-12}$%
Total correlated	$^{+22}_{-37}$%	$^{+28}_{-27}$%
Normalization uncertainties		
pp cross section norm.	3.5%	
$\langle T_{AA} \rangle$	4.7%	
Centrality class definition	2%	
Total normalization	6.2%	
Anti-correlated uncertainties		
Uncertainty on R_2	0.5%	0.5%
B feed-down v_2	in:$^{+4}_{-0}$%; out:$^{+0}_{-6}$%	in:$^{+7}_{-0}$%; out:$^{+0}_{-5}$%
Total anti-correlated	in:$^{+4}_{-0.5}$%; out:$^{+0.5}_{-6}$%	in:$^{+7}_{-0.5}$%; out:$^{+0.5}_{-5}$%

$12 < p_T < 16$ GeV/c. The uncertainties are grouped according to their correlation category.

6.11 Summary of Uncertainties on the Cross Section in p–Pb Collisions and on R_{pPb}

The measured cross sections have a global systematic uncertainty due to the branching ratio (1.3%) and to the determination of the integrated luminosity (3.7%) (see Equation (4.12)).

TABLE 6.4: Systematic uncertainties on the D^0 $\mathrm{d}\sigma/\mathrm{d}p_{\mathrm{T}}$ minimum-bias measurement in p–Pb collisions for two p_{T} intervals.

p_{T} interval (GeV/c)	1–2	16–24
Yield extraction	8%	11%
Correction for reflections	3%	4%
Tracking efficiency	6%	6%
Cut efficiency	8%	5%
PID efficiency	0	0
D^0 p_{T} distribution in MC	2%	0
B feed-down yield	$^{+5}_{-47}$%	$^{+4}_{-9}$%
Total (p_{T}-dependent)	$^{+14}_{-49}$%	$^{+15}_{-17}$%
Normalization	3.7%	
Branching ratio	1.3%	

Table 6.4 summarizes the various sources of systematic uncertainty for the D^0 $\mathrm{d}\sigma/\mathrm{d}p_{\mathrm{T}}$ measurement. The contribution for each source is reported for two p_{T} intervals: $1 < p_{\mathrm{T}} < 2$ GeV/c and $16 < p_{\mathrm{T}} < 24$ GeV/c.

TABLE 6.5: Systematic uncertainties on the D^0 R_{pPb} measurement. The data systematics were estimated for the cross section measurement, they include the contributions due to the yield extraction, correction for reflection, tracking/cut/PID efficiency and simulated D^0 p_{T} distribution.

p_{T} interval (GeV/c)	1–2	16–24
Data systematics	13%	14%
B feed-down yield	$^{+1}_{-7}$%	$^{+4}_{-11}$%
pp reference (data + scaling)	21%	$^{+31}_{-42}$%
Total (p_{T}-dependent)	$^{+25}_{-26}$%	$^{+34}_{-46}$%
Normalization	3.7%	

The D^0 R_{pPb} was calculated starting from the p_{T}-differential cross section, the final systematic uncertainties were obtained by combining in quadrature the pp $\mathrm{d}\sigma/\mathrm{d}p_{\mathrm{T}}$

and the p–Pb $\mathrm{d}\sigma/\mathrm{d}p_{\mathrm{T}}$ uncertainties (Table 6.4), except for the branching ratio uncertainty (which cancels in the ratio) and the feed-down correction contribution (which also partially cancels). Table 6.5 summarizes systematic uncertainties that affect the R_{pPb} measurement.

The summary of the systematic uncertainties estimated for the double p_{T}- and y-differential cross section measurement are reported in Tables 6.6, 6.7 and 6.8.

TABLE 6.6: Systematic uncertainties on the D^0 $\mathrm{d}^2\sigma/\mathrm{d}p_{\mathrm{T}}\mathrm{d}y$ measurement in $2 < p_{\mathrm{T}} < 5$ GeV/c for the five y_{lab} intervals considered in the analysis.

p_{T} interval (GeV/c)	2–5				
y_{lab} interval	$(-0.7, -0.4)$	$(-0.4, -0.1)$	$(-0.1, 0.1)$	$(0.1, 0.4)$	$(0.4, 0.7)$
Yield extraction	4%	3%	10%	3%	4%
Correction for reflections	3%	3%	3%	3%	3%
Tracking efficiency	6%	6%	6%	6%	6%
Cut efficiency	5%	5%	5%	5%	5%
PID efficiency	0	0	0	0	0
D^0 p_{T} distribution in MC	8%	8%	8%	8%	8%
B feed-down yield	$^{+4}_{-20}$%	$^{+5}_{-22}$%	$^{+5}_{-22}$%	$^{+5}_{-22}$%	$^{+5}_{-21}$%
Total (y_{lab}-dependent)	$^{+13}_{-23}$%	$^{+13}_{-25}$%	$^{+16}_{-27}$%	$^{+13}_{-25}$%	$^{+13}_{-24}$%
Normalization	3.7%				
Branching ratio	1.3%				

TABLE 6.7: Systematic uncertainties on the D^0 $\mathrm{d}^2\sigma/\mathrm{d}p_{\mathrm{T}}\mathrm{d}y$ measurement in $5 < p_{\mathrm{T}} < 8$ GeV/c for the five y_{lab} intervals considered in the analysis.

p_{T} interval (GeV/c)	5–8				
y_{lab} interval	$(-0.8, -0.4)$	$(-0.4, -0.1)$	$(-0.1, 0.1)$	$(0.1, 0.4)$	$(0.4, 0.8)$
Yield extraction	5%	5%	10%	5%	5%
Correction for reflections	3%	3%	3%	3%	3%
Tracking efficiency	6%	6%	6%	6%	6%
Cut efficiency	5%	5%	5%	5%	5%
PID efficiency	0	0	0	0	0
D^0 p_{T} distribution in MC	2%	2%	2%	2%	2%
B feed-down yield	$^{+5}_{-12}$%	$^{+5}_{-12}$%	$^{+5}_{-12}$%	$^{+5}_{-12}$%	$^{+5}_{-11}$%
Total (y_{lab}-dependent)	$^{+11}_{-15}$%	$^{+11}_{-15}$%	$^{+14}_{-18}$%	$^{+11}_{-15}$%	$^{+11}_{-15}$%
Normalization	3.7%				
Branching ratio	1.3%				

TABLE 6.8: Systematic uncertainties on the D^0 $\mathrm{d}^2\sigma/\mathrm{d}p_\mathrm{T}\mathrm{d}y$ measurement in $8 < p_\mathrm{T} < 16$ GeV/c for the five y_lab intervals considered in the analysis.

p_T interval (GeV/c)	8–16				
y_lab interval	$(-0.8, -0.4)$	$(-0.4, -0.1)$	$(-0.1, 0.1)$	$(0.1, 0.4)$	$(0.4, 0.8)$
Yield extraction	5%	5%	10%	5%	5%
Correction for reflections	4%	4%	4%	4%	4%
Tracking efficiency	6%	6%	6%	6%	6%
Cut efficiency	5%	5%	5%	5%	5%
PID efficiency	0	0	0	0	0
D^0 p_T distribution in MC	5%	5%	5%	5%	5%
B feed-down yield	$^{+4}_{-9}$%	$^{+5}_{-10}$ %	$^{+5}_{-10}$ %	$^{+5}_{-10}$ %	$^{+5}_{-10}$ %
Total (y_lab-dependent)	$^{+12}_{-14}$%	$^{+12}_{-15}$%	$^{+15}_{-17}$%	$^{+12}_{-15}$%	$^{12}_{15}$%
Normalization	3.7%				
Branching ratio	1.3%				

6.12 Summary of Uncertainties on Q_pPb and Relative Yields

The data systematic uncertainties on the corrected yields used to calculate the D^0 Q_pPb are the same as a function of p_T in the four event-activity classes and for the three estimators (CL1, V0A, ZNA). Table 6.9 reports the systematic uncertainties for two event classes (0–20% and 60–100%) defined with the ZNA estimator, for two p_T intervals: $1 < p_\mathrm{T} < 2$ GeV/c and $12 < p_\mathrm{T} < 16$ GeV/c. The uncertainties on $\langle T_\mathrm{pA} \rangle$ calculated with the Glauber approach or the hybrid method were also taken into account [108].

Table 6.10 reports the summary of the yield extraction systematics that were estimated in each p_T and $N_\mathrm{tracklets}$ interval and affect the relative corrected yields as a function of charged-particle multiplicity at central rapidity. A systematic uncertainty of 3% on the relative charged-particle multiplicity values was also estimated. The main contribution to this uncertainty originates from the deviation from a linear dependence of $\mathrm{d}N_\mathrm{ch}/\mathrm{d}\eta$ on $N_\mathrm{tracklets}$ and from the systematic uncertainty on the measurement of $\langle \mathrm{d}N_\mathrm{ch}/\mathrm{d}\eta \rangle$.

Table 6.11 reports the summary of the yield extraction systematics that were estimated in each p_T and N_V0A interval and affect the relative corrected yields as a function of charged-particle multiplicity at forward rapidity.

TABLE 6.9: Systematic uncertainties on the D^0 Q_{pPb} measurement in p–Pb collisions in two p_T intervals for the event-activity classes 0–20% and 60–100% defined with the ZNA estimator.

p_T interval (GeV/c)	1–2		12–16	
Event-activity class	0–20%	60–100%	0–20%	60–100%
Yield extraction	8%		8%	
Correction for reflections	3%		4%	
Tracking efficiency	6%		6%	
Cut efficiency	10%		5%	
PID efficiency	0		0	
D^0 p_T distribution in MC	2%		0	
Mult. distribution in MC	5%	10%	3%	3%
B feed-down yield	$^{+1}_{-7}$%	$^{+1}_{-5}$%	$^{+2}_{-5}$%	$^{+2}_{-5}$%
pp ref. (data + scaling)	21%		15%	
Total (p_T-dependent)	$^{+26}_{-27}$%	26%	$^{+18}_{-19}$%	$^{+18}_{-19}$%
$\langle T_{pA} \rangle$	6.6%	6.5%	6.6%	6.5%

TABLE 6.10: Summary table of the yield extraction systematics for the $N_{tracklets}$ and p_T intervals considered in the analysis of the relative corrected yields as a function of charged-particle multiplicity at central rapidity.

p_T (GeV/c)	$N_{tracklets}$ interval					
	1–24	25–44	45–59	60–74	75–99	100–199
1–2	4%	3%	3%	5%	6%	–
2–4	3%	3%	3%	3%	3%	5%
4–8	3%	3%	3%	3%	3%	5%
8–12	4%	3%	3%	3%	4%	5%
12–24	6%	3%	3%	5%	5%	–

TABLE 6.11: Summary table of the yield extraction systematics for the N_{V0A} and p_T intervals considered in the analysis of the relative corrected yields as a function of charged-particle multiplicity at forward rapidity.

p_T (GeV/c)	N_{V0A} interval				
	1–90	91–131	132–172	173–225	226–797
1–2	5%	5%	5%	5%	
2–4	5%	5%	5%	5%	5%
4–8	5%	5%	5%	3%	5%
8–12	5%	5%	5%	3%	5%
12–24	10%	8%	8%	5%	

7

Azimuthal Anisotropy of D^0 Production in Pb–Pb Collisions

The results on the azimuthal anisotropy of D meson production in Pb–Pb collisions at $\sqrt{s_{\rm NN}} = 2.76$ TeV are presented in this chapter. The azimuthal anisotropy was quantified in terms of the elliptic flow v_2 and of the nuclear modification factor $R_{\rm AA}$, measured in the direction of the event plane and orthogonal to it. Section 7.1 is devoted to the v_2 results: the D^0 elliptic flow is presented as a function of $p_{\rm T}$ in the 30–50% centrality class. v_2 was also measured in the 0–10% and 10–30% centrality classes to investigate its dependence on the collision centrality. The average D meson elliptic flow is compared in this section with the charged-particle v_2 measured with the event-plane method. The results of the D^0 $R_{\rm AA}$ measured in the in-plane and in the out-of-plane regions, in the 30–50% centrality class, are presented in Section 7.3. Section 7.4 is devoted to the comparison of the average D meson v_2 in the 30–50% centrality class, the average D meson nuclear modification factor in 0–20% Pb–Pb collisions, and the D^0 meson $R_{\rm AA}$ in-plane and out-of-plane to theoretical calculations.

7.1 Elliptic Flow

The D^0 elliptic flow v_2 measured in Pb–Pb collisions in the 30–50% centrality class with the event-plane method is shown as a function of $p_{\rm T}$ in Figure 7.1 [67]. The v_2 measurement was performed also for the D^+ and D^{*+} mesons (Figure 7.2). The event plane was estimated with TPC tracks in $0 < \eta < 0.8$, as explained in Section 5.2. The symbols are positioned horizontally at the average $p_{\rm T}$ of reconstructed D mesons. This value was determined as the average of the $p_{\rm T}$ distribution of candidates in the signal invariant mass region, after subtracting the contribution of the background candidates, which was estimated from the side bands. The average $p_{\rm T}$ of the reconstructed D mesons is larger

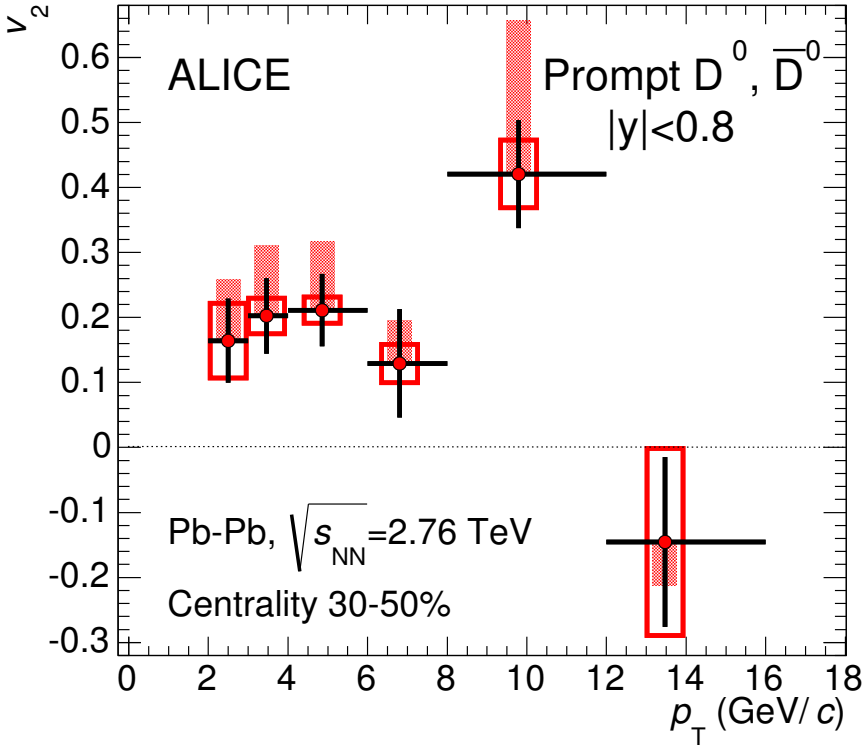

FIGURE 7.1: Elliptic flow v_2 as a function of p_{T} for prompt D^0 mesons measured with the event-plane method in Pb–Pb collisions in the 30–50% centrality class [67].

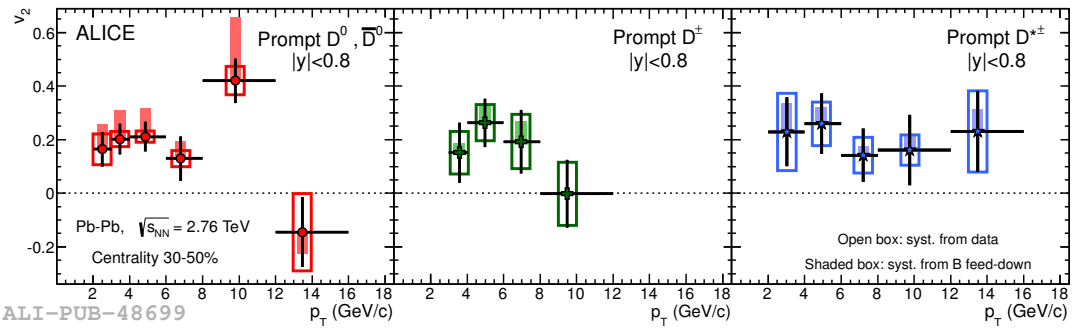

FIGURE 7.2: v_2 as a function of p_{T} for prompt D^0, D^+, and D^{*+} mesons for Pb–Pb collisions in the 30–50% centrality class [67].

than that of the produced D mesons, because the efficiency increases with increasing p_{T} (see Figure 5.25). The vertical error bars represent the statistical uncertainty, the open boxes are the systematic uncertainties from the anisotropy determination and the event-plane resolution, and the filled boxes are the uncertainties due to B feed-down contribution. The elliptic flow of the three D meson species is consistent within statistical uncertainties and ranges between 0.1 and 0.3 in the interval $2 < p_{\mathrm{T}} < 8$ GeV/c. For $p_{\mathrm{T}} > 12$ GeV/c, v_2 is consistent with zero within the large statistical uncertainties.

For the 30–50% centrality class, an average v_2 of D^0, D^+ and D^{*+} was computed

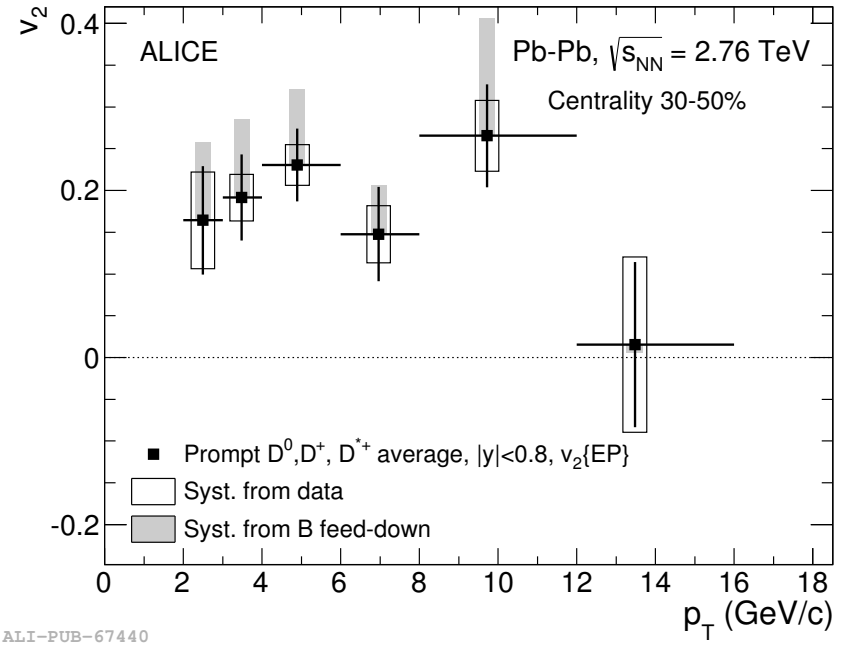

FIGURE 7.3: Average of D^0, D^+, and D^{*+} v_2 as a function of p_T in the 30–50% centrality class, measured with the event-plane method. The symbols are positioned horizontally at the average p_T of the three D meson species [67].

using the inverse of the statistical uncertainties as weights. The systematic uncertainties were propagated through the averaging procedure, treating the contributions from the event-plane resolution and the B feed-down correction as fully correlated among the three D meson species. The resulting D meson v_2, shown in Figure 7.3, has a value 0.204 ± 0.030 (stat.) ± 0.020 (syst.) $^{+0.092}_{-0}$ (B feed-down), averaged over the p_T intervals 2–3, 3–4, 4–6 GeV/c. This value is larger than zero with a significance, calculated from the combined statistical and systematic uncertainties, of 5.7σ.

The azimuthal anisotropy of D^0 mesons was also measured in more central Pb–Pb events. Figure 7.4 shows the D^0 v_2 in the three centrality classes 0–10%, 10–30% and 30–50% as a function of p_T. The D^0 meson v_2 is compared to that of charged particles [122], for the same centrality classes. D meson and charged particle results are obtained with the event-plane method using TPC and the VZERO detectors, respectively. The magnitude of elliptic flow is similar for charmed hadrons and light-flavour hadrons (π, K, p), which dominate the charged-particle sample.

The centrality dependence of the D^0 elliptic flow is shown in Figure 7.5 for three transverse momentum intervals in the range $2 < p_T < 6$ GeV/c. A decreasing trend of v_2 towards more central collisions is observed, as expected because of the decreasing initial geometrical anisotropy.

The results indicate that, during the collective expansion of the medium, the interactions between its constituents and charm quarks transfer to the latter information on

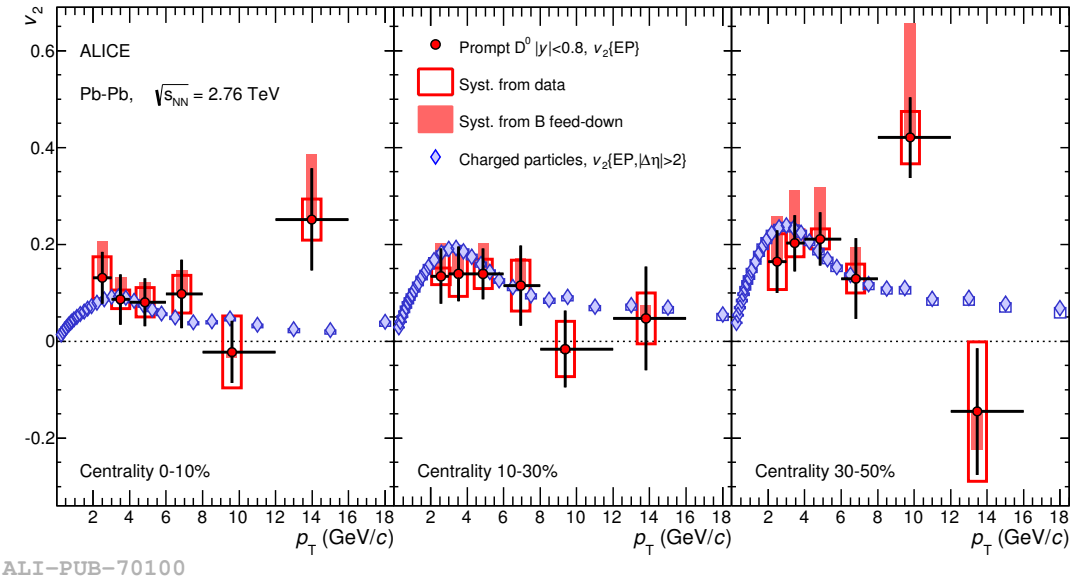

FIGURE 7.4: Comparison of prompt D^0 meson and charged-particle v_2 [122] in three centrality classes as a function of p_T. Both measurements were done with the event-plane method [111].

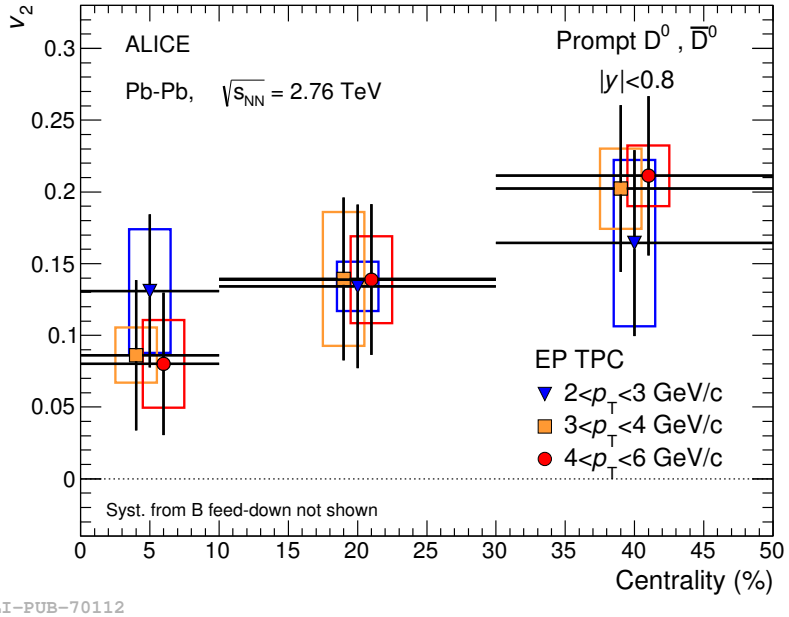

FIGURE 7.5: D^0 meson v_2 with the event-plane method in three p_T intervals as a function of centrality [111].

the azimuthal anisotropy of the system.

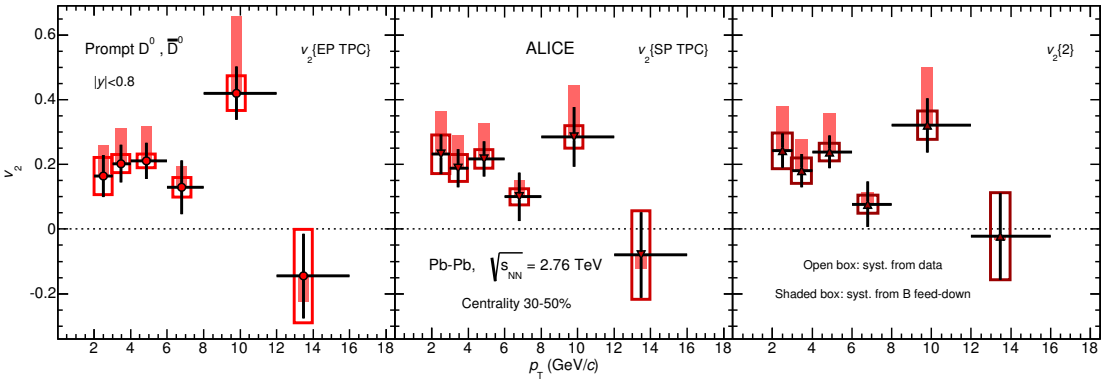

FIGURE 7.6: D^0 meson v_2 as a function of p_T in the 30–50% centrality class, with the event-plane, scalar product and two-particle cumulant methods. For the first method, the event plane was estimated with TPC tracks in the positive η region; for the other methods, TPC tracks in $-0.8 < \eta < 0.8$ were used as reference particles [111].

7.2 Comparison with Other Methods for v_2 Measurement

The v_2 measured with the event-plane method using reference particles from the TPC detector could be affected by non-flow correlations, because the η range of the reference particles overlaps with the D meson acceptance. Non-flow correlations originate from momentum conservation, quantum statistics, resonance or cascade-like decays and from jets. The D^0 v_2 was also measured [111] with respect to the event plane obtained from the VZERO detectors (i.e. with a large η-gap with respect to the D mesons), with a scalar product [123] and a two-particle cumulant [124] methods. These methods allow to reduce the the non-flow effects in the measured v_2. The elliptic flow was computed with the scalar product method by correlating D mesons from the positive η region with the charged particles in the negative η region, and vice versa. This separation in pseudorapidity suppresses two-particle correlations at short distance attributable to decays ($D^* \to D + X$ and $B^* \to D^{(*)} + X$). The two-particle cumulant is an average of two-particle correlation, different order cumulants provide independent estimates for the same harmonic coefficient v_n. Orders higher than two are less affected by non-flow effects, but the D meson analysis was doable considering two-particle correlations only, given the available statistics.

Figure 7.6 shows the D^0 v_2 measured with the event-plane, scalar product and two-particle cumulant methods. The results from the three methods are consistent within statistical uncertainties.

Figure 7.7 shows the elliptic flow of the D^0 mesons measured with the event-plane and scalar product methods using reference particles from the TPC detector or from the VZERO detectors (η-gap of $\Delta\eta \geq 0.9$ between D^0 mesons and reference particles). The

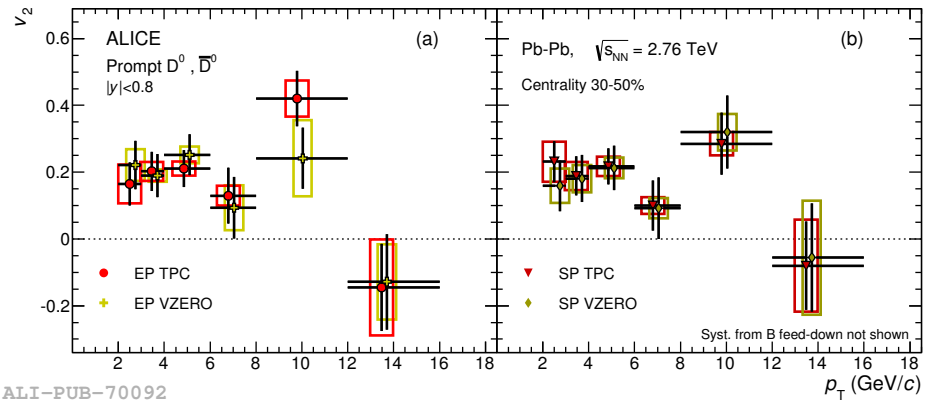

FIGURE 7.7: D^0 meson v_2 as a function of p_T in the 30–50% centrality class, with reference particles from TPC or from the VZERO detectors. (a) Event-plane method. (b) Scalar product method [111].

agreement between the results with and without η-gap indicates that the bias owing to non-flow correlations is within the statistical precision of the measurement.

7.3 R_{AA} In and Out of the Event Plane

The nuclear modification factors of D^0 mesons in the 30–50% centrality class are shown in Figure 7.8 for the in-plane and out-of-plane directions with respect to the event plane. The error bars represent the statistical uncertainties, which are to a large extent independent for the two azimuthal intervals, since they are dominated by the statistical uncertainties of the Pb–Pb data. The uncorrelated (empty boxes), correlated (brackets), and anti-correlated (shaded boxes) systematic uncertainties are shown separately (see Table 6.3 for the type of correlation between the in-plane and the out-of-plane cases of the various sources of uncertainty). The normalization uncertainty, shown as a box at $R_{AA} = 1$, is common to both measurements.

A large suppression is observed in both directions with respect to the event plane for $p_T > 4$ GeV/c. At lower transverse momentum, the suppression appears to be reduced, especially in the in-plane direction, where R_{AA} reaches unity at a p_T of 2–3 GeV/c. Overall, a stronger suppression in the out-of-plane direction is observed, where the average path length of heavy quarks through the medium is larger. The ordering $R_{AA}^{\mathrm{out-of-plane}} < R_{AA}^{\mathrm{in-plane}}$ is equivalent to the observation of $v_2 > 0$, since Equation (4.6) can be expressed also as

$$v_2\{\mathrm{EP}\} = \frac{\pi}{4} \frac{R_{AA}^{\mathrm{in-plane}} - R_{AA}^{\mathrm{out-of-plane}}}{R_{AA}^{\mathrm{in-plane}} + R_{AA}^{\mathrm{out-of-plane}}} . \tag{7.1}$$

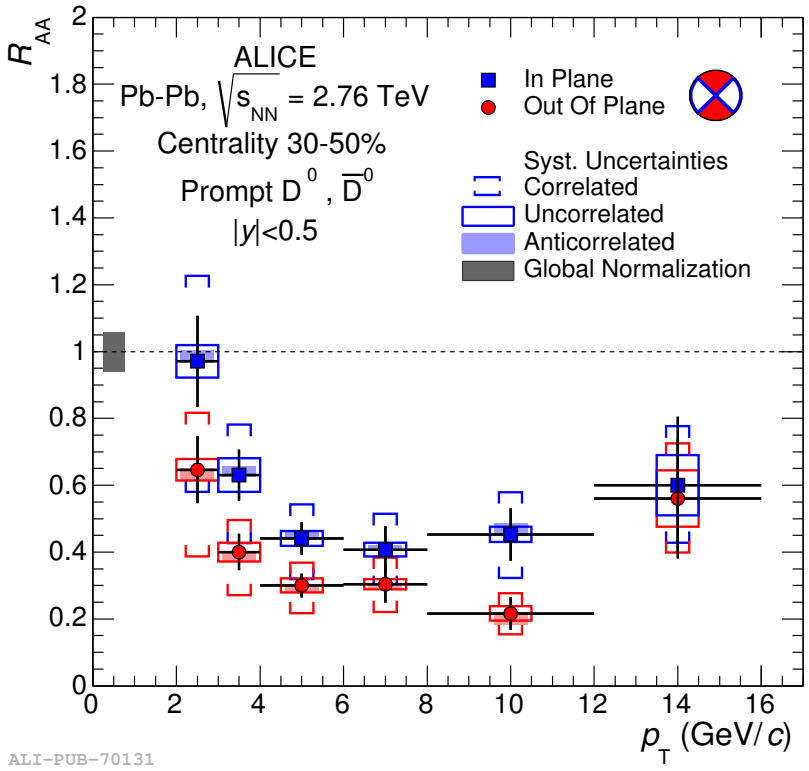

FIGURE 7.8: Nuclear modification factor R_{AA} of D^0 in the 30–50% centrality class in two 90°-wide azimuthal intervals centered on the in-plane and on the out-of-plane directions. The correlated, uncorrelated and anti-correlated contributions to the systematic uncertainty are shown separately [111].

7.4 Comparison with Model Calculations

Several theoretical model calculations are available for the elliptic flow coefficient v_2 and the nuclear modification factor R_{AA} of heavy-flavour hadrons. Figure 7.9 shows a comprehensive comparison of these models to measurements of the D^0 R_{AA} in-plane and out-of-plane in the 30–50% centrality class, the average R_{AA} of D^0, D^+ and D^{*+} in the 0–20% centrality class [63], and of the v_2 averaged over the D meson species in the centrality class 30–50% [67].

The models that were considered and compared to data are:

I WHDG [125–127]. It is a perturbative QCD calculation of parton energy loss, including both radiative (DGLV [128]) and collisional processes. A realistic collision geometry based on the Glauber model [15] is used, without hydrodynamical expansion, so that the anisotropy results only from path-length dependent energy loss. Hadronization is performed using vacuum fragmentation functions. The medium density is constrained on the basis of the π^0 R_{AA} in central collisions at

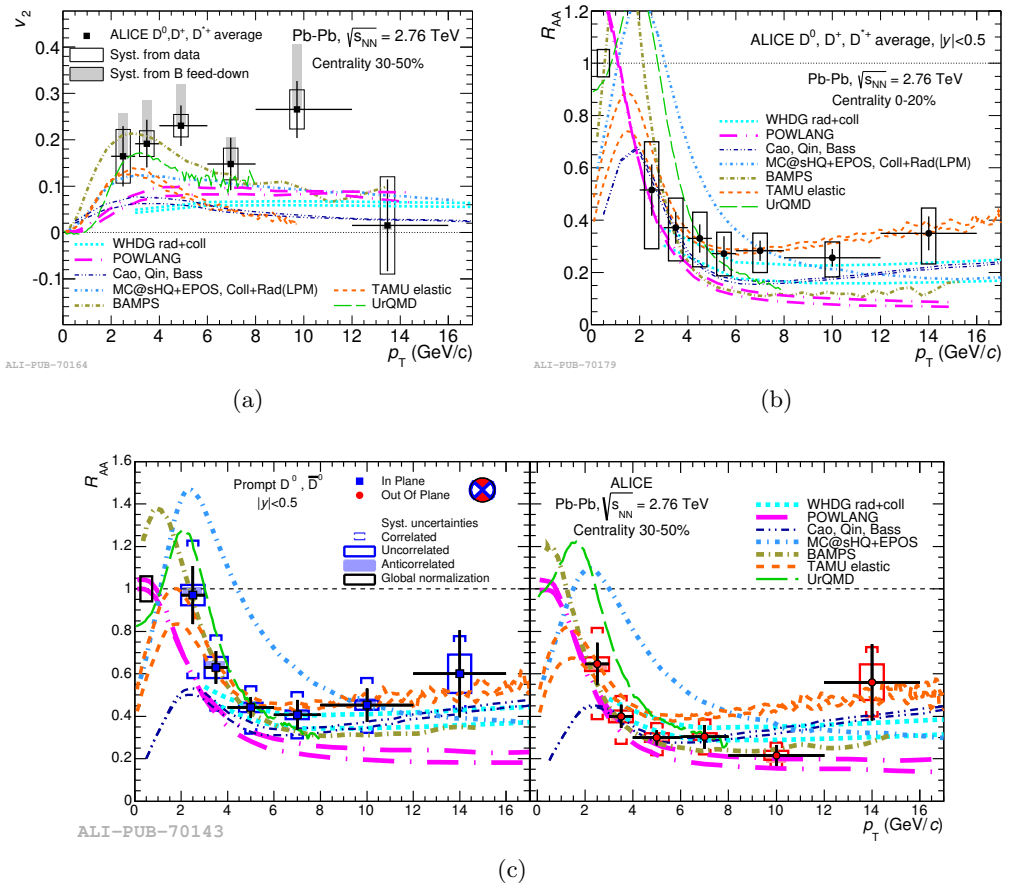

FIGURE 7.9: Model comparison for average D meson v_2 in the 30–50% centrality class [67] (a), average D meson $R_{\rm AA}$ in the 0–20% centrality class [63] (b), D^0 $R_{\rm AA}$ in-plane and out-of-plane in the 30–50% centrality class [111] (c). The seven models calculations are described in the text. The models WHDG rad+coll, POWLANG, TAMU elastic and UrQMD are shown by two lines that represent their uncertainty.

$\sqrt{s_{\rm NN}} = 200$ GeV and scaled to the LHC energy according to the increase of the charged-particle multiplicity. The model describes well the D meson $R_{\rm AA}$ in the centrality interval 0–20% (slightly overestimating the suppression, as it does also for charged particles [63]), and gives an almost $p_{\rm T}$-independent $v_2 \approx 0.06$, which is smaller than the measured values in the range $2 < p_{\rm T} < 6$ GeV/c. Consequently, the difference between the in-plane and the out-of-plane $R_{\rm AA}$ suppression is underestimated: the model describes well the out-of-plane $R_{\rm AA}$ and lies below the in-plane $R_{\rm AA}$.

II MC@sHQ+EPOS, Coll+Rad(LPM) [129]. This pQCD model includes collisional and radiative (with Landau-Pomeranchuk-Migdal correction [130]) energy loss mechanisms for heavy quarks with running strong coupling constant. The medium fluid dynamical expansion is based on the EPOS model [131, 132]. A component of recombination of heavy quarks with light-flavour quarks from the QGP is also

incorporated in the model. This model yields a substantial anisotropy ($v_2 \approx 0.12$–0.08 from low to high p_{T}), which is close to that observed in data. The nuclear modification factor is substantially overestimated below $p_{\mathrm{T}} \approx 5$ GeV/c and correctly described at higher p_{T}.

III TAMU elastic [133]. This is a heavy-flavour transport model based on collisional, elastic processes only. The heavy-quark transport coefficient is calculated within a non-perturbative T-matrix approach, where the interaction proceeds via resonance formation that transfers momentum from the heavy quarks to the medium constituents. The model includes hydrodynamical medium evolution, constrained by light-flavour hadron spectra and elliptic flow data, and a component of recombination of heavy quarks with light-flavour quarks from the QGP. Diffusion of heavy-flavour hadrons in the hadronic phase is also included. The model provides a good description of the observed suppression of D mesons over the entire p_{T} range. The maximum anisotropy, v_2 of about 0.13 at $2 < p_{\mathrm{T}} < 4$ GeV/c, is close to that observed in the data. Towards larger p_{T}, the model tends to underestimate v_2, as well as the difference of the in-plane and the out-of-plane R_{AA}.

IV POWLANG [134, 135]. This transport model is based on collisional processes treated within the framework of Langevin dynamics, within an expanding deconfined medium described by relativistic viscous hydrodynamics. The transport coefficients entering into the relativistic Langevin equation are evaluated by matching the hard-thermal-loop calculation of soft collisions with a perturbative QCD calculation for hard scatterings. Hadronization is implemented via vacuum fragmentation functions. This model overestimates the high-p_{T} suppression, it yields a value for v_2 significantly smaller than observed in data and also underestimates the difference between the in-plane and the out-of-plane suppression.

V BAMPS [119–121]. This partonic transport model is based on the Boltzmann approach to multi-parton scattering. Heavy quarks interact with the medium via collisional processes computed with running strong coupling constant. Hadronization is performed using vacuum fragmentation functions. The lack of radiative processes is accounted for by scaling the binary cross section with a correction factor, which is tuned to describe the heavy-flavour decay electron elliptic flow and nuclear modification factor at RHIC. When applied to calculation for LHC energy, this correction factor results in an underestimation of the D meson R_{AA} for $p_{\mathrm{T}} > 5$ GeV/c and a large azimuthal anisotropy, with v_2 values up to 0.20, similar to those observed in the data. The nuclear modification factors in-plane and out-of-plane are well described up to 5 GeV/c, while for higher p_{T} the in-plane R_{AA} is underestimated.

VI UrQMD [136, 137]. The Langevin approach for the transport of heavy quarks is in this case implemented within the UrQMD model [138, 139]. This model includes a realistic description of the medium evolution by combining hadronic transport and ideal hydrodynamics. The transport of heavy quarks is calculated on the basis of a resonance model with a decoupling temperature of 130 MeV. Hadronization via quark coalescence is included. The calculation parameters are tuned to reproduce the heavy-flavour measurements at RHIC ($\sqrt{s_{\rm NN}} = 200$ GeV) and kept unchanged for calculations at the LHC energy. The model describes the measured D meson v_2, as well as $R_{\rm AA}$ in the interval $4 < p_{\rm T} < 8$ GeV/c, but it fails to reproduce the significant suppression measured for $R_{\rm AA}$ at a $p_{\rm T}$ of 2–3 GeV/c.

VII Cao, Qin, Bass [140]. This model is also based on the Langevin approach. In addition to quasi-elastic scatterings, radiative energy loss is incorporated by treating gluon radiation as an additional force term. The space-time evolution of the medium is modeled using a viscous hydrodynamic simulation. The hadronization of heavy quarks has a contribution based on the recombination mechanism. With respect to [140], the curves shown in the figure were obtained with a more recent parametrization for the nuclear shadowing of the parton distribution functions. This model provides a good description of the $R_{\rm AA}$ data in central collisions, but it yields a value of v_2 significantly smaller than the measured one (similar to the WHDG and POWLANG models) and also underestimates the difference between the in-plane and the out-of-plane suppression.

Overall, the anisotropy is qualitatively described by the models that include both charm quark energy loss in a geometrically anisotropic medium and mechanisms that transfer to charm quarks the elliptic flow induced during the system expansion. These mechanisms include collisional processes (MC@sHQ+EPOS, Coll+Rad(LPM), BAMPS) and resonance scattering with hadronization via recombination (TAMU elastic, UrQMD) in a hydrodynamically expanding QGP. Models that do not include a collective expansion of the medium or lack a contribution to the hadronization of charm quarks from recombination with light quarks from the medium predict in general a smaller anisotropy than observed in the data. The comparison for $R_{\rm AA}$ and v_2 shows that it is challenging to simultaneously describe the large suppression of D mesons in central collisions and their anisotropy in non-central collisions. In general, the models that are best in describing $R_{\rm AA}$ tend to underestimate v_2 and the models that describe v_2 tend to underestimate the measured $R_{\rm AA}$ at high $p_{\rm T}$.

8

D^0 Production in p–Pb Collisions

In this chapter the results obtained from the analysis of the D^0 meson production in p–Pb collisions at $\sqrt{s_{NN}} = 5.02$ TeV are presented. The measured production cross sections for prompt D^0 mesons, as well as for prompt D^+, D^{*+} and D_s^+ mesons are presented in Section 8.1 as a function of p_T and rapidity. The nuclear modification factor R_{pPb} results are given in Section 8.2. In this section the average D meson R_{pPb} is also compared to theoretical calculations and to the D meson R_{AA} measured in central and semiperipheral Pb–Pb collisions at $\sqrt{s_{NN}} = 2.76$ TeV. The two last sections are devoted to the study of the multiplicity dependence of the D^0 production in p–Pb collisions: in Section 8.3 the Q_{pPb} as a function of event activity results are presented, and in Section 8.4 the measured relative yields as a function of relative charged-particle multiplicity are given.

8.1 Production Cross Section

The production cross section of D^0 mesons was measured in p–Pb collisions at the centre-of-mass energy per nucleon pair of $\sqrt{s_{NN}} = 5.02$ TeV. The same measurement was performed also for the other D meson species, D^+, D^{*+}, and D_s^+, that were reconstructed in the rapidity interval $|y_{lab}| < 0.5$ via their hadronic decay channels $D^+ \to K^-\pi^+\pi^+$, $D^{*+} \to D^0\pi^+$ and $D_s^+ \to \phi\pi^+ \to K^-K^+\pi^+$ [141].

Figure 8.1 shows the production cross sections as a function of transverse momentum for prompt D^0. The black bars indicate the statistical uncertainty while the boxes indicate the systematic uncertainties due to the measurement of the corrected D meson yields. The p_T-independent normalization uncertainty of 3.7% is indicated separately. The decay branching ratio uncertainty is not included in the boxes, as well. The measurement was performed at midrapidity in the laboratory frame, which corresponds to the interval $-0.96 < y_{cms} < 0.04$ in the centre-of-mass frame, due to the rapidity shift of the centre-of-mass induced by the different energies of the p and Pb beams.

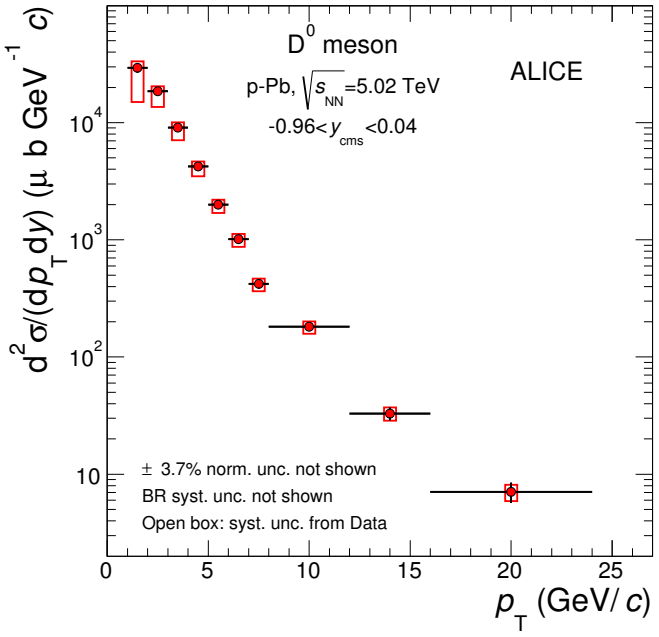

FIGURE 8.1: p_{T}-differential inclusive production cross section of prompt D^0 mesons in p–Pb collisions at $\sqrt{s_{\mathrm{NN}}} = 5.02$ TeV [141].

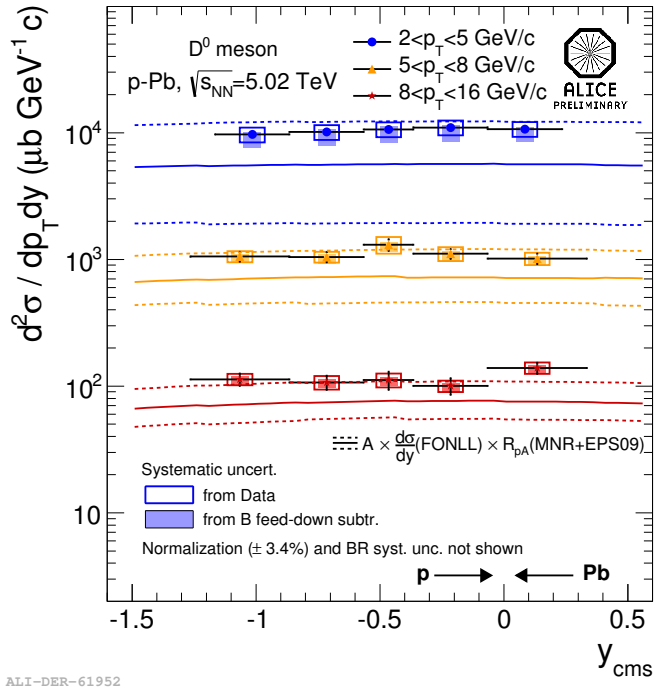

FIGURE 8.2: y-differential production cross section of prompt D^0 mesons in p–Pb collisions at $\sqrt{s_{\mathrm{NN}}} = 5.02$ TeV. The D^0 cross section is compared to a calculation based on NLO pQCD including the nuclear modification of the PDFs as parametrized in EPS09NLO [73], indicated with its uncertainty, by the curves.

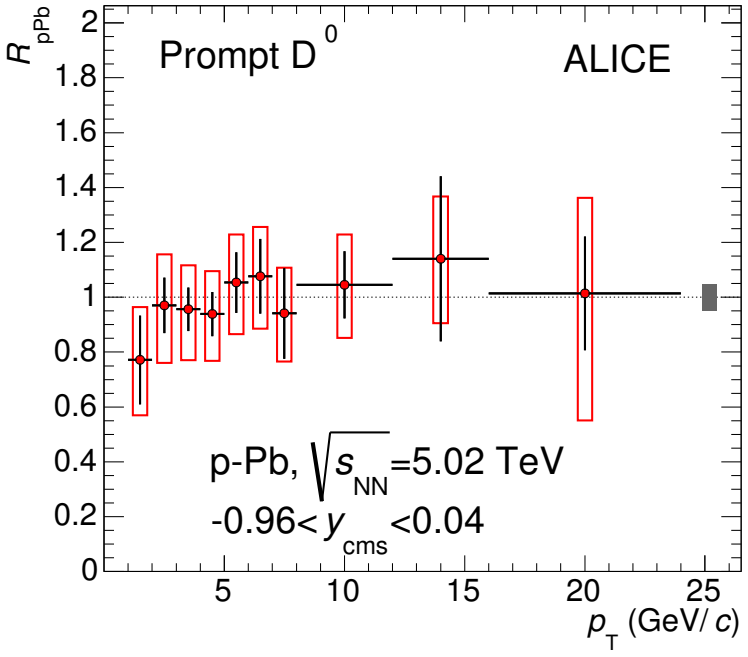

FIGURE 8.3: R_{pPb} as a function of p_{T} for prompt D^0 mesons in p–Pb collisions at $\sqrt{s_{\mathrm{NN}}} = 5.02$ TeV [141].

The y-differential production cross section of prompt D^0 mesons is shown in Figure 8.2. The measurement was carried out in the rapidity range $-1.265 < y < 0.355$, for three p_{T} intervals ($2 < p_{\mathrm{T}} < 5$, $5 < p_{\mathrm{T}} < 8$ and $8 < p_{\mathrm{T}} < 16$ GeV/c). The empty boxes represent the systematic uncertainty due to the corrected yield measurement, while the filled boxes represent the uncertainty arising from the feed-down subtraction. The cross section shows a flat rapidity dependence in the considered p_{T} intervals. The D^0 cross section was compared to a calculation based on next-to-leading order (NLO) pQCD (Mangano, Nason, and Ridolfi (MNR) [28]) including the nuclear modification of the Parton Distribution Functions as parametrized in EPS09NLO [73]. Data are described within uncertainties by this theoretical calculation.

8.2 Nuclear Modification Factor R_{pPb}

The nuclear modification factor, R_{pPb}, of prompt D^0 mesons is shown as a function of p_{T} in Figure 8.3. The vertical bars indicate the statistical uncertainty and the empty boxes indicate the systematic uncertainties. The normalization uncertainty is shown separately as a gray box.

The R_{pPb} was measured also for prompt D^+, D^{*+} and $\mathrm{D}_{\mathrm{s}}^+$ mesons and the nuclear modification factors of the four D meson species are shown in Figure 8.4. The results are consistent among the four D meson species, and they are compatible with unity within

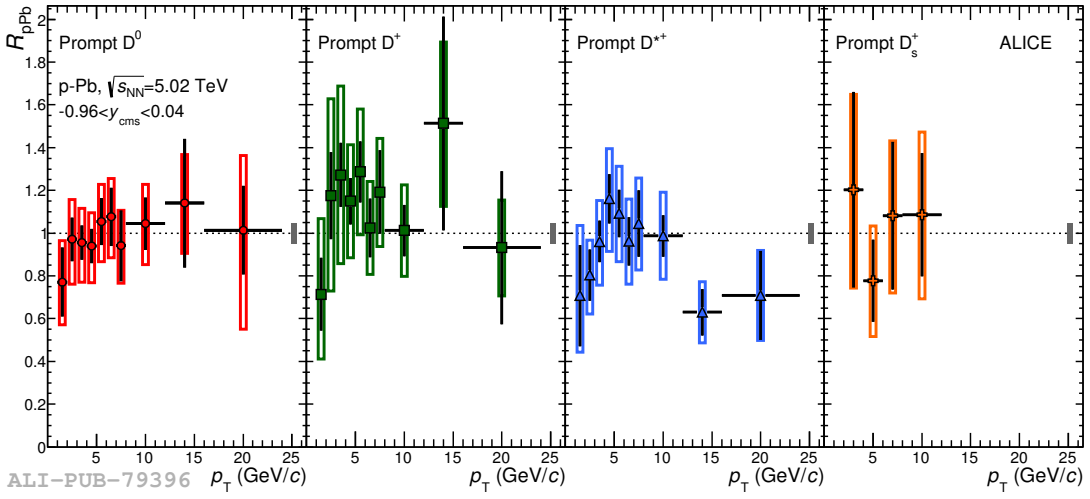

FIGURE 8.4: $R_{\rm pPb}$ as a function of $p_{\rm T}$ for prompt $\rm D^0$, $\rm D^+$, $\rm D^{*+}$ and $\rm D_s^+$ mesons in p–Pb collisions at $\sqrt{s_{\rm NN}} = 5.02$ TeV [141].

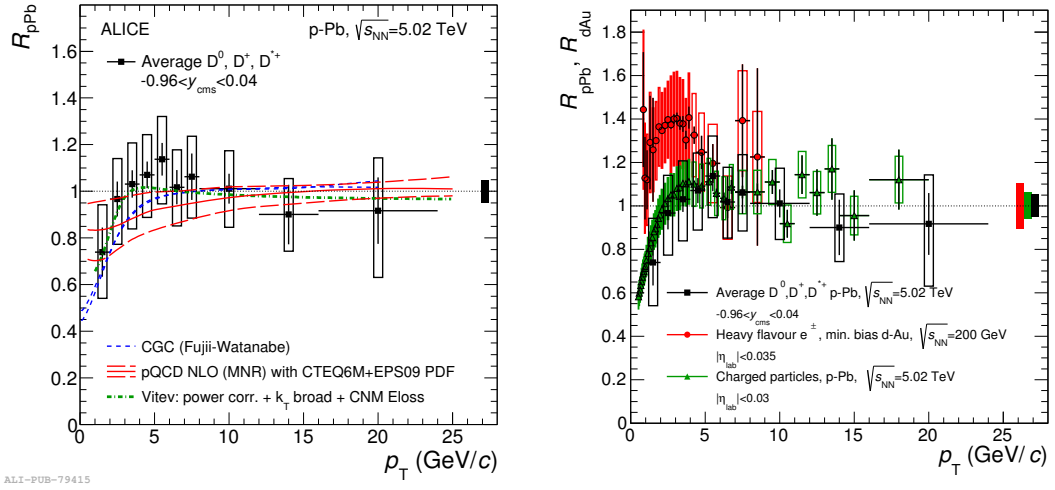

(a) (b)

FIGURE 8.5: Average $R_{\rm pPb}$ of prompt $\rm D^0$, $\rm D^+$, and $\rm D^{*+}$ mesons as a function of $p_{\rm T}$ (black) [141] compared to model calculations (a), and to heavy-flavour electron $R_{\rm dAu}$ measured in minimum bias d–Au collisions at $\sqrt{s_{\rm NN}} = 200$ GeV (red) [96], and to charged-particle $R_{\rm pPb}$ in minimum bias p–Pb collisions at $\sqrt{s_{\rm NN}} = 5.02$ TeV [110] (b).

uncertainties. The D meson production in p–Pb collisions is consistent within statistical and systematic uncertainties with the binary collision scaling of the production in pp collisions.

The average of the $R_{\rm pPb}$ of $\rm D^0$, $\rm D^+$, and $\rm D^{*+}$ in the $p_{\rm T}$ range $1 < p_{\rm T} < 24$ GeV/c was calculated using the inverse of the relative statistical uncertainties as weights [141]. The systematic error on the average was calculated by propagating the uncertainties through the weighted average, where the contributions from tracking efficiency, B feed-down correction and scaling of the pp reference were taken as fully correlated among

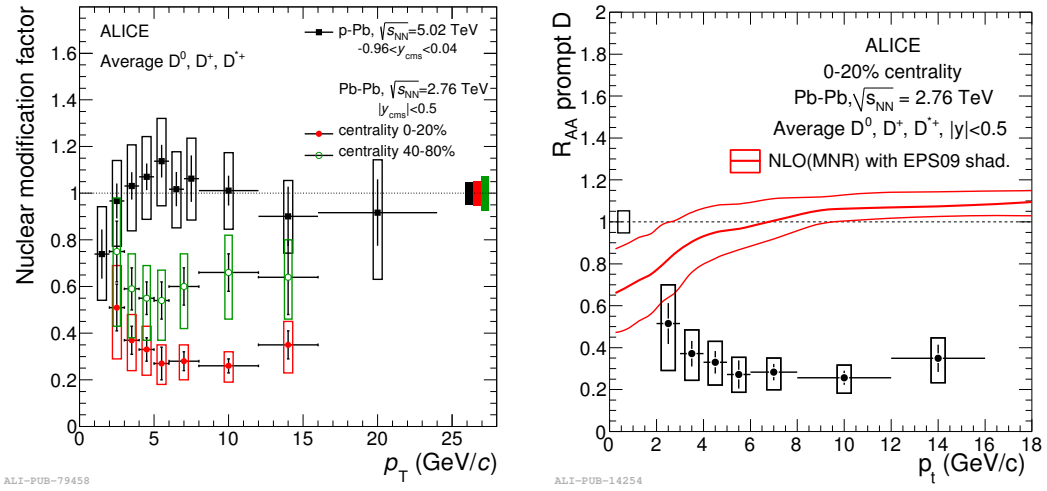

(a) (b)

FIGURE 8.6: (a) Average $R_{\rm pPb}$ of prompt $\rm D^0$, $\rm D^+$, and $\rm D^{*+}$ mesons as a function of $p_{\rm T}$ [141] compared to D meson $R_{\rm AA}$ in the 20% most central and in the 40–80% Pb–Pb collisions at $\sqrt{s_{\rm NN}} = 2.76$ TeV [63]. (b) Average D meson $R_{\rm AA}$ in the 20% most central Pb–Pb collisions at $\sqrt{s_{\rm NN}} = 2.76$ TeV compared to the expectation from NLO pQCD with nuclear shadowing.

the three species. Figure 8.5(a) shows the average $R_{\rm pPb}$ compared to theoretical calculations. Predictions based either on NLO pQCD calculations (MNR [28]) of D meson production including EPS09NLO [73] nuclear modification of the CTEQ6M PDF [142], or on calculations based on the Color Glass Condensate [77], can describe the measurement considering only initial state effects. The results are also well described by a calculation that includes energy loss in cold nuclear matter, nuclear shadowing, and $k_{\rm T}$ broadening [143]. The present uncertainties of the measurement do not allow any sensitivity to a possible effect due to the formation of a hydrodynamically expanding medium (Section 2.4), expected to be small in minimum-bias collisions at LHC energies. Figure 8.5(b) shows the average D meson $R_{\rm pPb}$ compared to the heavy-flavour electron $R_{\rm dAu}$ measured in minimum-bias d–Au collisions by PHENIX at $\sqrt{s_{\rm NN}} = 200$ GeV [96] (there are no measurements of D meson $R_{\rm pA}$ at RHIC yet), and to the charged-particle $R_{\rm pPb}$ measured in minimum-bias p–Pb collisions at $\sqrt{s_{\rm NN}} = 5.02$ TeV by ALICE [110]. The three measurements are compatible within statistical uncertainties and consistent with unity for $p_{\rm T} > 5$ GeV/c. The charged-particle $R_{\rm pPb}$ is compatible within uncertainty with the D meson $R_{\rm pPb}$ down to $p_{\rm T} = 1$ GeV/c, showing a less pronounced Cronin peak with respect to the heavy-flavour electron $R_{\rm dAu}$ measured at $\sqrt{s_{\rm NN}} = 200$ GeV. The D meson $R_{\rm pPb}$ measured at $\sqrt{s_{\rm NN}} = 5.02$ TeV indicates a smaller magnitude of the Cronin effect for charm production at the LHC.

In Figure 8.6(a), the average $R_{\rm pPb}$ of prompt D mesons in p–Pb collisions at $\sqrt{s_{\rm NN}} =$ 5.02 TeV is reported along with the average prompt D meson $R_{\rm AA}$ in central (0–20%)

and in semiperipheral (40–80%) Pb–Pb collisions at $\sqrt{s_{\rm NN}} = 2.76$ TeV [63], showing that cold nuclear matter effects are smaller than the uncertainties for $p_{\rm T} \gtrsim 3$ GeV/c. In addition, as reported in Ref. [63], the same EPS09 nuclear PDF parametrization that describes the D meson $R_{\rm pPb}$ results predicts small initial state effects (less than 10% for $p_{\rm T} > 5$ GeV/c) for Pb–Pb collisions (see Figure 8.6(b)). As a consequence, the suppression observed in central Pb–Pb collisions for $p_{\rm T} \gtrsim 2$ GeV/c is predominantly induced by final state effects, e.g. quark charm energy loss in the medium.

8.3 $Q_{\rm pPb}$ as a Function of Event Activity

The modification of the $\rm D^0$ $p_{\rm T}$ distribution in p–Pb collisions with respect to the $N_{\rm coll}$-scaled pp reference was measured in four event-activity classes, 0–20%, 20–40%, 40–60%, and 60–100%, defined with three different estimators: CL1, V0A, and ZNA. The results are shown in Figure 8.7. Figure 8.7(a) shows the $\rm D^0$ $Q_{\rm pPb}$ obtained by dividing the visible cross section in event classes defined by the CL1 estimator, and scaling the pp reference cross section with $\langle N_{\rm coll}^{\rm Glauber} \rangle$ obtained from the NBD-Glauber fit of the multiplicity distribution of the SPD clusters (CL1). Figure 8.7(b) shows the $\rm D^0$ $Q_{\rm pPb}$ obtained by dividing the visible cross section in event classes defined by the V0A estimator, and scaling the pp reference cross section with $\langle N_{\rm coll}^{\rm Glauber} \rangle$ obtained from the NBD-Glauber fit of the distribution of the amplitudes in the VZERO-A hodoscope. The $\rm D^0$ $Q_{\rm pPb}$ obtained with the hybrid method is shown in Figure 8.7(c). The bias on the $Q_{\rm pPb}$ introduced by the determination of $\langle N_{\rm coll} \rangle$ is maximum when the CL1 estimator is used, namely when the centrality determination was done in the same rapidity region of the measurement, while it decreases if the forward V0A estimator is used. The least biased measurement is obtained when defining the event-activity classes by slicing the ZN energy deposit in the Pb-going side and applying the hybrid method to calculate $\langle N_{\rm coll} \rangle$ [108]. In this case, the modification of the $\rm D^0$ $p_{\rm T}$ distribution with respect to pp collisions in the four event-activity classes is consistent with unity within uncertainties, indicating no significant event-activity dependence of the $\rm D^0$ production. The analysis was performed also for the $\rm D^+$ and $\rm D^{*+}$ mesons, showing consistent results [144].

8.4 Relative Yields as a Function of Multiplicity

The results on the $\rm D^0$ meson relative yields for each $p_{\rm T}$ interval are presented in Figure 8.8 as a function of the relative charged-particle multiplicity at midrapidity (Figure 8.8(a)) and as a function of the relative uncorrected multiplicity in the VZERO-A detector (Figure 8.8(b)). The relative yields are shown in the top panels with their statistical (vertical bars) and systematic (boxes) uncertainties, except the uncertainty

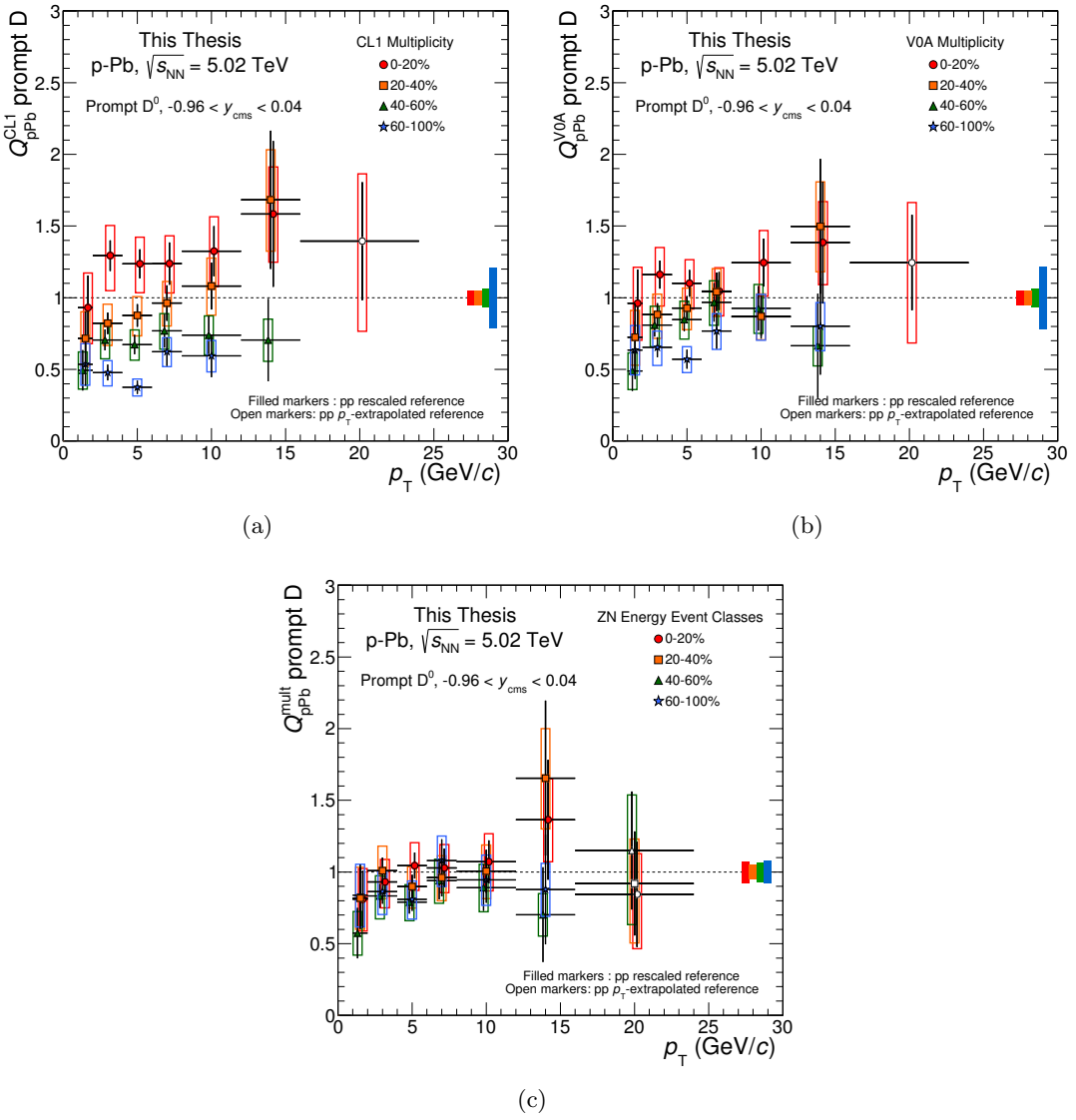

FIGURE 8.7: Q_{pPb} as a function of p_{T} for prompt D^0 measured in four event-activity classes: 0–20% (red), 20–40% (orange), 40–60% (green), and 60–100% (blue). The results are shown for the three event-activity estimators considered: CL1 (a), V0A (b), and ZNA (c).

on the feed-down fraction, which is drawn separately in the bottom panels in the form of relative uncertainties. The points are located on the x-axis at the average value of the relative charged-particle multiplicity, $(\mathrm{d}N_{\mathrm{ch}}/\mathrm{d}\eta)/\langle \mathrm{d}N_{\mathrm{ch}}/\mathrm{d}\eta \rangle$ for each $N_{\mathrm{tracklets}}$ interval (left panel), or $N_{\mathrm{V0A}}/\langle N_{\mathrm{V0A}} \rangle$ for each N_{V0A} interval (right panel). The relative D^0 yields are compatible within uncertainties in all p_{T} intervals and they show an increasing trend as a function of the relative charged-particle multiplicity. The relative D^0 yields increase with the charged-particle multiplicity at central rapidity by about a factor 25 in the range between 0.5 and 4.2 times $\langle \mathrm{d}N_{\mathrm{ch}}/\mathrm{d}\eta \rangle$, corresponding to an increase of relative multiplicity of about a factor 9. The relative D^0 yields increase by about a factor 5 in the range between 0.5 and 3.3 times the charged-particle multiplicity at forward rapidity,

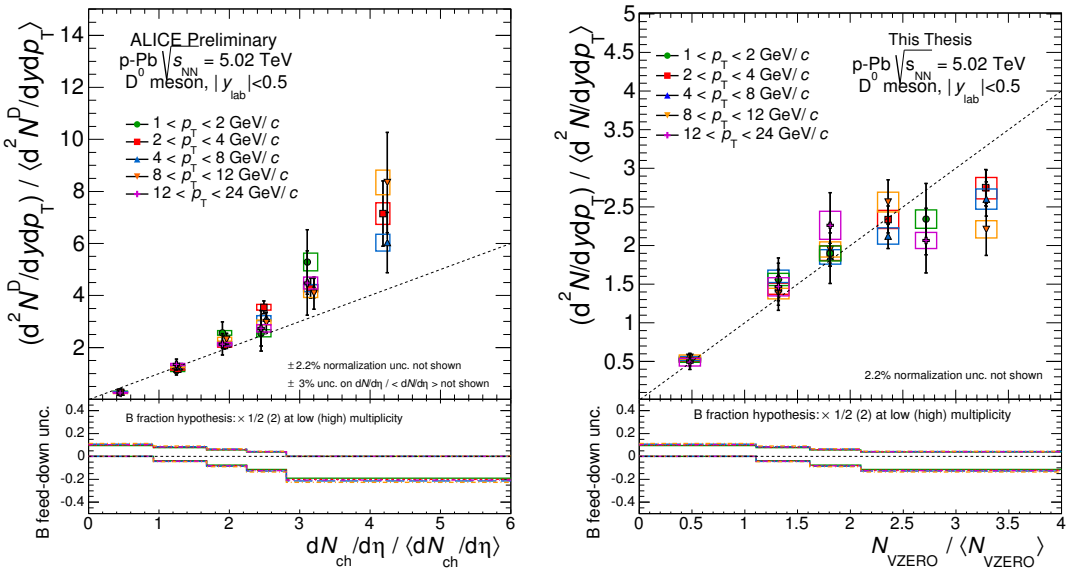

(a) (b)

FIGURE 8.8: D^0 meson relative yields as a function of relative charged-particle multiplicity. The relative yields, measured in six p_T intervals, are presented in the top panels with their statistical and systematic uncertainties, the relative uncertainty due to the B feed-down fraction is reported in the bottom panels. The points are located on the x-axis at the average value of $(dN_{ch}/d\eta)/\langle dN_{ch}/d\eta \rangle$ for every $N_{tracklets}$ interval (a) and of $N_{V0A}/\langle N_{V0A} \rangle$ for every N_{V0A} interval (b). The $x = y$ line is also shown.

corresponding to an increase of relative multiplicity of about a factor 7. The results are consistent with the Q_{pPb} measurements: the yields extracted in the event-activity classes defined with the CL1 and V0A estimators show the same increasing trends as a function of the average multiplicity in each event class as those observed in Figure 8.8. Events with high D^0 relative yield, thus with enhanced charm production with respect to the average, are typically events with high charged-particle multiplicity in the central rapidity region, as demonstrated in Figure 8.8(a), where the relative yields are shown as a function of the relative multiplicity measured in the same η region of the D^0 mesons. If the multiplicity is measured at forward rapidity, introducing an η-gap with respect to the region where the D^0 production is measured, the increase of charm production is less steep as a function of relative multiplicity. In Figure 8.8(a) the relative yields are higher than the diagonal at high relative multiplicity, while in Figure 8.8(b) they are lower. This is because the correlation between the multiplicity at forward and central rapidity is broad, therefore, an event with charm production (high multiplicity at midrapidity) can exhibit a lower relative multiplicity at forward rapidity.

Figure 8.9 shows the comparison of the D^0 relative yields as a function of relative charged-particle multiplicity, $(dN_{ch}/d\eta)/\langle dN_{ch}/d\eta \rangle$, for the p_T interval $2 < p_T < 4$ GeV/c, as measured in p–Pb collisions at $\sqrt{s_{NN}} = 5.02$ TeV and in pp at $\sqrt{s} = 7$ TeV. A similar increasing trend is observed as the relative multiplicity increases. In p–Pb

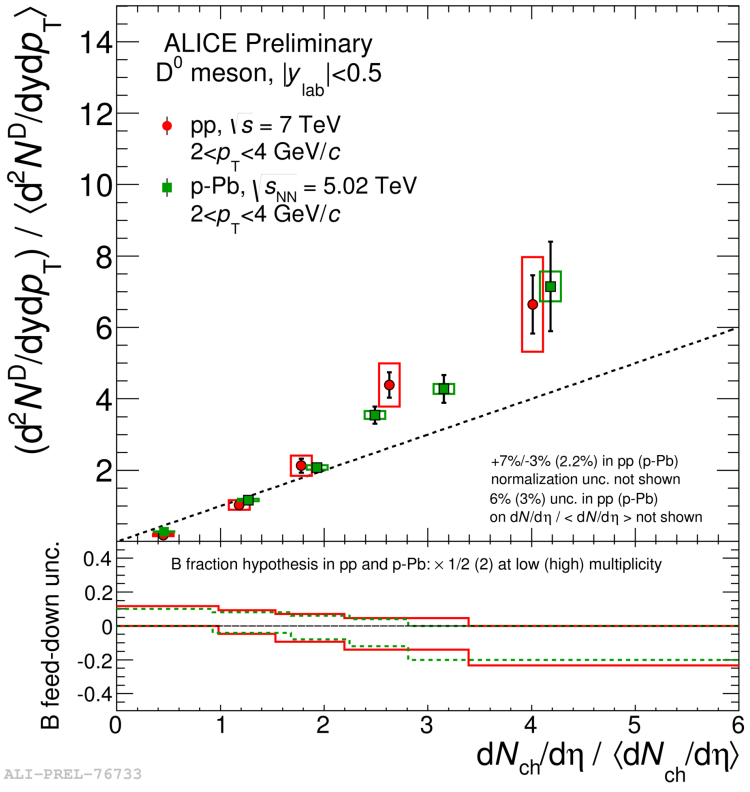

FIGURE 8.9: D^0 meson relative yields as a function of relative charged-particle multiplicity in p–Pb collisions at $\sqrt{s_{\rm NN}} = 5.02$ TeV and in pp at $\sqrt{s} = 7$ TeV. The relative yields, measured in the $2 < p_{\rm T} < 4$ GeV/c interval, are presented in the top panel with their statistical and systematic uncertainties, the relative uncertainty due to the B feed-down fraction is reported in the bottom panel. The points are located on the x-axis at the average value of $({\rm d}N_{\rm ch}/{\rm d}\eta)/\langle {\rm d}N_{\rm ch}/{\rm d}\eta\rangle$ for every $N_{\rm tracklets}$ interval.

high-multiplicity events originate from collisions with $N_{\rm coll} > 1$. The observed similar pattern in pp and p–Pb suggests that also in pp in higher multiplicity events, multiple hard scatterings among the partons occur.

Conclusions

The aims of the measurements presented in this thesis were:

- to investigate whether the charm quarks participate in the collective expansion of the QGP,
- to assess to which extent the large suppression of the prompt D meson $R_{\rm AA}$ in central Pb–Pb collisions is a final state state effect related to the charm energy loss in the medium.

The first question was addressed through the measurement of the azimuthal anisotropy of the $\rm D^0$ meson production in semicentral Pb–Pb collisions. The second through the measurement of the production of prompt $\rm D^0$ mesons in p–Pb collisions and the comparison to the results obtained in central Pb–Pb collisions.

The first results on the azimuthal anisotropy of $\rm D^0$ production at central rapidity in Pb–Pb collisions at $\sqrt{s_{\rm NN}} = 2.76$ TeV, obtained by reconstructing the decay $\rm D^0 \rightarrow K^-\pi^+$, were presented. The elliptic flow coefficient v_2 was measured with the event-plane method as a function of transverse momentum for semicentral collisions in the 30–50% quantile of the hadronic cross section. An average D meson v_2 ($\rm D^0$, $\rm D^+$, and $\rm D^{*+}$) was calculated and in the interval $2 < p_{\rm T} < 6$ GeV/c it is larger than zero with a significance of 5.7σ, combining statistical and systematic uncertainties. A positive v_2 is also observed for $p_{\rm T} > 6$ GeV/c, although with smaller significance, likely originating from the path-length dependence of the in-medium partonic energy loss. The azimuthal anisotropy of the $\rm D^0$ was also measured in the centrality classes 0–10% and 10–30%. For all the three centrality classes the $\rm D^0$ v_2 is comparable in magnitude to that of charged particles and an indication for a decrease of elliptic flow towards more central collisions is observed for $3 < p_{\rm T} < 6$ GeV/c. The anisotropy was also quantified in terms of the $\rm D^0$ nuclear modification factor $R_{\rm AA}$, measured in the direction of the event plane and orthogonal to it. For $p_{\rm T} > 3$ GeV/c, a stronger suppression relative to proton–proton collisions is observed in the out-of-plane direction, where the average path length of heavy quarks through the medium is larger. The results for v_2 and $R_{\rm AA}$ azimuthal dependence indicate that, during the collective expansion of the medium, the interactions between its constituents and charm quarks transfer to the latter information on

the azimuthal anisotropy of the system. The measured elliptic flow and $R_{\rm AA}$ in and out of the event plane, as well as the previously published $R_{\rm AA}$ in the most central Pb–Pb collisions [63], were compared with model calculations. The anisotropy is best described by the models that include mechanisms that transfer to charm quarks the elliptic flow induced during the expansion. These mechanisms include collisional energy loss and charm quark recombination with light quarks from the medium. Despite the fact that it is challenging for models to describe simultaneously the large D meson suppression in central collisions and their anisotropy in semiperipheral collisions, these results are crucial to provide important constraints on the mechanisms of heavy-quark energy loss and on the transport properties of the expanding medium produced in high energy Pb–Pb collisions.

This thesis also reported the results on the measurement of the $\rm D^0$ cross section and nuclear modification factor $R_{\rm pPb}$ in minimum-bias p–Pb collisions at $\sqrt{s_{\rm NN}} = 5.02$ TeV. The production cross section of prompt $\rm D^0$ mesons was measured as a function of transverse momentum and rapidity. The $R_{\rm pPb}$ is consistent with unity within statistical and systematic uncertainties showing that the $\rm D^0$ production in p–Pb collisions is consistent with the binary collision scaling of the production in pp collisions. The measurement is consistent with theoretical calculations that include initial state effects such as the modification of the parton distribution functions in the nuclear environment (e.g. nuclear shadowing and saturation of the gluon density at small parton fractional momentum), the $k_{\rm T}$ broadening induced by the multiple soft collisions of the partons before the production of the $c\bar{c}$ pair, as well as the energy loss in cold nuclear matter.

The modification of the $\rm D^0$ $p_{\rm T}$ distribution in p–Pb collisions with respect to the $N_{\rm coll}$-scaled pp reference was also measured as a function of event activity considering different estimators. The resulting $Q_{\rm pPb}$, obtained reducing at minimum the bias induced by $N_{\rm coll}$-determination, is consistent with unity within uncertainties in all event-activity classes, indicating no significant event-activity dependence of the $\rm D^0$ production. The measurement of the $\rm D^0$ relative yields as a function of the relative charged-particle multiplicity is also reported. An increasing trend as a function of the relative charged-particle multiplicity, with a milder increase at forward with respect to central rapidity is observed. The $\rm D^0$ relative yields as a function of the relative charged-particle multiplicity at midrapidity measured in p–Pb collisions were compared to those measured in pp collisions at $\sqrt{s} = 7$ TeV, showing a similar increasing trend. In p–Pb high-multiplicity events originate from collisions with $N_{\rm coll} > 1$, and the observed similar pattern in pp and p–Pb suggests that also in higher multiplicity pp events multiple hard scatterings among the partons occur.

The average D meson $R_{\rm pPb}$ was compared to the prompt D meson nuclear modification factor $R_{\rm AA}$ measured in central and semiperipheral Pb–Pb collisions at $\sqrt{s_{\rm NN}} =$ 2.76 TeV. This comparison shows that the cold nuclear matter effects are smaller than

the R_{AA} uncertainties for $p_{\mathrm{T}} \gtrsim 3$ GeV/c, demonstrating that the suppression observed in central Pb–Pb collisions for $p_{\mathrm{T}} \gtrsim 2$ GeV/c is predominantly induced by final state effects, e.g. the charm energy loss in the QGP.

Bibliography

[1] T. van Ritbergen, J.A.M. Vermaseren, and S.A. Larin. The Four Loop Beta Function in Quantum Chromodynamics. *Phys. Lett. B*, 400:379–384, 1997.

[2] David J. Gross and Frank Wilczek. Ultraviolet Behavior of Non-Abelian Gauge Theories. *Phys. Rev. Lett.*, 30:1343–1346, Jun 1973.

[3] David J. Gross and Frank Wilczek. Asymptotically Free Gauge Theories. I. *Phys. Rev. D*, 8:3633–3652, Nov 1973.

[4] David J. Gross and Frank Wilczek. Asymptotically Free Gauge Theories. II. *Phys. Rev. D*, 9:980–993, Feb 1974.

[5] H. David Politzer. Reliable Perturbative Results for Strong Interactions? *Phys. Rev. Lett.*, 30:1346–1349, Jun 1973.

[6] H. David Politzer. Asymptotic Freedom: An Approach to Strong Interactions. *Physics Reports*, 14(4):129–180, 1974. ISSN 0370-1573.

[7] K.A. Olive et al. Review of Particle Physics. *Chin. Phys. C*, 38:090001, 2014.

[8] Kenneth G. Wilson. Confinement of Quarks. *Phys. Rev. D*, 10:2445–2459, Oct 1974.

[9] R. Hagedorn. Statistical Thermodynamics of Strong Interactions at High Energy. *Suppl. Nuovo Cimento*, 3:147, 1965.

[10] N. Cabibbo and G. Parisi. Exponential Hadronic Spectrum and Quark Liberation. *Phys. Lett. B*, 59(1):67–69, 1975.

[11] F. Karsch. Lattice QCD at High Temperature and Density. *Lect. Notes Phys.*, 583:209–249, 2002.

[12] Bertrand C. Barrois. Superconducting Quark Matter. *Nucl. Phys. B*, 129:390, 1977.

[13] Kenji Fukushima and Tetsuo Hatsuda. The Phase Diagram of Dense QCD. *Reports on Progress in Physics*, 74(1):014001, 2011.

[14] F. Karsch and E. Laermann. Thermodynamics and In-Medium Hadron Properties from Lattice QCD. [arXiv:hep-lat/0305025]. 2003.

[15] Michael L. Miller, Klaus Reygers, Stephen J. Sanders, and Peter Steinberg. Glauber Modeling in High-Energy Nuclear Collisions. *Ann. Rev. Nucl. Part. Sci.*, 57:205–243, 2007.

[16] B. Abelev et al. Centrality Determination of Pb–Pb Collisions at $\sqrt{s_{\mathrm{NN}}} = 2.76$ TeV with ALICE. *Phys. Rev. C*, 88:044909, Oct 2013.

[17] K. Aamodt et al. Charged-Particle Multiplicity Density at Midrapidity in Central Pb–Pb Collisions at $\sqrt{s_{\mathrm{NN}}} = 2.76$ TeV. *Phys. Rev. Lett.*, 105:252301, Dec 2010.

[18] J. D. Bjorken. Highly Relativistic Nucleus–Nucleus Collisions: The Central Rapidity Region. *Phys. Rev. D*, 27:140–151, Jan 1983.

[19] Krisztián Krajczár on behalf of the CMS Collaboration. Charged Hadron Multiplicity and Transverse Energy Densities in Pb–Pb Collisions from CMS. *Journal of Physics G: Nuclear and Particle Physics*, 38(12):124041, 2011.

[20] Michael Annan Lisa, Scott Pratt, Ron Soltz, and Urs Wiedemann. Femtoscopy in Relativistic Heavy-Ion Collisions. *Ann. Rev. Nucl. Part. Sci.*, 55:357–402, 2005.

[21] K. Aamodt et al. Two-pion Bose-Einstein Correlations in Central Pb–Pb Collisions at $\sqrt{s_{\mathrm{NN}}}$=2.76 TeV. *Phys. Lett. B*, 696:328–337, 2011.

[22] A. Adare et al. Enhanced Production of Direct Photons in Au–Au Collisions at $\sqrt{s_{\mathrm{NN}}} = 200$ GeV and Implications for the Initial Temperature. *Phys. Rev. Lett.*, 104:132301, 2010.

[23] T. Matsui and H. Satz. J/ψ Suppression by Quark-Gluon Plasma Formation. *Phys. Lett. B*, 178(4):416–422, 1986.

[24] B. Abelev et al. Centrality, Rapidity and Transverse Momentum Dependence of J/ψ Suppression in Pb–Pb Collisions at $\sqrt{s_{\mathrm{NN}}}$=2.76 TeV. *Phys. Lett. B*, 734: 314–327, 2014.

[25] S. Chatrchyan et al. Suppression of Non-Prompt J/ψ, Prompt J/ψ, and Y(1S) in Pb–Pb Collisions at $\sqrt{s_{\mathrm{NN}}} = 2.76$ TeV. *JHEP*, 1205:063, 2012.

[26] S. et al. Chatrchyan. Observation of Sequential Υ Suppression in Pb–Pb Collisions. *Phys. Rev. Lett.*, 109:222301, Nov 2012.

[27] B. Abelev et al. Suppression of Υ(1S) at Forward Rapidity in Pb–Pb Collisions at $\sqrt{s_{\mathrm{NN}}}$=2.76 TeV. *Phys. Lett. B*, 738:361–372, 2014.

[28] Michelangelo L. Mangano, Paolo Nason, and Giovanni Ridolfi. Heavy-Quark Correlations in Hadron Collisions at Next-to-Leading Order. *Nucl. Phys. B*, 373: 295–345, 1992.

[29] B.A. Kniehl, G. Kramer, I. Schienbein, and H. Spiesberger. Hadroproduction of D and B Mesons in a Massive VFNS. *AIP Conf.Proc.*, 792:867–870, 2005.

[30] B.A. Kniehl, G. Kramer, I. Schienbein, and H. Spiesberger. Collinear Subtractions in Hadroproduction of Heavy Quarks. *Eur. Phys. J. C*, 41:199–212, 2005.

[31] B.A. Kniehl, G. Kramer, I. Schienbein, and H. Spiesberger. Inclusive Charmed-Meson Production at the CERN LHC. *Eur. Phys. J. C*, 72:2082, 2012.

[32] Stefano Frixione and Bryan R. Webber. Matching NLO QCD Computations and Parton Shower Simulations. *JHEP*, 0206:029, 2002.

[33] Stefano Frixione, Paolo Nason, and Bryan R. Webber. Matching NLO QCD and Parton Showers in Heavy-Flavor Production. *JHEP*, 0308:007, 2003.

[34] Matteo Cacciari, Mario Greco, and Paolo Nason. The p_{T} Spectrum in Heavy-Flavor Hadroproduction. *JHEP*, 9805:007, 1998.

[35] Matteo Cacciari, Stefano Frixione, and Paolo Nason. The p_{T} Spectrum in Heavy-Flavor Photoproduction. *JHEP*, 0103:006, 2001.

[36] Matteo Cacciari, Stefano Frixione, Nicolas Houdeau, Michelangelo L. Mangano, Paolo Nason, et al. Theoretical Predictions for Charm and Bottom Production at the LHC. *JHEP*, 1210:137, 2012.

[37] S. Alekhin, G. Altarelli, N. Amapane, J. Andersen, V. Andreev, et al. HERA and the LHC: A Workshop on the Implications of HERA for LHC physics. Proceedings, Part B. 2005.

[38] B. Abelev et al. Measurement of Charm Production at Central Rapidity in Proton–Proton Collisions at $\sqrt{s} = 7$ TeV. *JHEP*, 2012(1):128, 2012.

[39] B. Abelev et al. Measurement of Charm Production at Central Rapidity in Proton–Proton Collisions at $\sqrt{s} = 2.76$ TeV. *JHEP*, 2012(7):191, 2012.

[40] ATLAS Collaboration. Comparison of D^* Meson Production Cross Sections with FONLL and GM-VFNS Predictions. ATL-PHYS-PUB-2011-012, ATL-COM-PHYS-2011-912. 2011.

[41] ATLAS Collaboration. Measurement of D^* Meson Production Cross Sections in pp Collisions at $\sqrt{s} = 7$ TeV with the ATLAS Detector. ATLAS-CONF-2011-017, ATLAS-COM-CONF-2011-030. 2011.

[42] LHCb Collaboration. Prompt Charm Production in *pp* Collisions at $\sqrt{s}$=7 TeV. LHCb-CONF-2010-013. Dec 2010.

[43] Pavel M. Nadolsky, Hung-Liang Lai, Qing-Hong Cao, Joey Huston, Jon Pumplin, et al. Implications of CTEQ Global Analysis for Collider Observables. *Phys. Rev. D*, 78:013004, 2008.

[44] A. Adare et al. Heavy Quark Production in pp and Energy Loss and Flow of Heavy Quarks in Au–Au Collisions at $\sqrt{s_{\rm NN}} = 200$ GeV. *Phys. Rev. C*, 84:044905, 2011.

[45] L. Adamczyk et al. Measurements of D^0 and D^* Production in *pp* Collisions at $\sqrt{s} = 200$ GeV. *Phys. Rev. D*, 86:072013, 2012.

[46] C. Lourenco and H.K. Wohri. Heavy-Flavour Hadroproduction from Fixed-Target to Collider Energies. *Phys. Rept.*, 433:127–180, 2006.

[47] R.J. Fries, Berndt Muller, C. Nonaka, and S.A. Bass. Hadronization in Heavy-Ion Collisions: Recombination and Fragmentation of Partons. *Phys. Rev. Lett.*, 90: 202303, 2003.

[48] P. Koch, Berndt Muller, and Johann Rafelski. Strangeness in Relativistic Heavy-Ion Collisions. *Phys. Rept.*, 142:167–262, 1986.

[49] Inga Kuznetsova and Johann Rafelski. Heavy-Flavor Hadrons in Statistical Hadronization of Strangeness-Rich QGP. *Eur. Phys. J. C*, 51:113–133, 2007.

[50] Min He, Rainer J. Fries, and Ralf Rapp. $\mathbf{D_s}$-Meson as Quantitative Probe of Diffusion and Hadronization in Nuclear Collisions. *Phys. Rev. Lett.*, 110(11):112301, 2013.

[51] Stephane Peigne and Andre Peshier. Collisional Energy Loss of a Fast Heavy Quark in a Quark-Gluon Plasma. *Phys. Rev. D*, 77:114017, 2008.

[52] Ralf Rapp and Hendrik van Hees. Heavy Quarks in the Quark-Gluon Plasma. [arXiv:0903.1096]. 2009.

[53] H. van Hees, M. Mannarelli, V. Greco, and R. Rapp. Nonperturbative Heavy-Quark Diffusion in the Quark-Gluon Plasma. *Phys. Rev. Lett.*, 100:192301, 2008.

[54] Andre Peshier. Turning on the Charm. *Nucl. Phys. A*, 888:7–22, 2012.

[55] P.B. Gossiaux and J. Aichelin. Towards an Understanding of the RHIC Single Electron Data. *Phys. Rev. C*, 78:014904, 2008.

[56] Steven S. Gubser. Comparing the Drag Force on Heavy Quarks in N=4 Super-Yang-Mills Theory and QCD. *Phys. Rev. D*, 76:126003, 2007.

[57] R. Baier, Yuri L. Dokshitzer, Alfred H. Mueller, S. Peigne, and D. Schiff. Radiative Energy Loss of High-Energy Quarks and Gluons in a Finite Volume Quark-Gluon Plasma. *Nucl. Phys. B*, 483:291–320, 1997.

[58] R. Baier, Yuri L. Dokshitzer, Alfred H. Mueller, S. Peigne, and D. Schiff. Radiative Energy Loss and p_{T}-Broadening of High-Energy Partons in Nuclei. *Nucl. Phys. B*, 484:265–282, 1997.

[59] Yuri L. Dokshitzer and D.E. Kharzeev. Heavy-Quark Colorimetry of QCD Matter. *Phys. Lett. B*, 519:199–206, 2001.

[60] G. Aad et al. Observation of a Centrality-Dependent Dijet Asymmetry in Lead–Lead Collisions at $\sqrt{s_{\mathrm{NN}}} = 2.76$ TeV with the ATLAS Detector at the LHC. *Phys. Rev. Lett.*, 105:252303, 2010.

[61] S. Chatrchyan et al. Observation and Studies of Jet Quenching in Pb–Pb Collisions at Nucleon–Nucleon Center-of-Mass Energy = 2.76 TeV. *Phys. Rev. C*, 84:024906, 2011.

[62] L. Adamczyk et al. Observation of D^0 Meson Nuclear Modifications in Au–Au Collisions at $\sqrt{s_{\mathrm{NN}}}$=200 GeV. *Phys. Rev. Lett.*, 113:142301, 2014.

[63] B. Abelev et al. Suppression of High-Transverse Momentum D Mesons in Central Pb–Pb Collisions at $\sqrt{s_{\mathrm{NN}}} = 2.76$ TeV. *JHEP*, 1209:112, 2012.

[64] J/ψ Results from CMS in Pb–Pb Collisions, with $150\mu b^{-1}$ Data. Technical Report CMS-PAS-HIN-12-014, CERN, Geneva, 2012.

[65] Magdalena Djordjevic and Marko Djordjevic. LHC Jet Suppression of Light and Heavy-Flavor Observables. *Phys. Lett. B*, 734:286–289, 2014.

[66] P. Kovtun, Dan T. Son, and Andrei O. Starinets. Viscosity in Strongly-Interacting Quantum Field Theories from Black Hole Physics. *Phys. Rev. Lett.*, 94:111601, 2005.

[67] B. Abelev et al. D Meson Elliptic Flow in Non-Central Pb–Pb Collisions at $\sqrt{s_{\mathrm{NN}}}$=2.76 TeV. *Phys. Rev. Lett.*, 111:102301, 2013.

[68] G. Aad et al. Measurement of the Azimuthal Anisotropy for Charged Particle Production in $\sqrt{s_{\mathrm{NN}}} = 2.76$ TeV Lead–Lead Collisions with the ATLAS Detector. *Phys. Rev. C*, 86:014907, 2012.

[69] S. Chatrchyan et al. Measurement of the Elliptic Anisotropy of Charged Particles Produced in Pb–Pb Collisions at Nucleon–Nucleon Center-of-mass Energy = 2.76 TeV. *Phys. Rev. C*, 87:014902, 2013.

[70] J. Adams et al. Azimuthal Anisotropy in Au–Au Collisions at $\sqrt{s_{\rm NN}} = 200$ GeV. *Phys. Rev. C*, 72:014904, Jul 2005.

[71] K. Aamodt et al. Higher Harmonic Anisotropic Flow Measurements of Charged Particles in Pb–Pb Collisions at $\sqrt{s_{\rm NN}}$=2.76 TeV. *Phys. Rev. Lett.*, 107:032301, 2011.

[72] M. Arneodo. Nuclear Effects in Structure Functions. *Phys. Rept.*, 240:301–393, 1994.

[73] K.J. Eskola, H. Paukkunen, and C.A. Salgado. EPS09: A New Generation of NLO and LO Nuclear Parton Distribution Functions. *JHEP*, 0904:065, 2009.

[74] M. Hirai, S. Kumano, and T.H. Nagai. Determination of Nuclear Parton Distribution Functions and Their Uncertainties in Next-to-Leading Order. *Phys. Rev. C*, 76:065207, 2007.

[75] D. de Florian and R. Sassot. Nuclear Parton Distributions at Next-to-Leading Order. *Phys. Rev. D*, 69:074028, 2004.

[76] ALICE Collaboration. ALICE: Physics Performance Report, Volume II. *Journal of Physics G: Nuclear and Particle Physics*, 32(10):1295, 2006.

[77] Hirotsugu Fujii and Kazuhiro Watanabe. Heavy-Quark Pair Production in High-Energy pA Collisions: Open Heavy Flavors. *Nucl. Phys. A*, 920:78–93, 2013.

[78] P. Tribedy and R. Venugopalan. QCD Saturation at the LHC: Comparisons of Models to pp and AA Data and Predictions for p–Pb Collisions. *Phys. Lett. B*, 710:125–133, 2012.

[79] Javier L. Albacete, Adrian Dumitru, Hirotsugu Fujii, and Yasushi Nara. CGC Predictions for p–Pb Collisions at the LHC. *Nucl. Phys. A*, 897:1–27, 2013.

[80] Amir H. Rezaeian. CGC Predictions for p–A Collisions at the LHC and Signature of QCD Saturation. *Phys. Lett. B*, 718:1058–1069, 2013.

[81] J.W. Cronin, Henry J. Frisch, M.J. Shochet, J.P. Boymond, R. Mermod, et al. Production of Hadrons with Large Transverse Momentum at 200 GeV, 300 GeV, and 400 GeV. *Phys. Rev. D*, 11:3105, 1975.

[82] B.Z. Kopeliovich, J. Nemchik, A. Schafer, and A.V. Tarasov. Cronin Effect in Hadron Production Off Nuclei. *Phys. Rev. Lett.*, 88:232303, 2002.

[83] Xin-Nian Wang. Systematic Study of High-p_{T} Hadron Spectra in pp, pA and AA Collisions from SPS to RHIC Energies. *Phys. Rev. C*, 61:064910, 2000.

[84] M. Lev and B. Petersson. Nuclear Effects at Large Transverse Momentum in a QCD Parton Model. *Z. Phys. C*, 21:155, 1983.

[85] I. Vitev. Non-Abelian Energy Loss in Cold Nuclear Matter. *Phys. Rev. C*, 75: 064906, 2007.

[86] S. Chatrchyan et al. Observation of Long-Range Near-Side Angular Correlations in Proton–Lead Collisions at the LHC. *Phys. Lett. B*, 718:795–814, 2013.

[87] B. Abelev et al. Long-Range Angular Correlations on the Near and Away Side in p–Pb Collisions at $\sqrt{s_{\mathrm{NN}}} = 5.02$ TeV. *Phys. Lett. B*, 719:29–41, 2013.

[88] B. Abelev et al. Long-Range Angular Correlations of π, K and p in p–Pb Collisions at $\sqrt{s_{\mathrm{NN}}}$=5.02 TeV. *Phys. Lett. B*, 726:164–177, 2013.

[89] G. Aad et al. Observation of Associated Near-Side and Away-Side Long-Range Correlations in$\sqrt{s_{\mathrm{NN}}} = 5.02$ TeV Proton-Lead Collisions with the ATLAS Detector. *Phys. Rev. Lett.*, 110(18):182302, 2013.

[90] S.S. Adler et al. Nuclear Effects on Hadron Production in d–Au and pp Collisions at $\sqrt{s_{\mathrm{NN}}}$=200 GeV. *Phys. Rev. C*, 74:024904, 2006.

[91] A. Adare et al. Nuclear Modification of $\psi^{'}, \chi_c$, and J/ψ Production in d–Au Collisions at $\sqrt{s_{\mathrm{NN}}}$=200 GeV. *Phys. Rev. Lett.*, 111(20):202301, 2013.

[92] B. Abelev et al. Suppression of ψ(2S) Production in p-Pb Collisions at $\sqrt{s_{\mathrm{NN}}} =$ 5.02 TeV. *JHEP*, 1412:073, 2014.

[93] Anne M. Sickles. Possible Evidence for Radial Flow of Heavy Mesons in d–Au Collisions. *Phys. Lett. B*, 731:51–56, 2014.

[94] B. Abelev et al. Systematic Measurements of Identified Particle Spectra in pp, d–Au and Au–Au Collisions from STAR. *Phys. Rev. C*, 79:034909, 2009.

[95] B. Abelev et al. Multiplicity Dependence of Pion, Kaon, Proton and Lambda Production in p–Pb Collisions at $\sqrt{s_{\mathrm{NN}}}$=5.02 TeV. *Phys. Lett. B*, 728:25–38, 2014.

[96] A. Adare et al. Cold-Nuclear-Matter Effects on Heavy-Quark Production in d–Au Collisions at $\sqrt{s_{\mathrm{NN}}} = 200$ GeV. *Phys. Rev. Lett.*, 109(24):242301, 2012.

[97] G. Aad et al. Observation of a New Particle in the Search for the Standard Model Higgs Boson with the ATLAS Detector at the LHC. *Phys. Lett. B*, 716:1–29, 2012.

[98] S. Chatrchyan et al. Observation of a New Boson at a Mass of 125 GeV with the CMS Experiment at the LHC. *Phys. Lett. B*, 716:30–61, 2012.

[99] Lyndon Evans and Philip Bryant. LHC Machine. *Journal of Instrumentation*, 3 (08):S08001, 2008.

[100] LHC Physics Centre at CERN. http://lpcc.web.cern.ch/LPCC/.

[101] Aamodt, K. and The ALICE Collaboration. The ALICE Experiment at the CERN LHC. *Journal of Instrumentation*, 3(08):S08002, 2008.

[102] R. Fruhwirth. Application of Kalman Filtering to Track and Vertex Fitting. *Nuclear Instruments and Methods in Physics Research Section A: Accelerators, Spectrometers, Detectors and Associated Equipment*, 262(2–3):444–450, 1987.

[103] B. Abelev et al. Performance of the ALICE Experiment at the CERN LHC. *Int. J. Mod. Phys. A*, 29:1430044, 2014.

[104] Sergei A. Voloshin, Arthur M. Poskanzer, and Raimond Snellings. Collective Phenomena in Non-Central Nuclear Collisions. [arXiv:0809.2949]. 2008.

[105] K. Aamodt et al. Harmonic Decomposition of Two-Particle Angular Correlations in Pb–Pb Collisions at $\sqrt{s_{\rm NN}} = 2.76$ TeV. *Phys. Lett. B*, 708:249–264, 2012.

[106] David G. d'Enterria. Hard Scattering Cross-Sections at LHC in the Glauber Approach: From pp to pA and AA Collisions. [arXiv:nucl-ex/0302016]. 2003.

[107] B. Abelev et al. Measurement of Visible Cross Sections in Proton–Lead Collisions at $\sqrt{s_{\rm NN}}$=5.02 TeV in van der Meer Scans with the ALICE Detector. *JINST*, 9 (11):P11003, 2014.

[108] J. Adam et al. Centrality Dependence of Particle Production in p–Pb Collisions at $\sqrt{s_{\rm NN}}$= 5.02 TeV. [arXiv:1412.6828]. 2014.

[109] B. Abelev et al. Pseudorapidity Density of Charged Particles in p–Pb Collisions at $\sqrt{s_{\rm NN}} = 5.02$ TeV. *Phys. Rev. Lett.*, 110:032301, Jan 2013.

[110] B. Abelev et al. Transverse Momentum Distribution and Nuclear Modification Factor of Charged Particles in p–Pb Collisions at $\sqrt{s_{\rm NN}} = 5.02$ TeV. *Phys. Rev. Lett.*, 110:082302, 2013.

[111] B. Abelev et al. Azimuthal Anisotropy of D Meson Production in Pb–Pb Collisions at $\sqrt{s_{\rm NN}} = 2.76$ TeV. *Phys. Rev. C*, 90:034904, 2014.

[112] A. Dainese. Charm Production and In-Medium QCD Energy Loss in Nucleus–Nucleus Collisions with ALICE: A Performance Study. [arXiv:nucl-ex/0311004]. 2003.

[113] F. James and M. Winkler. Minuit User's Guide. http://seal.web.cern.ch/seal/documents/minuit/mnusersguide.pdf.

[114] Rene Brun, Federico Carminati, and Simone Giani. GEANT Detector Description and Simulation Tool. CERN-W5013, CERN-W-5013. 1994.

[115] Xin-Nian Wang and Miklos Gyulassy. HIJING: A Monte Carlo Model for Multiple Jet Production in pp, pA and AA Collisions. *Phys. Rev. D*, 44:3501–3516, 1991.

[116] Torbjorn Sjostrand, Stephen Mrenna, and Peter Z. Skands. PYTHIA 6.4 Physics and Manual. *JHEP*, 0605:026, 2006.

[117] Peter Zeiler Skands. Tuning Monte Carlo Generators: The Perugia Tunes. *Phys. Rev. D*, 82:074018, 2010.

[118] D.J. Lange. The EvtGen Particle Decay Simulation Package. *Nucl. Instrum. Meth. A*, 462:152–155, 2001.

[119] O. Fochler, J. Uphoff, Z. Xu, and C. Greiner. Jet Quenching and Elliptic Flow at RHIC and LHC within a pQCD-Based Partonic Transport Model. *J. Phys. G*, 38: 124152, 2011.

[120] Jan Uphoff, Oliver Fochler, Zhe Xu, and Carsten Greiner. Elliptic Flow and Energy Loss of Heavy Quarks in Ultra-Relativistic Heavy-Ion Collisions. *Phys. Rev. C*, 84:024908, 2011.

[121] Jan Uphoff, Oliver Fochler, Zhe Xu, and Carsten Greiner. Open Heavy Flavor in Pb–Pb Collisions at $\sqrt{s_{\mathrm{NN}}} = 2.76$ TeV within a Transport Model. *Phys. Lett. B*, 717:430–435, 2012.

[122] B. Abelev et al. Anisotropic Flow of Charged Hadrons, Pions and (Anti-)Protons Measured at High Transverse Momentum in Pb–Pb Collisions at $\sqrt{s_{\mathrm{NN}}}$=2.76 TeV. *Phys. Lett. B*, 719:18–28, 2013.

[123] C. Adler et al. Elliptic flow from two and four particle correlations in Au+Au collisions at $\sqrt{s_{\mathrm{NN}}} = 130$ GeV. *Phys. Rev. C*, 66:034904, 2002.

[124] Ante Bilandzic, Raimond Snellings, and Sergei Voloshin. Flow Analysis with Cumulants: Direct Calculations. *Phys. Rev. C*, 83:044913, 2011.

[125] Simon Wicks, William Horowitz, Magdalena Djordjevic, and Miklos Gyulassy. Elastic, Inelastic, and Path Length Fluctuations in Jet Tomography. *Nucl. Phys. A*, 784:426–442, 2007.

[126] W.A. Horowitz and Miklos Gyulassy. The Surprising Transparency of the sQGP at LHC. *Nucl. Phys. A*, 872:265–285, 2011.

[127] W.A. Horowitz. Testing pQCD and AdS/CFT Energy Loss at RHIC and LHC. *AIP Conf. Proc.*, 1441:889–891, 2012.

[128] Magdalena Djordjevic and Miklos Gyulassy. Heavy-Quark Radiative Energy Loss in QCD Matter. *Nucl. Phys. A*, 733:265–298, 2004.

[129] Marlene Nahrgang, Joerg Aichelin, Pol Bernard Gossiaux, and Klaus Werner. Influence of Hadronic Bound States Above T_c on Heavy-Quark Observables in Pb–Pb collisions at the CERN Large Hadron Collider. *Phys. Rev. C*, 89(1):014905, 2014.

[130] R. Baier, D. Schiff, and B.G. Zakharov. Energy Loss in Perturbative QCD. *Ann. Rev. Nucl. Part. Sci.*, 50:37–69, 2000.

[131] K. Werner, Iu. Karpenko, T. Pierog, M. Bleicher, and K. Mikhailov. Event-by-Event Simulation of the Three-Dimensional Hydrodynamic Evolution from Flux Tube Initial Conditions in Ultra-Relativistic Heavy-Ion Collisions. *Phys. Rev. C*, 82:044904, 2010.

[132] K. Werner, Iu. Karpenko, M. Bleicher, T. Pierog, and S. Porteboeuf-Houssais. Jets, Bulk Matter, and their Interaction in Heavy-Ion Collisions at Several TeV. *Phys. Rev. C*, 85:064907, 2012.

[133] Min He, Rainer J. Fries, and Ralf Rapp. Heavy Flavor at the Large Hadron Collider in a Strong Coupling Approach. *Phys. Lett. B*, 735:445–450, 2014.

[134] W.M. Alberico, A. Beraudo, A. De Pace, A. Molinari, M. Monteno, et al. Heavy-Flavour Spectra in High Energy Nucleus–Nucleus Collisions. *Eur. Phys. J. C*, 71: 1666, 2011.

[135] M. Monteno, W.M. Alberico, A. Beraudo, A. De Pace, A. Molinari, et al. Heavy-Flavor Dynamics in Nucleus–Nucleus Collisions: from RHIC to LHC. *J. Phys. G*, 38:124144, 2011.

[136] Thomas Lang, Hendrik van Hees, Jan Steinheimer, and Marcus Bleicher. Heavy-Quark Transport in Heavy-Ion Collisions at RHIC and LHC within the UrQMD Transport Model. [arXiv:1211.6912]. 2012.

[137] Thomas Lang, Hendrik van Hees, Jan Steinheimer, Yu-Peng Yan, and Marcus Bleicher. Heavy-Quark Transport at RHIC and LHC. *J.Phys.Conf.Ser.*, 426: 012032, 2013.

[138] S.A. Bass, M. Belkacem, M. Bleicher, M. Brandstetter, L. Bravina, et al. Microscopic Models for Ultra-Relativistic Heavy-Ion Collisions. *Prog. Part. Nucl. Phys.*, 41:255–369, 1998.

[139] M. Bleicher, E. Zabrodin, C. Spieles, S.A. Bass, C. Ernst, et al. Relativistic Hadron–Hadron Collisions in the Ultra-Relativistic Quantum Molecular Dynamics Model. *J. Phys. G*, 25:1859–1896, 1999.

[140] Shanshan Cao, Guang-You Qin, and Steffen A. Bass. Heavy-Quark Dynamics and Hadronization in Ultra-Relativistic Heavy-Ion Collisions: Collisional Versus Radiative Energy Loss. *Phys. Rev. C*, 88(4):044907, 2013.

[141] B. Abelev et al. Measurement of Prompt D-Meson Production in p–Pb Collisions at $\sqrt{s_{\rm NN}} = 5.02$ TeV. *Phys. Rev. Lett.*, 113:232301, Dec 2014.

[142] Daniel Stump, Joey Huston, Jon Pumplin, Wu-Ki Tung, H.L. Lai, et al. Inclusive Jet Production, Parton Distributions, and the Search for New Physics. *JHEP*, 0310:046, 2003.

[143] Rishi Sharma, Ivan Vitev, and Ben-Wei Zhang. Light-Cone Wave Function Approach to Open Heavy Flavor Dynamics in QCD Matter. *Phys. Rev. C*, 80:054902, 2009.

[144] R. Russo. Measurement of Heavy-Flavour Production as a Function of Multiplicity in pp and p–Pb Collisions with ALICE. *Nucl. Phys. A*, 931:552–557, 2014.

Acknowledgements

I would like to thank my supervisor, Andrea Dainese, for his constant support during my PhD and for being always available for discussion in case of any questions or doubts I had in these three years, his suggestions were fundamental to improve this write up. I am also very grateful to Rosario Turrisi for his experience and the stimulating discussions I had with him, and to all the ALICE group in Padova, that gave me the possibility to attend schools and conferences and allowed me to spend an amazing and fruitful year at CERN. It was a pleasure to work with Davide on the analysis and I am very grateful to him for his help and suggestions and for the time spent learning and discussing about physics, he became also a good friend. Thanks also to Zaida, Francesco and Ralf, they have been great coordinators and I learnt a lot about heavy-flavour physics from the discussions with them during the meetings of the working group. I thank Andrea, Riccardo, Cristina and Grazia, it was a pleasure to cooperate with them in the D meson analysis.

I am very thankful to my parents for their love and for allowing me to pursue my studies and researches, to my sister for being always with me, and to my grandparents for being always proud of my work even if so far from their experiences.

Last, I wish to thank my dear friends Andrea, Luca, Emanuela, Carlo, Emil and Federica, they accompanied me during these years and we shared many enjoying and relaxing moments.